Shock Train Structure and Dynamics

by

Robin L. Hunt

A dissertation submitted in partial fulfillment
of the requirements for the degree of
Doctor of Philosophy
(Aerospace Engineering)
in the University of Michigan
2018

Doctoral Committee:

Assistant Professor Mirko Gamba, Chair
Dr. Jeffrey M. Donbar, Air Force Research Laboratory
Professor James F. Driscoll
Associate Professor Eric Johnsen
Professor Venkatramanan Raman

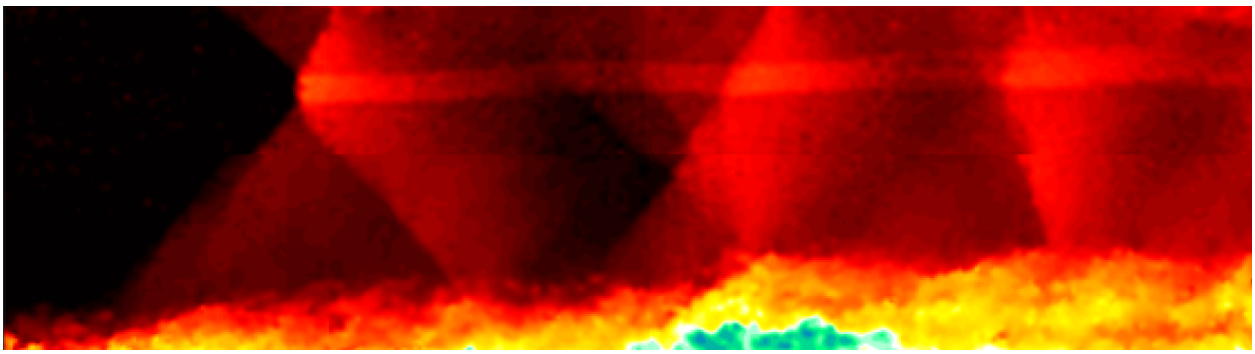

Robin L. Hunt
robinlk@umich.edu
ORCID iD: 0000-0002-8522-3128

ACKNOWLEDGMENTS

I would like to thank the people below who have helped make my research successful:

- ◇ My advisor, Dr. Gamba for his vital support and assistance.
- ◇ Dr. Driscoll, for his guidance throughout my graduate career.
- ◇ My committee members, for their questions and thoughtful contributions.
- ◇ All the staff members and technicians of the Aerospace Department, who made my research possible.
- ◇ Rohan Morajkar and Louis Edelman, for helping me with experiments (without which I would have no thesis).
- ◇ My family and friends, who have encouraged me along the way.

Table of Contents

List of Figures

List of Tables

List of Appendices

List of Abbreviations

PIV particle image velocimetry

SPIV stereo particle image velocimetry

1D one-dimensional

IW interrogation window

PDF probability density function

CFD computational fluid dynamics

List of Symbols

a	Speed of sound (m/s)
B	Blockage area ratio; i.e., the ratio of the cross-sectional area that is blocked by the control valve to the total cross-sectional area.
C_ξ	Confinement based on ξ; $C_\xi = 2\xi/H$
$Co(X, Y)$	Coherence of signals X and Y
D_H	Hydraulic diameter (mm)
E_{pb}	Hysteresis of the back pressure; $E_{pb} = p_{b,u\to d} - [p_{b,d\to u} + \max(p_b) + \min(p_b)]$ (kPa)
E_{x1}	Hysteresis of the leading shock position; $E_{x1} = x_{1,u\to d} - [x_{1,d\to u} + \max(x_1) + \min(x_1)]$ (mm)
f	Frequency (Hz)
H	Isolator height (69.3 mm)
L	Characteristic length scale of the shock train used to non-dimensionalize the frequency content of the inherent unsteadiness; $L = \theta/\sqrt{C_\theta}$ (mm)
L_b	Length of the pseudoshock (mm)
L_m	Length of the mixing region (mm)
L_s	Length of the shock train (mm)
M	Mach number
$\max(\xi)$	Maximum value of ξ (units of ξ)
$\min(\xi)$	Minimum value of ξ (units of ξ)
p	Wall static-pressure (kPa)
p_b	Back pressure measured at the end of the isolator (kPa)
p_f	Pressure at the foot of the shock train (kPa)
p_s	Pressure at the end of the shock train (kPa)
$(p_2/p_1)_\perp$	Pressure rise across a normal shock
$PSD(\xi)$	Power spectral density of signal ξ (units of ξ^2/Hz)
Q	Waltrup and Billig correction factor, $Q = (M^2 - 1)Re_\theta^{1/4} C_\theta^{-1/2}$
Re_ξ	Reynolds number based on ξ
s	Mach stem height (mm)
St	Dimensionless Strouhal number; $St = fL/u_\infty$.
T	Temperature (K)
T_c	Characteristic time of the inherent unsteadiness; $T_c = x_c'/u_c$ (ms)
T_{pb}	Back pressure rise time (ms)
T_{x1}	Leading shock position rise time (ms)
T_Θ	Disturbance rise time; i.e., the time it takes the valve to change angles (ms)

t	Time (ms)
u	Component of flow velocity along the streamwise x-direction (m/s)
u_c	Characteristic velocity of the shock train as it fluctuates due to inherent unsteadiness; $u_c = \text{rms}(u_i)$ (m/s)
u_i	Streamwise speed of the ith shock in the shock train (m/s)
u_{pert}	Propagation speed of a perturbation (m/s)
u_∞	Freestream flow velocity in the streamwise x-direction prior to the shock train (m/s)
v	Component of flow velocity along the transverse y-direction (m/s)
W	Isolator width (57.2 mm)
w	Component of flow velocity along the vertical z-direction (m/s)
x	Coordinate in the streamwise direction (mm)
$\widetilde{x}$	x-location relative to the leading shock foot, $\widetilde{x} = x - x_f$ (mm)
x^*	x-location relative to the leading shock Mach stem, $x^* = x - x_1$ (mm)
x_b	Location where the pseudoshock ends and the back pressure is measured (mm)
x_c'	Characteristic length scale of the inherent unsteadiness; $x_c' = \text{rms}(x')$ (mm)
x_f	Location of the pseudoshock foot (mm)
x_i	x-location of the ith shock in the shock train relative to the wind tunnel throat with $i \in \{1, 1l, 1r, 2c, 2b, 2t, 3b, 3t, 4b, 4t\}$ (mm)
x_s	Location where the shock train ends (and mixing region begins) (mm)
y	Coordinate in the transverse direction (mm)
z	Coordinate in the vertical direction (mm)
α_L	Angle of the leading leg in the first shock lambda foot (deg)
α_R	Angle of the trailing leg of the first shock lambda foot (deg)
ΔB	Change in the blockage area ratio during forcing; i.e., the disturbance magnitude
Δp_b	Change in back pressure during forcing (kPa)
Δt	Time the the valve angle is stationary during a forcing cycle (ms)
Δx_1	Change in leading shock position during forcing (mm)
$\Delta\Theta$	Change in valve angle during forcing (deg)
δ	Boundary layer thickness (mm)
δ^*	Boundary layer displacement thickness (mm)
Γ	Dimensionless vortex identifier
Ω	Forcing frequency; $\Omega = 1/[2(T_\Theta + \Delta t)]$ (Hz)
$\sigma(\xi)$	Standard deviation of ξ (units of ξ)
$\tau(X, Y)$	Time delay computed from the cross-spectrum of signals X and Y (ms)
τ_{pb}	Delay time from the onset of the valve angle change to the back pressure response (ms)
τ_{x1}	Delay time from the onset of the valve angle change to the shock position response (ms)
Θ	Angle of the control valve
θ	Boundary layer momentum thickness (mm)

Subscripts

ξ_u	Value of ξ when the shock train is at its upstream state during the forcing process (units of ξ)
ξ_d	Value of ξ when the shock train is at its downstream state during the forcing process (units of ξ)

Superscripts

ξ'	Fluctuation component of ξ; $\xi' = \xi - \langle\xi\rangle$ (units of ξ)

Operations

$\lvert(\xi)\rvert$	Absolute value of ξ (units of ξ)
$\langle\xi\rangle$	Time-averaged value of ξ (units of ξ)
$\widetilde{\xi}$	Normalized value of ξ between 0 and 1; $\widetilde{\xi} = [\xi - \min(\xi)]/[\max(\xi) - \min(\xi)]$

Other

$\mathrm{u} \rightarrow \mathrm{d}$	The value of ξ during the upstream to downstream transition
$\mathrm{d} \rightarrow \mathrm{u}$	The value of ξ during the upstream to downstream transition

Abstract

The structure and dynamics of a shock train are studied experimentally using a direct-connect isolator model with a nominal inflow Mach number of 2.0. The experiments mimic the flow in high-speed air-breathing engines, where the shock train is responsible for slowing and compressing the flow prior to the combustor. In place of a combustion process, a control valve is situated downstream of the isolator model and is used to induce a downstream pressure rise, thus generating the shock train and controlling its location in the isolator. Quantifying and understanding the shock train is critical to the development of more predictive modeling tools for high-speed engine design.

First, schlieren imaging is used to study the shock train oblique-to-normal transition as the pressure downstream of the isolator is increased. During this process, the shock system moves upstream where the approach conditions are different, as these quantities vary naturally along the isolator length. Thus, the sensitivity of the structural features to changes in the approach conditions is effectively evaluated. Pressure measurements are used to quantify how the transition process impacts important isolator design properties, including the system length and pressure rise. It is found that the shock train becomes shorter and provides less of the overall compression as it moves upstream, but these quantities are constant when normalized by the approach conditions. Thus, the mixing region adjusts so that the overall conditions meet the imposed downstream pressure condition. These results indicate an axisymmetric flow that does not appear in schlieren images. Stereo PIV is used to investigate the three-dimensional shock structure and it is found that large separated regions confine the flow and lead to a conical leading shock structure.

One of the primary contributions of this work is the development of a theory that explains why the shock train is inherently unsteady even when the bulk inflow and outflow conditions are constant. Cross-spectral analysis of pressure and shock position fluctuations is used to identify perturbations that travel through the isolator and determine how they interact with the shock system. Oil flow visualization and PIV are used to uncover the physical structure of the perturbations and the fluid phenomenon that generates them. The results identify a complex, frequency-dependent dynamical system that is influenced by several perturbations including: acoustic waves emanating from separation bubbles that interact with the leading shock; vortices shed from separation bubbles that convect downstream and interact with downstream shocks; acoustic waves generated in

the diffuser section that propagate upstream and impact the leading shock.

The inherent unsteadiness theory introduces several mechanisms that explain how perturbations influence the shock system. One mechanism links downstream disturbances to the isolator dynamics. To examine this further, oscillatory downstream forcing imposed and the resulting shock train response is investigated using schlieren imaging and pressure measurements. It is found that the shock system response is delayed from the onset of the disturbance due to the relatively low speed of an acoustic wave that travels upstream through the boundary layer before impacting the shock position. This is the same mechanism introduced by the inherent unsteadiness theory, emphasizing similar forcing and inherent unsteadiness dynamics. Generally, increasing the disturbance magnitude induces a larger shock displacement with a significant hysteresis effect where the shock position has a different time history as it travels upstream and downstream. However, the magnitude of the shock response is mitigated by short disturbance rise times.

Chapter 1

Introduction

1.1 Background and Broad Motivation

A shock train is a complex, three-dimensional system of shock and compression waves that decelerates a supersonic flow in a duct. It is essentially a system of coupled shock wave boundary layer interactions. If the duct is sufficiently long, the shock train is followed by a mixing region where no shocks exist but a heterogeneous supersonic-subsonic velocity distribution causes turbulent mixing that leads to additional static pressure rise. The entire region from the beginning of the shock train to the end of the mixing region is called the pseudoshock [Matsuo *et al.*, 1999; Gnani *et al.*, 2015].

The pseudoshock is a critical fluid phenomenon in high-speed air-breathing engines, such as ramjets and dual mode scramjets. Consider the typical operation of these engines as illustrated in figure 1.1. The incoming flow is first compressed by shocks formed by the forebody and inlet. After the compression process in the inlet, a substantial amount of additional compression is provided by the pseudoshock, which is housed in a short length of duct called the isolator section. Together, the external and internal compression processes decelerate the incoming supersonic flow from the inlet to provide the necessary static pressure rise for efficient combustion downstream.

The pseudoshock is highly coupled with the combustion process because the heat release generates a local downstream pressure rise that ultimately sustains the pseudoshock within the isolator.

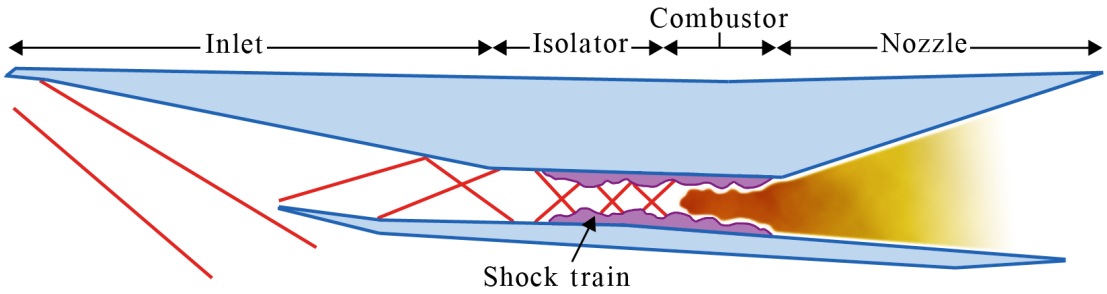

Figure 1.1: Diagram of a high-speed air-breathing engine adapted from NASA Langley.

The pseudoshock must be positioned at a location in the isolator such that the approach flow conditions (i.e., the local flow conditions just upstream of the shock train) can be processed by the shock system to match the downstream boundary condition imposed by the combustor. If the local pressure rise in the combustor changes as the vehicle follows its desired flight trajectory, for example if the fueling scheme is altered, then the pseudoshock responds by moving to a new location in the isolator.

Excessive heat release in the combustor may generate a pressure rise that is too large for the pseudoshock to accommodate, and in extreme cases the shock system propagates upstream until it is disgorged from the inlet in a transient process known as engine unstart. When the shock train is ejected, a bow shock forms outside of the inlet leading to flow spillage and reduced mass flow rate through the engine. As a consequence, there is loss of engine thrust, significantly increased aerodynamic loads, and potentially intense oscillatory flow [Rodi *et al.*, 1996; Wagner *et al.*, 2009]. The threat of engine unstart emphasizes the importance of the isolator section as this component essentially buffers the inlet from the downstream disturbances caused by the combustion process.

From a design point of view, the isolator is optimized by balancing three elements: 1) the weight of the isolator and the associated drag; 2) the amount of pressure rise needed for efficient combustion; and 3) the robustness of the isolator across a range of operating conditions to ensure unstart is avoided. Thus, the ability to predict and control the properties of the pseudoshock could improve the overall performance of the engine. Developing a better understanding of the pseudoshock properties to aid engine design is the overarching motivation of this work.

Pseudoshocks have been studied extensively ever since Crocco [1958] pointed out that the transition from supersonic to subsonic conditions in ducted flows is normally a complex and gradual flow diffusion process, not a single discontinuity from a normal shock as predicted by inviscid theory. In particular, there is ample research with interest in the shock train structure as well as the overall pseudoshock length and pressure rise. These properties have been found to depend on various parameters including the duct geometry, Mach number, Reynolds number, and boundary layer properties, which emphasizes the complex nature of the pseudoshock system [Matsuo *et al.*, 1999; Gnani *et al.*, 2015].

Several empirical and analytical models have been developed to predict the net changes in the flow properties across the pseudoshock without detailed knowledge of the flow structure [Waltrup & Billig, 1973; Ikui *et al.*, 1981; Smart, 2015]. However, these models cannot accurately predict the pseudoshock characteristics across a wide range of flow conditions because the results depend on a multitude of different parameters as discussed previously. Thus, the detailed properties of the pseudoshock need to be considered to generate more predictive models of these flows.

More recently, computational simulations have become an important tool to better model the complexity of the pseudoshock system [Cox-Stouffer & Hagenmaier, 2001; Koo & Raman, 2012;

Morgan *et al.*, 2014; Fiévet *et al.*, 2017]. These simulations in conjunction with experiments have aided in developing a better understanding of how the pseudoshock depends on the duct geometry and flow conditions [Carroll, 1993; Sun *et al.*, 2003; Lin *et al.*, 2006]. Despite great effort in this research area, many aspects of pseudoshocks are still not well understood because the complex interplay between the multiple types of interactions makes quantification and prediction of this flow field very challenging.

1.2 Overview of What is Accomplished in This Work

In this work, we experimentally study the shock train structure and, more importantly, the complex dynamics of the shock system over a range of approach conditions. Quantifying and understanding these properties and processes, as well as their relationships to the underlying approach flow, is critical to the development and improvement of more predictive modeling tools for isolator design. A direct-connect isolator model with a nominal inflow Mach number of 2.0 is used to study the shock train. A downstream valve (analogous to the combustor) mechanically controls the downstream pressure and thus influences the shock train position within the isolator.

The first subject of this study, structure and three-dimensionality, is a necessary starting point used to characterize the basic properties of a shock train. Specifically, high-speed schlieren imaging is used to look at how the shock structure changes when the shock train is positioned at different points in the isolator section. The analysis of these schlieren videos clarifies what is called the oblique-to-normal transition process. Shock train structure is well studied in the literature but the details of the transition process have not been discussed and it is unclear if these structural changes impact critical design parameters such as the pressure rise and length of the system. To address this topic, an objective method based on time-averaged pressure measurements is proposed to identify the end of the shock train region (i.e., the beginning of the mixing region). Thus, the pressure rise and length of both the shock train and mixing region are quantified. Unlike most empirical and analytical models presented in the literature, we specifically separate the shock train from the mixing region and argue that these components contribute to the overall pseudoshock properties differently because they are dominated by different phenomena. That is, the properties of the shock train and mixing region scale differently with the approach conditions. The recognition of this aspect is a critical contribution of this work. Finally, the results of the time-averaged pressure measurements indicate a highly three-dimensional structure, which is confirmed using stereo particle image velocimetry (SPIV) measurements of the leading shock. This work contributes to the understanding where flow separation occurs in the shock train and how these large separated regions confine the flow, leading to a degree of axisymmetry that is associated with a conical shock structure. While not the main contribution of the work, this section provides interesting and valuable information

on the shock train that has not been examined before.

One of the main contributions of this work is the development of a theory that explains why the shock train is inherently unsteady even when the bulk inflow and outflow are constant. That is, the shock system fluctuates about its time-averaged position despite the isolator's constant boundary conditions. While inherent unsteadiness has been mentioned in the literature, it is unclear if the unsteady behavior depends on the downstream pressure condition in the combustor. In addition, very few works have tried to explain the fundamental physics that drive this process. In particular, the fluid phenomena that cause the unsteadiness have not been identified. Three theories have been presented in the literature that propose different sources of the unsteadiness [Ikui *et al.*, 1974*b*; Yamane *et al.*, 1984*a*; Sugiyama *et al.*, 1988], but these theories are incomplete and have not been verified or reconciled. Inherent unsteadiness is widely recognized as a complicating factor that hinders both experimental studies and computational modeling. A better understanding of the physics is needed to properly account for these effects and ultimately, the ability to predict and control shock wave structures in the isolator will enhance engine performance and is essential for developing control strategies. The inherent unsteadiness theory we present is explained in terms of perturbations that travel through the isolator and influence the shock motion. The basis of the theory is developed using cross-spectral analysis on high-speed pressure measurements and schlieren movies to determine the location where perturbations originate, the direction they travel, and how they influence the shock system. Then, oil flow visualization and particle image velocimetry (PIV) are used to confirm what fluid phenomenon generate the perturbations. The PIV measurements of the shock train are the first of their kind. In addition to supporting the unsteadiness theory, this information is useful for developing shock train models and validating computational work.

The unsteadiness theory introduces a possible mechanism that explains how downstream disturbances travel through the isolator and impact the shock motion. Understanding this mechanism would explain how the combustor dynamics are coupled to the shock train response. This is important because the ability to predict the shock train response to changes in combustor conditions is useful for implementing control mechanisms and avoiding unstart. To examine this idea further, low frequency, high magnitude forcing is applied to the system by slowly oscillating the downstream valve (analogous to oscillating the pressure induced by the combustion process). As a result, the shock train oscillates between two positions in the isolator. High-speed schlieren imaging is used to study the shock train dynamics for different cases where the following are varied: 1) the rate at which the downstream pressure is changed and 2) the magnitude of the downstream pressure change. A thorough investigation of these parameters has not been presented in the literature before. In fact, the majority of past work has considered the dynamics during unstart [Rodi *et al.*, 1996; Tan & Guo, 2007; Wagner *et al.*, 2009; Tan *et al.*, 2011; Do, 2011; Laurence *et al.*, 2013]. Fewer studies have considered the shock train response to a relatively smaller downstream distur-

bances (i.e., without causing unstart) and primarily in the context of shock location identification methods and examining the effectiveness of control methods [Sajben *et al.*, 1992; Le *et al.*, 2008; Weiss & Olivier, 2012; Hutzel *et al.*, 2011; Hoeger *et al.*, 2011; Valdivia *et al.*, 2014; Huang *et al.*, 2014]. Thus, this work contributes to the understanding of shock train dynamics when perturbed by changes in the downstream pressure at varied rates and magnitudes.

In the following three sections, each topic of interest is motivated by reviewing the pertinent literature. Then, the specific objectives of the current work are discussed.

1.3 Shock Train Structure and Three-Dimensionality

1.3.1 Literature Review

Figure 1.2 shows two schematics, inspired by Matsuo *et al.* [1999], of different types of shock trains typically encountered in the pseudoshock system: the *normal* and *oblique* shock trains. A normal shock train generally has a leading bifurcated normal shock followed by several non-bifurcated shocks. After each normal shock is a re-acceleration region where the core flow speed increases back to supersonic conditions. In an oblique shock train, right-running and left-running oblique shock waves are generated from opposite walls of the duct and cross to form an "X" pattern. Multiple "X" structures form the shock train.

Based on the literature, the approach Mach number is the most influential parameter on shock train structure and strongly influences whether the shock train is oblique or normal [Ikui *et al.*, 1974*a*; Nill & Mattick, 1996; Matsuo *et al.*, 1999; Miyazato *et al.*, 2009]. While less work has investigated the Reynolds number based on the duct geometry, Merkli [1976] showed that this parameter is perhaps not important. Another parameter to consider is the degree of flow confinement, typically defined as the ratio of boundary layer thickness or momentum thickness to test section half height. The degree of flow confinement just upstream of the shock train also has an effect, although secondary, on shock train structure. In particular, confinement can impact the length of the shock train and the spacing between consecutive shocks [Carroll, 1988; Nill & Mattick, 1996; Fotia & Driscoll, 2012]. For example, Fiévet *et al.* [2017] conducted a computational study on the effects of confinement where the simulation configuration is chosen to replicate the experimental setup used in this work. They found that the pseudoshock moves downstream in the isolator when there is a reduction in the boundary layer thickness. Simultaneously, the normal-like portion of the leading bifurcating shock increases, the shocks become stronger, and less shocks form the shock train. This means the pseudoshock becomes more spatially compressed as the confinement ratio decreases.

While there is a substantial amount of work in the literature that examines the shock train struc-

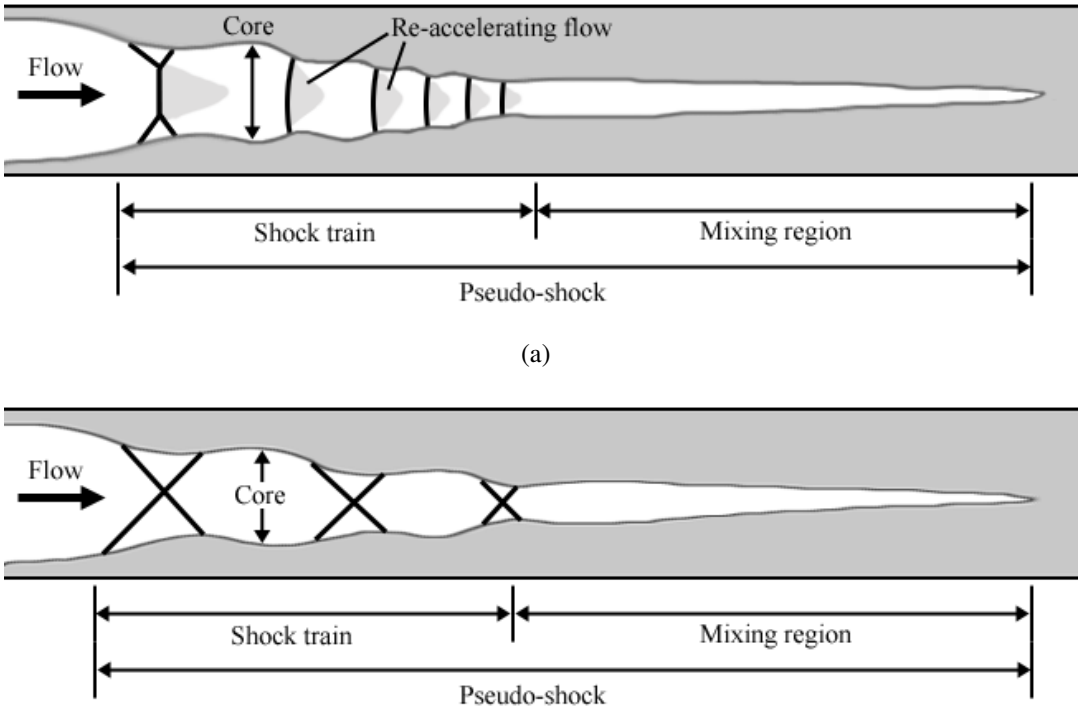

Figure 1.2: Schematic of a pseudoshock adapted from Matsuo *et al.* [1999]: (a) normal shock train; (b) oblique shock train.

ture, there is little discussion about the process by which the shock train transitions from oblique to normal. For example, consider the regime diagram shown in figure 1.3 that was developed by collecting the results of several prior studies where the shape of the leading shock could be visually confirmed (i.e., shadowgraph or schlieren images are available). The results demonstrate that normal shock trains (blue symbols) exist at Mach numbers less than 1.7 and oblique shock trains (red symbols) form at Mach numbers above 2.2. Within the transition regime (Mach 1.7 to 2.2) both oblique and normal shock waves have been observed and it appears that flow confinement may play some role in determining the shock train structure.

To date, much about the oblique-to-normal transition process is unknown although it occurs in many practical situations. For example, the Mach number range associated with the transition process is common in many flight trajectories. In this scenario, a change in the inflow conditions or a change in the downstream pressure generated by the combustion process will move the shock train to a new position in the isolator where the approach Mach number and confinement are different. As a result, the shock train structure is altered. The transition process is potentially important because it may be accompanied by changes in other properties including the length and pressure rise of the system. These two properties are of interest because the isolator must be

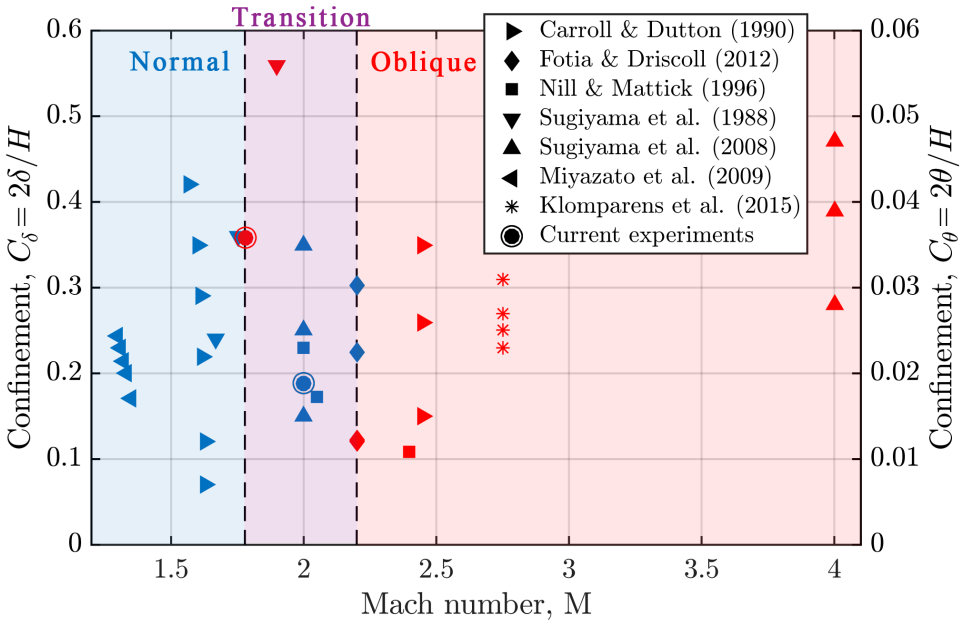

Figure 1.3: Shock train regime diagram distinguishing between oblique shock trains(red markers) and normal shock trains (blue markers). The maximum and minimum cases of confinement for the current experiments are indicated by the circles.

designed to provide sufficient compression of the flow entering the combustor while minimizing the length and weight of the isolator itself. Thus, isolator designs can be optimized by clarifying the transition process and evaluating its effects on important shock train design properties.

To emphasize the dependence of the pseudoshock length and pressure rise on the approach conditions, consider figure 1.4 which is adapted from the review work of Matsuo *et al.* [1999]. Part (a) of the figure demonstrates how the maximum length of the pseudoshock normalized by the equivalent diameter of the duct depends on the approach Mach number. Note that the maximum pseudoshock length may only be observed if the duct / isolator is sufficiently long to hold the entire shock train and mixing region, downstream of which the pressure begins to slowly decrease. Part (b) of the figure shows how the maximum pressure rise across the pseudoshock, p_b/p_f, varies with Mach number. In this case, the maximum pseudoshock pressure rise is normalized by the pressure rise across a normal shock at the same approach Mach number, $(p_2/p_1)_\perp$. Clearly, there is significant spread in both parts (a) and (b) of the figure. This is likely due to the fact that the other approach flow conditions, including flow confinement, varies across the experiments. To reduce the scattering, the effects of these other parameters need to be accounted for.

Several models have been proposed in the literature to predict the pseudoshock length and pressure rise but these typically do not take the shock structure into account. In addition, no model can properly predict the pseudoshock characteristics with good accuracy across a wide range of

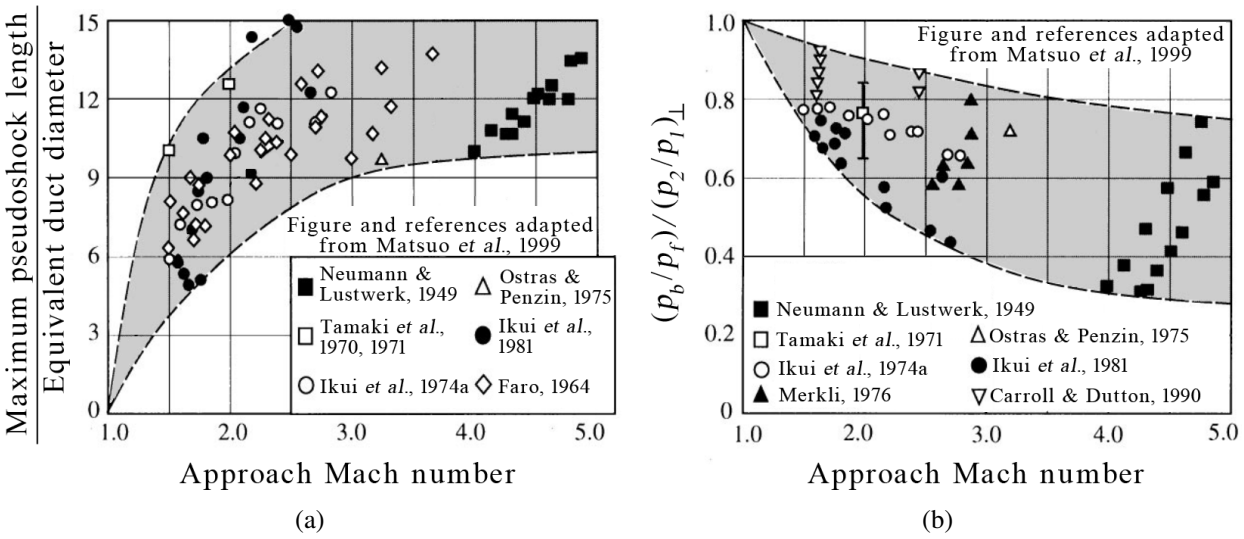

Figure 1.4: Figures adapted from Matsuo *et al.* [1999]: (a) maximum pseudoshock length versus approach Mach number; (b) maximum pressure rise across the pseudoshock versus Mach number.

flow conditions. For example, Waltrup and BilligWaltrup & Billig [1973] proposed the following simple quadratic relationship based on empirical data. The relationship uses the approach flow properties to describe the pressure distribution along the length of the pseudoshock as follows:

$$50\left(\frac{p}{p_f}-1\right)+170\left(\frac{p}{p_f}-1\right)^2=\frac{\widetilde{x}(M^2-1)Re_\theta^{1/4}}{\sqrt{H\theta}} \tag{1.1}$$

where p is the pressure a distance $\widetilde{x}$ away from the leading shock foot, p_f is the pressure at the leading shock foot, M is the upstream Mach number, Re_θ is the upstream Reynolds number based on boundary layer momentum thickness, H is the tunnel height, and θ is the upstream boundary layer momentum thickness. While this relationship collapses the data well for the Waltrup and Billig experimental setup, it fails to accurately predict both the overall pseudoshock length and the pressure distribution in many other cases [Wang *et al.*, 2006; Fotia & Driscoll, 2012; Geerts & Yu, 2015; Oka *et al.*, 2014]. Corrections to the Waltrup and Billig relationship have been introduced but these are not well tested and often introduce significant complexity. For example, Fischer & Olivier [2014] added a correction for wall temperature effects and Geerts & Yu [2015] proposed a correction based on the differences in momentum thicknesses observed on different walls.

Several analytical models have also been presented in the literature in order to predict the pseudoshock length and pressure rise. Crocco [1958] proposed the *shockless model* which assumes that the presence of shocks may be disregarded entirely and the main flow is uniform and isentropic. While this model describes the general characteristics of the pseudoshock, its assumptions are grossly inaccurate and thus it cannot be used to quantitatively compute the pseudoshock properties.

Ikui *et al.* [1974*a*] improved on Crocco's shockless model by removing the assumption that the core flow is isentropic and by adding a diffusion term between the core flow and boundary layer within the pseudoshock. Their final *modified diffusion model* also adds in the effects of the upstream boundary layer and wall friction [Ikui *et al.*, 1981]. When compared to experiments, the importance of the wall friction term becomes clear. In particular, at low approach Mach numbers this term is needed to accurately capture the pressure distribution. They hypothesize that at high Mach numbers there is a large separated region of the flow and thus the wall friction is negligible. This would explain why the model is more accurate for these higher Mach number cases.

Recently, Smart [2015] proposed a pseudoshock model based on the diffuser equation of Ortwerth [2001] and the differential equations of mass, momentum, and energy developed for the control volume following the method of Shapiro [1953]. This set of three differential equations uses the one-dimensional flux conserved properties of the flow to compute the complete pressure distribution of pseudoshocks in variable area ducts with friction, heat transfer, and heat release from combustion. The model adequately predicts the length and pressure distribution for cases where the approach Mach number is high (e.g., $M = 2.87$). However, at lower Mach numbers the accuracy is much worse. This problem may stem from the assumption that the skin friction coefficient is zero throughout the pseudoshock. In addition, the results of the model are sensitive to an arbitrary constant and the minimum skin friction coefficient at the initial separation point, which is difficult to measure experimentally or otherwise know in practical situations.

The above discussion outlines some examples of the numerous pseudoshock models available in the literature. However, it is important to emphasize again that none of these models can properly predict the pseudoshock characteristics with good accuracy across a wide range of flow conditions. Generally, these models are very simple, one-dimensional representations of a truly complex flow field. A more detailed knowledge of the pseudoshock may need to be considered to improve model accuracy. For example, the analytical models mentioned above describe the entire pseudoshock as a primarily inviscid system that is controlled by the growth rate of the boundary layers. While the core flow of the shock train may be well described as an inviscid flow, the mixing region is dominated by turbulent, viscous forces. Thus, the two components of the pseudoshock may need to be modeled differently because they are dominated by different physics. A proper model for the mixing region would improve length and pressure rise estimations. In addition, side-wall effects and the resulting three-dimensionality of the pseudoshock are not typically included in models. As we see in the discussion below, these effects may greatly influence the pseudoshock properties and it is worth investigating this topic further.

Thus far, the shock train structure has been discussed in a two-dimensional sense. That is, the structure of the shock train is classified as oblique or normal based on a two-dimensional projected image (i.e., schlieren or shadowgraph images). In reality, the physical structure of the system is

more complex due to the overall three-dimensionality of the flowfield itself. For example, Sullins & McLafferty [1992] hypothesized that the shock train in their experimental setup is roughly symmetric because the pressure distributions on different walls of the isolator are very similar despite major differences in the boundary layers. While this is not a universal feature across all experimental setups, it motivates the discussion on three-dimensionality. One reason for differences across experiments is that the aspect ratio of the duct (i.e., the ratio between the height and width of the duct) has been found to contribute to the three-dimensionality of the system, with high aspect ratio ducts showing more symmetrical structures [Geerts & Yu, 2016]. To understand the precise flow structure, Handa *et al.* [2005] used a laser-induced-fluorescence method to visualize parts of the shock train. They specifically examine the structure of the shock train in the corner of a duct and propose that the leading shock is formed by the interaction between two bifurcated shock waves developed on two perpendicularly adjacent walls.

Side-wall boundary layers have proven to be important in computational models as well. Morgan *et al.* [2012, 2014] found that the overall diffusion process through the shock train better agrees with experiments when the side-wall boundary layers are fully resolved in their computational model. In addition, they showed that the inclusion of the side-wall confinement effect may lead to unstart.

Clearly, the boundary layers and inevitable side-wall effects play a large role in determining the three-dimensionality of the shock train system but given the limited number of studies on this topic there are many unanswered questions. For instance, the rapid boundary layer growth along the shock train length raises the question of where flow separation within the shock train might occur. This is important because as the amount of separation increases, the core flow becomes more restricted and the state of the boundary layer will affect the unstart dynamics [Do, 2011]. In many cases, separated regions are inferred from schlieren or shadowgraph images but these do not definitively prove that there is reverse flow (separation). Some studies have used oil visualization or similar methods to identify separation regions [Carroll, 1988; Om & Childs, 1985]. However, the results are not consistent, are purely qualitative, and only indicate flow directions at the surface.

1.3.2 Objectives of the Current Work

There are three objectives related to the structure and three-dimensionality of the shock train. The first objective is to formalize the oblique-to-normal transition process by quantifying how morphological features of the shock train, such as the shock angles and Mach stem height, change when the downstream pressure is increased. Increasing the downstream pressure also causes the shock train to move upstream where the approach conditions (including Mach number and confinement) are different, as these quantities vary along the isolator length. Thus, the sensitivity of shock train structural features to changes in the approach conditions are effectively evaluated. The second

objective is to evaluate how the length and pressure rise of the shock train and mixing region are impacted by a change in the downstream pressure. This information tells us if the structural transition process is associated with changes in pseudoshock properties that are important for isolator design. In addition, by separately evaluating the shock train and the mixing region, we determine if the design quantities scale differently with the approach conditions, as the pseudoshock components are dominated by different physics. The final objective is to quantify the three-dimensional shape of the leading shock front and the amount of flow separation under this shock. Ultimately, this work contributes the understanding of how large separated regions confine the flow and lead to a degree of axisymmetry that is associated with a conical shock structure.

1.4 The Physics of Shock Train Inherent Unsteadiness

1.4.1 Literature Review

As discussed in the previous section, the shock train characteristics depend on a large number of variables including Mach number, duct geometry, boundary layer properties, and the downstream pressure condition. To complicate matters, the fluid system exhibits *inherent unsteadiness*, which are self-excited fluctuations of the shock train system about its time-averaged position even with constant bulk inflow and outflow isolator conditions. This mode of operation is defined as *quasi-steady state* due to the existence of the shock train inherent unsteadiness.

The magnitude of the shock position fluctuations varies depending on the flow conditions, with some experimental studies reporting shock displacements reaching up to a duct height [Ikui *et al.*, 1974*b*; Carroll, 1988; Sugiyama *et al.*, 2008; Lindstrom *et al.*, 2009]. For the experimental setup of this work, the shock train fluctuates up to 0.26 duct heights away from its time-averaged position and travels at speeds up to 16 m/s, i.e., 3% of the freestream flow speed (see chapter 5). Recently, Xiong *et al.* [2017*a*] also proposed that the shock system unsteadiness depends on the boundary layer. In their experiments they found that the leading shock fluctuates over a smaller region and fluctuates at a higher frequency when the boundary layer is smaller. While characterizing the shock motion in this work, we did not see this trend. In fact, for the current experiments the unsteadiness does not appear to depend on the back pressure condition, i.e., where the shock train is located in the isolator section. Clearly, these discrepancies must be explained.

The unsteady movement of the shock train is of practical importance because it may feed instabilities to the combustor and induce pressure fluctuations that generate noise and fluctuating wall loads, both of which need to be minimized [Ikui *et al.*, 1974*b*; Nill & Mattick, 1996]. Also, large fluctuation amplitudes may lead to premature engine unstart and thus reduce the operating margin of the engine.

While the existence of shock train inherent unsteadiness has been documented in past studies, few studies have examined the underlying fundamental flow physics that govern the unsteadiness. To date, three principal theories have been proposed to explain shock train inherent unsteadiness. Each of these theories suggest a different origin for perturbations, the flow phenomena that instigate a change in the shock system.

Ikui *et al.* [1974*b*] were among the first to present a theory. Based on schlieren photographs, they found that the first shock in the train oscillates before the second shock. In addition, wall static pressure measurements taken upstream of the shock train exhibited small fluctuations. Given these experimental data they conjecture that the shock train unsteadiness is due to the interaction of the leading shock with small perturbations in the upstream supersonic flow. This theory is supported by a one-dimensional viscous adiabatic flow model for a single normal shock presented in their paper. When a small upstream perturbation is input into the model, the resulting shock and pressure fluctuation amplitudes agree well with measurements. Although they measure pressure fluctuations in the incoming flow (i.e., upstream of the shock train) and their observation is supported by their model, the authors do not show a direct correlation between upstream pressure fluctuation and shock motion.

Yamane *et al.* [1984*a*] investigated shock train unsteadiness further in a blowdown wind tunnel with a variable duct length. They found that longer ducts are choked at the duct exit leading to 1) different dominant oscillation modes in the pressure fluctuations at the rear of the duct and in the diffuser section of the wind tunnel and 2) lower shock oscillation amplitudes. The opposite was found to be true for unchoked ducts. Based on these results, the authors conjecture that the oscillation of the shock train in an unchoked duct is caused by acoustic resonance in the "divergent passage" (i.e., the diffuser section). When the duct is choked, then the flow upstream is isolated from these oscillations. In their follow-up study [Yamane *et al.*, 1984*b*], cross-correlations between pressure measurements at different locations are used to supplement their theory. The cross-correlations show that there exists a high and low frequency component to the shock motion that correspond to a downstream and upstream propagating perturbation moving at 230 m/s and 100 m/s, respectively. Given the low speed of the upstream propagating perturbation, the authors hypothesize that this perturbation is a pressure wave generated in the divergent passage, which then excites the leading shock prompting a downstream propagating perturbation that is convected with the main flow. Yamane *et al.* [1984*a*] present a theory with emerging evidence of multiple perturbation pathways as demonstrated by the cross-correlation results. However, their connection between the fluid movement in the divergent passage and the shock fluctuations does not fully explain the observed unsteadiness. For instance, the shock train still exhibits unsteady fluctuations in a choked duct even though it is isolated from the source of unsteadiness.

Sugiyama *et al.* [1988] suggest that the source of unsteadiness is within the shock train it-

self. Using schlieren images, they found that the boundary layer thickness under the first shock is weakly correlated with the shock position. A growth in boundary layer thickness leads to the shock moving upstream while a decrease in boundary layer thickness leads to the shock moving downstream. The authors describe this as an aerodynamic "throat" effect where the low-momentum boundary layers act as a converging-diverging nozzle. Once the leading shock fluctuates, the second and third shocks respond in order, as demonstrated by cross-correlations between different shock position time traces. They find that the shock wave oscillation propagates to the downstream shocks at 60 – 100 m/s. This work presents a new and plausible theory but with insufficient evidence because the cross-correlation between boundary layer thickness and shock position is weak (the maximum magnitude of the cross-correlation amplitude was found to be less than 0.2). The authors also fail to explain 1) why the boundary layer thickness is changing and 2) why the frequency content of the boundary layer thickness fluctuation is significantly different than that of the shock position fluctuation.

The three theories described above propose different causes of shock train inherent unsteadiness and it is possible that any, or even all of them, influence the shock train to some extent. However, these works have not been verified or reconciled. Further research on this topic is motivated by the desire to develop a better understanding of the underlying flow physics that govern the unsteadiness. Ultimately, the ability to predict and control motion of the shock waves in the isolator will enhance engine performance and is essential for developing control strategies.

1.4.2 Objectives of the Current Work

The objective of the current work is to combine some of the previous theory with new experimental observations to develop a new comprehensive explanation for the inherent unsteadiness of the shock train system. This theory is presented in terms of a complex frequency-dependent system of perturbations and their interactions with the shock system. The following information is identified for each perturbation: 1) the *source* of the perturbation, which is defined to be the fluid phenomenon that generates the perturbation; 2) the *pathway* of the perturbation, which is defined to be the region the perturbation originates from and where it travels to along the duct; and 3) the *mechanism* of the perturbation, which is defined to be how the perturbation propagates and interacts with the shock waves. Thus, a clear cause-and-effect relationship is established between the fluid phenomena that generate perturbations and the unsteady motion of the shock system.

1.5 Shock Train Dynamics with Forcing Applied

1.5.1 Literature Review

In chapter 5, one of the many perturbations that contribute to the shock train inherent unsteadiness is identified originating downstream of the isolator and propagating upstream through the boundary layer. It is hypothesized that this is the mechanism by which downstream information is communicated to the shock train, thus coupling the dynamics in the isolator and combustor. In order to gain additional insight on this mechanism, low-frequency oscillation of the downstream pressure (without causing unstart) is used as a way to mimic the perturbation. This is analogous to the combustor experiencing transient combustion processes; for example during the initial ignition stage or as the fueling scheme is changed (e.g., fueling rate, position, etc.). These transient combustion phenomena alter the combustor pressure and subsequently change the shock train position in the isolator. The resulting motion of the shock train is termed the *forced dynamics* of the system. The threat is that a large downstream pressure increase induced by rapid combustion transients may lead to engine unstart. Understanding the forced dynamics of the shock train and the mechanism by which the shock train is coupled with the combustor dynamics is important for 1) optimizing engine performance, 2) developing engine control strategies, and 3) predicting and preventing unstart.

In recent years, many studies have analyzed the unstart process and the resulting unsteady flow that follows [Rodi *et al.*, 1996; Tan & Guo, 2007; Tan *et al.*, 2011; Do, 2011; Laurence *et al.*, 2013]. In addition, some passive and active flow control methods including suction slots [Weiss & Olivier, 2012], vortex generators [Valdivia *et al.*, 2014], and mass injection [Huang *et al.*, 2014] have been applied to the isolator flow in an attempt to prevent or delay unstart. In these unstart studies, the isolator dynamics are the result of a massive downstream pressure rise. Thus, these studies are not quite applicable to the current problem because the desire is to study the dynamics prior to unstart in an effort to avoid this detrimental process altogether. Nonetheless, similarities between the two cases may exist and thus important insight can be gained from these unstart studies. For example, Wagner *et al.* [2010] found that the shock train propagates upstream at approximately 4.7% of the freestream flow velocity ($0.047u_\infty$) during the unstart process. They also showed that the speed of the shock train during unstart is independent of how fast the downstream pressure is applied for their range of experimental conditions. However, the time scale of the pressure forcing is limited in this study to values much higher than that of the unstart process. The question is whether or not the unstart dynamics are the same as the isolator dynamics induced by smaller downstream pressure perturbations (that do not cause unstart).

Methods for detecting the shock train leading edge using wall pressure measurements have

also been studied in an effort to better predict the onset of unstart [Laurence *et al.*, 2013; Le *et al.*, 2008; Srikant *et al.*, 2010; Hutzel *et al.*, 2011]. If unstart is detected, actions must be taken to avoid unstart which may include changing the fueling conditions or applying one of the flow control mechanisms mentioned earlier. However, these leading edge detection methods are normally applied to an isolator flow field with a constant downstream pressure. Relatively few studies have examined the dynamics of the system under changing downstream conditions, as in the case of a transient combustion process. This type of study is particularly difficult for computations because most solvers use time-averaged physics and the addition of time-dependency greatly increases the complexity and cost of the analysis.

Nonetheless, Hoeger *et al.* [2011] used a 2-D transient computational model to compare the propagation of the shock train in Mach 1.8 flow at different downstream forcing rates. They found that when a large instantaneous downstream pressure is applied, the shock train first propagates upstream (against the incoming flow) with speeds up to 300 m/s. The shock train overshoots and then travels back downstream to its final rest position at up to 20 m/s. Decreasing the magnitude of the downstream pressure change reduces the shock train speed and the amount of overshoot. In comparison, when the downstream pressure change is applied gradually (at 8,500 kPa/s) the computational model predicts a maximum speed of 110 m/s as the shock rain travels monotonically upstream to the same rest location with no overshoot. Note that the difference in speeds contrasts with the results found in the unstart study of Wagner *et al.* [2009]. Thus, further investigation into the subject is required.

Su *et al.* [2016] used a computational fluid dynamics (CFD) model to study the shock train dynamics under high frequency ($f > 59$ Hz) oscillatory forcing. They found that 1) the frequency of the shock train response matches that of the downstream back pressure forcing and 2) the amplitude of the response is proportional to that of the downstream forcing. Interestingly, there is a slightly reduction in the amplitude of the shock train motion as the frequency of forcing is reduced. In addition, the leading shock foot location moves slightly upstream for their lowest frequency case (59 Hz) whereas the shock foot location is independent of the forcing frequency at all of the other higher frequency cases. To investigate these trends further, low frequency forcing needs to be studied.

The forced dynamics of the shock train can also be studied by varying the approach conditions and keeping the bulk downstream isolator conditions constant. For example, Fiévet *et al.* [2017] conducted a computational study where the inflow boundary layer thickness is varied in time. Similar to the computational studies with downstream forcing, the study by Fiévet *et al.* [2017] found that the shock train response is complex and depends on the excitation frequency. They specifically looked at forcing frequencies from 20 to 1000 Hz and tracked two features: 1) the location where the pressure rises to 10% of overall pressure rise in the isolator and 2) the location

where the pressure rises to 80% of the overall pressure rise in the isolator. As expected, the 10% and 80% pressure rise locations vary in time due to the inflow variation. More interestingly, it is also observed that the pseudoshock length (i.e., the difference between the two pressure rise locations) oscillates in time for all of the forcing conditions studied. A resonant frequency was identified where the change in pseudoshock length is at a maximum value. This resonant frequency corresponds to where the the beginning and end of the pseudoshock are oscillating 90 degrees out of phase. Fiévet *et al.* [2017] also conjecture that the length of the pseudoshock is constant (i.e., the beginning and end of the system fluctuate coincidentally) for very high or very low frequencies. More work is needed to identify if these trends are also observed for downstream forcing cases.

1.5.2 Objectives of the Current Work

The objective of the current work is to experimentally evaluate the shock train response to low frequency forcing imposed by a large amplitude downstream disturbance that does not induce unstart. The downstream disturbance is created by oscillating the angle of the downstream control valve in time. The shock train response is compared over a wide range of cases to identify how the magnitude and rise time of the disturbance impact the shock system. Then, the response to forcing is compared to the shock motion due to the low magnitude perturbation associated with the inherent unsteadiness of the system. Thus, the results of the inherent unsteadiness research are translated to the case of the forced dynamics in order to gain a better understanding of the underlying physics of these transient phenomena.

1.6 Outline

First, the experimental setup is described in chapter 2. This includes information on the isolator model and the diagnostic techniques used to study the shock train. In chapter 3, a baseline understanding of the flow field in the isolator section without a pseudoshock present is established. This information is then utilized to explain some of the results in chapter 4, where the shock train structure and three-dimensionality are discussed. In chapter 5, the inherent unsteadiness of the shock train is explored. Here, a theory is presented that identifies the flow phenomena that generate perturbations and explain how these perturbations impact the shock motion. Finally, in chapter 6, the forced dynamics of the shock train are examined. The results demonstrate how perturbations generated downstream of the isolator interact with the shock train system. A summary of the results is presented in chapter 7.

The appendices also provide useful information, although they are not the main interest of the thesis. In particular, appendix A contains example PIV velocity vector fields of the shock train that are valuable for understanding the general properties through the system and could be useful

for validating computational models. Appendix B describes the algorithm used to automatically detect shock features from schlieren images, including the shock positions, angles, and Mach stem height. Appendices C and D describe the mathematical relations in the cross-spectral analysis and give additional examples of the cross-spectral analysis results, respectively.

Chapter 2

Experimental Setup

2.1 Direct-Connect Isolator Model

The current experiments are performed in a low aspect ratio direct-connect isolator model at the University of Michigan. The isolator is a component of a suction type wind tunnel facility illustrated schematically in figure 2.1. Room air enters the wind tunnel intake and passes through a flow conditioning section before it is expanded through a one-sided converging-diverging nozzle. Flow then enters the isolator section. The low-aspect ratio isolator section is approximately 800 mm in length and has a constant, rectangular cross-section measuring 57.2 mm in width (W) and 69.3 mm in height (H). The flow through the isolator has a nominal freestream Mach number of 2.0. However, the Mach number decreases slightly along the length of the constant area isolator section due to the natural growth of the boundary layers. The Mach number as well as the other conditions of the undisturbed isolator flow (i.e., when the shock train is not present) are discussed in chapter 3.

It is important to note that the inflow boundary layer properties are different on the top- and bottom-walls of the isolator due to the one-sided nozzle. This is representative of a real high-speed air breathing engine where one wall typically has a larger boundary layer due to the geometry of the inlet. In this work, the thicker bottom-wall boundary layer is used to describe the approach conditions of the pseudoshock. For example, the confinement ratio, which essentially describes the proportion of the cross-sectional area that is blocked by the boundary layer, is defined in this work as the ratio of the boundary layer momentum thickness to the half height of the isolator, i.e., $C_\theta = 2\theta/H$. This is essentially a one-dimensional approximation of the confinement ratio. To better represent the confinement ratio in this study (as well as other studies), the boundary layer properties on all four of the isolator walls are required.

Downstream of the isolator section is a diffuser leading to a butterfly valve and then a vacuum chamber. This butterfly valve is referred to as the *control valve* of the isolator. By partially closing the control valve, the downstream area for airflow is reduced leading to an increase in pressure that replicates the pressure rise that would exist in the combustor of a real engine. A shock train is

produced in the isolator section in response to the increased downstream pressure. Further closing the control valve causes the shock train to move upstream in the isolator. The valve position is monitored using an optical incremental encoder with a resolution of 20,000 steps per 90° of rotation.

To establish nominally constant boundary conditions (i.e., a quasi-steady state shock train), the valve is operated in one of two ways: 1) the valve maintains a constant position for the entire duration of the run; 2) a pressure measurement downstream of the shock train is used as feedback to an on-board valve controller that slightly changes the valve position in order to maintain a constant pressure. Both valve control methods produce the same results for short run times (less than 2 minutes). When the valve position is constant, the shock train eventually creeps forward in the isolator section due to the increase in back pressure that occurs as the vacuum chamber fills. To study the forced dynamics of the shock train, the valve position is oscillated, causing the shock train to move back and forth in the isolator section. We find that the shock train location is highly sensitive to the valve angle. For example, the amplitude of the valve angle oscillation is less than 2 degrees in the forcing cases but the shock train displacement is large, up to 2.8 duct heights. In addition, the speed of the valve is limited due to the control mechanism. Thus, the forcing frequency is limited to less than 10 Hz. More detail on the valve oscillations, including the time history of the valve angle, is presented in section 6.

Capacitance manometers (MKS 626C Baratron) are used to monitor the overall pressure conditions of the isolator section including: 1) the pressure at the beginning of the isolator section, termed the *inflow pressure*; 2) the pressure just upstream of the diffuser section, termed the *back pressure*, p_b; 3) the pressure just upstream of the control valve, termed the *diffuser pressure*. These three manometers are located on the centerline of the top-wall as demonstrated in figure 2.1. The manometers have an accuracy of 0.25% of the reading and a response time of about 20 ms.

For the quasi-steady state shock train cases, the inflow and diffuser pressure measurements are particularly important because they verify that the bulk inflow and outflow conditions of the isolator

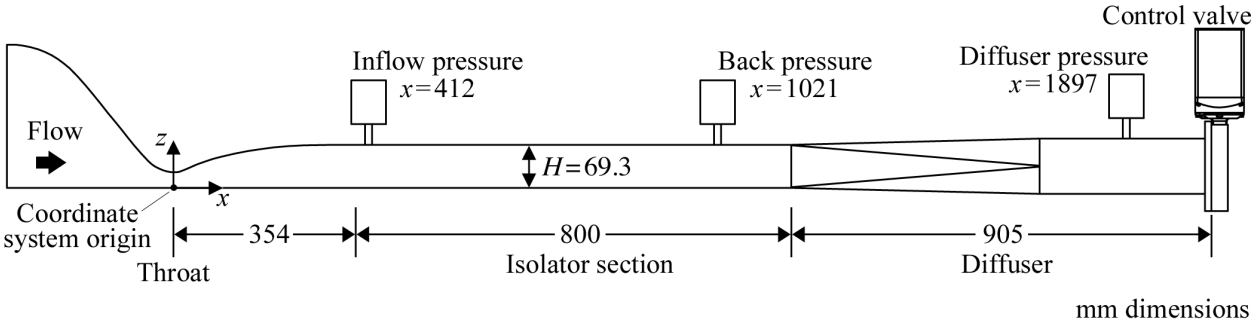

Figure 2.1: Schematic diagram of the direct connect isolator facility (side-view).

are constant. Specifically, these pressure fluctuations are less than 1% of their respective time-averaged values. For both the quasi-steady and forced shock train cases, the back pressure is used as a way to describe the shock train location. Compared to the diffuser pressure, the back pressure exhibits higher fluctuations (up to 5% of its time-averaged value) due to turbulence generated by the pseudoshock. That is, the heterogeneous supersonic-subsonic velocity distribution in the mixing region leads to turbulent mixing that impacts the downstream pressure measurement in the isolator section. However, the back pressure is more sensitive to the shock train location which is why this value is used instead of the diffuser pressure to describe the shock train location. In this work, the back pressure is typically normalized by the pressure of the undisturbed flow just upstream of the shock train (i.e., the pressure at the foot of the shock train), p_f. The ratio, p_b/p_f, is termed the *pressure ratio*. Note that the pressure at the foot of the shock train is measured using the low-speed pressure scanners (see section 2.2.2) or interpolated from the pressure measurements along the undisturbed isolator section given the x-location of the shock foot (see section 3.1).

Finally, a right-handed coordinate system is used in this work. The x, y, and z coordinate directions are oriented streamwise (i.e., in the direction of the bulk fluid flow), normal to the side-wall, and normal to the bottom-wall, respectively. The origin of the coordinate system is located at the throat of the nozzle, on the lower right corner of the isolator cross-section as one looks downstream.

2.2 Diagnostic Techniques

The isolator section is modular in design. That is, the side- and bottom-walls can be easily removed and replaced with pieces instrumented for different measurement diagnostics. The details of the diagnostic techniques used in this thesis are discussed below.

2.2.1 High-Speed Schlieren Imaging

A schlieren system is used to visualize the temporal evolution of the shock train system, from which several morphological features of the shock train are defined and extracted. Borosilicate glass side-walls provide optical access along the entire length of the isolator section and a z-type schlieren setup with a horizontal knife-edge is used to capture vertical density gradients in the flow. The light source was fabricated in-house and uses a high brightness LED (Luminus SBR-70) for continuous illumination. Images are recorded with a high speed camera (Phantom v711) at a rate of 8–10 kHz with an exposure time of 1–2 μs. The camera field of view covers 90-100% of the entire test section height and up to 241 mm (i.e., $3.5H$) in the streamwise direction, which is sufficient to image the first four shocks of the shock train. The image resolution is approximately 3.0–3.5 px/mm depending on the exact dimensions of the field of view for a particular run.

An example instantaneous schlieren image of a shock train is shown in figure 2.2. Flow is from left to right. For this example, the pressure ratio is 2.82 and the leading shock has a normal structure, demonstrated by the Mach stem in between two very large lambda feet. The upper x-axis is labeled in terms of the normalized distance from the wind tunnel throat. For comparison, the lower x-axis is labeled in terms of relative distance from the time-averaged location of the leading shock Mach stem, x^*. The instantaneous schlieren image shown in the figure was intentionally selected for illustration purposes to have the Mach stem at its time-averaged location. Both of these coordinate systems are often used throughout the thesis.

Note the streamwise locations of thirteen morphological features of the shock train marked in figure 2.2:

- x_1, the location of the leading shock Mach stem;
- x_{1l} and x_{1r}, the location where the leading and trailing legs of the first shock lambda foot intersect the bottom-wall boundary layer;
- x_{2t} and x_{2b}, the location where the second shock intersects the top- and bottom-wall boundary layer, respectively;
- x_{2c}, the location where the left- and right-running components of the second shock intersect;
- x_{3t} and x_{3b}, the location where the third shock intersects the top- and bottom-wall boundary layer, respectively;
- x_{4t} and x_{4b}, the location where the fourth shock intersects the top- and bottom-wall boundary layer, respectively;
- s, the leading shock Mach stem height;
- α_L and α_R, the angles of the leading leg and trailing leg of the first shock lambda foot (relative to horizontal direction), respectively.

By locating these thirteen morphological features in each schlieren image, the time history of each quantity is obtained and used for analysis. For example, the time-averaged values of α_L, α_R, and s are used to describe the leading shock structure at a given back pressure (see chapter 4). In addition, the shock position fluctuations, x_i' with $i \in \{1, 1l, 1r, 2c, 2b, 2t, 3b, 3t, 4b, 4t\}$, are used to characterize the shock train inherent unsteadiness (see chapter 5). The automatic feature detection algorithm used to identify the thirteen morphological features in each instantaneous schlieren image is described in appendix B. This algorithm correctly identifies the shock features in over 98% of the schlieren images. The features that are incorrectly identified by the algorithm are quantified manually.

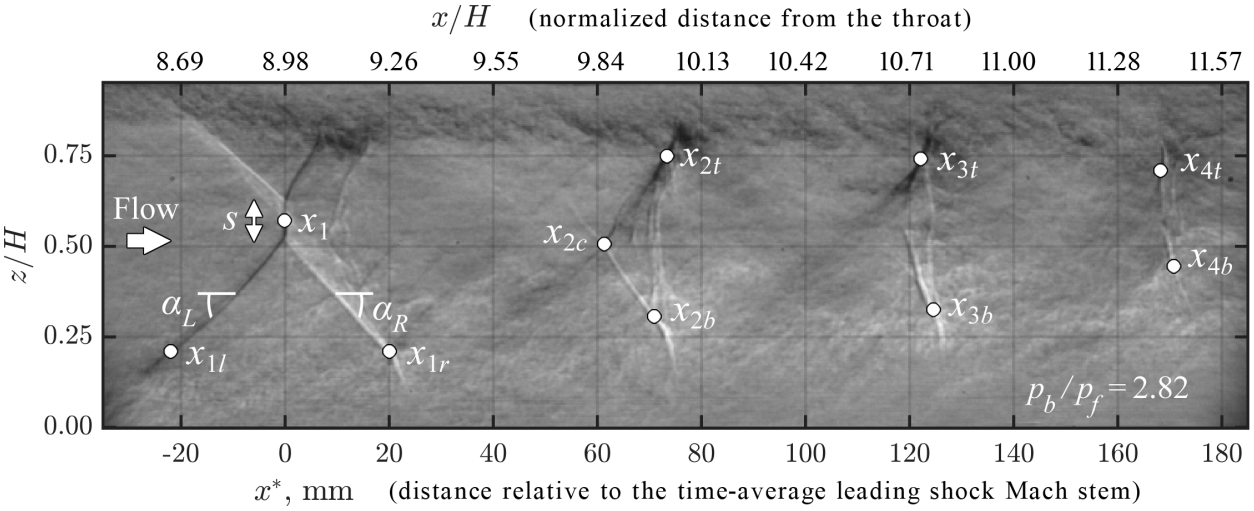

Figure 2.2: Instantaneous schlieren image demonstrating the morphological features of the shock train that are tracked in time.

2.2.2 Low-Speed Pressure Measurements

Low-speed wall static pressure measurements are used to evaluate the time-averaged pressure profile in the isolator section. These are differential measurements collected using a Scanivalve DSA3217 and three NetScanner model 9116 digital sensor arrays at a rate of 20 Hz. The inflow pressure measured on the top-wall using the MKS Baratron (see section 2.1) is used as a common reference pressure. The pressure sensor arrays have a quoted accuracy of $\pm 0.05\%$ of the full scale differential range, corresponding to approximately 0.009 kPa for three of the four arrays. This quoted accuracy includes the influence of hysteresis, linearity, and repeatability. One of the Netscanner arrays has a larger differential pressure range and an accuracy of 0.052 kPa. Given the uncertainties in the pressures measured by the digital sensor arrays and the reference manometer, the overall uncertainty in the absolute pressure measurement is approximately 0.013 kPa (or 0.061 kPa for the Netscanner array with a larger differential pressure range).

Tygon flexible tubing (inner diameter of 1.6 mm and outer diameter of 3.2 mm) is used to connect the pressure sensor arrays to stainless-steel tubing (inner diameter of 0.8 mm and outer diameter of 1.6 mm). Each stainless steel tube is press-fit into an aluminum isolator wall instrumented with pressure taps, thus connecting the pressure transducer to the pressure tap. The pressure tap diameter is 0.8 mm on the flow side of the isolator wall. Figure 2.3(a) schematically illustrates the tubing and pressure tap configuration in the aluminum wall. Bottom-wall pressure taps are located along $y = W/2$ (i.e., the centerline of the bottom-wall). Side-wall pressure taps are located along $z = H/2$ (i.e., the centerline of the side-wall) and $z = 0.2H$. Wall pressure taps are spaced 12.7 mm (i.e., $0.18H$) apart for high spatial-resolution results. Figure 2.3(b) illustrates the pressure tap

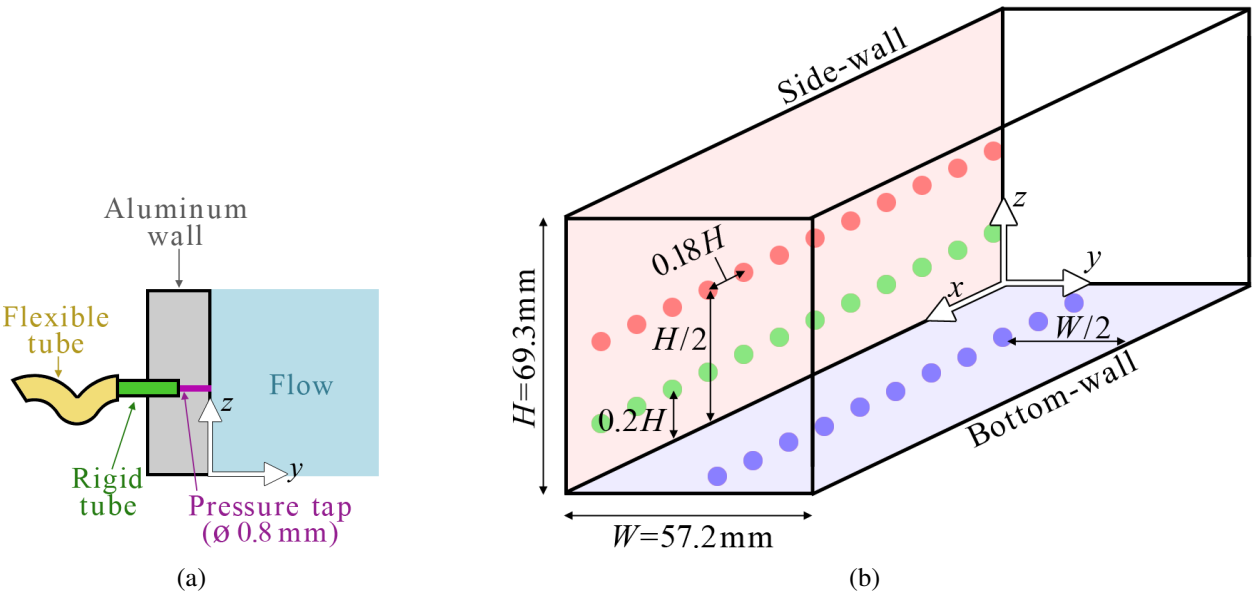

Figure 2.3: Schematics of: (a) tubing and pressure tap configuration in the aluminum wall; (b) pressure tap locations in the isolator.

locations schematically.

2.2.3 High-Speed Pressure Measurements

High-speed wall static pressure measurements are used to study the pressure fluctuations induced by the shock train. The measurements are collected with five high-sensitivity absolute pressure transducers (Kulite XCS-062). The Kulite transducers have a pressure range of 103 kPa and a diaphragm resonance frequency of approximately 200 kHz in a cylindrical housing of 1.7 mm diameter. The signals are amplified, low pass filtered at 50 kHz, then sampled at 200–500 kHz. It is important to note that all five transducers are simultaneously sampled. This allows us to accurately and precisely quantify the time delay between fluctuations measured by different transducers.

The transducers are flush mounted to the aluminum side- or bottom-wall of the isolator. Thus, simultaneous side- and bottom-wall pressure measurements are possible. Alternatively, the aluminum side-wall with pressure ports is replaced with a glass side-wall for simultaneous bottom-wall pressures measurements and schlieren imaging. Figure 2.4 schematically illustrates the pressure port locations in a portion of the isolator. The bottom-wall contains 46 pressure ports: 40 pressure ports spaced 10.9 mm (i.e., $0.16H$) apart along $y = 28.6$ mm and 6 pressure ports spaced 32.8 mm (i.e., $0.47H$) apart along $y = 50.8$ mm. Note that $y = 28.6$ mm is the $y = W/2$ centerline of the bottom-wall and $y = 50.8$ mm is equivalent to $y = 0.89W$, which is 6.4 mm from the corner of the duct. The aluminum side-wall contains 20 pressure ports: 10 pressure ports spaced 21.8 mm (i.e., $0.31H$) apart along $z = 6.4$ mm and 10 pressure ports spaced 21.8 mm (i.e., $0.31H$) apart

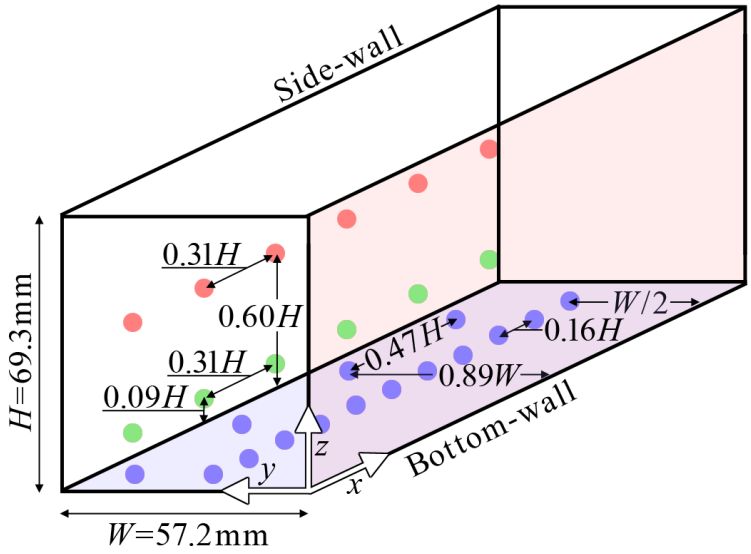

Figure 2.4: Schematic illustrating the possible locations of the high speed pressure transducers (flush mounted to the wall).

along $z = 41.3$ mm. Note that $z = 6.4$ mm is equivalent to $z = 0.09H$ and is near the corner of the duct while $z = 41.3$ mm is equivalent to $z = 0.60H$. The five Kulite transducers are positioned at any arbitrary combination of the 66 port choices and the remaining ports are filled with blank housings.

2.2.4 Oil-Flow Visualization

Oil flow visualization is used to gain insight into the flow structure on the walls of the isolator. For each test, a thin base coat of Xiameter PMX-200 silicon oil is painted onto the aluminum side- and bottom-walls of the isolator. Then, a mixture of oil and titanium dioxide is spattered over the base coat. Finally, the wind tunnel is started and the valve is partially closed, thus dragging the oil in the direction of the flow field generated by the shock train. Two cameras recording at 100 Hz are used to simultaneously image the oil pattern development on the side- and bottom-walls. The procedure was repeated for oil viscosities ranging from 20 to 350 cSt and the observed flow pattern was found to be independent of the oil viscosity used.

2.2.5 Particle Image Velocimetry

PIV measurements are collected to quantify the flow velocities in the isolator section. Figure 2.5 schematically illustrates the experimental setup for two PIV configurations used in this thesis. In the first configuration, shown in figure 2.5(a), two-component PIV measurements are conducted with the laser sheet oriented parallel to the side-walls and extending in the streamwise direction. In

this configuration, the streamwise (u) and vertical (w) velocity components on an $x - z$ plane are measured. Figure 2.5(b) illustrates the second PIV configuration. In this case, SPIV measurements are conducted with the laser sheet oriented parallel to the isolator cross-section. Thus, all three velocity components (u, v, and w) are measured on a $y - z$ plane.

For both PIV configurations, a portable Laskin nozzle aerosol generator (ATI Model TDA-4B) is used to seed the flow with polydispersed submicrometer particles composed of poly-alpha olefin oil with a density of 819 kg/m^3. The particle diameter is approximately 0.7 μm and was quantified from a measure of the relaxation distance of a particle across an oblique shock [Morajkar, 2017]. For the Mach 2.0 flow presented in this work, this particle diameter corresponds to a Stokes number of approximately 0.16. According to Samimy & Lele [1991], this Stokes number is low enough that the particles are expected to track the large scale motions of the compressible flow. Note that the particle tracking error is largest near regions with high velocity gradients (e.g., shock waves and separation regions). Thus, the shapes of the shock front and separation regions are impacted by the particle tracking error the most. Based on the particle relaxation distance, the uncertainty in locating the shock front and separation contours is estimated to be ± 2 mm. However, this uncertainty is relatively small and does not impact the results discussed in the thesis.

The double-pulse illumination of the particles is provided by a pair of low-repetition-rate frequency-doubled Nd:YAG lasers producing a 532 nm beam with a pulse duration of approximately 10 ns and a pulse energy of approximately 150–200 mJ/pulse. The time delay between the two laser pulses is 600 – 1800 ns depending on the run conditions and camera configuration. For each run, the effective time delay between pulses is measured with a fast response photodiode (Thorlabs DT10A, 1 ns response time) and a digital oscilloscope (LeCroy Waverunner 6030, 350 MHz).

Consider the PIV configuration for the $x - z$ measurement planes illustrated in figure 2.5(a). Both laser beams are sent through a combination of cylindrical lenses to generate an illumination sheet that is parallel to the flow and illuminates a long streamwise section of the isolator. Lens L1 is a plano-convex cylindrical lens with a long focal length that focuses the beam and ultimately reduces the laser sheet thickness. Lens L2 is a plano-concave cylindrical lens with a very short focal length that expands the beam into a diverging sheet. Four interline transfer charge-coupled device cameras (SensiCam PCO) recording at 3.33 Hz with a resolution of 1280 $\times$ 1024 pixels are used to image the particles illuminated by this laser sheet. The cameras are arranged side-by-side to obtain high spatial resolution measurements over a wide field of view. Two cameras are placed on each side of the isolator section due to space constraints. The fields of view from two adjacent cameras share an overlap region that extends approximately 7 – 10 mm ($0.10H$ – $0.14H$) in the streamwise direction. This corresponds to approximately 12 – 17% of one camera's field of view. As described later in this section, these overlap regions are used to define the uncertainty of the

two-component PIV measurements.

Next, consider the PIV configuration for the $y - z$ measurement planes illustrated in figure 2.5(b). Both laser beams are sent through a combination of cylindrical lenses to generate an illumination sheet that is perpendicular to the flow. Lens L3 is a cylindrical lens that focuses the beam in the horizontal plane and is ultimately responsible for reducing the laser sheet thickness. Lenses L4 and L5 expand and focus the beam in the vertical plane, respectively. The result is a collimated laser sheet that illuminates particles in a cross-sectional slice of the isolator. The beam width, measured using the scanning knife-edge method, is 1.25 ± 0.25 mm, which is approximately four times the particle displacement in the freestream in 600 ns. Two SensiCam PCO cameras recording at 3.33 Hz are used in forward-scattering stereoscopic configuration to image the illuminated particles. The cameras are oriented at 33° relative to the measurement plane and are equipped with a Sigma 70-300 mm f/4-5.6 apochromatic macro lens.

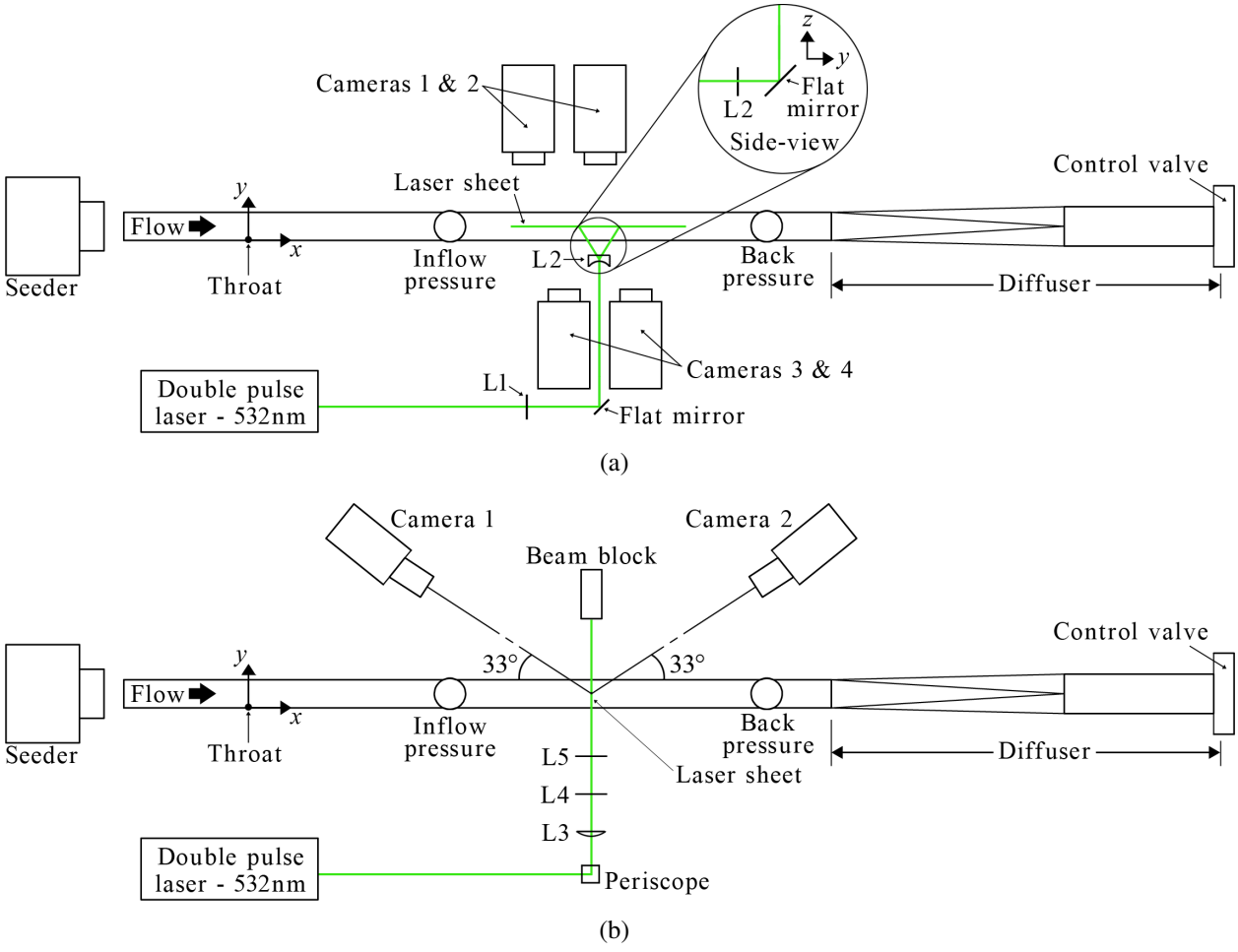

Figure 2.5: Schematic diagram of the PIV experimental setup (top view): (a) two-component PIV on an $x - z$ measurement plane; (b) stereo PIV configuration for a $y - z$ measurement plane.

After images are acquired, LaVision DaVis 8 software is used to process the data. The velocity fields are reduced from the particle images using a multipass scheme. Two passes are first conducted with a 64 $\times$ 64 pixel interrogation window size with 75% overlap, followed by two passes at a reduced 32 $\times$ 32 pixel interrogation window size with Gaussian weighting and 75% overlap. Post processing within multiple passes includes deleting a vector if its correlation value is less than 0.8 or the first to second correlation peak ratio is less than 1.1. In addition, groups with less than 5 vectors are removed. Valid vectors are found more than 95% of the time. Missing or rejected vectors are interpolated using the method by Garcia [2010]. No additional smoothing is applied after interpolation. For the measurements collected on $x - z$ planes, one final step is required after vector validation and interpolation. Since four cameras are used to image different regions of the measurement plane, the post-processed velocity fields from the four cameras are stitched together. In the overlap regions, the velocities measured by two different cameras are averaged together.

In total, five different regions of the flow field are studied using PIV in this thesis. Four of these regions are slices of the flow oriented parallel to isolator side-walls and are studied using two-component PIV on an $x - z$ plane. The last region is a slice of the flow field oriented perpendicular to the side-walls and is studied using stereo PIV on a $y - z$ plane. For convenience, the five measurement regions are named CL1, CL2, SW1, SW2, and TV. Note that "CL", "SW", and "TV" stand for "centerline", "side-wall", and "transverse", respectively. The orientation and relative location of the different measurement regions within the isolator section are schematically illustrated in figure 2.6. In addition, the approximate extent of each measurement region, the final interrogation window (IW) size, and PIV vector resolution are detailed in table 2.1. Note that the specified field of view excludes the regions closest to the walls due to interference from the laser sheet reflections. Approximately 20% of the boundary layer height is not captured by the PIV.

The overall uncertainty of the velocity measurements is estimated by evaluating the individual sources of uncertainty. Table 2.2 summarizes the uncertainty contribution from each source, defined as the 95% confidence value, for both the stereo and two-component PIV setups.

First, consider the uncertainty in the u, v, and w velocity components found using the SPIV experimental setup. The influence of peak locking is estimated using the LaVision DaVis software and is found to be negligible. The LaVision DaVis software also gives a direct estimate of the random uncertainty of the displacement vectors using the correlation statistic method proposed by Wieneke [2015]. This method accurately accounts for factors like pixel noise, seeding density, particle image size, and out-of-plane particle motion [Sciacchitano *et al.*, 2015]. The random uncertainty is higher when a shock train is present, probably because the shock distorts the image of the particles or reduces the seeding density [Elsinga *et al.*, 2005]. For example, figure 2.7 shows the contour map of the random uncertainty for an instantaneous u-velocity vector field on a cross-sectional slice of the flow. The regions with higher uncertainty correspond to the flow that has

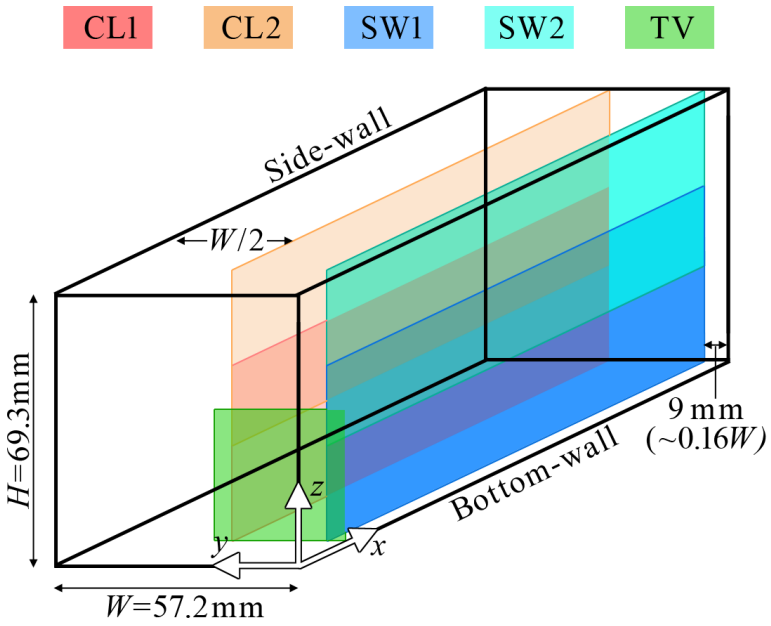

Figure 2.6: Schematic illustrating the locations of the PIV measurement planes.

	CL1	CL2	SW1	SW2	TV	
x-location	499 – 714	499 – 714	499 – 714	499 – 714	501	mm
x/H	7.20 – 10.30	7.20 – 10.30	7.20 – 10.30	7.20 – 10.30	7.23	
y-location	28.6	28.6	9.0	9.0	1.6 – 32.2	mm
y/W	0.50	0.50	0.16	0.16	0.03 – 0.56	
z-location	2.0 – 48.0	22.0 – 65.0	2.0 – 48.0	22.0 – 65.0	1.3 – 32.2	mm
z/H	0.03 – 0.69	0.32 – 0.94	0.03 – 0.69	0.32 – 0.94	0.02 – 0.46	
IW size	1.5 × 1.5	1.5 × 1.5	1.5 × 1.5	1.5 × 1.5	1.6 × 1.6	mm × mm
Resolution	0.38 × 0.38	0.38 × 0.38	0.38 × 0.38	0.38 × 0.38	0.40 × 0.40	mm × mm

Table 2.1: Location and extent of PIV measurement planes in the isolator section.

passed through the leading leg of the first shock in the train. The uncertainty results listed in table 2.2 are 2 standard deviations of the uncertainty distribution compiled from all of the velocity vector locations in a contour map across multiple instantaneous vector fields and multiple runs.

Finally, sampling uncertainty contributes to the overall SPIV uncertainty for time-averaged velocities. In this work, the average velocities from SPIV are only computed for the flow field without a shock train. Thus, these instances are used to quantify the sampling uncertainty for each velocity vector location as follows:

$$\text{sampling uncertainty} = 1.96\,\sigma(u)/\sqrt{n} \tag{2.1}$$

Stereo PIV uncertainty	u	v	w	
Peak locking	0.0	0.0	0.0	m/s
Random (with shock)	14.7	7.8	6.1	m/s
Random (without shock)	10.2	5.0	4.0	m/s
Sampling (without shock)	2.4	1.1	1.0	m/s
Overall (time-averaged, without shock)	10.5	5.1	4.1	m/s
Overall (instantaneous, with shock)	14.7	7.8	6.1	m/s
Two-component PIV uncertainty	u	v	w	
Overlap analysis	24.5	-	13.3	m/s
Sampling	1.0	-	0.5	m/s
Overall (time-averaged)	24.5	-	13.3	m/s
Overall (instantaneous)	24.5	-	13.3	m/s

Table 2.2: Uncertainty of velocities measured using PIV.

where $\sigma(u)$ is the standard deviation in velocity across all of the measurements and n is the number of samples. Figure 2.8 shows the resulting contour map of the u-velocity sampling uncertainty that was computed by averaging all 300 images of the undisturbed flow. Note that the uncertainty is higher in the boundary layer, probably due to the turbulence in that region. The sampling uncertainty listed in table 2.2 is the 95% confidence value computed using all of the velocity vector locations in this contour map.

Assuming the above sources of SPIV uncertainty are uncorrelated, the overall uncertainty is equal to the square root of the sum of squared values [Kirkup & Frenkel, 2006]. In a very conservative way, the overall uncertainties of time-averaged SPIV velocities without a shock present are equal to 10.5, 5.1, and 4.1 m/s for the u, v, and w components, respectively. Similarly, the overall uncertainty of the instantaneous SPIV velocities with a shock present are equal to 14.7, 7.8, and 6.1 m/s for the u, v, and w components, respectively. These values correspond to 0.8 – 2.9% of the freestream flow velocity, u_∞.

Next, the uncertainty of the u- and w-velocity components are evaluated for the two-component PIV measurements. In this experimental setup, four side-by-side cameras image regions centered at different locations on the same $x - z$ plane but approximately 12 – 17% of one camera's field of view is also measured by an adjacent camera. The velocity uncertainty is evaluated by subtracting the spatially overlapped instantaneous velocity fields measured by the two cameras. Note that the cameras are triggered simultaneously so the measured velocities should theoretically be the same. Figure 2.9 shows three histograms of the u-velocity differences. Each histogram is constructed using the velocity differences at all of the vector locations in an overlap region for a set of 200

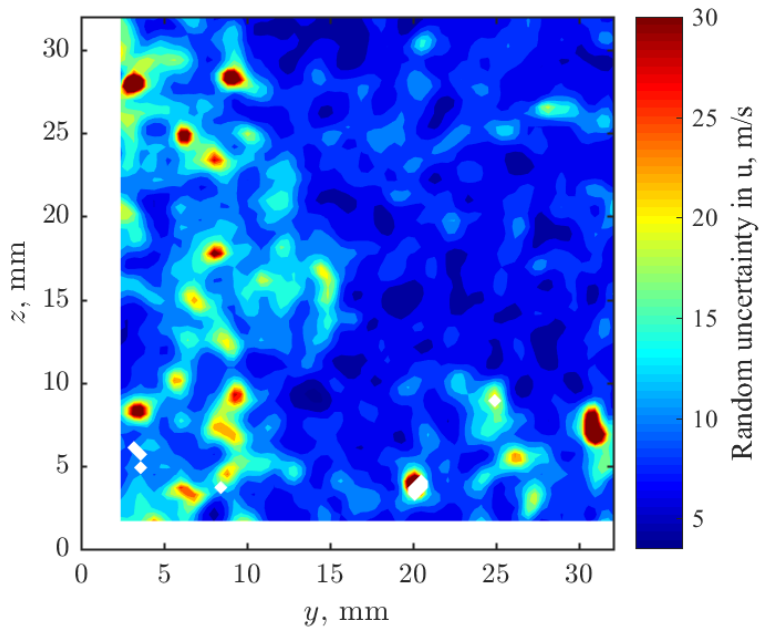

Figure 2.7: Example contour map of the random uncertainty in u-velocity measured using SPIV. The velocity field associated with this uncertainty map is influenced by the leading shock of the train.

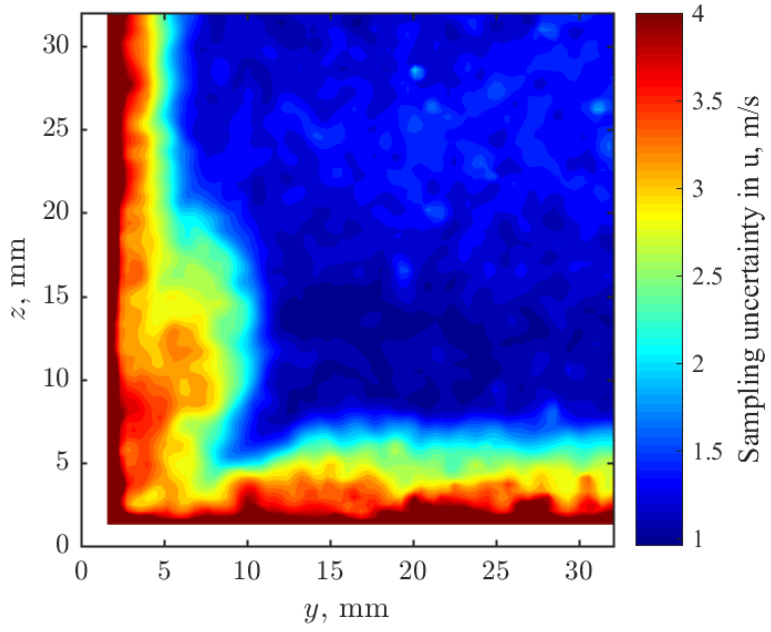

Figure 2.8: Example contour map of the sampling uncertainty in u-velocity measured using SPIV. No shock train is present in this example.

vector fields in one run. The blue, red, and yellow histograms correspond to the results of the overlap region between cameras 1 and 2, 2 and 3, and 3 and 4, respectively. Note that there is a slight bias in the measurements of different cameras equal to the mean value of each histogram. In addition, the width of each histogram demonstrates that there is a random component of the uncertainty. In order to capture the random and bias components, the uncertainty for each overlap region is defined from the histogram as the absolute value of the mean plus two standard deviations of the velocity difference. The uncertainty found from this overlap analysis does not appreciably change if a shock train is present or not. Thus, these values generally represent the uncertainty of any instantaneous measurement. The values reported in table 2.2 are the average uncertainties across all of the runs and all of the overlapped regions.

Sampling uncertainty also influences the overall uncertainties of the time-averaged velocities measured using two-component PIV. This uncertainty component is computed using the same method described in the SPIV analysis above. For the undisturbed flow (i.e., without a shock train), 1400 images are used to construct the average velocity field which results in a 1.0 and 0.5 m/s uncertainty in the u- and w-velocity components, respectively. Note that this sampling uncertainty is negligible compared to the uncertainty found from the overlap analysis. Time-averaged velocity fields with a shock train are also used in this work, however, the sampling uncertainty cannot be computed with these measurements due to the unsteady shock motion. Therefore, it is assumed that the sampling uncertainty is the same whether or not a shock is present.

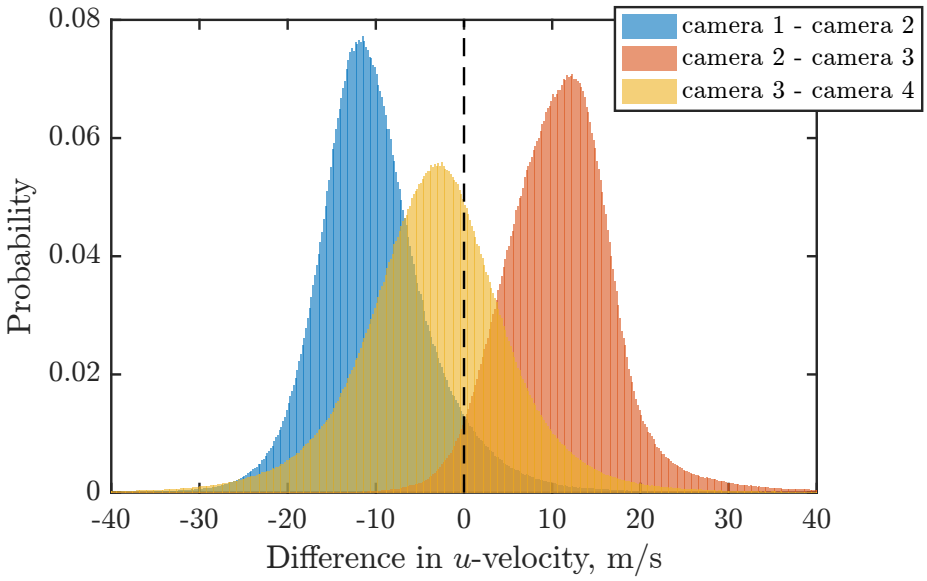

Figure 2.9: Example histogram of the velocity differences within the spatially overlapped region measured by multiple cameras.

Once again, the different components of velocity uncertainty are assumed to be uncorrelated and the overall two-component PIV uncertainty is computed as the square root of the sum of squared values. For instantaneous vector fields, the uncertainty from the overlap analysis is the only component that contributes to the overall uncertainty. Thus, the u- and w-velocity components have a conservative uncertainty of 24.5 and 13.3 m/s, respectively. The time-averaged velocities have approximately the same uncertainty as the instantaneous velocities because the sampling uncertainty is very small. In general, these velocity uncertainties correspond to 2.6 – 4.9% of the freestream flow velocity u_∞ and are slightly higher than the uncertainties for the SPIV experimental setup. Also note that the uncertainties listed in table 2.2 are in addition to the particle tracking error. Thus, the uncertainty is higher for regions close to the shock wave as discussed at the beginning of this section.

Chapter 3

Undisturbed Isolator Flow Field

In this chapter, the main characteristics of the undisturbed isolator flow are presented. That is, the control valve is fully open and the flow conditions that develop along the isolator in the absence of the shock train are studied. It is important to fully characterize the undisturbed flow because the shock train is a local phenomenon that is impacted by its approach conditions. For instance, in chapter 4 the back pressure is varied, which moves the shock train to a new location in the isolator section. At each location, the shock train experiences different approach conditions as many of the undisturbed flow properties (including boundary layer thickness, boundary layer momentum thickness, pressure, Mach number, and Reynolds number) are a function of location in the isolator. Ultimately, this leads to changes in some of the quasi-steady state shock train properties. Thus, meaningful comparison between different experimental cases requires an accurate description of the undisturbed flow conditions.

3.1 Total Pressure and Wall Static Pressure

Assuming nearly isentropic acceleration through the wind tunnel nozzle, the total pressure of the undisturbed flow is equal to the room conditions. This property is measured prior to every run using the MKS Baratrons (see section 2.1) and is approximately equal to 98 kPa. The run-to-run variation of the total pressure is equal to ± 1.3 kPa.

The undisturbed wall static pressures along the isolator length are measured with the pressure scanners discussed in section 2.2.2 and the time-averaged values are reported in figure 3.1. The blue, red, and yellow lines represent the static pressure measured along the bottom-wall $y = W/2$ centerline, the side-wall $z = H/2$ centerline, and the side-wall at $z = H/5$, respectively. Note that the static pressures measured at these different locations are approximately the same. For the conditions of this run, the static pressure rises drastically at $x/H = 10.3$ because a shock train naturally exists in the rear of the isolator section even though the control valve is fully open. The exact location of the shock train and its induced pressure rise varies slightly from run-to-run depending on the total pressure. For the portion of the isolator that is undisturbed by the shock

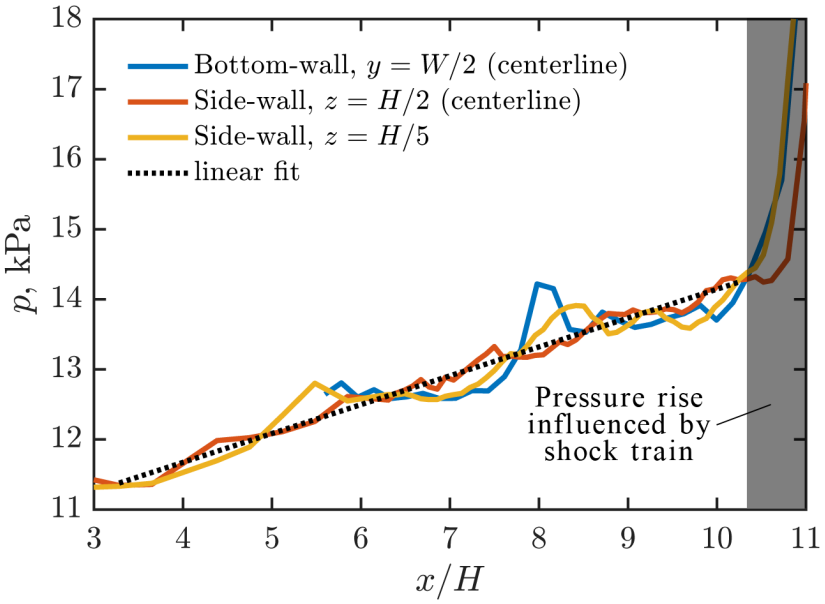

Figure 3.1: Wall static pressure along the isolator length (when the control valve is fully open).

train (i.e., $x/H < 10.3$), the static pressure rise is nearly a linear function of x/H as demonstrated by the dotted line in the figure. The linear fit deviates from the measured values by less than 1.5%. Given the relatively good accuracy of the linear fit, this relationship can be used to describe the pressure just upstream of the shock train, p_f, by interpolating at the specific location of the shock foot. In addition, by assuming that static pressure is constant through the turbulent boundary layer, the values reported in figure 3.1 also represent the static pressure in the core flow upstream of the shock train.

3.2 Velocity Fields

The undisturbed flow velocities in the isolator section are found using PIV. First, consider the two-component PIV measurements on an $x - z$ plane extending along the $y = W/2$ centerline of the isolator section. Figures 3.2(a) and 3.2(b) show the time-averaged streamwise and vertical velocity fields, respectively, constructed by stitching together the results from PIV measurement regions CL1 and CL2 (see figure 2.6). Note that these are two-component PIV measurements and therefore the transverse velocity, v, is not measured.

Figures 3.2(a) and 3.2(b) show that there is a weak uncanceled wave in the isolator that originates from the nozzle section of the wind tunnel. That is, Mach waves are formed as the flow expands in the diverging portion of the nozzle. The nozzle geometry is theoretically designed so that a flow straightening section with a decreasing wall angle turns the flow parallel to the nozzle

centerline, thus preventing any further reflection of the waves. If this geometry is even slightly incorrect then the waves are not canceled and therefore are capable of influencing the downstream flow. These uncanceled waves are a common experimental problem that are also evident in this study. As demonstrated by figure 3.2(a), the uncanceled wave and the boundary layer growth slows the streamwise flow velocity as x increases. In addition, figure 3.2(b) demonstrates that the uncanceled wave induces a small vertical velocity with a magnitude less than 10 m/s. However, this measured vertical velocity has a magnitude less than the uncertainty of the two-component

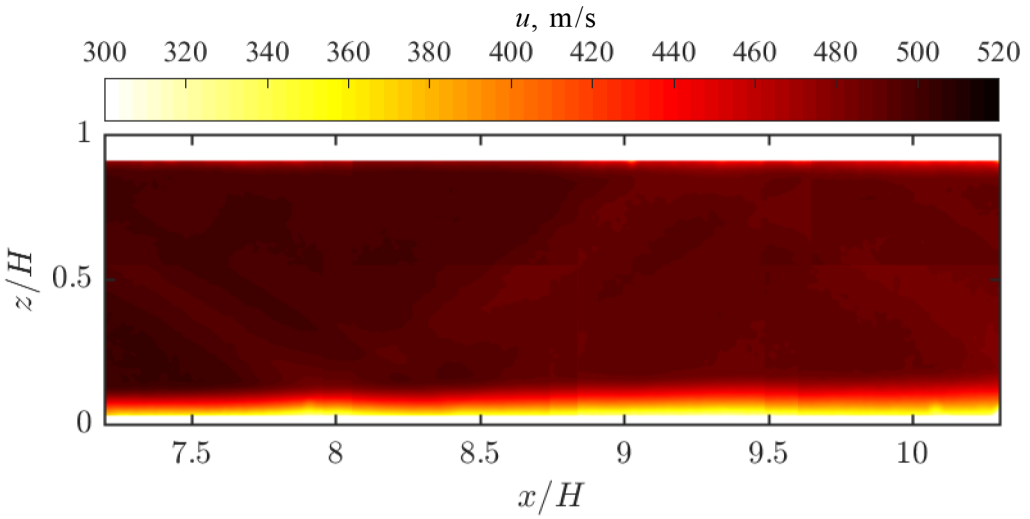

(a)

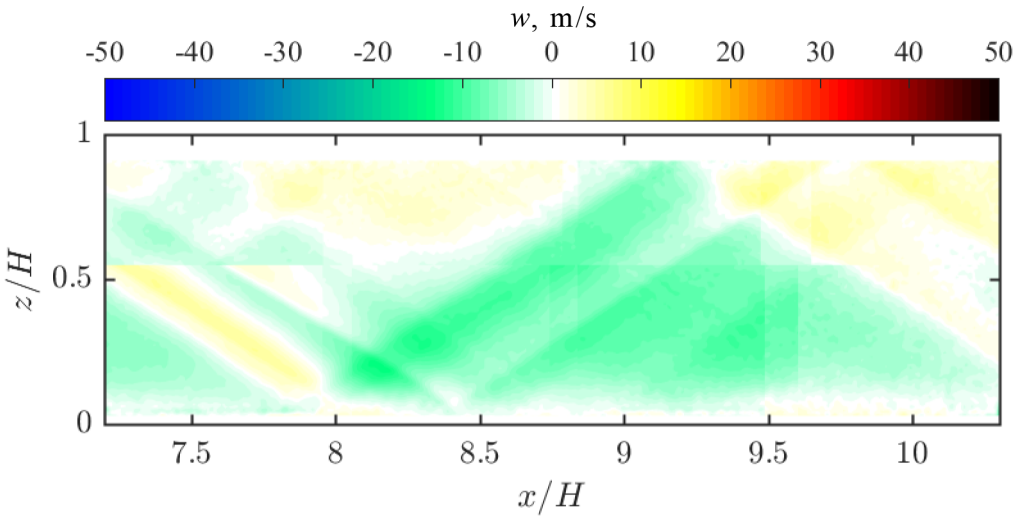

(b)

Figure 3.2: Undisturbed, time-averaged velocity fields measured on an $x - z$ plane in the center of the duct (i.e., measurement regions CL1 and CL2 as seen in figure 2.6): (a) streamwise velocity, u; (b) vertical velocity, w.

PIV experiments. Thus, the distortion in the flow caused by the uncanceled wave has a minimal influence on the results discussed later on in the thesis.

Figures 3.3(a), 3.3(b), and 3.3(c) show the time-averaged streamwise, transverse, and vertical velocity fields, respectively, measured on a cross-sectional $y-z$ plane located at $x/H = 7.23$. That is, the three-components of velocity are the result of stereo PIV measurements in PIV measurement region TV (see figure 2.6). For reference, the upper limits of the horizontal and vertical axes are equal to the test section half-width (i.e., $y = W/2$) and half-height (i.e., $z = H/2$), respectively. Again, the slight upwards velocity ($w \approx 10\,\mathrm{m/s}$) is evidence of a weak uncanceled wave. Also note that even in the absence of the shock train, the corner of the duct has a thick boundary layer. Figure 3.3(b) demonstrates that this corner region impacts the transverse velocity by creating a low-speed ($v \approx 10\ \mathrm{m/s}$) fluid movement directed away from the corner. The properties of the corner flow at different streamwise locations in this facility have been extensively studied by Morajkar [2017]. Generally speaking, the measurements presented here agree well with the previously collected data. In chapter 4.4 it is found that the corner region grows when influenced by the shock train.

3.3 One-Dimensional Core Flow Properties

In the undisturbed isolator section, the core flow is defined as the flow outside of the boundary layer. For any given flow property, the one-dimensional (1D) core flow value at a streamwise x-location is found by averaging across the portion of the cross-section that is within the core flow.

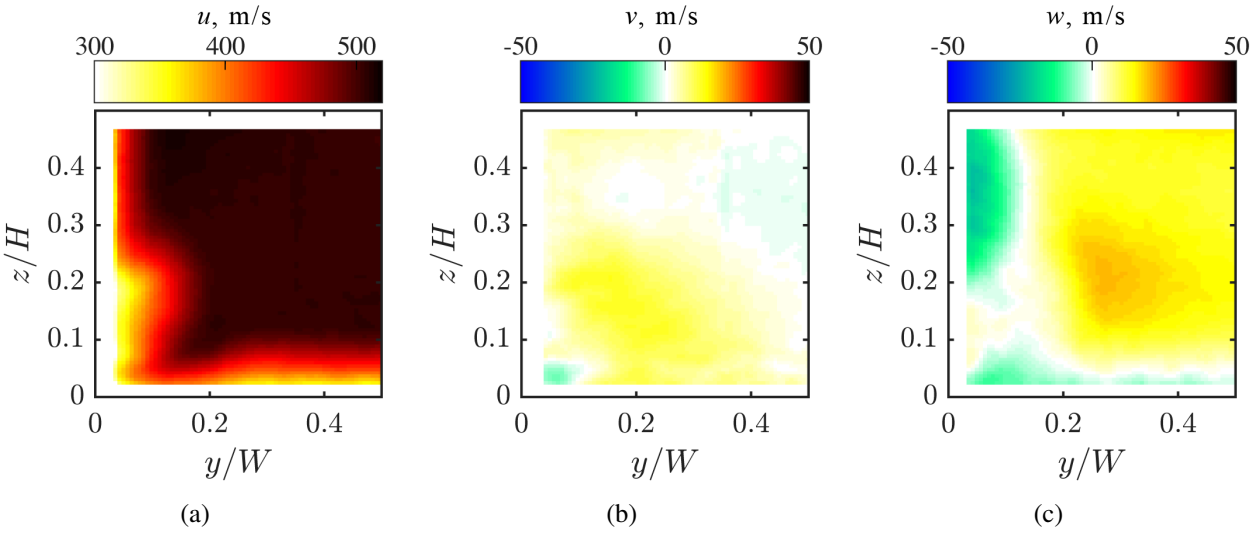

Figure 3.3: Undisturbed, time-averaged velocity fields on cross-sectional slice of the isolator section at $x/H = 7.23$ (i.e., measurement region TV as seen in figure 2.6): (a) streamwise velocity, u; (b) transverse velocity, v; (c) vertical velocity, w.

For instance, the 1D core flow u-velocity is calculated using the time-averaged PIV measurements in figure 3.2(a). First, the top- and bottom-wall boundary layer heights are estimated for every axial location. Specifically, the boundary layer is approximated by finding the distance from the isolator wall where the flow velocity is equal to 99% of the streamwise flow velocity on the centerline of the duct (i.e., along $z = H/2$). Then, the u-velocities which are measured between the upper and lower boundary layers are averaged for every column of the velocity matrix. The resulting 1D core flow u-velocity is plotted as a function of x in figure 3.4(a). For comparison, the dashed line in the figure represents the velocity distribution through the isolator assuming a 1D, steady Fanno flow. Note that even in the presence of the weak uncanceled wave, the measured velocity distribution only varies by at most 4 m/s compared to the Fanno flow case. This difference corresponds to less than 1% of the measured flow velocity.

The Mach number, temperature, and Reynolds number of the undisturbed flow are derived from the velocity measurements by assuming that the flow through the nozzle and isolator section is adiabatic. Thus, the total temperature is equal to the room conditions and is measured prior to every run using a room hygrometer station. The total temperature is approximately equal to 294 K and has a day-to-day variation of ± 2 K. With this information, the 1D core flow Mach number, temperature, and Reynolds number are derived and the results are plotted as a function of x in figures 3.4(b), 3.4(c), and 3.4(d), respectively. The dashed lines represent the corresponding distribution assuming 1D, steady Fanno flow. Again, the difference between the measured values and the Fanno flow case is small. Specifically, the Fanno flow curves deviate from the measured Mach number, temperature, and Reynolds number by less than 1%, 1%, and 3%, respectively. Given the good accuracy of the Fanno flow fits for the 1D flow properties presented in this section, these relationships are used in the following chapters to describe the approach conditions just upstream of the shock train.

3.4 Bottom-Wall Boundary Layer Properties

The properties of the undisturbed bottom-wall boundary layer are determined using the streamwise velocity field shown in figure 3.2(a). For example, the boundary layer thickness, δ, is defined as the distance above the bottom-wall where the flow velocity is equal to 99% of the 1D core flow u-velocity. Figure 3.5(a) shows the bottom-wall boundary layer thickness as a function of x. Note the local peak centered at $x/H = 8$, which is due to the interaction between the boundary layer and the weak uncanceled wave. In general, we find that this uncanceled wave does not impact the subsequent analysis significantly, especially since its effects are localized to a specific region of the boundary layer.

The boundary layer thickness measurements shown in figure 3.5(a) fall closely around Prandtl's

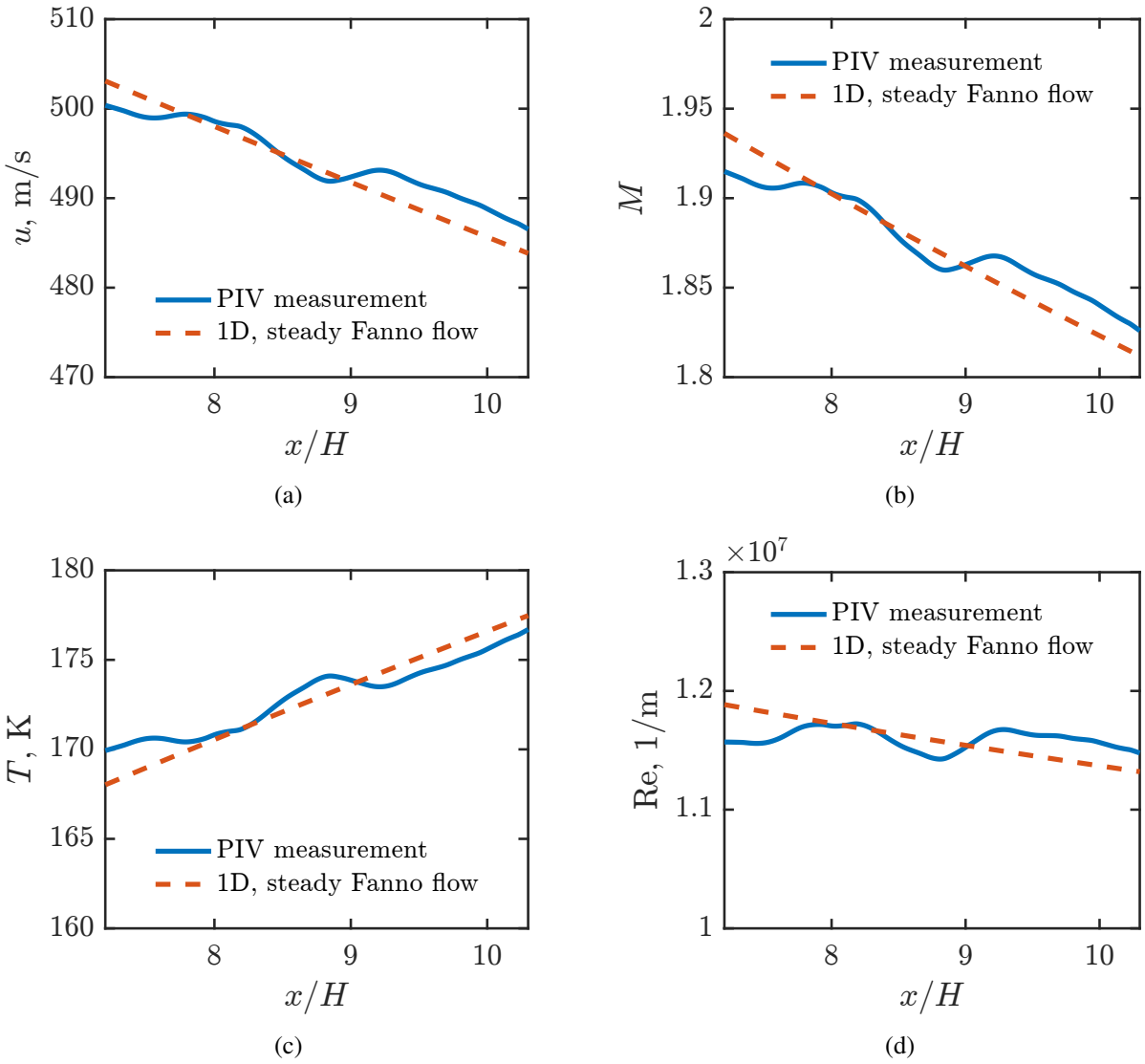

Figure 3.4: 1D core flow properties as a function of x: (a) streamwise flow velocity, u; (b) Mach number, M; (c) temperature, T; (d) Reynolds number, Re.

power law approximation for a (incompressible) turbulent flat plate boundary layer:

$$\delta = 0.16 X Re_X^{-1/7} \tag{3.1}$$

where X is the distance from the hypothetical leading edge of the flat plate (i.e., $X = x + b$ where b is the distance between the virtual origin of the flat plate and the throat of the nozzle) and Re_X is the Reynolds number based on X. The best fit between the measured data points and the power law occurs with $b \approx -54$ mm. With this value of b, the difference between the measurements and the power law fit is less than 0.57 mm (i.e., less than 6% of the measured value). For these velocity

measurements, the PIV vectors have a spacing of 0.38 mm so much of the error can be attributed to the relatively low resolution of the collected data.

An estimate of the density variation through the boundary layer is needed to compute the other boundary layer properties. This is done using the ideal gas law and by assuming that: 1) the pressure through the boundary layer is constant and thus equal to the measurements presented in figure 3.1 and 2) the flow is adiabatic and thus the temperature variation through the boundary layer computed knowing the velocity measured with PIV. With this information, the bottom-wall boundary layer momentum thickness, θ, the displacement thickness, δ^*, and shape factor, δ^*/θ, are found. These quantities are plotted as a function of x in figures 3.5(b), 3.5(c), and 3.5(d), respectively. Once again, notice the local peak centered at $x/H = 8$, which is due to the interaction between the boundary layer and the weak uncanceled wave.

For comparison, the dashed lines in figures 3.5(b)–3.5(d) represent the boundary layer properties estimated based on Prandtl's power law as follows:

$$\theta = 0.016 X_2 Re_{X_2}^{-1/7} \tag{3.2}$$

$$\delta^* = c X_2 Re_{X_2}^{-1/7} \tag{3.3}$$

where c is a constant equal to 0.044 and X_2 is the same hypothetical distance described above but with $b = -198$ mm. The constant c and the offset distance b had to be changed because the boundary layer in the isolator section is not perfectly described by the incompressible, turbulent flat plate approximation. However, the modified Prandtl approximation varies from the measured values by less than 12%.

Given the boundary layer and 1D core flow properties discussed previously, we compute additional flow parameters that are important for our analysis. For example, the confinement ratio based on momentum thickness, $C_\theta = 2\theta/H$, is shown as a function of x/H in figure 3.6(a). The confinement ratio computed using Prandtl's power law approximation for momentum thickness is also plotted as a dashed line. This fit deviates from the confinement ratio computed from PIV measurements by less than 12%.

Also consider the Waltrup and Billig correction factor, Q. In their 1973 paper, Waltrup & Billig [1973] proposed that the wall pressure distribution of the pseudoshock scales with the following combination of approach conditions:

$$Q = \frac{(M^2 - 1) Re_\theta^{1/4}}{\sqrt{C_\theta}} \tag{3.4}$$

In chapter 4, the correction factor provides valuable additional insight on the shock train structure. For completeness, the correction factor is presented in this section with the other undisturbed

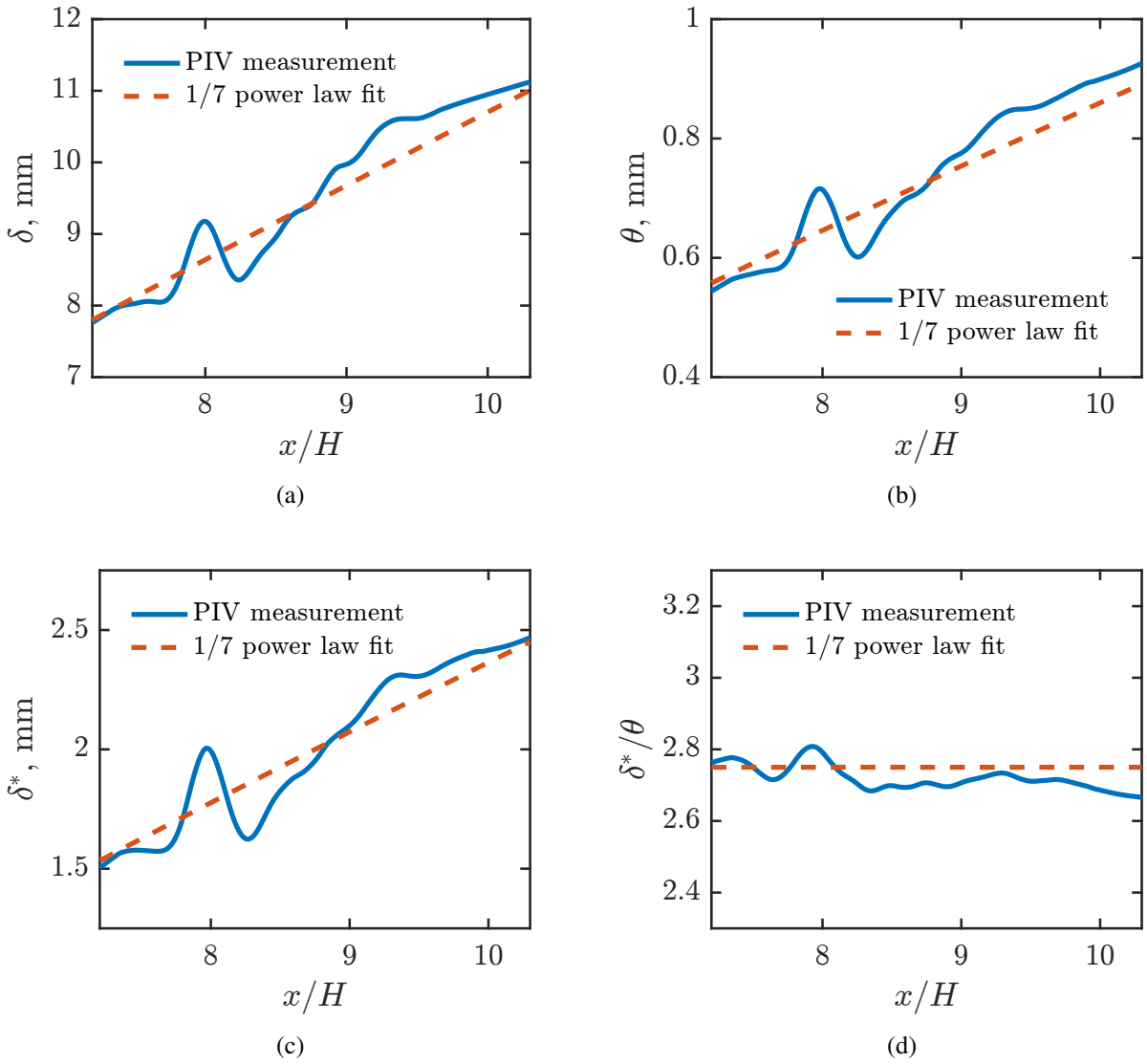

Figure 3.5: Bottom-wall boundary layer properties as a function of x: (a) boundary layer thickness, δ; (b) momentum thickness, θ; (c) displacement thickness, δ^*; (d) shape factor, δ^*/θ.

flow properties but the significance of Q will be discussed more thoroughly in later chapters. Figure 3.6(b) shows the correction factor (computed using the Mach number, Reynolds number, and confinement ratio of the undisturbed flow that were presented previously) as a function of x. The dashed line is computed using the Fanno flow approximation for Mach number and Reynolds number as well as Prandtl's power law approximation for confinement ratio. This fit deviates from the correction factor computed using measurements by less than 3%.

For all of the flow properties presented in this section, the measurements are well represented by their respective fits (e.g., the Prandtl power law approximation or Fanno flow fit). The largest deviation between he measurements and the fitted curves occurs at the location where the uncanceled

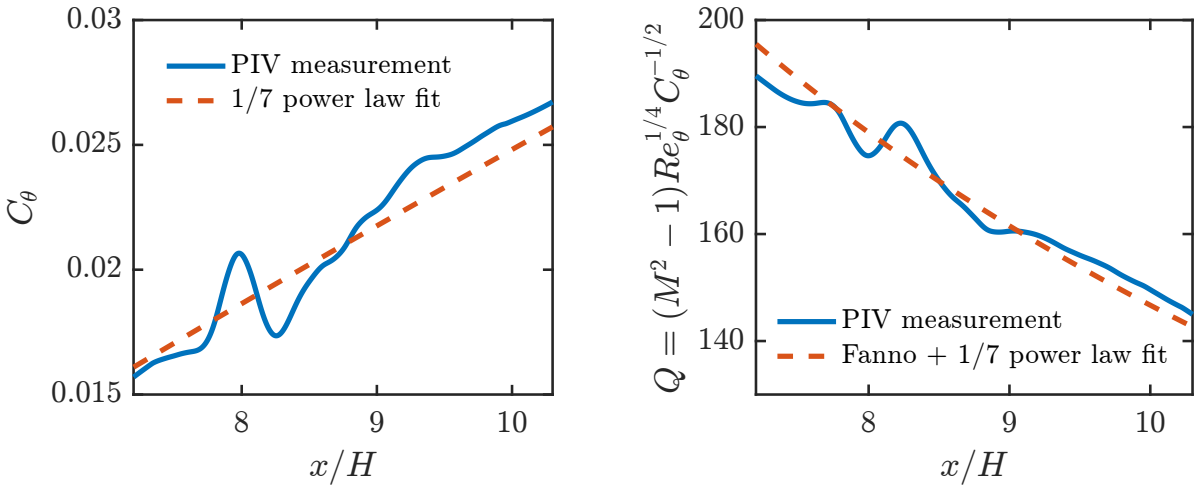

(a) (b)

Figure 3.6: Undisturbed flow properties as a function of x: (a) confinement, C_θ; (b) Waltrup and Billig correction factor, Q.

wave interacts with the bottom-wall boundary layer. However, this error is not remarkably larger than the error at other x-locations. Therefore, the uncanceled wave does not significantly alter any of the subsequent analysis. We use these fits in future chapters to describe the approach conditions of the shock train by interpolating or extrapolating the fits at the x-location of the leading shock foot.

Chapter 4

Shock Train Structure

In this chapter, the structure of the shock train is studied as a starting point used to characterize the basic properties of this complex system. For these experiments, the valve angle is kept constant as data is collected and thus, the back pressure of the isolator model, p_b, is approximately constant as well. Then, the experiments are repeated for different valve angle and back pressure cases. The shock train location and approach conditions are dependent on the back pressure. Thus, the sensitivity of the shock train structure to changes in the approach conditions is effectively evaluated.

In section 4.1, the oblique-to-normal transition process is evaluated by quantifying the Mach stem height and shock angles of the leading shock at different pressure ratios, p_b/p_f, using high-speed schlieren movies. The time-averaged profiles of the pseudoshock are introduced in section 4.2. The variance of the measured pressure is used in section 4.3 to determine how the length and pressure rise across the shock train and mixing region change as the pseudoshock moves upstream. The length and pressure rise of each component are scaled by the approach conditions to determine if the shock dominated region responds to changes in pressure ratio differently than the viscous dominated mixing region. Finally, the pressure measurements indicate a complex three-dimensional structure. To investigate this further, the three-dimensional structure of a normal leading shock is examined and the amount of boundary layer separation is quantified using SPIV (see section 4.4).

For this work the pressure ratio, p_b/p_f, is varied between 2.09 and 3.43. The pressure ratio cannot be raised too far above the upper bound presented in this paper because the shock train moves out of the isolator section and into the diverging portion of the wind tunnel nozzle. Conversely, the pressure ratio cannot be lowered past 2.09 because the shock train enters the diffuser section. Note that the range of pressure ratios studied corresponds to 60% – 76% of the pressure rise across a normal shock at the same approach Mach number. That is: $0.60 < (p_b/p_f)/(p_2/p_1)_\perp < 0.76$ where $(p_2/p_1)_\perp$ is the ratio of pressures before and after a normal shock. According to Matsuo *et al.* [1999] the maximum pressure ratio across a pseudoshock is approximately 80% of the pressure ratio across a normal shock in a Mach 2 flow. Thus, almost the entire pseudoshock structure is

contained within the isolator section for the highest pressure ratio case (i.e., when the shock train is at its most upstream location).

4.1 The Oblique-to-Normal Transition Process

Schlieren imaging of the shock train in conjunction with pressure measurements provide the necessary data to compare the shock train location at various pressure ratios. Figure 4.1 shows the time-averaged shock locations, $\langle x_1 \rangle$, $\langle x_{2t} \rangle$, $\langle x_{3t} \rangle$, and $\langle x_{4t} \rangle$, versus the time-averaged pressure ratio, $\langle p_b/p_f \rangle$, with each symbol representing the result from individual repetitions of the experiment. Note that only one morphological feature of each shock is plotted for clarity but similar results are obtained for the other shock morphological features. As demonstrated by the trendlines in the figure, all of the time-averaged shock locations move upstream linearly with increased pressure ratio. For any given pressure ratio, the spacing between consecutive shocks decreases along the length of the shock train (i.e., $\langle x_2 - x_1 \rangle = 74$ mm $> \langle x_3 - x_2 \rangle = 47$ mm $> \langle x_4 - x_3 \rangle = 44$ mm). This trend has been observed in many other studies [Carroll, 1988; Ikui *et al.*, 1974*a*]. Also note that the slopes of the trendlines in figure 4.1 are approximately the same for all four shocks. Thus, the amount of space between consecutive shocks does not depend on pressure ratio for this experiment. Other studies claim that the shock spacing depends on the Mach number and confinement, but these studies contradict each other [Carroll, 1988; Lin *et al.*, 1991]. One reason could be that the inflow conditions of the isolator are typically measured and not the approach conditions of the

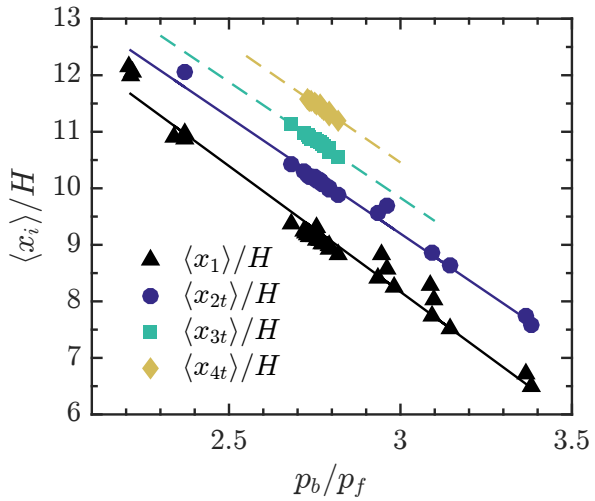

Figure 4.1: Time-averaged locations of the first four shocks as a function of pressure ratio. Note that the back pressure, p_b, is measured at $x/H = 14.73$ and the diffuser section starts just downstream of this location.

shock train. Thus, these studies do not account for changes along the isolator length due to the natural boundary layer growth.

To study how the leading shock structure changes with pressure ratio, first consider the angles of the leading and trailing legs of the first shock lambda foot, α_L and α_R, which are found using schlieren imaging and are defined from the horizontal x-direction as shown in figure 2.2. Figure 4.2 shows the time-averaged shock angles, $\langle\alpha_L\rangle$ and $\langle\alpha_R\rangle$, versus the pressure ratio. The standard deviation of the shock angle for any given case is approximately $1.6°$. Interestingly, the angle of the trailing leg (α_R) scales as $1.48\sin^{-1}(1/M)$, where M is the approach Mach number. This statement is demonstrated in the figure by the blue line. That is, the angle of the trailing leg is approximately 1.48 times greater than the Mach wave angle. Thus, increasing the pressure ratio (or equivalently moving the shock train upstream) causes the angle of the trailing leg to decrease slightly. Simultaneously, the angle of the leading leg increases with pressure ratio. Note that the leading leg angle has a nearly linear relationship with pressure ratio despite some run-to-run variation. The instantaneous values of α_L and α_R are also weakly correlated with x_1. The correlation with α_L and α_R are negative and positive, respectively, agreeing with trend seen in the time-averaged results. Thus, as the shock train moves upstream, the leading shock in the lambda foot becomes stronger and the trailing shock becomes weaker both instantaneously and in a time-averaged sense.

The Mach stem height of the leading shock, s, is also found from schlieren imaging. Figure 4.3(a) shows the time-averaged Mach stem height, $\langle s\rangle$, as a function of pressure ratio. From the figure it is apparent that the average Mach stem height increases non-linearly with pressure ratio (i.e., as the shock train moves upstream). This trend is perhaps better visualized using the

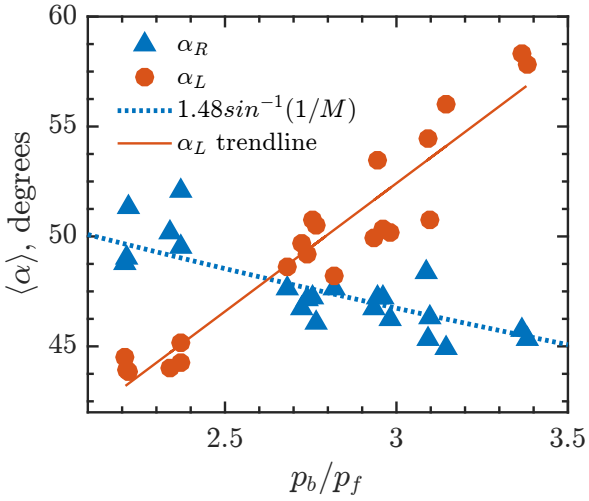

Figure 4.2: Time-averaged shock angles of the leading shock lambda foot versus pressure ratio.

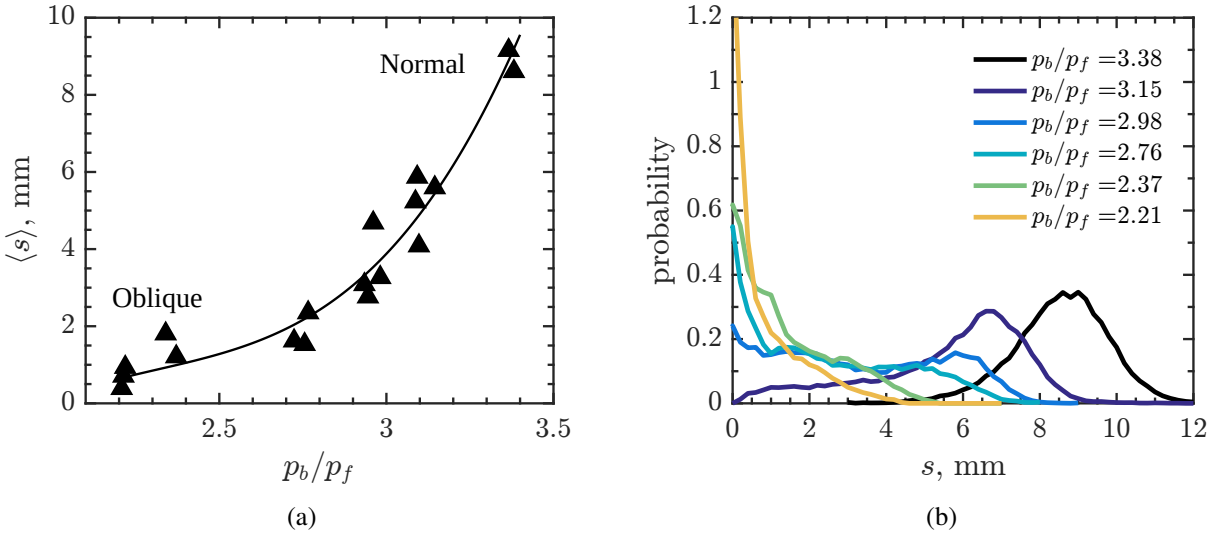

(a) (b)

Figure 4.3: (a) Time-averaged height of the leading shock Mach stem as a function of pressure ratio; (b) probability density function of the leading shock Mach stem height at different pressures ratios.

probability density functions of the Mach stem height for select pressure ratios as shown in figure 4.3(b). At low pressure ratios the distribution is strongly peaked at zero thus, a Mach stem is not present in most instances and the leading shock can be considered oblique. At intermediate values of pressure ratio the distribution has a broad, flat shape and the shock train cannot be clearly defined as normal or oblique because the Mach stem height has a large amount of variability. At high pressure ratios the distribution is bell-shaped. For $p_b/p_f > 3.37$ the shock train is fully a bifurcated normal shock train because the Mach stem height is always greater than zero. At the highest pressure ratio, the Mach stem averages 9 mm long (13% of the isolator height) so the system can be defined as a normal shock train with a significantly large lambda foot. Contrary to the mean result, the instantaneous Mach stem height does not correlate with the instantaneous shock position during the unsteady motion. This suggests that other variables, which are independent of the shock train location, influence the shock train structure during the normal-to-oblique transition process.

Figures 4.2 and 4.3 exemplify how the leading shock transitions from oblique to normal as pressure ratio is increased. It is also important to discuss these structural changes in terms of the approach conditions. From the discussion in chapter 3, we know that increasing the back pressure causes the shock train to move upstream where the Mach number is higher and the confinement is smaller. With this in mind, recall the regime diagram (figure 1.3) discussed in section 1. The upper and lower cases of confinement for the current study are shown as circles in figure 1.3. These results clearly push the bounds of the transition regime. That is, large flow confinement keeps the shock train oblique even as Mach number is decreased. Conversely, a small confinement

allows for a normal shock train even at high Mach numbers. While most of the literature has emphasized the impact of Mach number on shock train structure, the current study emphasizes the role of confinement. Classifying the transition regime as a large range of Mach numbers may be too simplistic. In reality, the transition regime is a more complex function of Mach number and confinement. In other words, the point at which a shock train will transition from oblique to normal depends on the local Mach number and confinement upstream of the shock train.

4.2 Time-Averaged Pressure Profiles

The oblique-to-normal transition process is also evident in the time-averaged pressure profiles along the test section, as demonstrated by figure 4.4. The solid lines in the figure represent the side-wall measurements (taken along $z = H/2$) and the dashed lines represent bottom-wall measurements (taken along $y = W/2$). First, notice that the shape of the side-wall pressure profile changes as pressure ratio is increased. The lowest pressure ratio case (i.e., an oblique leading shock) has a non-monotonic side-wall pressure profile with many distinct steps and regions of decreasing pressure. The regions of decreasing pressure could be due to the flow re-accelerating after each shock. The highest pressure ratio case (i.e., a normal leading shock) has a smooth, monotonically increasing side-wall pressure profile. Next, consider the bottom-wall pressure profiles that are smoother and always monotonically increasing. The similarity in side- and bottom-wall pressure profiles in the normal shock train case indicates a degree a axisymmetry in the shock train. As the

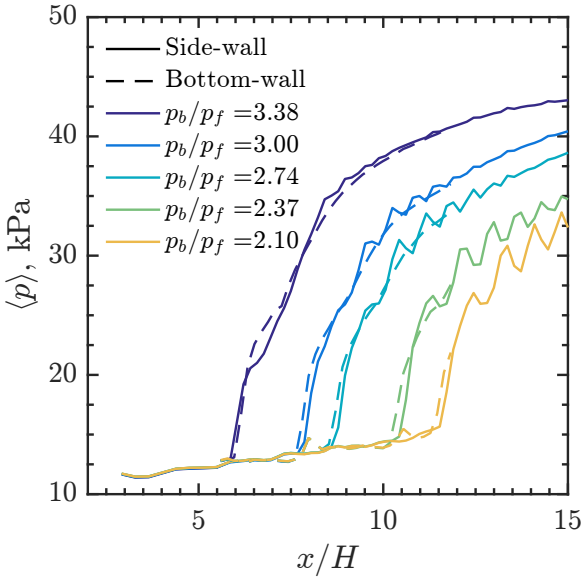

Figure 4.4: Time-averaged pseudoshock pressure profiles for various pressure ratios.

shock train becomes more oblique this axisymmetry is lost and the two surfaces exhibit different pressure distributions (one pressure profile is smooth and the other has distinct steps).

Figure 4.4 also shows that the beginning of the bottom-wall pressure rise differs from the beginning of the side-wall pressure rise by less than $0.1H$. This result is unexpected because the schlieren images show a substantial lambda foot that would induce a pressure rise on the bottom-wall much earlier than the Mach stem would induce a pressure rise on the side-wall. The closer (than expected) pressure profiles indicate that the leading shock might have a three-dimensional structure that cannot be visualized with the schlieren configuration used in this study. This topic is discussed further when the particle image velocimetry measurements are analyzed in section 4.4.

Next, consider figure 4.5 which plots the time-averaged pressure profiles less their corresponding shock foot pressures, $\langle p - p_f \rangle$, versus the distance from the shock foot, $\widetilde{x}$. That is, all of the pressure curves are shifted so that the pressure rise associated with the pseudoshock begins at the origin of the plot. Notice that the data collapse in the upstream portion of the pseudoshock, i.e., for $\widetilde{x} < 2H$. The normalized pressure profiles diverge away from each other in the downstream portion of the system. Thus, changing the pressure ratio will influence the shock train structure and the downstream pressure distribution. However, for the range of conditions in this study, the pressure ratio does not significantly influence the upstream portion of the pressure rise despite major changes in the shock morphology. Based on the measured shock angles and estimated Mach numbers just upstream of the shock train, the pressure rise across the leading oblique shock of the lambda foot more than doubles across the range of pressure ratios. Thus, it is interesting that the

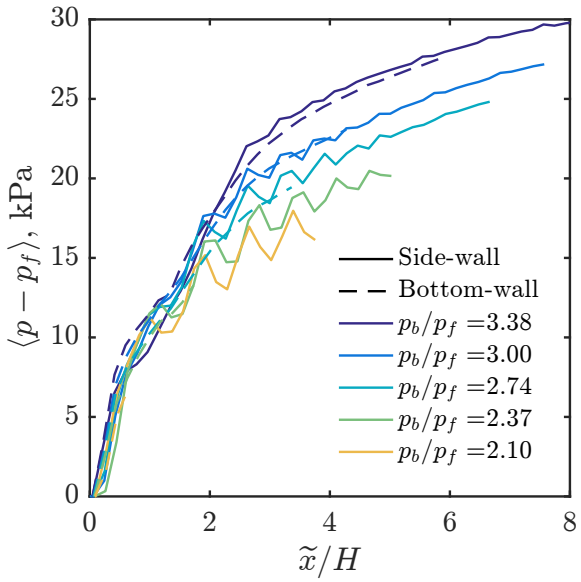

Figure 4.5: Time-averaged pseudoshock pressure profiles for various pressure ratios.

leading shock structure visibly changes and the expected pressure rise across the leading shock should vary with pressure ratio but the measured pressure distribution is similar for all cases. Once again, these results suggest that the schlieren images do not adequately capture the complex system of compression waves that develops along the duct wall. The three-dimensionality and complex compression system are discussed in section 4.4.

In an attempt to scale the pressure profiles based on the approach conditions, the empirical relationship introduced by Waltrup & Billig [1973] is utilized. See section 1.3 for a review of this model. The model is a simple quadratic relationship that uses the flow properties just upstream of the shock train to describe the wall pressure profiles along the length of the shock train. Here, this relationship is written in a slightly different form as follows:

$$50\left(\frac{p}{p_f}-1\right)+170\left(\frac{p}{p_f}-1\right)^2=\frac{\sqrt{2}Q\widetilde{x}}{H} \tag{4.1}$$

where p is the pressure a distance $\widetilde{x}$ away from the leading shock foot, p_f is the pressure at the leading shock foot, and H is the tunnel height. Q is the correction factor defined in equation 3.4 and is a short-hand way of representing the fraction of flow conditions just upstream of the shock train. By writing the Waltrup and Billig relationship in the alternative form of equation 4.1, the (quadratic) pressure profile can be easily interpreted as a linear function of the normalized distance away from the leading shock foot, $\widetilde{x}/H$, where the slope of the linear relationship is the correction factor, Q. When the shock train moves to a new location, the correction factor accounts for changes in the approach conditions including the Mach number, Reynolds number, and confinement ratio.

The scaled pressure distributions shown in figure 4.6 result from transforming the original pressure data (shown in figure 4.4) in two ways. First, the pressure profiles are normalized by the pressure at the foot of the shock train, p_f, such that all of the curves start at a value of 1 on the y-axis. Second, the normalized pressures are plotted as a function of the distance relative to the leading shock foot, $\widetilde{x}$, corrected by the Waltrup and Billig factor, Q. That is, the length of pressure distribution is scaled based on the approach conditions. When plotted this way, the data collapse the best for $\widetilde{x}Q/H < 300$, where the slope of the pressure rise is highest. From schlieren images it is evident that $\widetilde{x}Q/H < 300$ corresponds to the region under the first two shock systems, whose shock morphology is visibly different between different pressure ratio cases. For $\widetilde{x}Q/H > 300$ the pressure profiles begin to diverge such that the lower pressure ratio cases have a shallower slope.

Generally, the normalized curves in figure 4.6 resemble the shifted curves in figure 4.5 but the data arguably collapse better when corrected using the Waltrup and Billig factor. However, neither shifting or correcting the data by Q will collapse the downstream portion of the pressure rise. Thus, the Waltrup and Billig relationship (as well as many other pseudoshock models) fails to accurately predict the pressure rise across the entire length of the system. One reason for this could be that

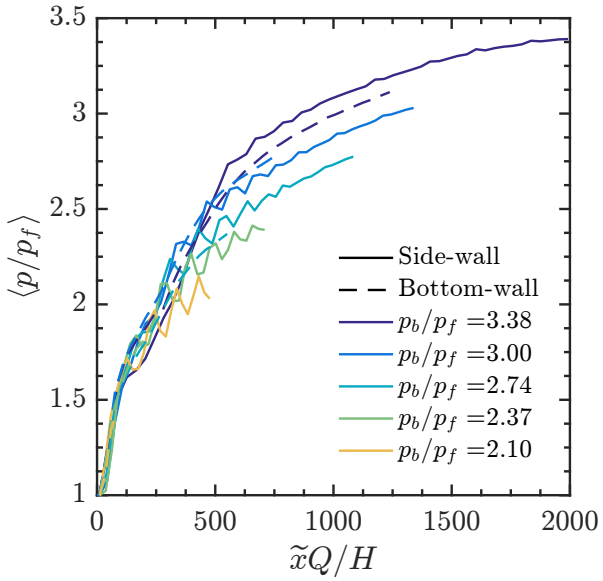

Figure 4.6: Normalized pseudoshock pressures versus the corrected location in the duct.

the upstream and downstream portions of the pseudoshock are scaled the same way. However, the core flow in the shock train region is dominated by shocks (i.e., viscous forces are less significant in comparison) whereas the mixing region is dominated by by viscous, turbulent forces. Therefore, the differences in physics are not accounted for. This topic is explored further in the next section.

4.3 Shock Train and Mixing Region Properties From Pressure Measurements

4.3.1 The Variance Method

In order to better understand the results of the previous section, the pressure rise is decomposed into two components: 1) the pressure rise due to the shock train and 2) the pressure rise due to the mixing region. In the literature, the shock train region is traditionally identified as the region where shock waves are visibly present and is determined using schlieren or shadowgraph imaging. This approach can be limited by the size of the available field of view and most importantly, the results can be subjective or at least limited by the sensitivity of the imaging technique.

In this work, we propose a more objective and mathematically formal method for defining the end of the shock train (i.e., the beginning of the mixing region) which relies on wall static pressure measurements. This is called the *variance method* because the derivative of pressure variance in time with respect to x (i.e., $\mathrm{d}(\sigma^2(p))/\mathrm{d}x$) is used. Objectively defining the beginning and end of the

shock train region allows one to quantify important properties of the shock train including its length and overall pressure rise. To introduce the variance method, consider the following argument:

1. The measured pressure fluctuations at a given point can be caused by 1) turbulent fluctuations due to thickened or separated boundary layers, p'_{turb}, or 2) fluctuations induced by the presence of a shock that sweeps back and forth over the measurement point, p'_{shock}.

2. Under the assumption that the two contributions are uncorrelated, the variance of the measured pressure is equal to the sum of the variances of the individual fluctuation components:

$$\sigma^2(p) = \sigma^2(p'_{turb}) + \sigma^2(p'_{shock}) \tag{4.2}$$

3. For the moment, just consider the pressure fluctuations due to shock movement. Given that the shock moves by an amount x' and that the shock imposes a pressure rise per unit length of $\mathrm{d}p/\mathrm{d}x$, then the pressure fluctuation can be approximated as:

$$p'_{shock} = (\mathrm{d}p/\mathrm{d}x)x' \tag{4.3}$$

4. The variance of the pressure fluctuation due to shock movement is:

$$\sigma^2(p'_{shock}) = \int_T [(\mathrm{d}p/\mathrm{d}x)x']^2 dt \tag{4.4}$$

   where T indicates the integration of a sufficiently long time period. For small shock position fluctuations, the slope of the pressure profile, $\mathrm{d}p/\mathrm{d}x$, is nearly constant as the shock fluctuates in space. By assuming that $\mathrm{d}p/\mathrm{d}x$ is also constant in time then the variance becomes:

$$\sigma^2(p'_{shock}) = (\mathrm{d}p/\mathrm{d}x)^2\sigma^2(x') \tag{4.5}$$

5. Thus, the variance in time of the measured pressure is related to the slope of the pressure distribution:

$$\sigma^2(p) = \sigma^2(p'_{turb}) + (\mathrm{d}p/\mathrm{d}x)^2\sigma^2(x') \tag{4.6}$$

6. Take the derivative of the variance with respect to x to get:

$$\mathrm{d}(\sigma^2(p))/\mathrm{d}x \approx 2(\mathrm{d}p/\mathrm{d}x)(\mathrm{d}^2p/\mathrm{d}x^2)\sigma^2(x') \tag{4.7}$$

   We argue that the contribution from turbulence is negligible because the pressure rise of this component is gradual (i.e., $\mathrm{d}(\sigma^2(p'_{turb}))/\mathrm{d}x \approx 0$). That is, the contribution of turbulence

slowly varies in space.

The simple, first order model discussed above shows that the inherent unsteadiness of the shock train system will lead to variation in the pressure measurements as shocks fluctuate over a transducer. More importantly, it is argued that the derivative of variance with respect to x is highly dependent on these shock fluctuations. These two fundamental ideas are essential for describing how the variance method we propose successively identifies the boundary between the shock train and the mixing region.

Figure 4.7(a) shows the pressure variance (red line) and the derivative of the variance (black line) versus x for a single case of $p_b/p_f = 2.63$. These curves are computed using the pressures measured along the side-wall at $z = H/2$ because the available pressure measurement locations extend across a wider length of the isolator section compared to the bottom-wall. Also recall that the pressures are measured 12.7 mm apart. For smoother results the computed values of $\mathrm{d}[\sigma(p)^2]/\mathrm{d}x$ are interpolated onto a finer grid, with a resolution of 0.254 mm, and then smoothed with a moving average filter of 50 points (which corresponds to the original resolution of 12.7 mm). The variance method is then applied to the resulting smoothed curve.

With figure 4.7(a) in mind, consider three regions in the isolator: 1) the undisturbed upstream flow, 2) the shock train, and 3) the mixing region. In the undisturbed upstream flow the variance of pressure is low (i.e., $\sigma^2(p) \approx 0$) because the only contribution to pressure fluctuations is from turbulence in the undisturbed boundary layer. Furthermore, only negligible changes are expected in the pressure variance for different x-locations upstream of the shock train (i.e., $\mathrm{d}(\sigma^2(p))/\mathrm{d}x \approx 0$). Within the shock train the pressure variance is expected to be significantly higher than the undisturbed flow because of pressure fluctuations due to shocks and their induced turbulence (i.e., $\sigma^2(p) > 0$). In addition, large changes in pressure variance (i.e., $\mathrm{d}(\sigma^2(p))/\mathrm{d}x$ is high) are expected where shocks are located based on the simple model presented in the previous paragraph. Within the mixing region, the elevated turbulence will lead to a non-zero pressure variance (i.e., $\sigma^2(p) > 0$). However, no shocks exist in this region and thus the derivative of variance is expected to be negligible (i.e., $\mathrm{d}(\sigma^2(p))/\mathrm{d}x \approx 0$).

Based on the above considerations, it is assumed that the shock train begins at a location x_f, defined as the first local peak in $\mathrm{d}[\sigma(p)^2]/\mathrm{d}x$. The triangle marker in figure 4.7(a) denotes the shock foot location for the given example. Note that the first peak in $\mathrm{d}[\sigma(p)^2]/\mathrm{d}x$ has the largest magnitude and thus is a reliable feature that can be utilized with the variance method to identify the shock foot location. It is also assumed that the shock train ends at a location x_s, defined as the last point in $\mathrm{d}[\sigma(p)^2]/\mathrm{d}x$ that is larger than a cutoff value. As discussed later on in this section, the shock train and mixing region characteristics are fairly insensitive to the choice of the cutoff value. The circular marker in figure 4.7(a) indicates the boundary between the shock train and mixing region, x_s, for this example. For comparison, the square marker in figure 4.7(a) indicates the back

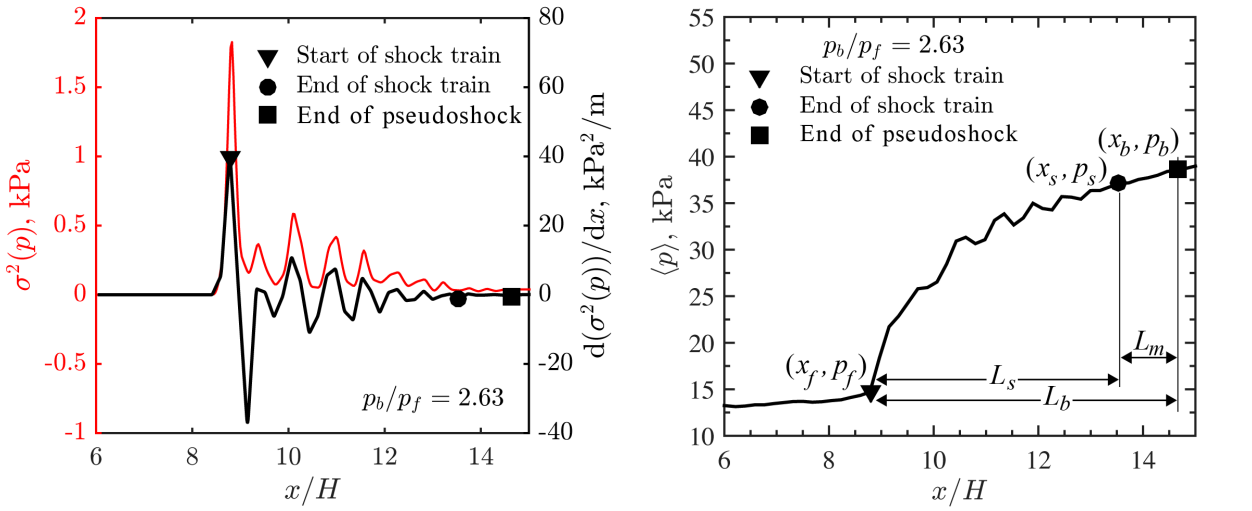

Figure 4.7: (a) Example of how the shock train region is defined using the variance method; (b) corresponding pressure profile illustrating the important features of the system including the length of the shock train, L_s, length of the mixing region, L_m, length of the pseudoshock, L_b, pressure at the foot of the shock train, p_f, pressure at the end of the shock train, p_s, and pressure at the end of the pseudoshock, p_b.

pressure measurement location, x_b. This location is defined as the end of the pseudoshock because the diffuser section begins just downstream of this point.

Figure 4.7(b) shows the original time-averaged pressure profile that corresponds with the pressure variances shown in figure 4.7(a) (for $p_b/p_f = 2.63$). Once again, the locations of the shock train foot, the end of the shock train, and the end of the pseudoshock are marked by the triangle, circle, and square markers, respectively. Given the shock foot location, the pressure at the foot of the pseudoshock, p_f, is directly found from the original time-averaged pressure distribution and the location of the shock train can be discussed in terms of the pressure ratio, p_b/p_f. Similarly, the pressure at the end of the shock train, p_s, is quantified from the original time-averaged pressure distribution given the location x_s. With the above information, the length of the shock train is defined as $L_s = x_s - x_f$ and the length of the mixing region is defined as $L_m = x_b - x_s$. Comparatively, the length of the entire pseudoshock is $L_b = x_b - x_f$. The total pressure rise across the pseudoshock is p_b/p_f. The total pressure rise is further broken down into two components: 1) the pressure rise across the shock train, equal to p_s/p_f, and 2) the pressure rise across the mixing region, equal to $p_b/p_f - p_s/p_f = (p_b - p_s)/p_f$.

Before examining the results of the variance method across multiple cases, consider how the cutoff value is chosen. Recall that x_s is found using the variance method by identifying the last point in $\mathrm{d}[\sigma(p)^2]/\mathrm{d}x$ that is above a certain cutoff value. In this study, a cutoff value of 0.006

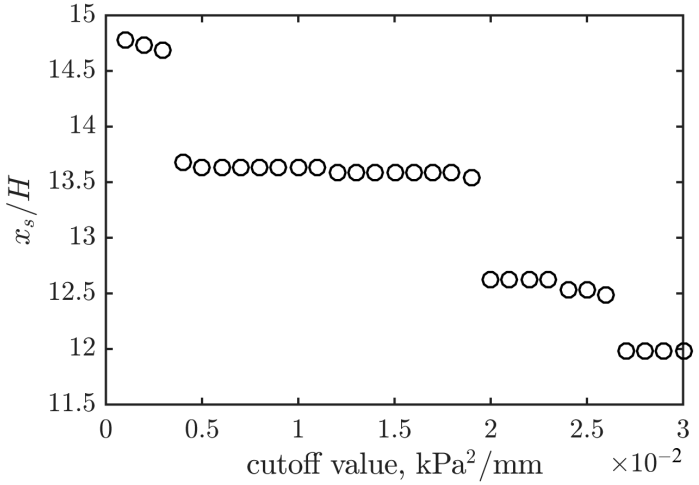

Figure 4.8: Effects of the chosen cutoff value on the location of the shock train and mixing region boundary.

kPa^2/mm is chosen, below which any pressure fluctuations are deemed insignificant. A parametric study on the effects of this cutoff value suggest that x_s is fairly insensitive to the specific cutoff chosen. However, the cutoff must be selected from an appropriate range of values for the given data set. For example, figure 4.8 shows the value of x_s found by applying the variance method with different cutoff values to a single pseudoshock case. Specifically, these are the results of the $\mathrm{d}[\sigma(p)^2]/\mathrm{d}x$ distribution for the case of $p_b/p_f = 2.63$ plotted in figure 4.7(a). In this case, a cutoff value higher than 0.019 kPa^2/mm will significantly underestimate the shock train length by ignoring the smaller (but still significant) downstream peaks in $\mathrm{d}[\sigma(p)^2]/\mathrm{d}x$. This has been confirmed using schlieren imaging. In addition, a cutoff value less than 0.004 kPa^2/mm is not reliable because the algorithm detects a random local peak in the mixing region where the pressure variance slowly changes due to the mixing process. These local peaks in the mixing region are not consistent from run-to-run and thus low cutoff values do not produce consistent estimates of x_s. A cutoff between 0.004 and 0.019 kPa^2/mm results in a value of x_s between $13.54H$ and $13.67H$. The location of the shock train and mixing region boundary is considered insensitive to the specific cutoff value chosen within this range of cutoff values because there is less than a 1% difference in the resulting value of x_s. The final cutoff of 0.006 kPa^2/mm is chosen because it is reliably within the range of satisfactory values for all the different pseudoshock cases.

It is acknowledged that measured pressure fluctuations presented in this study are effectively low-passed filtered due to the narrow bandwidth of the pressure scanners. In general, the magnitude of the $\mathrm{d}[\sigma(p)^2]/\mathrm{d}x$ is dependent on the bandwidth of the transducers. To further validate the variance method, the standard deviation of the pressure scanner measurements are compared to the standard deviation measured using high-speed pressure transducers (Kulite XCS-062). The

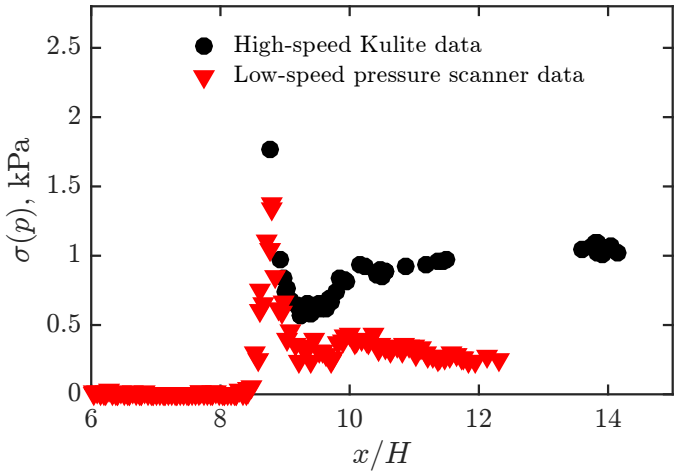

Figure 4.9: Comparison of the pressure standard deviation when measured using high-speed Kulites and low-speed pressure scanners.

high speed data is recorded at 500 kHz but the response of the gages are limited to 52 kHz by a signal conditioner. Figure 4.9 shows an example of the pressure standard deviation through the isolator for both types of transducers. Due to the availability of Kulite measurements, both the pressure scanners and Kulites are used to measure the wall static pressure on the bottom-wall of the isolator section for this comparison. The figure demonstrates that both sets of data have the same overall trend but the standard deviation of the pressure scanner data is generally smaller. The important features, i.e., the large spike in pressure standard deviation due to the shocks in the train, are evident in both cases. Thus, if the cutoff value is properly chosen then the location corresponding to the end of the shock train, which is identified using the derivative of the pressure variance, is independent of bandwidth. This emphasizes another benefit of the variance method. Specifically, this method does not require expensive, high-speed transducers. In comparison to the traditional methods that require optical access, defining the boundary between the shock train and the mixing region is relatively simple using the variance method because only static wall pressure measurements are required.

4.3.2 Length and Pressure Rise as a Function of Pressure Ratio

Using the variance method described above, the length and pressure rise across the shock train and mixing region are identified for a range of different pressure ratio cases. That is, the location of the pseudoshock in the isolator section is varied in order to determine the effects of changing the approach conditions on these two design parameters. Note that very low pressure ratios were not used in the following analysis because the end of the shock train was not located in the isolator

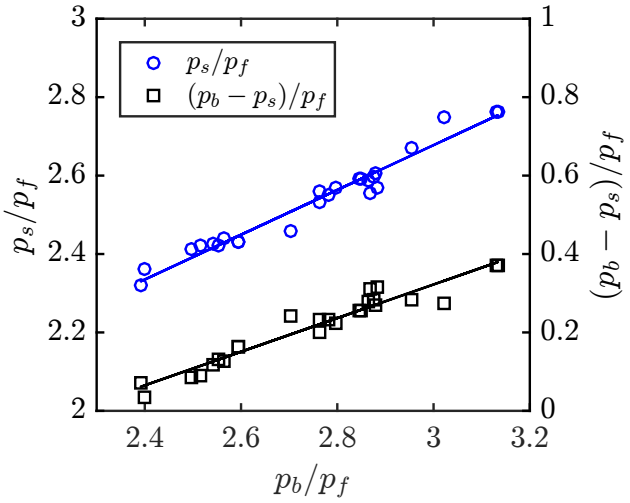

Figure 4.10: The pressure rise across the shock train and mixing region increases as the shock train moves upstream (i.e., as pressure ratio increases).

section.

Figure 4.10 shows that the pressure rise across the shock train, p_s/p_f, and the pressure rise across the mixing region, $(p_b - p_s)/p_f$, both increase as the pseudoshock moves upstream. The magnitude of the mixing region pressure rise is significantly smaller compared to that of the shock train which is why these quantities are plotted on different y-axes. Note that the scales of these axes are the same. With this in mind, it appears that the mixing region pressure rise increases at nearly the same rate as the shock train pressure rise across the range of pressure ratios for this experiment. Specifically, the linear trendlines of p_s/p_f and $(p_b - p_s)/p_f$ increase by 0.57 and 0.43 per unit pressure ratio, respectively.

It is convenient to consider the pressure rise of each pseudoshock component as a fraction of the total pressure rise of the system. Figure 4.11 shows that the amount of compression provided by the shock train becomes a smaller fraction of the total pseudoshock compression as the pseudoshock moves upstream. That is, p_s/p_b decreases nearly linearly with pressure ratio. Simultaneously, the fraction of compression provided by the mixing region, $1 - p_s/p_b$, increases. For example, 98% of the pressure rise is provided by the shock train at the most downstream pseudoshock position. At the most upstream position (just prior to unstart), the shock train provides approximately 88% of the overall compression. The mixing region provides the remaining 12% of the compression at this state.

Recall that the approach Mach number of the pseudoshock is slightly different across the various pressure ratio cases. To account for this Mach number variation, the measured pressure rises are normalized by the pressure rise across a normal shock at the approach Mach number, $(p_2/p_1)_\perp$.

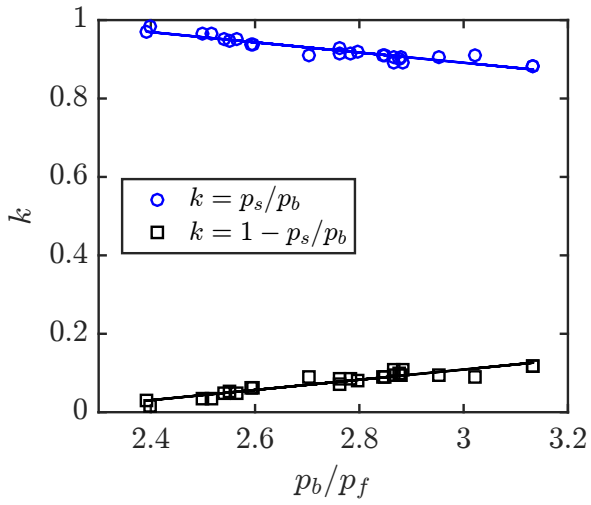

Figure 4.11: The shock train pressure rise accounts for less of the overall compression as the shock train moves upstream (i.e., as pressure ratio increases). Simultaneously, the mixing region accounts for more of the overall compression.

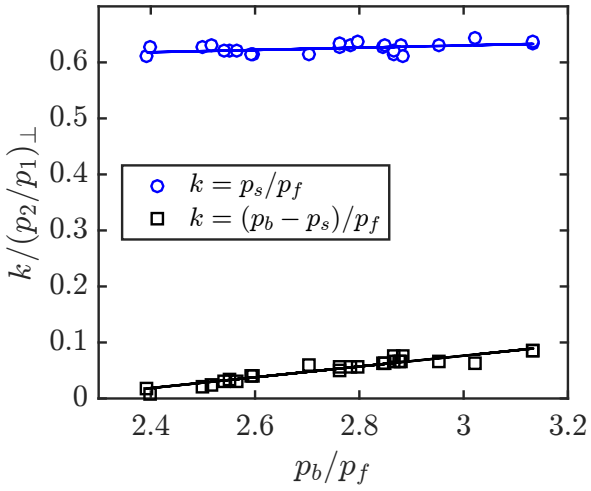

Figure 4.12: The shock train pressure rise is nearly a constant fraction of the pressure rise across a normal shock at the approach Mach number. The normalized mixing region pressure rise increases as the shock train moves upstream (i.e., as pressure ratio increases).

For each case, the approach Mach number is estimated using the undisturbed flow conditions discussed in chapter 3. The corrected pressure rises, $(p_s/p_f)/(p_2/p_1)_\perp$ and $[p_b - p_s)/p_f]/(p_2/p_1)_\perp$, are shown in figure 4.12. Interestingly, the compression due to the shock train region is approximately a constant fraction of the normal shock pressure rise under the conditions of this experimental configuration: $p_s/p_f \approx 0.64(p_2/p_1)_\perp$. This value is objectively defined as constant because the linear trendline has less than a 3% change in value across the entire range of pressure ratios. Because the corrected pressure rise across the shock train is constant and the total pressure rise increases to meet the enforced downstream boundary condition, the mixing region must adjust in order to provide the necessary additional pressure rise. The square symbols in figure 4.12 show that this is indeed the case. To interpret the results of figure 4.12 in a slightly different way, consider a hypothetical experiment where the pseudoshock approach Mach number is constant throughout the isolator. As the pseudoshock moves upstream, the pressure rise across the shock train remains a constant fraction of $(p_2/p_1)_\perp$ and the mixing region grows at a rate proportional to $(p_2/p_1)_\perp$.

Figure 4.13 shows that the length of the shock train, L_s, decreases and the length of the mixing region, L_m, increases with pressure ratio. Specifically, the linear trendline of the shock train length decreases by $1.4H$ per unit pressure ratio. Simultaneously, the linear trendline of the mixing region length, L_m, increases by $5.8H$ per unit pressure ratio.

Increasing pressure ratio moves the pseudoshock upstream and therefore increases the total length of the system. It is convenient to think of the length of each component normalized by the total length of the pseudoshock, i.e., L_s/L_b and L_m/L_b. Figure 4.14 illustrates these quantities as a function of back pressure. In this figure it is clear that the length of the shock train accounts for less

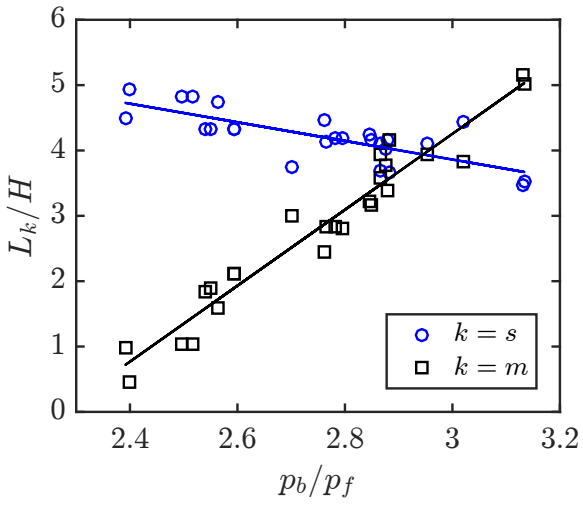

Figure 4.13: The shock train length decreases and the mixing region length increases as the shock train moves upstream (i.e., as pressure ratio increases).

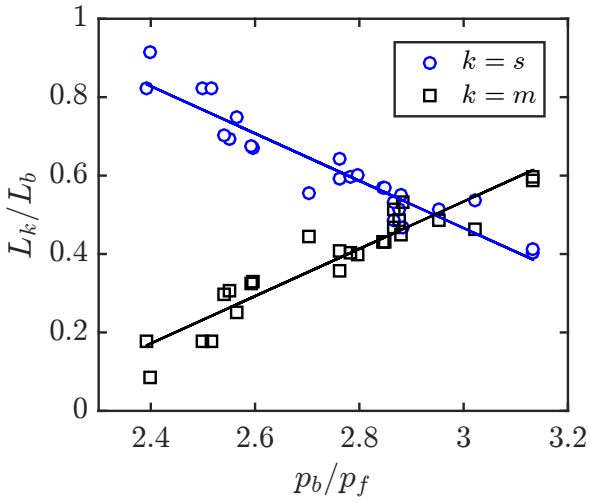

Figure 4.14: The shock train accounts for less of the overall length as the shock train moves upstream (i.e., as pressure ratio increases). Simultaneously, the mixing region accounts for more of the overall length.

of the total pseudoshock length as the pseudoshock moves upstream. Thus, the mixing region must grow in order for the total pseudoshock length to match the imposed downstream condition. For example, the shock train comprises approximately 83% of the total length at the most downstream pseudoshock location. At the most upstream location the shock train constitutes only 39% of the total length while the mixing region is much more prominent and constitutes approximately 61% of the total length.

To account for the variation in approach conditions along the isolator (including M, Re_θ, and θ), the measured lengths are normalized by the correction factor Q introduced by Waltrup and Billig (see equation 3.4). In doing so, Q acts as a representative length scale for the system. Figure 4.15 illustrates how the corrected length of the shock train (L_sQ/H) and mixing region (L_mQ/H) vary with pressure ratio. Interestingly, L_sQ/H changes by less than 8% across the entire range of pressure ratios and can be considered approximately constant given the scatter of the data. In other words, the length of the shock train can be thought of solely as a function of the approach conditions: M, Re_θ, and C_θ. In comparison, the corrected mixing region length increases by approximately 1270 per unit pressure ratio. Returning again to the hypothetical experiment where the shock train approach conditions are constant throughout the isolator, the length of the shock train is expected to stay constant as the leading shock moves upstream (i.e., as the length of the pseudoshock increases). As a consequence, the mixing region adjusts to provide the necessary length required by the downstream boundary condition. The results shown in figures 4.12 and 4.15 point to the importance of the mixing region on providing the necessary length and flow diffusion

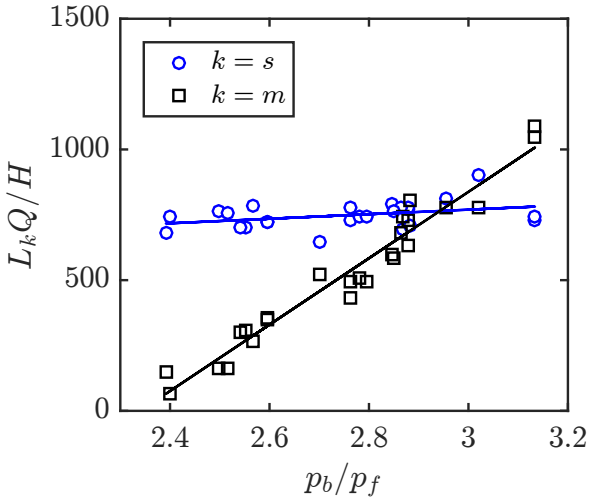

Figure 4.15: The shock train length is nearly constant when normalized by the Waltrup and Billig correction factor. The normalized length of the mixing region grows as the shock train moves upstream (i.e., as pressure ratio increases).

over what is provided by the shock train.

Finally, consider the pressure rise per unit length for each pseudoshock component. Specifically, the results are effectively cast in terms of Q by finding the ratio of the uncorrected pressure rise to the corrected length. Figure 4.16 demonstrates that this normalized quantity for the shock train region, $(p_s/p_f)/(L_s Q/H)$, is approximately constant because its value changes by less than 4% across the entire range of pressure ratios. Thus, the pressure rise per unit length of the shock train is completely described by this combination of approach conditions. In addition, the corrected pressure rise per unit length across the mixing region, $[(p_b - p_s)/p_f]/(L_m Q/H)$, is constant. This quantity changes by less than 3% across the entire range of pressure values. Thus, the mixing region demonstrates a characteristic pressure distribution.

The results shown in figures 4.12, 4.15, and 4.16 demonstrate that the properties of the shock train and mixing region scale differently with the approach conditions. Thus, it is important for pseudoshock models to consider these differences.

We have also repeated the above experiments with a different wind tunnel nozzle that produces a nominal inflow Mach number of 2.75 in the isolator section [Hunt *et al.*, 2018]. Thus, the variance method has been used to compare the shock train and mixing region length and pressure rise across a wider range of approach conditions. For these two experiments, the static wall pressure, Mach number, and Reynolds number are quite different along the isolator section. However, the boundary layer thickness, momentum thickness, and confinement are very similar. For the nominally Mach 2.75 flow, the same cutoff value of 0.006 kPa^2/mm is used to locate the end of the shock train so

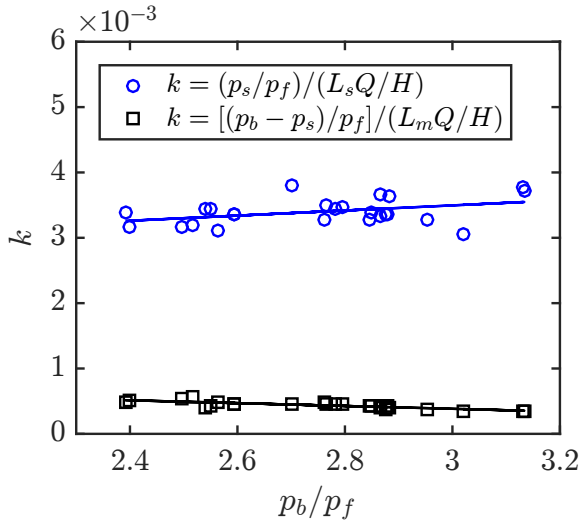

Figure 4.16: Corrected pressure rise per unit length is approximately constant for the shock train and mixing region.

that the results of the two experiments can be fairly compared. Several interesting similarities and differences were found including:

1. The linear relationship between the shock position and the pressure ratio is different for the two experiments. That is, $x_f/H = A \quad p_b/p_f + B$, where the constants A and B are different depending on which nozzle is used. The shock train position is more sensitive to changes in pressure ratio for the nominally Mach 2.0 flow (i.e., the magnitude of A is larger).

2. The shock train and mixing region pressure rise both increase with pressure ratio at approximately the same rate for the nominally Mach 2.0 flow. For the nominally Mach 2.75 flow, the pressure rise across the mixing region, $(p_b - p_s)/p_f$, increases faster than the shock train pressure rise, p_s/p_f. For both nozzles, the shock train provides less of the overall compression as the pseudoshock moves upstream despite the increase in pressure rise for this component.

3. The normalized shock train pressure rise, $(p_s/p_f)/(p_2/p_1)_\perp$, is constant as pressure ratio increases. However, magnitude of the normalized pressure rise is different for the two experiments: $p_s/p_f \approx 0.64(p_2/p_1)_\perp$ for the nominally Mach 2.0 flow; $p_s/p_f \approx 0.40(p_2/p_1)_\perp$ for the nominally Mach 2.75 flow. Clearly, the shock train pressure rise scales with more flow parameters other than the approach Mach number. However, we can say that the core flow of the shock train (i.e., the flow away from the boundary layer) is well described as an inviscid process because its pressure rise is a constant fraction of the pressure rise across a normal shock. The normalized mixing region pressure rise, $[(p_b - p_s)/p_f]/(p_2/p_1)_\perp$, in-

creases with pressure ratio. This is because the pseudoshock is growing to adjust for an increase in the downstream boundary condition but the shock train is only capable of providing a constant amount of pressure rise. In addition, the normalized mixing region pressure rise of the different experiments collapse to a single curve. This indicates that the pressure rise in the mixing region is based on a similar physical process.

4. For both experiments the length of the shock train, L_s, decreases and the length of the mixing region, L_b, increases with pressure ratio. For the nominally Mach 2.0 flow, these lengths are more sensitive to pressure ratio.

5. The corrected shock train length, $L_s Q/H$, is independent of pressure ratio and is the same value for both experiments. Thus, this combination of approach conditions adequately represents the driving factors that influence the interaction length of the shock dominated region. The normalized mixing region length, $L_m Q/H$, increases because the normalized length of the shock train is fixed and the overall pseudoshock length is increasing due to the increase in downstream pressure condition. However, the corrected mixing region length does not collapse to a single curve for the two experiments. Thus, the Waltrup and Billig correction factor does not properly scale the region of the flow that is dominated by turbulent, viscous forces.

4.4 Three-Dimensionality Due to Large Side-Wall Separation Regions

The schlieren images have provided insight on the two-dimensional projected structure of the shock train. However, the pressure measurements presented in the previous section hint at a more radially-symmetric, three-dimensional structure that is not captured using the current schlieren configuration. In this section SPIV measurements of the flow field near the leading shock of a normal shock train are presented in order to: 1) quantify all three components of velocity; 2) evaluate the amount of separation under the leading shock lambda foot; and 3) develop a three-dimensional representation of the leading shock structure.

As described in chapter 2.2.5, the laser sheet is oriented perpendicular to the flow so that velocity fields of the duct cross-section (i.e., the viewer's perspective as they look upstream through the isolator) are obtained at $x = 501$ mm ($x/H = 7.23$). The control valve is partially closed to set the pressure ratio, p_b/p_f, to approximately 3.2. At this pressure ratio the shock train is positioned in the isolator such that the time-averaged location of the leading shock Mach stem is just downstream of the SPIV measurement plane (i.e., $x_1 \approx 505$ mm $\approx 7.29H$). At this location, the leading shock

is a bifurcated normal shock with an average Mach stem height of approximately 7 mm.

The instantaneous leading shock position can differ from the time-averaged position by up to $\pm 0.26H$ due to the inherent unsteadiness of the shock train system. Thus, the leading shock fluctuates about the SPIV measurement plane. As a result, the flowfield at different locations relative to the leading shock foot are effectively measured, allowing one to map the flowfield under the lambda foot. If the reference frame is changed such that it is at a fixed shock train location, then the measurement plane moves along the shock train. This change in reference frame is done by determining the location of each instantaneous SPIV velocity field relative to the stationary shock train structure using the following information: 1) the measured angle of the leading shock in the lambda foot from schlieren (α_L) and 2) the wall-normal height of the core flow measured in each SPIV measurement (i.e., the portion of the flow above the lambda foot). Since α_L is apporximately constant in time (see section 4.1) it follows that the instantaneous location of each measurement plane relative to the stationary shock train can be consistently determined.

Instantaneous velocity fields at four different measurement planes in the fixed shock train reference frame are presented as a representative example of the SPIV measurements. The approximate streamwise locations and wall-normal height of the four SPIV measurement planes are indicated by the colored lines in figure 4.17. For convenience, the four measurement planes are referred to as a, b, c, and d (see labels in figure 4.17).

The instantaneous streamwise velocity (u) fields for measurement planes a, b, c, and d are

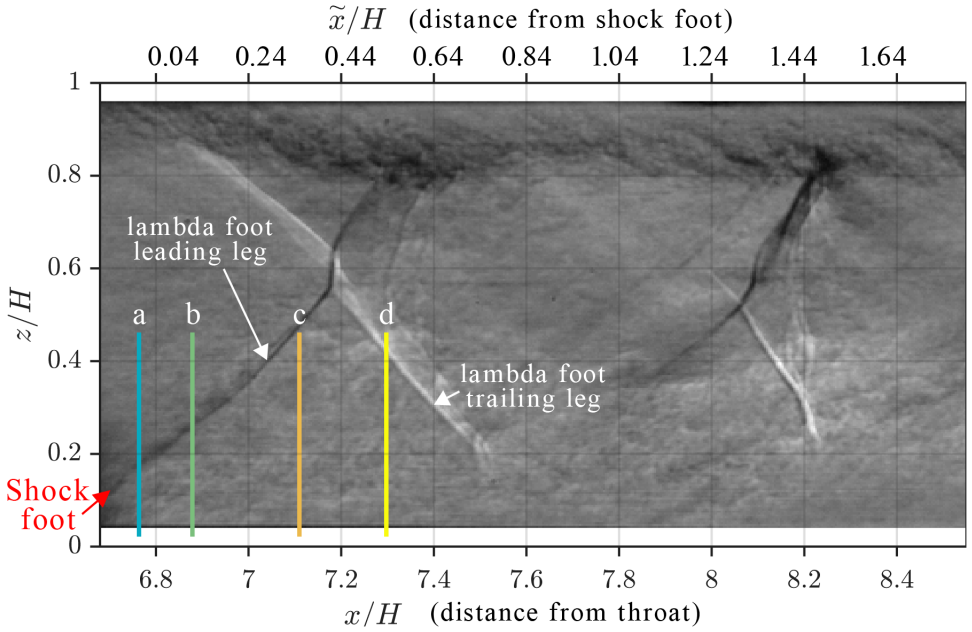

Figure 4.17: Schlieren image indicating where the four SPIV images in figure 4.18 are located in the shock train.

shown in figures 4.18(a), 4.18(b), 4.18(c), and 4.18(d), respectively. For convenience, warm colors indicate positive velocities and cool colors indicate negative velocities. Measurement plane a, shown in figure 4.18(a), is located near the foot of the leading shock. The magenta contour line in the velocity field indicates the boundary of the core flow (labeled region I in the figure) that has not been processed by a shock wave (i.e., $u = 0.99u_\infty$). Region II in the figure is the flow that has passed through the leading shock of the lambda foot. The black contour line indicates the approximate sonic line and thus the extent of the low-speed boundary layer, defined as the region where $u < 250$ m/s. Note that the boundary layers (region III in the figure) have already thickened significantly relative to the undisturbed flow (compare to figure 3.3). On the side-wall, there are small regions of reversed flow (i.e, boundary layer separation), indicated by the cool colors.

Measurement plane b, shown in figure 4.18(b), is located slightly further downstream, under the leading shock of the lambda foot. The size of the core flow (region I) is reduced because more of the flow has passed through the lambda foot leading shock (region II). Measurement plane c, shown in figure 4.18(c), is located just upstream of the leading shock Mach stem. At this point, all of the flow has passed through the leading shock of the lambda foot and thus the streamwise velocity throughout the entire field of view is less than u_∞. Also, notice the development of a high-speed region of flow that reaches into the corner of the duct (see label h).

Finally, measurement plane d, shown in figure 4.18(d), is located under the trailing shock of the lambda foot. In this instance, a portion of the flow (labeled region IV in the figure) has passed through both legs of the lambda shock, producing a region with an average streamwise velocity of 370 m/s. The magenta contour line indicates the boundary of the flow with a streamwise velocity of $u = 370$ m/s. A high-speed corner flow region is also evident in this measurement plane (see label h). Moving downstream from measurement plane *a* to measurement plane *d*, the low-speed boundary layer (region III in the figures) grows and more separation is evident. By measurement plane d, the side-wall separation is approximately 13 mm (or 23% of the tunnel width) in thickness. This is a significant reduction in the available area for the core flow to move through.

The instantaneous transverse velocity fields for measurement planes a–d are shown in figures 4.19(a)–4.19(d), respectively. Also, consider the instantaneous vertical velocity fields for measurement planes a–d shown in figures 4.20(a)–4.20(d), respectively. In the core flow (region I enclosed by the magenta contour lines) the transverse and vertical velocity components are approximately zero. Similarly, the flow that has passed through both legs of the lambda foot (region IV in measurement plane d) has average v and w velocity components of 0 m/s. In all four measurement planes, the flow processed by the leading shock of the lambda foot (region II) is pushed upwards and towards the center of the duct, inducing positive v and w velocities. For a single instant in time, the fluid elements converging towards the core have approximately the same u, v, and w velocities suggesting a degree of radial symmetry in the flow pattern. Finally, the low-speed boundary layers

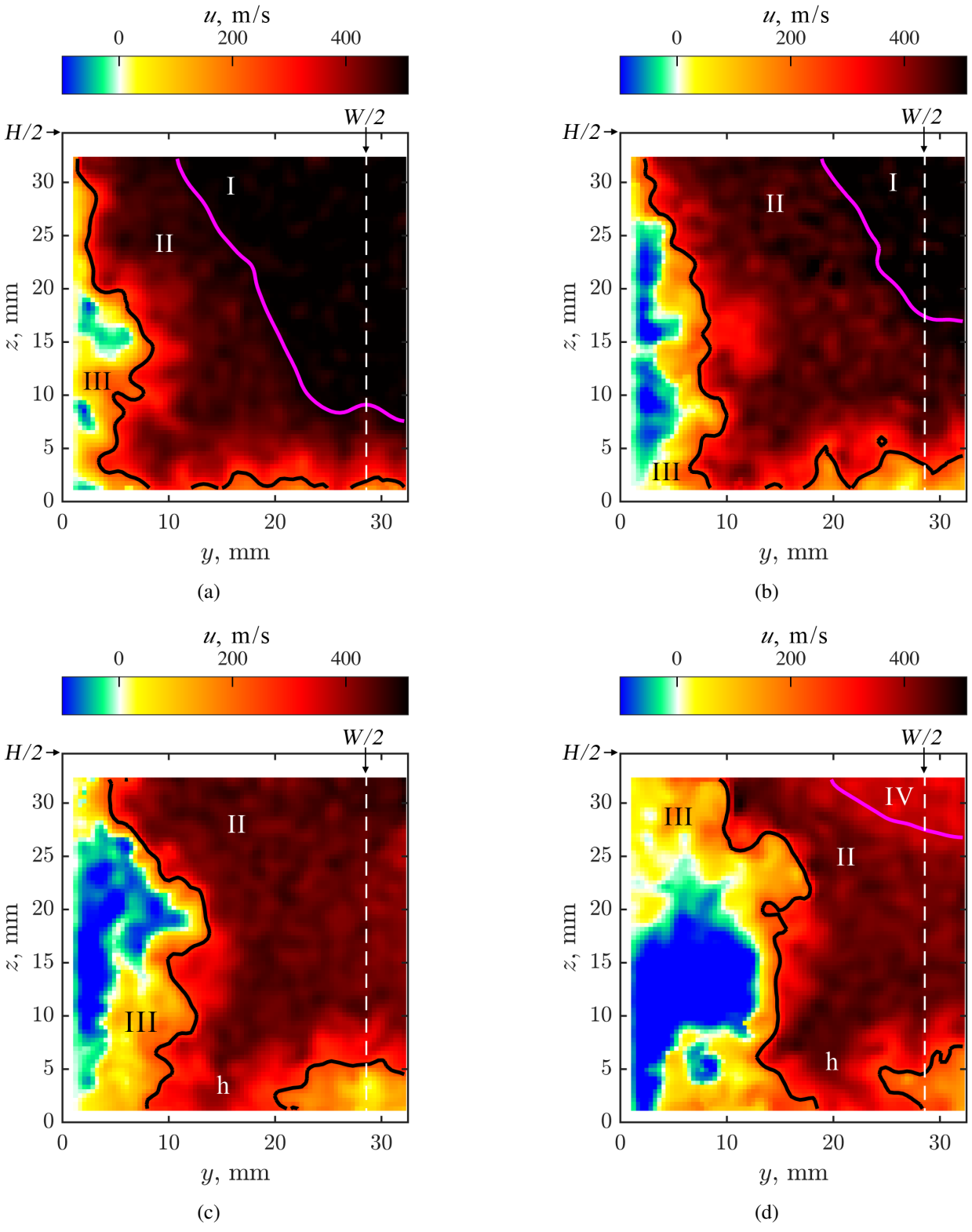

Figure 4.18: Instantaneous streamwise velocity field: (a) image plane a; (b) image plane b; (c) image plane c; (d) image plane d. The magenta contour indicates the extent of the core flow and the black contour line indicates the sonic line.

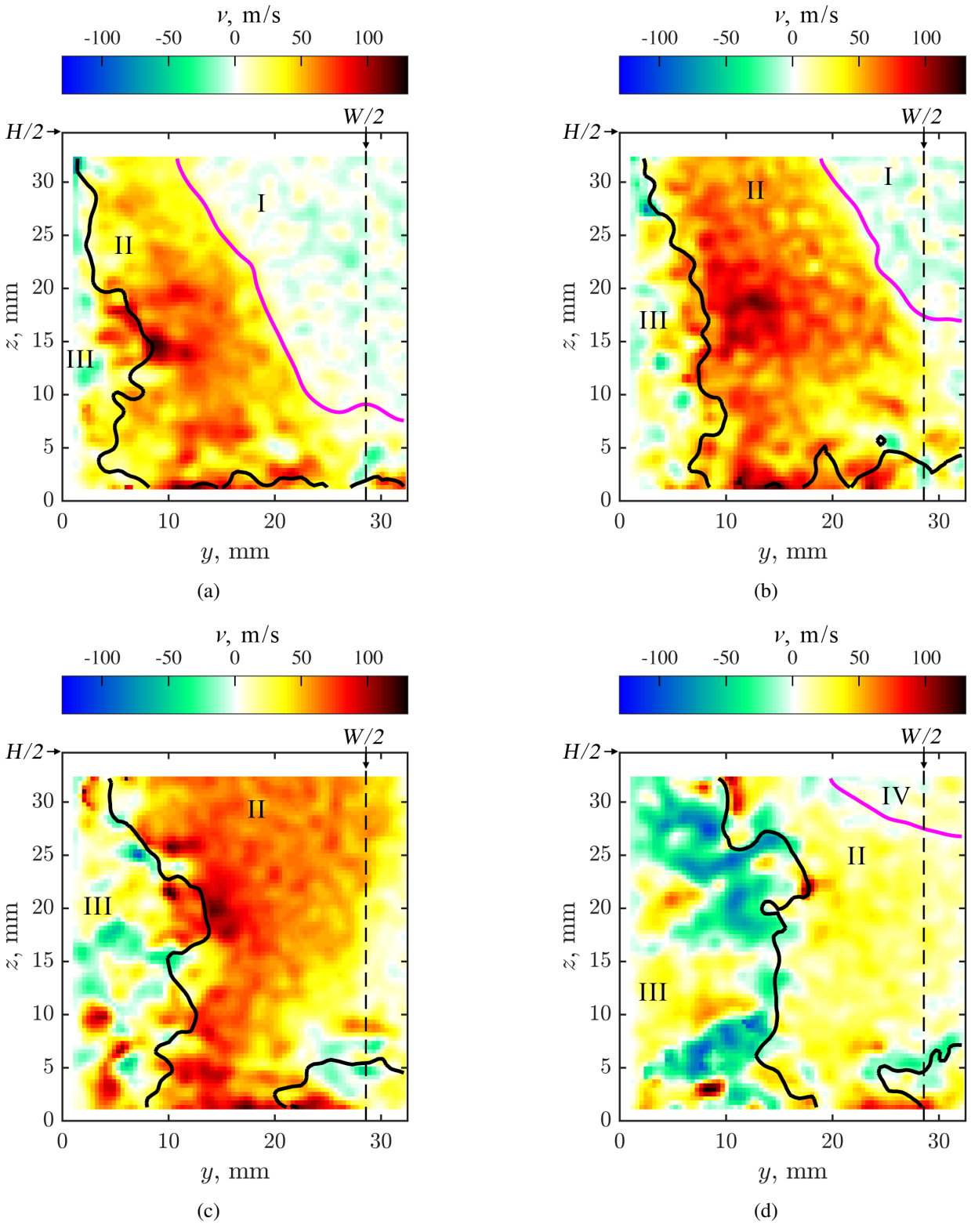

Figure 4.19: Instantaneous transverse velocity field: (a) image plane a; (b) image plane b; (c) image plane c; (d) image plane d. The magenta contour indicates the extent of the core flow and the black contour line indicates the sonic line.

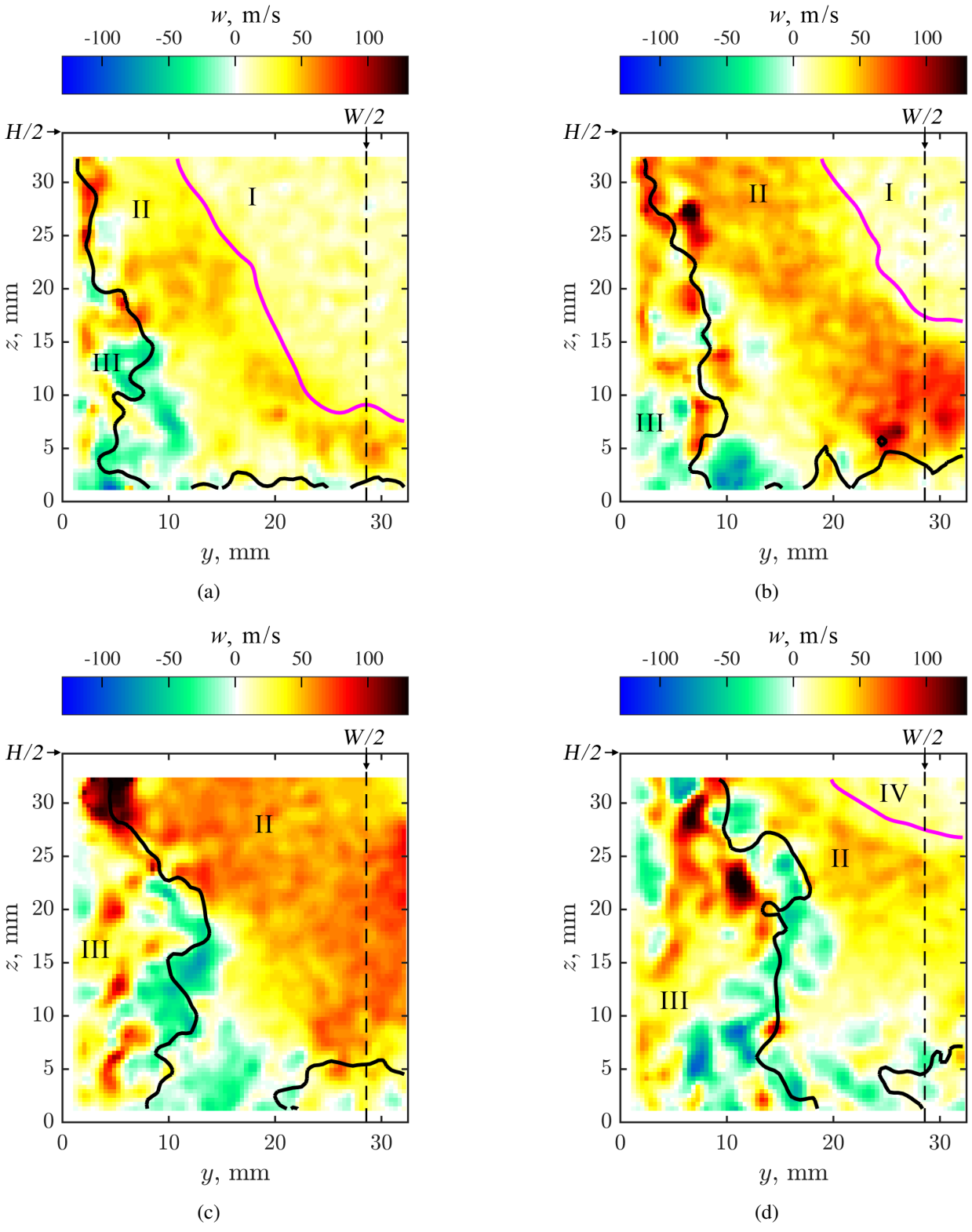

Figure 4.20: Instantaneous vertical velocity field: (a) image plane a; (b) image plane b; (c) image plane c; (d) image plane d. The magenta contour indicates the extent of the core flow and the black contour line indicates the sonic line.

(region III) show mixed positive and negative v and w velocities.

Next, consider the separation regions in more detail. Figure 4.21 illustrates the local probability of finding reverse flow in the SPIV field of view. The probability map is calculated using all 400 instantaneous SPIV images available, thus it describes the likelihood of separation between the leading shock foot and the most downstream measurement plane (measurement plane *d*). Separation is likely to occur on the side-wall, with the most probable separation region at $z = 15$ mm. No separation is evident on the bottom-wall in this portion of the shock train, although in figure 4.18 a low velocity region is observed on the bottom-wall near the centerplane, which might indicate that separation exists on the bottom-wall, but further downstream. Note that the SPIV measurements do not reach all the way to the bottom-wall due to interference from the laser sheet reflections. Thus, it is possible that bottom-wall separation occurs very close to the wall, outside of the measurement region (i.e., for $z < 1.3$ mm).

It is clear from schlieren and SPIV images that the bottom-wall boundary layer is significantly thick and raises the question of why there is no bottom-wall separation. Benek [2016] studied the effects of duct aspect ratio (i.e., the ratio between the height and width of the duct) on a single oblique shock reflection and hypothesized that thick boundary layers in the duct corners produce weak compression waves that influence the bottom-wall centerline separation. They speculate that if the compression waves from opposite corners interact upstream of the shock impingement then

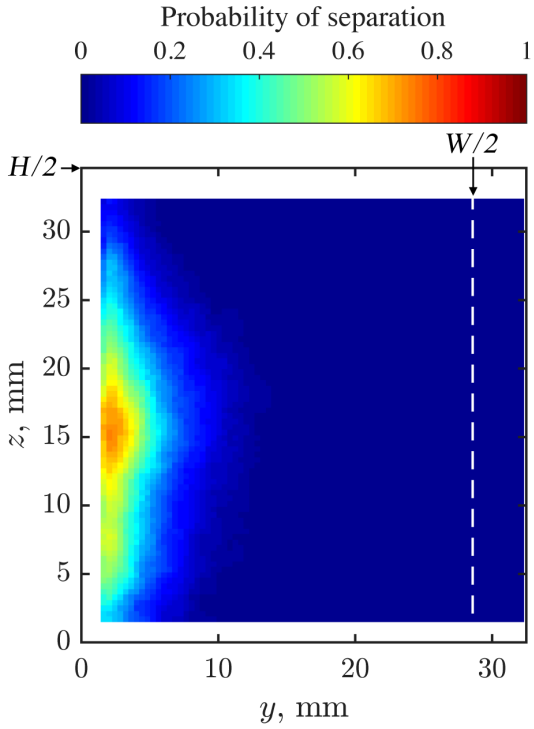

Figure 4.21: Probability of flow separation under the leading shock bottom-wall lambda foot.

the adverse pressure gradient is spread over a larger distance and it is easier for the flow to stay attached. The compression waves generated in the corners should intersect after a short distance (i.e., more upstream of the shock impingement) if 1) the duct aspect ratio is small or 2) the corner blockage is large and generates compression waves at a large angles away from the side-wall. In the current study there is clear evidence of thick corner regions in the undisturbed flow and within the shock train. The thick corner regions in conjunction with the low aspect ratio duct suggest that the theory of Benek [2016] could hold for the shock train.

Next, the total amount of (side-wall) separation in each instantaneous SPIV image is determined by quantifying the cross-sectional area over which there are negative streamwise velocities. The red line in figure 4.22(a) shows the percentage of area in the field of view that is separated flow. Note that the measured results have been smoothed slightly to show the overall trend. For comparison, the percentage of core area (where $u > 0.99u_\infty$) is represented by the black line. Close to the leading shock foot the core area is large and there is no separation. The core area shrinks and the separated area grows non-linearly as the measurement plane moves towards the Mach stem. The core area is reduced to zero when the measurement plane is near the Mach stem because the entirety of the flow in the field of view has been processed by the leading shock of the lambda foot. Note that the location of the measurement plane relative to the leading shock foot cannot be determined when the core flow is entirely out of the field of view. Therefore, the separated and core areas are only plotted for measurement planes located at or upstream of measurement plane c

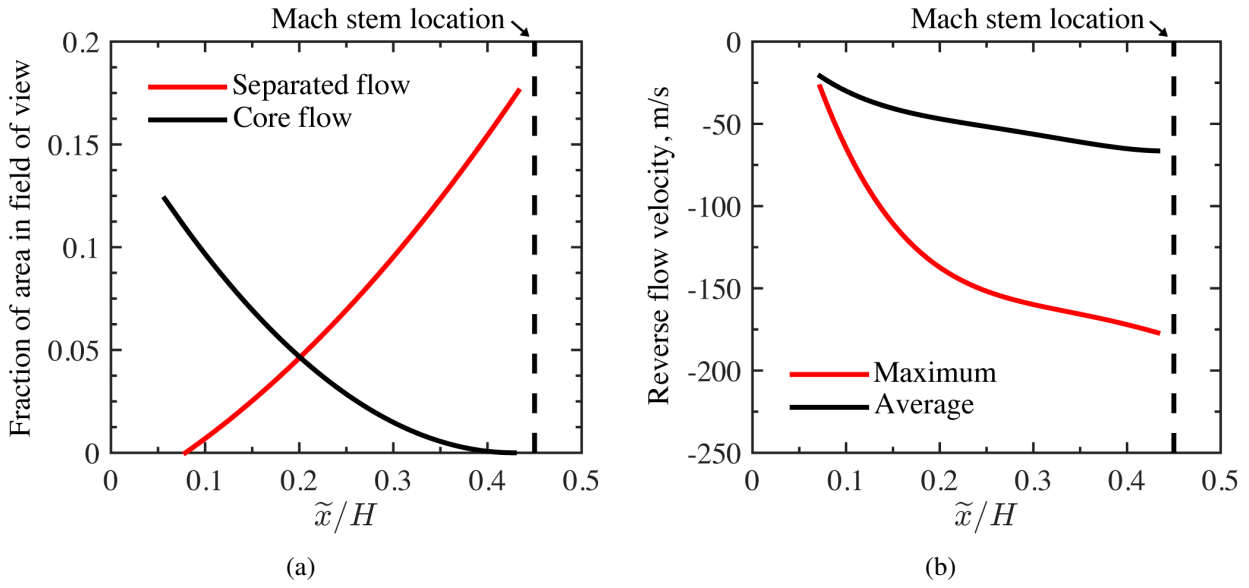

Figure 4.22: (a) Amount of separated flow and core flow in the field of view versus distance from the leading shock foot, $\widetilde{x}$; (b) average and maximum reverse flow velocities in the separation bubble versus $\widetilde{x}$.

in figure 4.17. Figure 4.22(a) emphasizes that the available area for the core flow to pass through becomes more restricted as the separated regions grow.

Now consider the speed of the reverse flow in the separation bubble. Figure 4.22(b) shows how the maximum and average reverse flow velocities vary with distance from the leading shock foot, $\widetilde{x}$. At the start of the separation bubble ($\widetilde{x}/H \approx 0.1$) the average reverse flow speed is 25 m/s (i.e., $|u| \approx 0.05u_\infty$). The average reverse speed increases with x and reaches 70 m/s (i.e., $|u| \approx 0.14u_\infty$) near the Mach stem ($\widetilde{x}/H \approx 0.4$). The maximum reverse flow speed inside of the separation bubble can reach up to 200 m/s, corresponding to 40% of the freestream flow speed (u_∞). At the Mach stem location the average and maximum reverse speeds have not begun to decrease, suggesting that the side-wall separation bubble continues much further downstream and may exhibit even faster reverse flow.

Finally, the shape of the leading shock front is determined by evaluating the contour shape of the core flow (i.e., where $u = 0.99u_\infty$) for multiple measurement planes in the shock-fixed reference frame. First, the distance between the stationary shock foot and each individual SPIV image is found. Then, the core flow contour of each measurement plane is evaluated. Five contour lines from different instantaneous measurement planes at approximately the same relative location are averaged to determine the typical shape of the core flow at that location. The averaging process is repeated along the length of the leading shock in the shock train to generate the core flow isosurface. The side-wall separation isosurface is calculated in the same manner but instead using $u = 0$ m/s contour lines. Note that the isosurfaces on only one side of the test section are acquired because SPIV measurements were only collected in one corner of the duct. Given the symmetry of the wind tunnel nozzle and test section across the y-centerline of the duct ($y = W/2$), the isosurfaces are mirrored to get a complete qualitative view of the lower half of the test section.

Figure 4.23 is a planar view (as if the viewer is looking upstream) of the core flow and separation isosurfaces found using the average contours. These isosurfaces represent the leading shock front and the boundary of the side-wall separation region under the lambda foot along all three coordinate directions between the shock foot and the Mach stem. Too few measurements were collected downstream of the leading shock Mach stem to generate a representation of the core flow shape. The dashed line indicates the plane of symmetry ($y = W/2$) and the color of the isosurface corresponds to $\widetilde{x}$, the distance from the leading shock foot. From this view, it is apparent that the large corner boundary layer near the leading shock foot (i.e., $\widetilde{x} \approx 0$) deforms the cross-sectional shape of the shock front in this upstream region. The separated region grows with distance, further restricting the available area for the core flow to pass through. The large separation region in conjunction with the thick bottom- and side-wall boundary layers cause the flow to converge towards the center of the duct and the shock cross-sectional shape quickly becomes more conical, indicating a degree of axisymmetry.

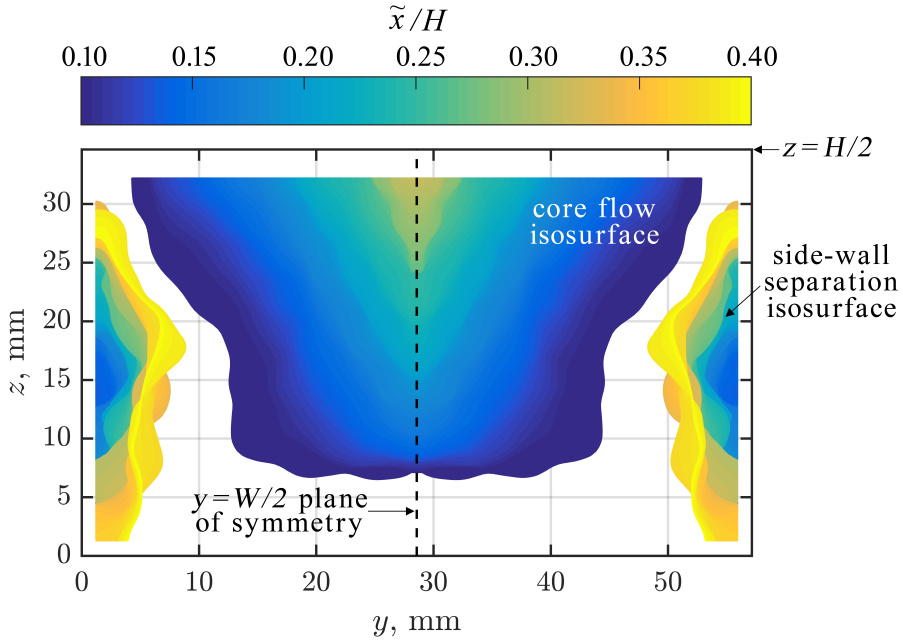

Figure 4.23: Cross-sectional view of the core flow and separation region isosurfaces.

The conical shock structure explains why the side- and bottom-wall pressure profiles have a similar shape and begin to rise at approximately the same x-location (see section 4.3). From the two-dimensional projected structure of the shock train seen in a schlieren image (e.g., figure 2.2), the bottom-wall pressure profile is expected to rise prior to the side-wall pressure profile due to the significant lambda foot that reaches upstream of the Mach stem. What is not visible in a schlieren image is the large side-wall separated area that significantly confines the flow, especially near the corner. The thick boundary layers evident in figure 4.18 displace the shock structure away from both the side- and bottom-walls, resulting in the conical structure seen in figure 4.23. Thus, the conical structure of the normal leading shock explains why the pressure profiles on the side- and bottom-wall are so similar.

Figure 4.24 is a representation of the three-dimensional leading shock structure if the lambda foot conical shape is extrapolated to parts of the shock that were not measured with SPIV. In particular, the top half of the duct was not studied using SPIV so the conical shape is mirrored across the z-centerline plane of the duct ($z = H/2$). In addition, only a few measurement planes were captured downstream of the Mach stem (see measurement plane d in the above figures). Nevertheless, a similar conical structure emerges from these limited number of examples. The overall shock structure resembles two truncated cones (frusta) with their small ends coinciding to form the Mach stem. The frustum downstream of the Mach stem is expected to have a smaller base than the upstream frustum since the boundary layer continues to thicken. The three-dimensional representation of the leading shock emphasizes a more radially symmetric flow pattern than what

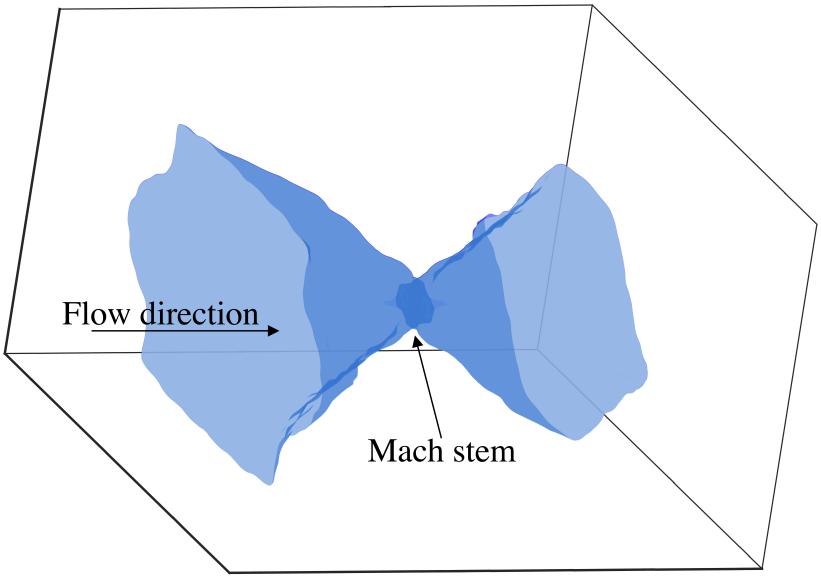

Figure 4.24: Three-dimensional representation of the leading shock in the shock train.

the schlieren images initially suggested.

4.5 Conclusions

The structure of the shock train system is investigated at various pressure ratios. To do so, a downstream valve (analogous to a combustor in a real high-speed air-breathing engine) is used to mechanically control the back pressure of the system and is responsible for the formation of a shock train in the isolator model. Increasing the back pressure increases the pressure ratio across the pseudoshock, p_b/p_f, and ultimately causes the shock train to move upstream where the approach conditions are different, as these quantities vary along the duct length. The pressure ratio is held constant as data is collected and then the shock structure is compared at different pressure ratios.

Schlieren movies are used to quantify the structural properties of the leading shock. As pressure ratio increases and the shock train moves upstream, the Mach stem height increases and the leading shock of the lambda foot becomes stronger demonstrating an oblique-to-normal transition of the leading shock structure. This study has contributed to the shock train regime diagram (figure 1.3) by clarifying the role of confinement on the shock train structure within the transition regime. Specifically, the new observations show that confinement can push the Mach number bounds of the transition regime. Large flow confinement keeps the shock train oblique even as Mach number is decreased. Conversely, a small confinement allows for a normal shock train even at high Mach numbers.

The pressure ratio also influences the overall pseudoshock structure. As the shock train moves

upstream (i.e., as the leading shock becomes normal): 1) the length of the shock train decreases and 2) the pressure rise across the shock train increases. That is, the shock train becomes more compact and compresses the flow more. Simultaneously, the mixing region becomes longer and compresses the flow more. Normalizing the length and pressure rise by the approach conditions leads to different trends as the shock train moves upstream: 1) the pressure rise across the shock train is a constant fraction of the pressure rise across a normal shock at the approach Mach number and 2) the length of the shock train is constant when corrected using the Waltrup and Billig factor, Q. In other words, for the range of flow conditions considered in this study, the shock train properties are independent of pressure ratio when the approach conditions are properly accounted for. The above idea can also be thought of in terms of a hypothetical experiment where the approach conditions are constant throughout the isolator. In these conditions, the pressure rise and length of the shock train are constant regardless of the pressure ratio (or where the shock train is located). As a consequence, the mixing region must adjust to provide the additional length and amount of compression required by the downstream boundary conditions as the pressure ratio is increased. This result points to the importance of the mixing region on providing the necessary flow diffusion over what is provided by the shock train. It also emphasizes that the shock train and mixing region properties scale differently with the approach conditions. It is important for pseudoshock models to account for these differences in order to accuratley predict the overall pseudoshock length and pressure rise.

Several features of the pressure measurements indicate a highly three-dimensional flow pattern that is not apparent from schlieren images. To explore the shock train three-dimensionality, SPIV measurements of the flow under a normal leading shock lambda foot are collected. The results show significant side-wall separation but no bottom-wall separation in this region. The lack of bottom-wall separation is believed to be caused by the relatively low aspect ratio isolator cross-section and the presence of thick boundary layers in the corners of the isolator. This result emphasizes that flow separation is not synonymous with the front of the shock train, a common misconception in the literature. On the other hand, the large side-wall separation grows significantly along the length of the leading shock and the measured reverse flow speeds reach up to 200 m/s. The thick bottom- and side-wall boundary layers restrict the available area for the core flow to travel through and cause the flow to converge towards the center of the duct, resulting in a conical shock structure. This conical structure has a degree of axisymmetry that explains the observed pressure measurements.

Chapter 5

Shock Train Inherent Unsteadiness

The goal of this chapter is to explain why the shock train is inherently unsteady even when the bulk inflow and outflow conditions are constant. To begin this work, the shock train inherent unsteadiness is characterized for the current experimental configuration. Statistics that describe the magnitude of the shock position fluctuations are presented and the frequency content of those fluctuations are examined in section 5.1. It is found that the unsteadiness statistics are independent of pressure ratio. Thus, the underlying causes of inherent unsteadiness and the shock system dynamics are expected to be similar as the pressure ratio is varied. For the remainder of the chapter, a pressure ratio of $p_b/p_f = 2.76 \pm 0.10$ is chosen such that the shock train is optimally positioned for diagnostic testing.

A theory that explains the underlying physics that drive the shock train inherent unsteadiness is then developed as follows. In section 5.2, high-speed schlieren imaging is used to quantify the time delay between the fluctuations of different shocks in order to identify the order in which shocks respond to perturbations. In section 5.3, high-speed pressure measurements are used to determine the perturbation pathways. These results, along with oil flow images, provide insight to what fluid phenomenon generates the perturbations. In section 5.4, the time delay between pressure and shock position fluctuations is quantified to determine how and when perturbations impact the shock motion. Then, in section 5.5, velocity fields obtained from particle image velocimetry measurements are used to develop a better understanding of what fluid structure is associated with a given perturbation (e.g., whether it is a vortex, an acoustic wave, etc.). Finally, a scaling argument for the unsteadiness characteristics is presented in section 5.6.

5.1 Characterization of the Shock Position Unsteadiness

A schlieren video is available online (https://youtu.be/jcPaHGBTOv8) for the reader to visualize the inherent unsteadiness of the shock system. In lieu of a schlieren movie, figure 5.1 shows twelve instantaneous snapshots of the shock train to contextualize the inherent unsteadiness of the system. The snapshots were taken 50 ms apart, starting from an arbitrary time t_1. The

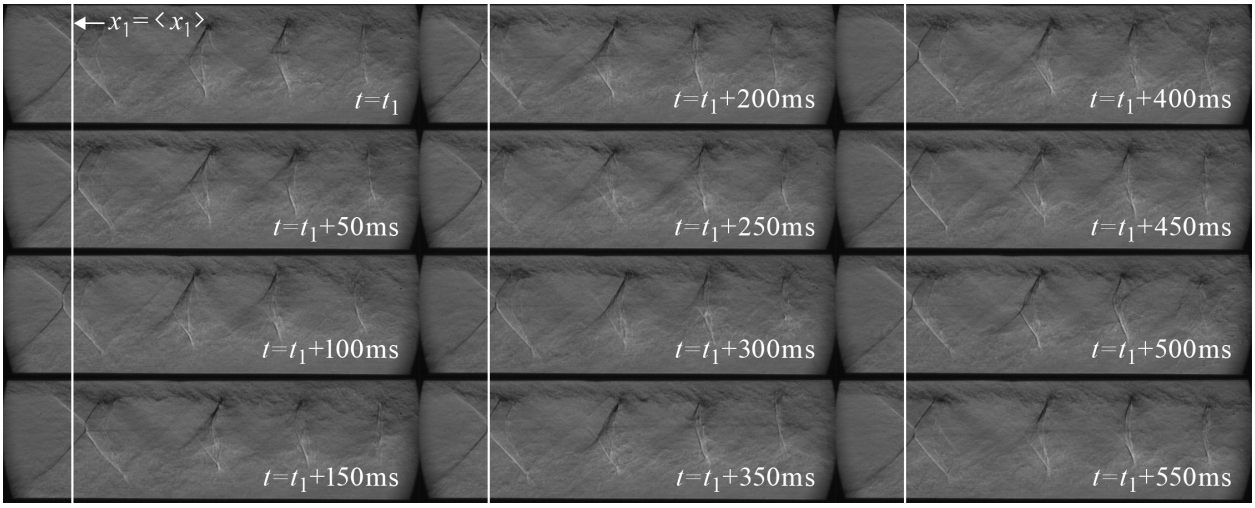

Figure 5.1: Example instantaneous schlieren images to demonstrate the inherent unsteadiness of the system.

vertical white line demonstrates where the time-averaged leading shock location is in the field of view. As the shock system fluctuates in time, the leading shock position crosses back and forth over this line.

The shock positions, x_i' with $i \in \{1, 1l, 1r, 2c, 2b, 2t, 3b, 3t, 4b, 4t\}$, are identified from the schlieren images using the automatic feature detection algorithm described in appendix B. Recall that an example instantaneous schlieren image with the shock positions labeled is shown in figure 2.2. By locating the shocks in every instantaneous schlieren snapshot, the time histories of the shock positions are effectively sampled at the camera rate of 10 kHz. Figure 5.2 shows an example

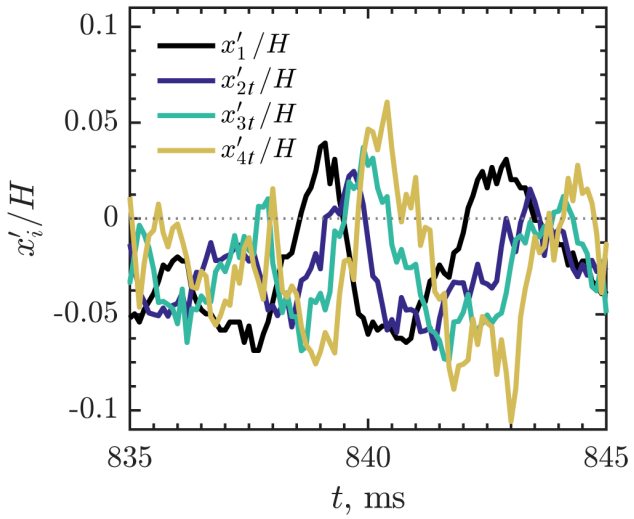

Figure 5.2: Example time trace of the shock positions.

time trace of the first four shock position fluctuations (x'_1, x'_{2t}, x'_{3t}, and x'_{4t}) for a short 10 ms time period.

To characterize the unsteadiness of the shock train for the current experimental configuration, first consider the unsteadiness of the leading shock Mach stem, x'_1, at different pressure ratios. The velocity of the leading shock Mach stem as it fluctuates, u_1, is calculated from the time-history measurement of the shock position using the central difference method of adjacent points. How the unsteadiness of the system changes as the shock train moves upstream is determined by quantifying the magnitude of leading shock Mach stem fluctuations, $|x'_1|$, and the speed of the leading shock as it fluctuates, $|u_1|$. These statistics are plotted against pressure ratio, p_b/p_f, in figures 5.3(a) and 5.3(b), respectively. The standard deviation, mean, and maximum values are represented by square, triangular, and circular symbols, respectively. The results do not appreciably change with pressure ratio indicating that the leading shock Mach stem position unsteadiness and shock speed are independent of back pressure. For the isolator geometry and flow conditions of this study, the instantaneous deviation of the shock position from its time-averaged position can be as large as 0.26 tunnel heights. The leading shock can also reach speeds up to 16 m/s, which is only 3% of the freestream flow speed.

Figure 5.4 shows the power spectral density of the leading shock Mach stem position fluctuations, $PSD(x'_1)$, for varied pressure ratios. An important observation is that the frequency content of the leading shock motion does not show any significant change as the pressure ratio is increased. The spectra are relatively broadband and the majority of the power is confined to low frequencies. In addition, there are no significant local modes that would indicate a preferred frequency in the

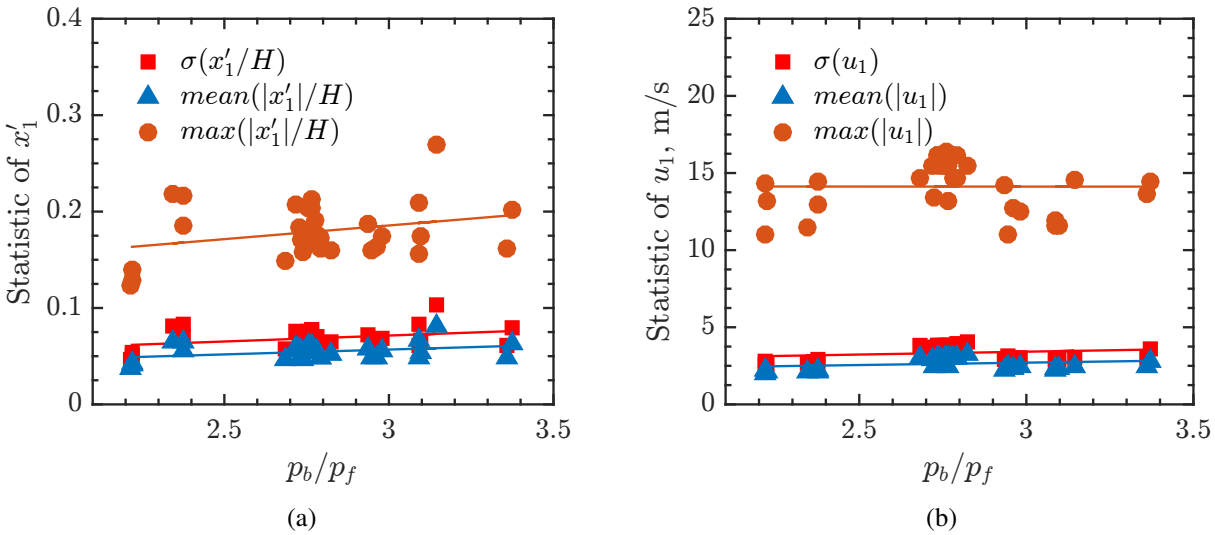

Figure 5.3: Statistics of the leading shock unsteadiness versus pressure ratio: (a) position fluctuation amplitude; (b) speed of the shock as it fluctuates.

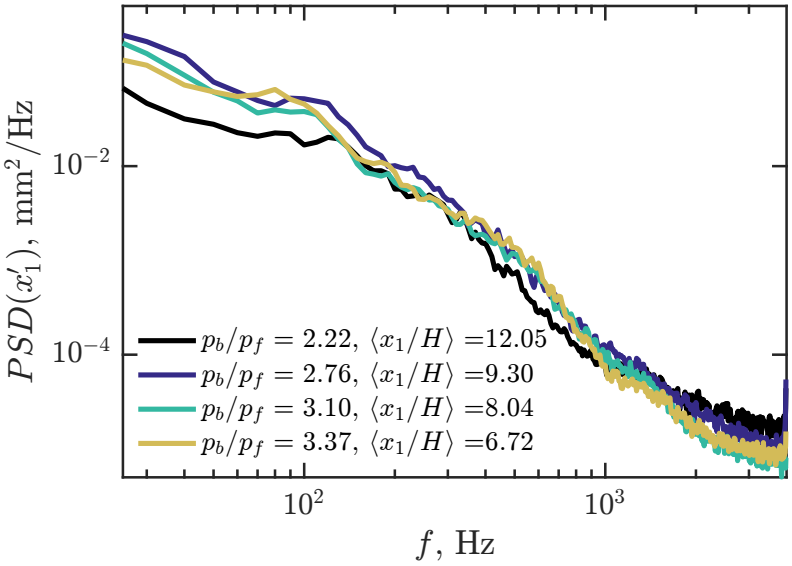

Figure 5.4: Power spectral density of the leading shock position fluctuations for varied pressure ratios.

shock motion. Many studies in the literature have noted the dominant low-frequency motion of the shock train. Some studies observe preferred modes but the frequency ranges of these modes are inconsistent from one study to the next [Yamane *et al.*, 1984*a*; Sugiyama *et al.*, 1988, 2008; Lindstrom *et al.*, 2009; Ping *et al.*, 2017; Xiong *et al.*, 2017*b*]. Differences in the flow conditions and the isolator geometry may contribute to the variation in the fluctuation content of the shock motion. As we discuss later on in this section, different parts of a shock may exhibit different fluctuation content which may also contribute to the scatter in the observations across multiple studies in the literature.

The results illustrated in figures 5.3(a), 5.3(b), and 5.4 show that the unsteadiness characteristics of the leading shock Mach stem are constant as pressure ratio is varied. This strongly suggests that the underlying physics that drive the unsteadiness are not significantly impacted by the change in shock train position. Thus, the unsteadiness of the shock train at a specific pressure ratio is examined in detail for the remainder of this chapter.

Next, the unsteadiness of the first four shocks in the shock train are compared for a pressure ratio of $p_b/p_f = 2.76$. Figure 5.5(a) shows the probability density function (PDF) of the shock position fluctuation amplitudes, x_i'. All of the PDFs are approximately symmetric. Also, it is evident that all four shocks have approximately the same maximum fluctuation amplitude and fluctuation standard deviation. Note that the results of x_{2c}', x_{2b}', x_{3b}', and x_{4b}' are not plotted for clarity but these results are nearly identical to the ones shown. Figure 5.5(b) shows the probability density function of the shock speeds, u_i. Unlike the shock displacement distribution, the speed distributions for

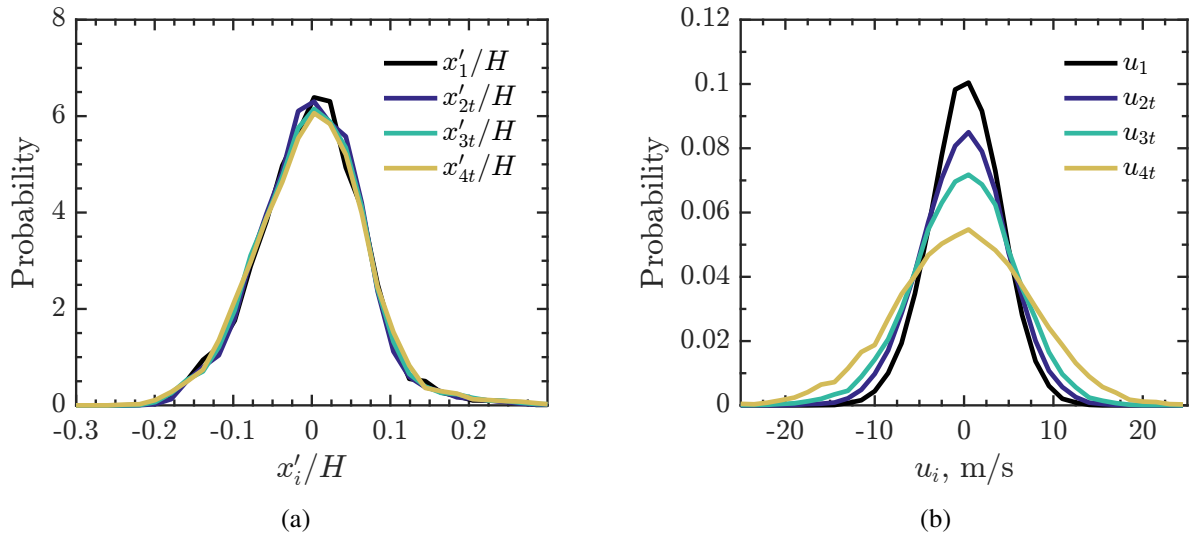

Figure 5.5: Probability density functions of shock unsteadiness parameters for a pressure ratio of $p_b/p_f = 2.76$: (a) shock position fluctuation amplitude; (b) shock speed.

each shock are different. The narrow probability distribution of the leading shock speed indicates that this shock exhibits lower speeds more often. The downstream shocks progressively exhibit higher speeds, broadening the distribution. The shock speed has also been calculated using alternative schemes, such as a forward difference, Richardson extrapolation, and least squares schemes, but nearly identical results are obtained.

The power spectral density of each shock position fluctuation time trace, $PSD(x_i')$, is plotted as a function of frequency, f, in figure 5.6. For clarity, parts a–d of the figure show the results for shocks 1, 2, 3, and 4, respectively. Each curve represents the average spectrum across 14 different runs conducted under similar conditions. The shaded regions in part (a) of the figure are examples of the run-to-run variation, and it is defined as the local maximum and minimum values obtained at each frequency value within the dataset. Note that the results, including minor modes at high frequencies, are very repeatable.

As mentioned previously, the leading shock Mach stem fluctuations, x_1', are relatively broadband with the majority of the power confined to low frequencies. This spectrum rolls off as f^{-2}. In comparison, the fluctuations exhibited by legs of the leading shock lambda foot, x_{11}' and x_{1r}', have more content at frequencies above 200 Hz. In addition, a local mode is emerging in these spectra at approximately 1300 Hz indicating that this specific frequency is more prominent in the shock motion.

Similar to the leading shock Mach stem location, the spectra of x_{2c}' has no significant local modes and rolls off as f^{-2}. Once again, the fluctuations exhibited by the shock morphological features near the boundary layer have more content at the higher frequencies, raising the tail of the

spectrum. They also tend to show more preferred modes (see labels in figure 5.6(b)). For instance, the spectra of x'_{2t} and x'_{2b} have a bulge in frequency content near 500 Hz that persists in the motion of all the downstream shocks. In addition, x'_{2t} has distinct high frequency modes at approximately 1.8 and 3.0 kHz that are not present for x'_{2b} or x'_{2c}.

The power spectra discussed so far have exemplified how morphological features belonging to the same shock can exhibit different frequency content. This indicates that the shock feet respond independently to modes fed to them by the boundary layer. For example, the modes exhibited by x'_{2t} are attributed to the top-wall boundary layer. Due to the one-sided nature of the converging-diverging nozzle used in these experiments, the bottom-wall boundary layer is different and thus x'_{2b} exhibits different modes. Much of the information fed to the shock feet from the boundary layer does not reach the center of the core flow and thus the mode does not appear in the spectrum of x'_1 or x'_{2c}. Note that the modes at approximately 500 Hz, 2 kHz, and 3 kHz persist through the third and fourth shock fluctuation power spectra although with varied magnitudes. The morphological features of the third and fourth shocks are also close to the boundary layer and further enforce the postulate that the boundary layer is locally supplying high frequency modes to the dynamics of the separate shocks within the shock train.

Finally, note that the frequency content of x'_{3t} and x'_{3b} are very similar. In subsequent analysis (see section 5.3), it is made clear that information propagates from the boundary layer on one wall to the next through the corner of the duct. In addition, the communication through the boundary layer increases in the downstream region of the shock train where the boundary layers are thick. The communication in the downstream region explains why the top and bottom features of the third shock exhibit similar fluctuations and thus similar power spectra. The same argument is used to explain why x'_{4t} and x'_{4b} have similar frequency content.

The above analysis shows that all four shocks in the train exhibit the same fluctuation amplitude but the downstream shocks often travel faster and have different frequency content with well-defined unsteady modes. These results are for a single pressure ratio ($p_b/p_f = 2.76$) but similar answers are obtained at other pressure ratios, as demonstrated by the results presented at the beginning of the section.

5.2 Orderly Response of Shock Waves in the Train

In this section cross-spectral analysis is used to evaluate the temporal evolution of the various shock wave positions in relation to one another. That is, the order in which shocks fluctuate is identified. In essence, the cross-spectrum provides a frequency-dependant evaluation of the correlation between two time-varying signals [Oppenheim *et al.*, 1989]. Here, the cross-spectrum is computed using the position fluctuation time traces of two shock morphological features, x'_i and

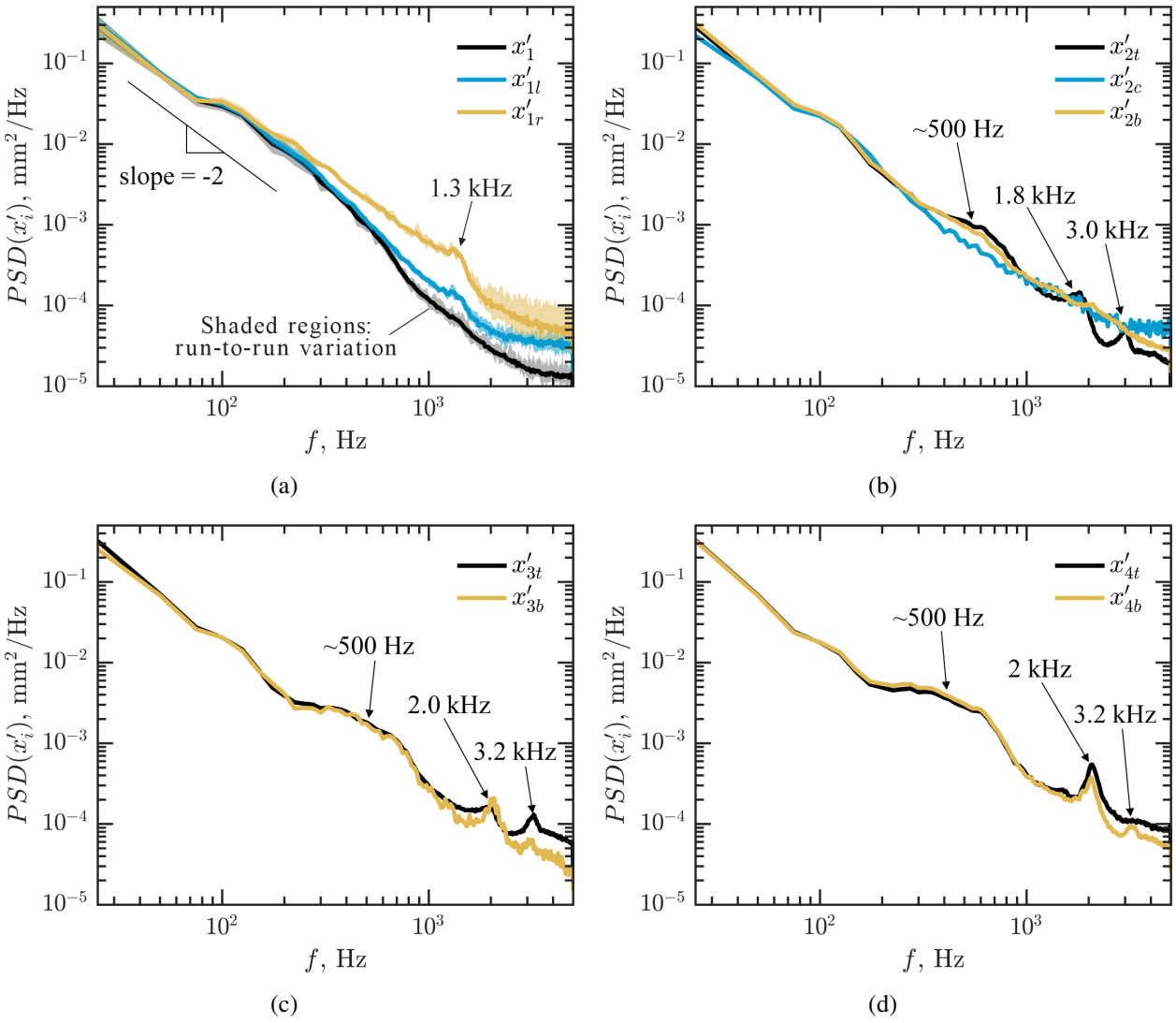

Figure 5.6: Power spectral density of shock position fluctuations for the eight shock morphological features marked in figure 2.2.

x'_j, thus it is referred to as the $x_i - x_j$ *cross-spectrum*. The coherence spectrum, $Co(x'_i, x'_j)$, and the narrowband time delay, $\tau(x'_i, x'_j)$, are quantified from the cross-spectrum as defined in appendix C. The coherence describes how well correlated the two signals are and the narrowband time delay is used to determine which shock feature fluctuates first.

As an example, the fluctuations of the leading shock morphological features (x'_1, x'_{1l}, x'_{1r}) are compared. The resulting coherence spectra are shown in figure 5.7(a). The coherence values are highest for low frequencies meaning that the low frequency fluctuations of all three leading shock features are well correlated with each other. The fluctuations of the lambda foot leading leg are also particularly well correlated with the Mach stem and lambda foot trailing leg fluctuations in the 800-1500 Hz frequency range as evidenced by the local peak in coherence (see label in figure).

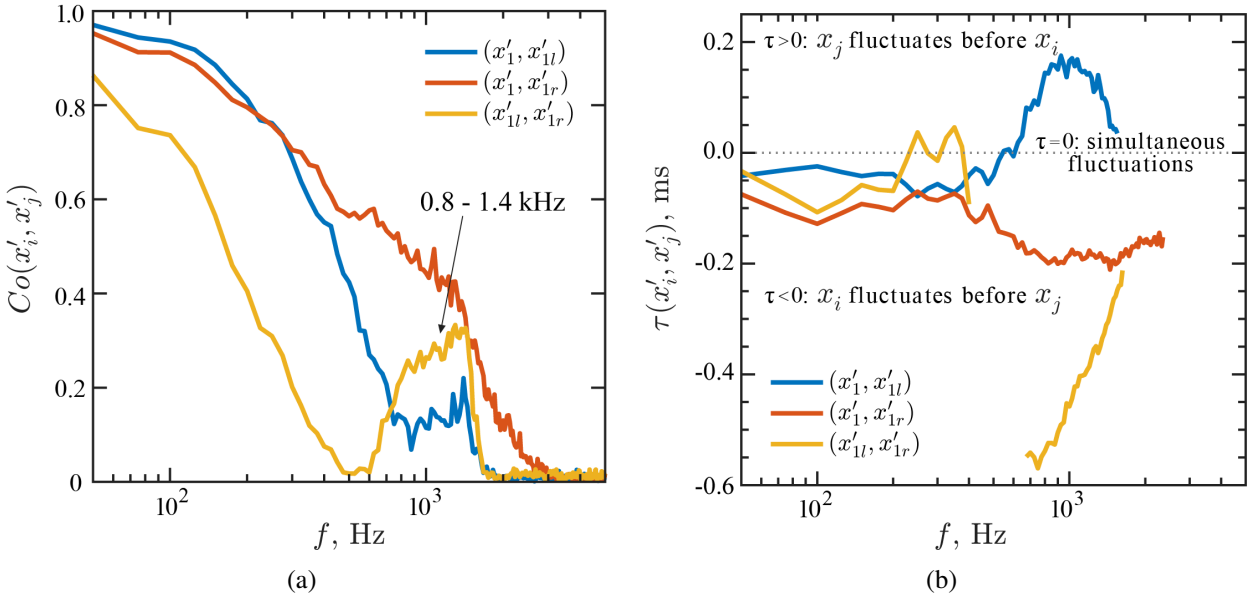

Figure 5.7: $x_i - x_j$ cross-spectra computed using the position fluctuations of two morphological features on the leading shock: (a) coherence; (b) time delay. See figure 2.2 for definitions of the shock morphological features.

It is worth noting that this mode is in the same frequency range as the mode found in the power spectra of the shock position time traces presented in figure 5.6. The power spectra show that there is an elevated amount of the energy in the shock motion at these specific frequencies, while the high level of coherence shows that the motion of the shock features at these frequencies are well correlated. Compared to the leading leg, the lambda foot trailing leg fluctuations are correlated with the leading shock Mach stem fluctuations over a broader range of frequencies. By 2.5 kHz the fluctuations in all three shock features are uncorrelated as the coherence drops to zero.

Using figure 5.7(a), a cutoff value for coherence of 0.1 is defined, below which the two signals are assumed to be uncorrelated. For all frequencies with a coherence above 0.1, the corresponding narrowband time delays derived from the $x_i - x_j$ cross-spectra are plotted in figure 5.7(b). Note that the schlieren image acquisition rate limits the shock position time series resolution to 0.1 ms. Thus, the narrowband time delay has an uncertainty up to 0.1 ms away from the reported value. Accounting for the measurement uncertainty, it is apparent that all three time delay curves plotted in the figure are approximately zero for frequencies below 500 Hz. In other words, x_1, x_{1l}, and x_{1r} fluctuate simultaneously in this frequency range and the leading shock can be thought of as a solid body. For frequencies above 500 Hz, $\tau(x_1', x_{1l}')$ is positive meaning the lambda foot leading leg fluctuates before the Mach stem. In addition, $\tau(x_1', x_{1r}')$ is negative for $f > 500$ Hz meaning that the lambda foot trailing leg fluctuates after the Mach stem. Thus, for high frequencies the instantaneous shape of the leading shock is deformed during the shock motion.

Next, the order in which consecutive shocks fluctuate is determined by computing the cross-spectrum using x_i' and x_{i+1}'. The resulting coherence spectra are shown in figure 5.8. Part (a) of the figure shows the coherence between the leading shock position and the positions of the three features of the second shock; i.e., $Co(x_1', x_{2t}')$, $Co(x_1', x_{2c}')$, and $Co(x_1', x_{2b}')$. In all of these cases the coherence spectrum is highest at low frequencies and drops to zero by 3 kHz meaning that the frequency content of the unsteady motion is well correlated for frequencies below approximately 3 kHz and uncorrelated for frequencies above 3 kHz. Note that the coherence spectra of x_{2t}' and x_{2b}' have a minor peak at 1.3 kHz. Thus, the 1.3 kHz fluctuations in the leading shock features discussed earlier are shared with the features of the second shock.

Figure 5.8(b) shows the coherence spectra for the downstream sets of consecutive shocks; i.e., $Co(x_{2t}', x_{3t}')$, $Co(x_{2c}', x_{3t}')$, $Co(x_{2b}', x_{3t}')$, and $Co(x_{3t}', x_{4t}')$. Note that the coherence calculated using x_{3t}' and x_{4t}' are nearly identical to the coherence calculated using x_{3b}' and x_{4b}', respectively. Local peaks centered at 500 Hz, 2 kHz, and 3 kHz start to emerge in some of these cases and are specific to particular regions of the flow field. Once again, these modes are at the same frequencies as the modes found in the power spectra of the shock position time traces. For example, recall that x_{2t} and x_{3t} have a strong fluctuation component at 3 kHz that is evident in the shock position power spectra (see figure 5.6). Figure 5.8(b) demonstrates that this mode is well correlated between shocks x_{2t} and x_{3t}. Because the 3 kHz mode is not observed in the motion of shock one, some forcing is generated locally in the top-wall boundary layer that feeds information to shocks two and three. The mode dissipates by shock 4 as demonstrated by the low coherence between the 3 kHz fluctuations of shocks 3 and 4. Similar arguments apply to the 500 Hz and 2 kHz modes.

Figure 5.9 shows the corresponding time delays computed from the cross-spectra of consecutive shock features as a function of frequency. Once again, a coherence cutoff of 0.1 is chosen, below which the two signals are assumed to be uncorrelated. For clarity, part (a) of the figure shows the narrowband time delays computed using morphological features defined from the first and second shocks; i.e., $\tau(x_1', x_{2t}')$, $\tau(x_1', x_{2c}')$, and $\tau(x_1', x_{2b}')$. Part (b) of the figure shows the same quantity computed between the downstream consecutive shocks; i.e., $\tau(x_{2t}', x_{3t}')$, $\tau(x_{2c}', x_{3t}')$, $\tau(x_{2b}', x_{3t}')$, and $\tau(x_{3t}', x_{4t}')$. For the lowest measurable frequencies ($f < 50$ Hz) the time delays approach zero, indicating that the upstream and downstream shocks are displaced at approximately the same time. Thus, the entire shock train moves as a solid-body for the lowest frequency range. As frequency increases above 50 Hz, the narrowband time delay transitions to large negative values meaning that the upstream shock fluctuates before the downstream shock. In other words, shocks respond to a perturbation sequentially with the upstream shock responding before the downstream shocks.

Using figure 5.9(a), note that the various morphological features of the second shock respond at different times. For example, consider the 500 Hz component of motion where the core, top, and

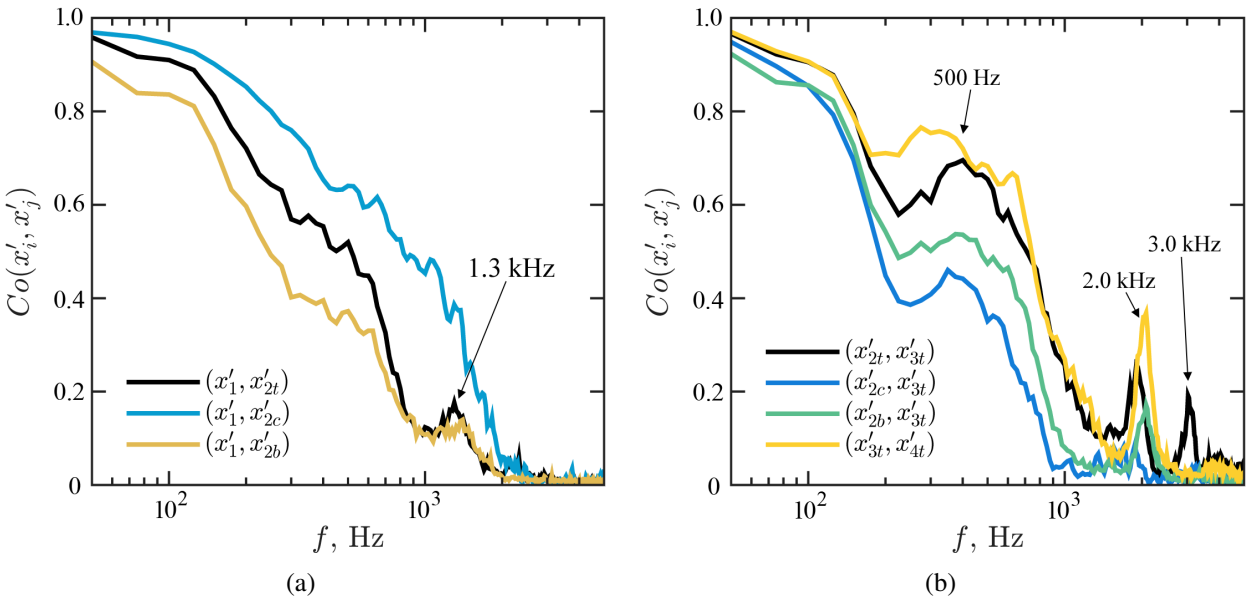

Figure 5.8: $x_i - x_j$ coherence spectra calculated using the position fluctuations of two consecutive shock morphological features. See figure 2.2 for definitions of the shock morphological features.

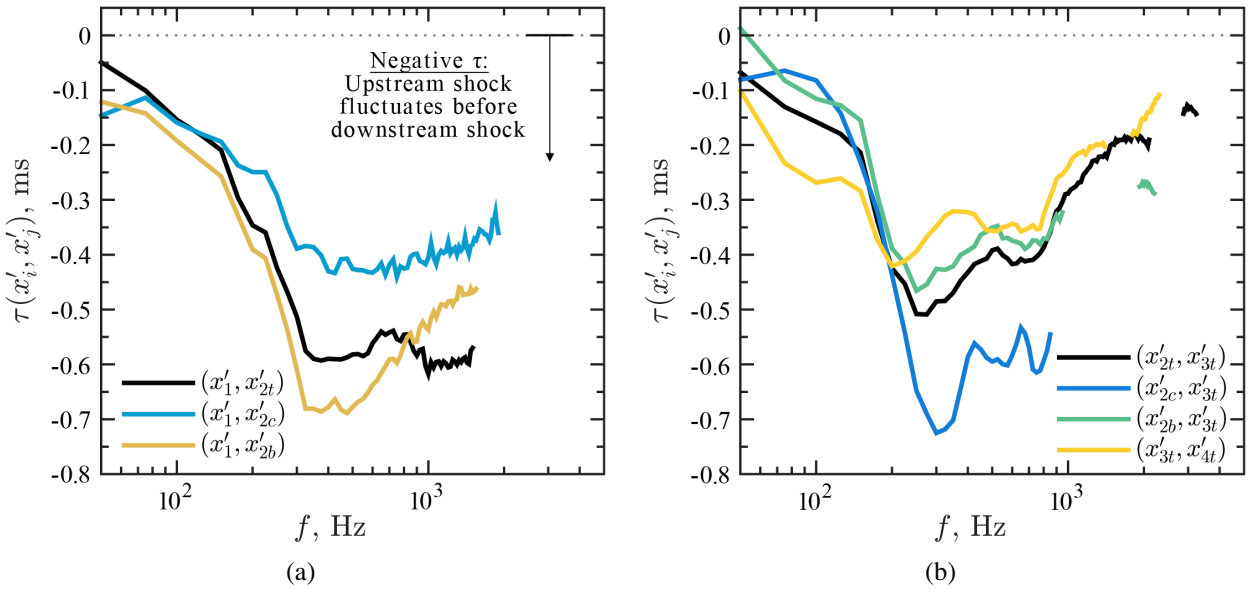

Figure 5.9: $x_i - x_j$ cross-spectral narrowband time delay calculated using the position fluctuations of two consecutive shock morphological features. See figure 2.2 for definitions of the shock morphological features.

bottom points of the second shock are displaced 0.42, 0.58, and 0.67 ms after the leading shock displacement, respectively. That is, the central portion of the shock responds faster than regions close to the wall. In figure 5.9(b), only the time delays calculated using x'_{3t} and x'_{4t} are plotted for clarity. The narrowband time lags calculated using x'_{3b} and x'_{4b} follow the same trend as x'_{3t} and x'_{4t},

respectively, but have slightly different magnitudes. The difference in response time suggests that the instantaneous shape of these downstream shocks become deformed during the motion. This is similar to the deformation of the leading shock for frequencies above 500 Hz that was discussed earlier.

5.3 Identification of Perturbations Using Pressure Fluctuations

In this section, the high-speed wall pressure measurements are analyzed to identify the spatio-temporal properties of potential perturbations that affect the motion of the shocks within the shock train. To this end, the wall pressure frequency content along the length of the shock train is presented and cross-spectral analysis computed using pairs of wall pressure fluctuation measurements is discussed.

5.3.1 Frequency Content of the Wall Static Pressure

Figure 5.10 illustrates the pressure fluctuation power spectra, $PSD(p')$, in the form of a contour map. The contour map is constructed using the fluctuation component of wall static pressure, p', measured at varied axial distances away from the time-averaged leading shock Mach stem location, x^*. For parts (a)–(d) of the figure, the pressures are measured on the side-wall away from the corner ($z = 41.3$ mm), on the side-wall near the corner of the duct ($z = 6.4$ mm), on the bottom-wall $y = W/2$ centerline ($y = 28.6$ mm), and on the bottom-wall near the corner of the duct ($y = 50.8$ mm), respectively. The diagram at the top of the figure illustrates the pressure measurement locations relative to a schlieren image projected on one of the side-walls.

Generally, the majority of power is contained within the low-frequency range ($f < 1$ kHz). Notably, the low-frequency pressure fluctuations near the leading shock foot have significantly more power compared to the rest of the shock system, especially the region between the first and second shock ($0 < x^* < 50$ mm) where very little power is observed. In addition, there are no well-defined modes and very little power is contained at high frequencies within the region upstream of the leading shock Mach stem. Downstream of the leading shock, the power at high frequencies increases and local high-frequency modes start to appear. For instance, consider figure 5.10(a) where the pressures are measured along the side-wall at $z = 41.3$ mm. High frequency modes at approximately 1.8, 3.2, 5, and 6 kHz are clearly evident. The 1.8 kHz mode forms between shocks 1 and 2 while the other modes begin between shocks 2 and 3. The pressure fluctuations measured along the bottom-wall $y = W/2$ centerline exhibit high-frequency modes at approximately the same frequencies as the side-wall measurements but the power associated with

these modes is much smaller (see figure 5.10(c)). Note that the high frequency modes at 1.8 and 3.2 kHz are evident in the shock position fluctuations (see figure 5.6) and the pressure fluctuations indicating that the unsteadiness of these two features is related. It is possible that the shock position fluctuations also have modes at 5 and 6 kHz but the schlieren image acquisition rate is too low to resolve these frequencies.

Next, consider the power spectra of pressure fluctuations near the corner of the duct (see figures 5.10(b) and 5.10(d)). Generally, the pressure fluctuations measured in the corner have increased power across all frequencies in the region between shocks 1 and 2 (approximately $-20 < x^* < 70$ mm) compared to the pressures measured away from the corner. The 1.8, 3.2, and 5 kHz modes exist in the same region of the shock train but the power associated with these modes is much smaller. The 6 kHz mode has almost completely dissipated.

5.3.2 Cross-Spectral Analysis of Pressure Time Traces: Bottom-Wall Centerline

As a perturbation travels past a pressure transducer it induces a fluctuation in the measured pressure. Thus, the cross-spectrum calculated using pairs of wall pressure fluctuation measurements collected simultaneously during the same run provides information on where perturbations originate and the direction in which they travel. For convenience, this is termed the $p_i - p_j$ *cross-spectrum*. As an example, a detailed discussion is presented in this subsection for the $p_i - p_j$ cross-spectra computed using the pressure fluctuation measurements from two transducers spaced 10.9 mm apart on the bottom-wall $y = W/2$ centerline (i.e., $y = 28.6$ mm). The coherence, $Co(p_i', p_j')$, and narrowband time delay, $\tau(p_i', p_j')$, derived from these cross-spectra (see appendix C for details) are shown in figures 5.11(a) and 5.11(b), respectively. Both quantities are plotted as a function of x^*, the average location of the pressure transducer pair relative to the time-averaged leading shock Mach stem location.

First, consider the coherence results shown in figure 5.11(a). The coherence plot describes the frequency-dependent degree of correlation between the two pressure fluctuation time traces. Generally, pressure fluctuations with frequency less than 3 kHz are highly correlated throughout the shock train. A local peak in the coherence at 1.8 kHz means that this frequency component is highly correlated between the pair of pressure fluctuation measurements. The presence of the higher frequency modes (e.g., the 5 and 6 kHz modes) are also evident in the plot, however their level of correlation is quite low (less than 0.2), and it is therefore not considered significant.

Figure 5.11(b) illustrates the corresponding narrowband time delays from the $p_i - p_j$ cross-spectra. Regions in the spectrum where the coherence is less than 0.3, which is taken as the cutoff value below which there is no correlation between signals, are masked out in black. Note that this cutoff value is higher than the one used for the $x_i - x_j$ cross-spectral analysis due to noise contamination. In figure 5.11(b) the sign of the narrowband time delay is of particular interest because

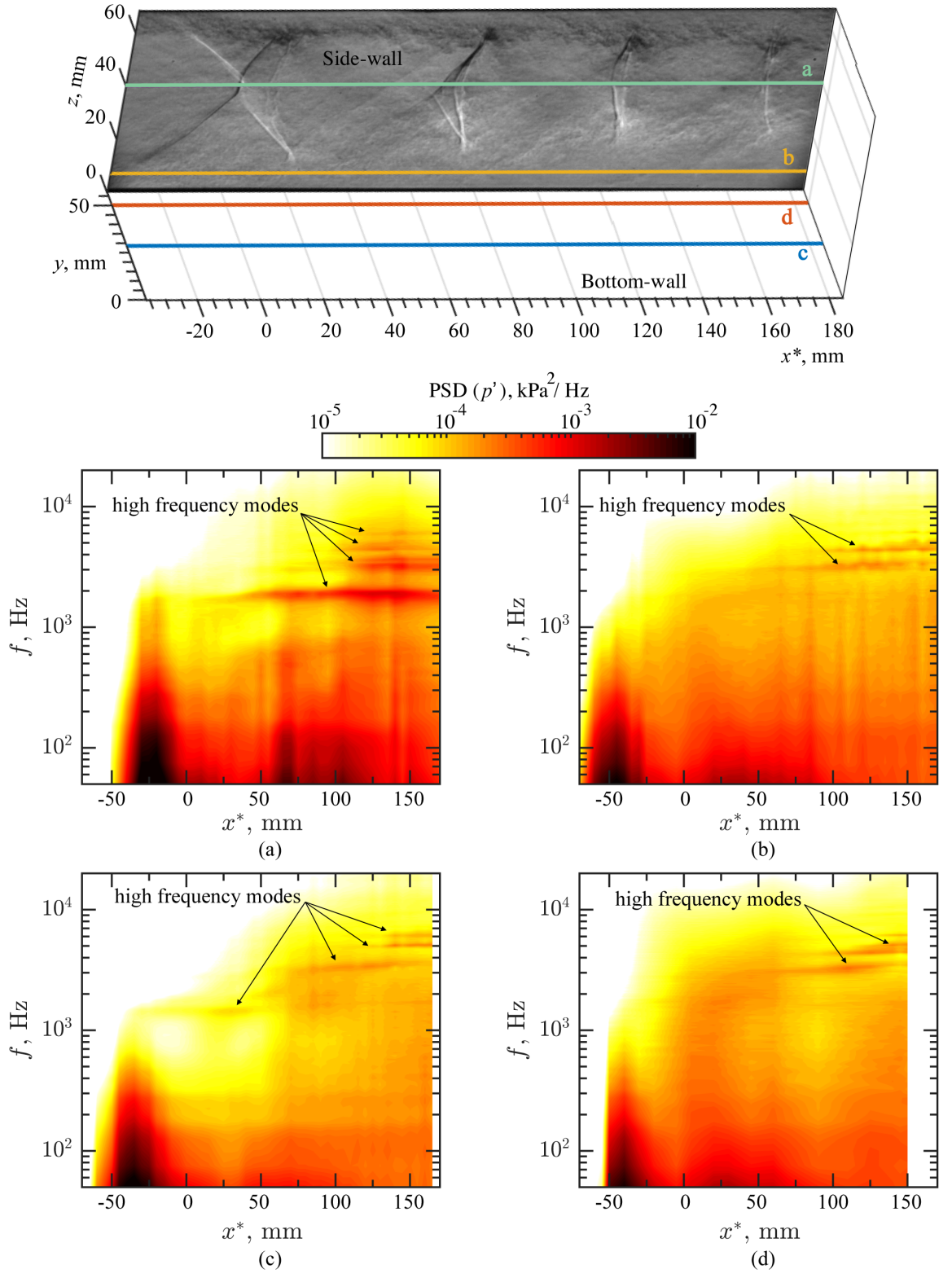

Figure 5.10: Pressure fluctuation power spectra throughout the shock train. Pressures measured on the: (a) side-wall away from the corner; (b) side-wall near the corner; (c) bottom-wall $y = W/2$ centerline; (d) bottom-wall near the corner.

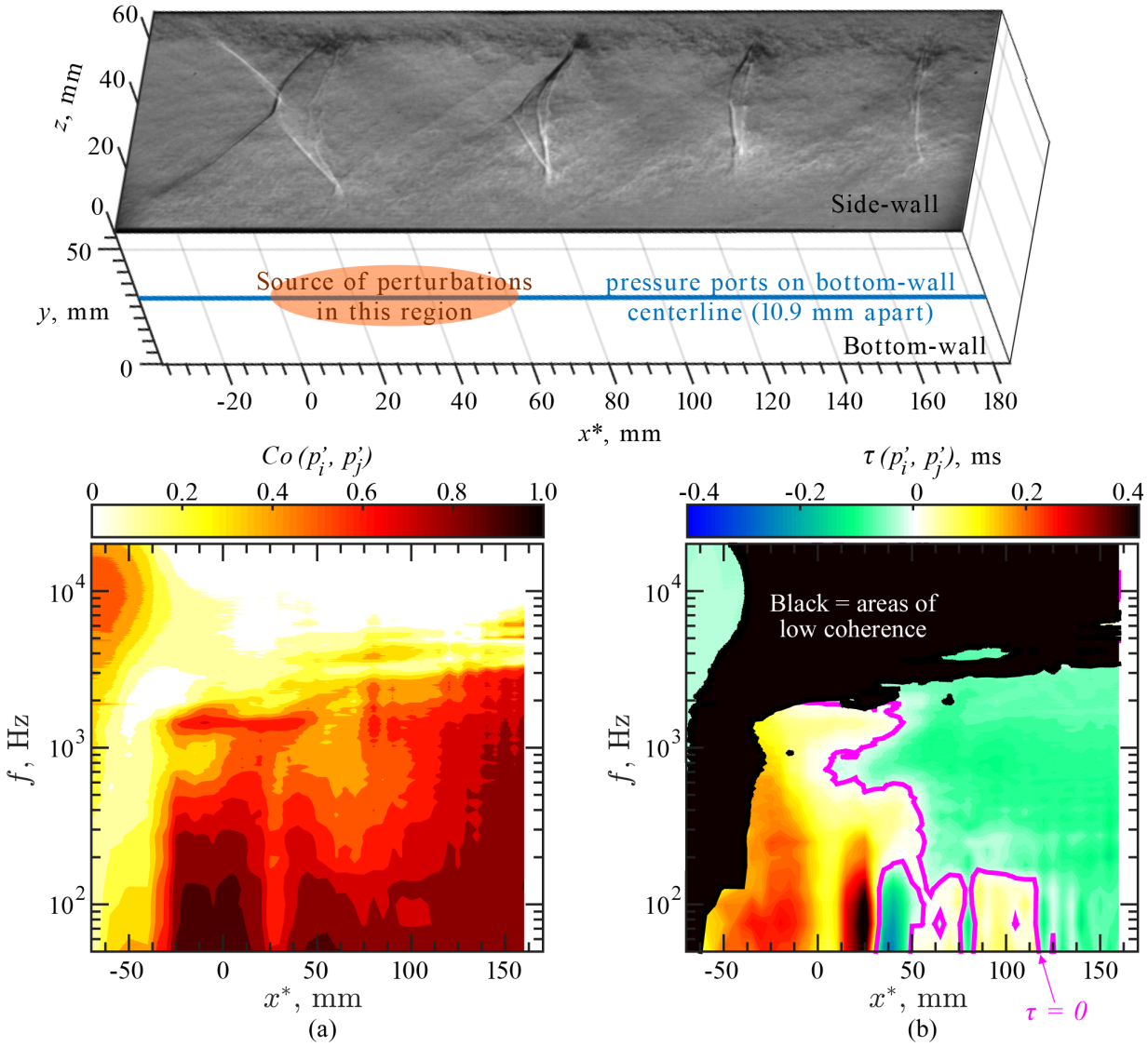

Figure 5.11: Results of the $p_i - p_j$ cross-spectra calculated using pressure fluctuation time traces measured along the bottom-wall $y = W/2$ centerline: (a) coherence; (b) narrowband time delay.

it describes the direction in which the perturbation is propagating. A negative narrowband time delay indicates that the upstream transducer captures a pressure fluctuation before the downstream transducer. Thus, the perturbation is traveling downstream. Conversely, a positive narrowband time delay indicates the perturbation is traveling upstream. The magenta contour line shows where the narrowband time delay is zero (i.e., the two pressures fluctuate simultaneously). Note that the potential uncertainty of these time delays is taken to be ± 0.02 ms, which is the time corresponding to the cutoff frequency of the low pass filter of the signal conditioner used to low pass filter the pressure measurements.

Consider two distinct frequency ranges in figure 5.11(b): $300 < f < 3000$ Hz and $f < 300$

Hz. For the higher frequency range ($300 < f < 3000$ Hz) the narrowband time delay is positive (i.e., the perturbation travels upstream) in the upstream region of the shock train but negative (i.e., the perturbation travels downstream) in the downstream region of the shock train. Thus, perturbations travel away from the streamwise location where the sign of the narrowband time delay switches. This indicates that a source of perturbations is within the shock train, somewhere between the leading shock Mach stem, x_1, and the second shock, x_{2c}. Interestingly, the location of the perturbation source varies across this 60 mm region depending on the frequency.

The narrowband time delays for frequencies below 300 Hz are more complex because the sign of the delay switches multiple times. That is, the direction in which the perturbation travels changes along the length of the shock train suggesting that there are multiple independent, superimposed perturbations. Similar to the results for frequencies above 300 Hz, the sign of the time delay switches from positive to negative at a location in between the first and second shocks indicating that perturbations are generated at that point and propagate away in both directions. In addition, for $x^* > 50$ mm there are select regions where a second upstream propagating perturbation is evident. It is hypothesized that this perturbation originates in the diffuser section and travels upstream. As will be discussed later, the results of section 5.4 support this hypothesis. At low frequencies ($f < 300$ Hz), all of these perturbations are superimposed in the shock train but the cross-spectral analysis only distinguishes the perturbation that induces the strongest correlation in pressure fluctuation measurements. For example, when the time delay is negative then the downstream propagating perturbation has a stronger correlation than the upstream propagating perturbation.

For ease of discussion, each perturbation travelling along the bottom-wall $y = W/2$ centerline is designated a name as follows:

1. **Perturbation $\mathbf{D}^-$**: Originates in the diffuser and propagates upstream. This perturbation is associated with fluctuation frequencies less than 300 Hz.

2. **Perturbation $\mathbf{S}^-$**: Originates within the shock train and propagates upstream. This perturbation is associated with fluctuation frequencies up to approximately 3 kHz.

3. **Perturbation $\mathbf{S}^+$**: Originates within the shock train and propagates downstream. This perturbation is associated with fluctuation frequencies up to approximately 3 kHz.

The letter designates where the perturbation originates. That is, "D" stands for "diffuser" and "S" stands for "within the shock train". The superscript designates the direction of travel: positive for a downstream propagating perturbation or negative for an upstream propagating one.

5.3.3 Perturbation Pathways and Insight on the Source of Perturbations

The cross-spectra calculated using pairs of pressure fluctuations measured on the bottom-wall $y = W/2$ centerline have been thoroughly discussed. A similar analysis is conducted for pressure measurements at other available locations and the same type of information is extracted. A complete analysis of the remaining $p_i - p_j$ cross-spectra is not reported in the main text for the purpose of brevity and because the process of extracting information from the $p_i - p_j$ cross-spectra is essentially the same for all locations. Instead, the main results are given in appendix D for reference. By combining the results of the $p_i - p_j$ cross-spectral analysis from all available measurement locations, a comprehensive description of how perturbations travel along the side-wall, through the corners, and along the bottom-wall of the isolator is constructed. These are called the perturbation *pathways*.

Figures 5.12(a)-(c) are schematics of the overall perturbation pathways (with sufficiently high coherence) for three distinct frequency ranges: $600 < f < 3500$ Hz, $300 < f < 600$ Hz, and $f < 300$ Hz, respectively. The pathways for frequencies above 3500 Hz are not available because the cross-spectral coherence results are deemed too low and thus the measurements are uncorrelated. In each figure presented, an arrow is drawn connecting the locations of the pressure transducers used to compute the cross-spectrum if the coherence is above the cutoff value of 0.3. The arrow direction indicates where the perturbation is traveling based on the time delay of the cross-spectrum. In addition, the perturbation pathways are overlaid on top of an oil flow visualization of the bottom- and side-wall to identify the general flow topology. In doing so, additional insight is gained on the fluid phenomenon that causes the perturbations.

First, consider the perturbation pathways for the 600–3500 Hz frequency range as shown in figure 5.12(a). As discussed previously, perturbations $S^{\pm}$ are associated with a broad range of frequencies ($f < 3$ kHz) and originate within the shock train on the bottom-wall. The perturbations then emanate away from this point in both directions (i.e., upstream and downstream). The exact location of the perturbation source is frequency dependent (see figure 5.11). The oil flow visualization image demonstrates that these source points (collectively labeled "$S^{\pm}$" in the figure) are within a separation bubble located in the middle of the isolator bottom-wall (labeled "1" in the figure). The bubble begins between shocks 1 and 2, and ends just downstream of shock 3. The full length movie of the oil flow visualization provided online (https://youtu.be/3wG4oLhHr2Y) shows that the bubble position and size vary in time. Thus, it is concluded that the perturbations are generated by the instabilities of the separation bubble either intrinsic to the bubble itself or externally induced (e.g., driven by the incoming turbulent boundary layers). For example, a separation bubble that translates or grows/shrinks will generate perturbations in the form of acoustic waves as the surrounding flow adjusts to its new conditions. Perturbations can also take the form of vortices that shed off the downstream side of the bubble.

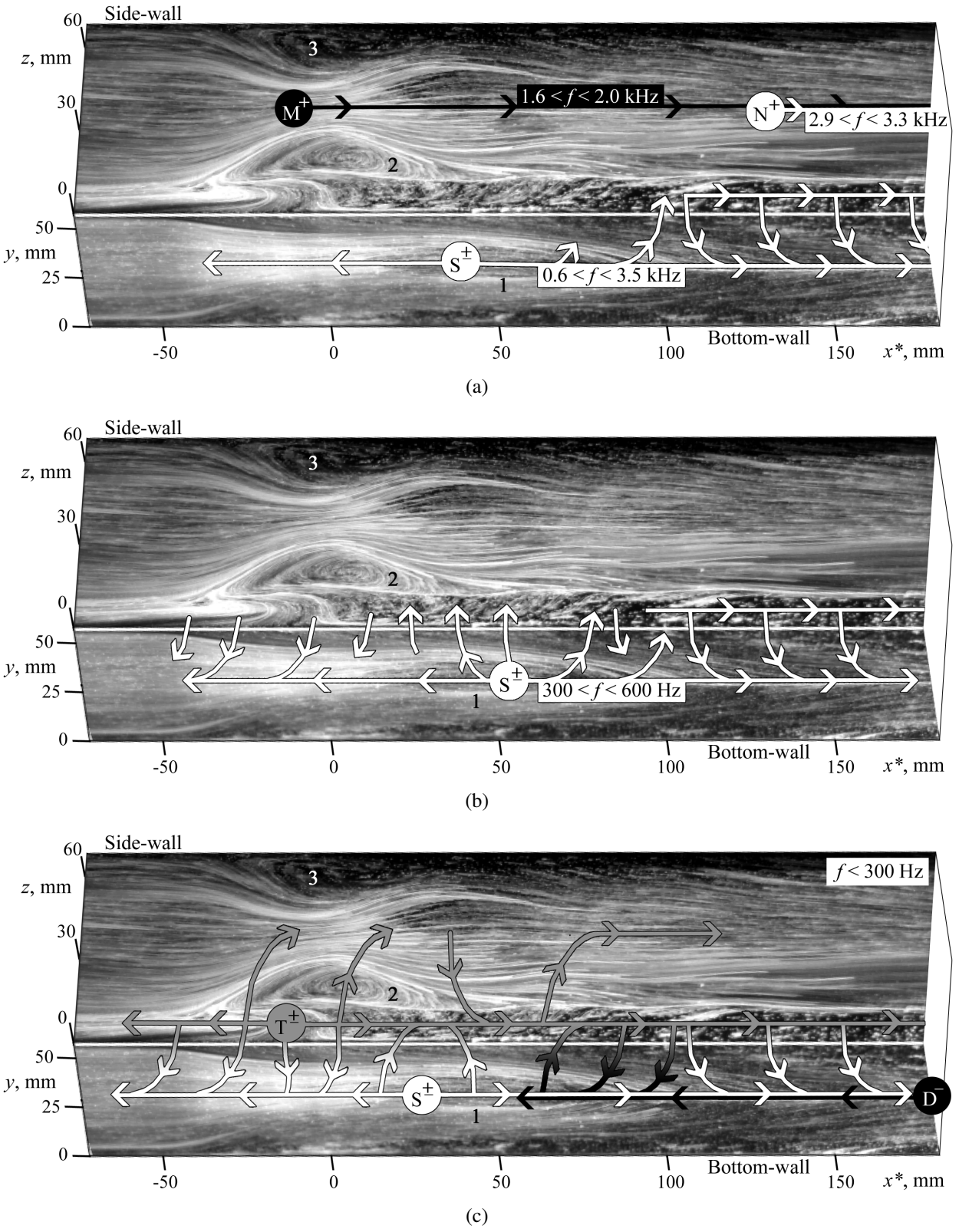

Figure 5.12: Perturbation pathways: (a) $600 < f < 3500$ Hz; (b) $300 < f < 600$ Hz; (c) $f < 300$ Hz.

Now consider the narrow band of frequencies ($1.6 < f < 2.0$ kHz) associated with a perturbation propagating downstream along the side-wall, away from $x^* = 0$ mm. For convenience, this perturbation is called M^+ (see label in figure 5.12(a)). Perturbation M^+ is first evident in the higher speed "core" region of the flow between the two large side-wall separation bubbles marked "2" and "3" in the figure. Note that the 1.6–2.0 kHz frequency range associated with perturbation M^+ is identical to the first high frequency mode evident in the shock and pressure fluctuation power spectra. The second high frequency mode evident in the shock and pressure fluctuation power spectra (at approximately 3.0 kHz) is attributed to a similar perturbation traveling downstream along the side-wall, away from $x^* = 120$ mm. This perturbation is called N^+ (see label in figure 5.12(a)). In this case, the oil flow does not clearly indicate what fluid phenomenon creates perturbations M^+ and N^+. Further analysis will be needed to identify the cause of these perturbations.

Figure 5.12(a) also illustrates that there is communication through the corners of the duct for $x^* > 70$ mm. That is, perturbations propagate to the side-wall from the bottom-wall and vice versa. Interestingly, at these high frequencies ($600 < f < 3500$ Hz) there is no strongly correlated communication through the boundary layer in the region upstream of the separation bubble. Recall from section 5.2 that the various morphological features of the second shock have different frequency content and cross-spectra. However, these qualities are nearly identical for different morphological features of the third and fourth shocks. This is due to the communication of perturbations through the boundary layer in the downstream region.

Next, consider the perturbation pathways associated with frequencies between 300 and 600 Hz in figure 5.12(b). The bottom-wall separation bubble (labeled "1" in the figure) still generates perturbations $S^\pm$ in this mid-frequency range but now the communication through the boundary layer has increased (i.e., the coherence between side- and bottom-wall pressure time traces is higher meaning they are better correlated). Near the center of the bottom-wall separation bubble (approximately $0 < x^* < 100$ mm) the perturbations tend to emanate away from the bottom-wall, through the corner, and finally to the side-wall. In the other regions (approximately $x^* < 0$ and $x^* > 100$ mm) the perturbations start on the side-wall and travel towards the bottom-wall.

Finally, consider the low frequency perturbation pathways shown in figure 5.12(c). Once again, the coherence between side- and bottom-wall pressure time traces is higher at these frequencies meaning there is an increased amount of communication through the corner of the duct. On the $y = W/2$ centerline of the bottom-wall there are multiple superimposed perturbations: perturbations $S^\pm$ and D^- (see labels in the figure). Perturbations $S^\pm$ are generated by the bottom-wall separation bubble instabilities and propagate away from the bubble. Perturbation D^- is generated downstream of the isolator section and propagates upstream along the bottom-wall. It is important to note that this perturbation is originating from the part of the facility used to replicate the combustor. Thus, this perturbation could exist in a real high-speed air-breathing engine. Unfortunately, there

is no optical access into the diffuser section and thus oil flow visualization cannot be used to assist in determining what fluid process generates perturbation D^-. The potential sources of this perturbation are discussed in section 5.5.

For the low-frequency perturbation pathways shown in figure 5.12(c), there is also an additional source of low frequency perturbations evident near the corner of the side-wall. The perturbations emanating away (both upstream and downstream) from this point are called perturbations $T^{\pm}$ (see label in the figure). From the oil flow visualization image it is evident that the perturbations are generated near the foot of the lower separation bubble on the side-wall (labeled "2" in the figure). Just like in the case of perturbations $S^{\pm}$, the generation of the perturbations is attributed to the instabilities of the separation bubble. Finally, note that the low-frequency $T^{\pm}$ perturbations generally propagate upwards along the side-wall (i.e., in the positive z-direction). In a small region on the downstream side of the separation bubble the perturbations are carried downwards on the side-wall (i.e., in the negative z-direction) due to the flow field inside the bubble.

5.4 Cause and Effect Relationship Between Perturbations and Shock Motion

In this section, the cause-and-effect relationship between the shock motion and the perturbations traveling through the isolator is considered. To accomplish this, the $x_i - p_j$ *cross-spectrum* is calculated using one shock position fluctuation signal and one pressure fluctuation signal. The pressures are measured along the bottom-wall $y = W/2$ centerline while the shock position is recorded simultaneously with schlieren imaging where glass side-walls provide the necessary optical access. Since side-wall optical access is required, this analysis is limited to the interaction between the shock waves and the perturbations traveling along the bottom-wall (i.e., perturbations $S^{\pm}$ and D^-). For each pressure fluctuation signal measured on the bottom-wall, the cross-spectral analysis is repeated for all four shock position signals. To properly compute the cross-spectrum, a second order low-pass Butterworth filter with a cutoff frequency of 5 kHz is applied to the pressure measurements and then the signal is downsampled to 10 kHz to match the acquisition rate of the schlieren images.

5.4.1 $x_i - p_j$ Coherence Spectra

Figure 5.13 shows how the coherence, $Co(x_i', p_j')$, varies with x^*, the location of the pressure transducer relative to the time-averaged location of the leading shock Mach stem. Parts (a), (b), (c), and (d) of the figure are results of the cross-spectra calculated using x_1', x_{2b}', x_{3b}', and x_{4b}', respectively. The coherence spectra contours found using other morphological features of the

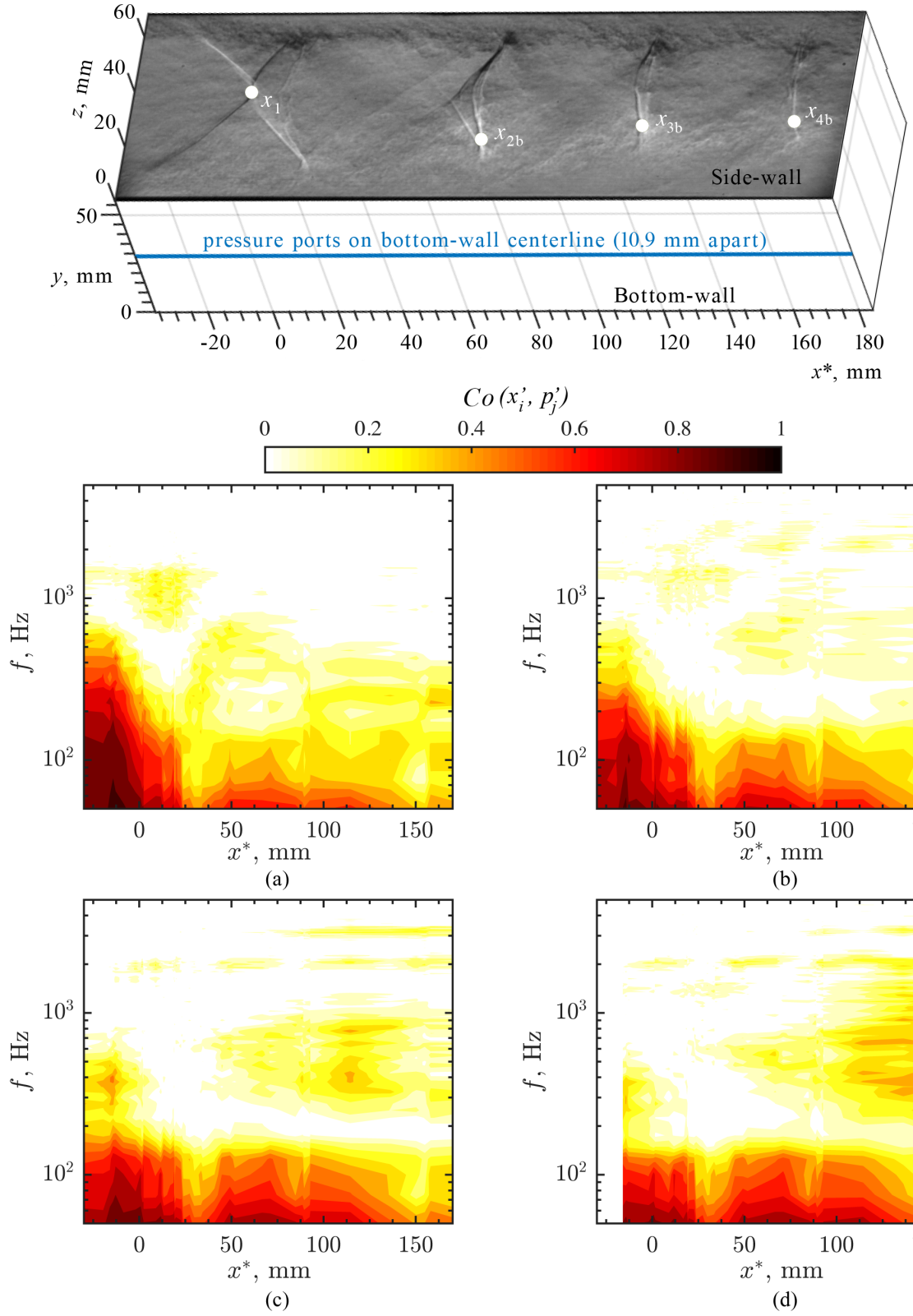

Figure 5.13: $x_i - p_j$ coherence spectra throughout the shock train calculated using: (a) x_1; (b) x_{2b}; (c) x_{3b}; (d) x_{4b}.

same shock wave are nearly identical (e.g., the coherence results of x'_{2t} are the same as the results found using x'_{2b}). In all of these cases the coherence is highest for frequencies less than 200 Hz meaning that the shock position is best correlated with pressure measurements for low frequencies. Each contour plot also shows additional pockets of high correlation in the downstream region of the shock train for frequencies between 200 and 3500 Hz. These high frequency fluctuations are most strongly correlated with the third and fourth shock position fluctuations. Above 3500 Hz the fluctuations are poorly correlated.

5.4.2 $x_i - p_j$ Narrowband Time Delay Example

To best illustrate the narrowband time delays of the $x_i - p_j$ cross-spectra, scatter plots are presented of the narrowband time delay, $\tau(x'_i, p'_j)$, as a function of the pressure transducer location relative to the time-averaged location of the leading shock Mach stem, x^*. For example, consider the sample of narrowband time delay results in figure 5.14. Each point in the figure represents the time delay at a specific frequency between 300 and 400 Hz for a cross-spectrum computed using time traces of the leading shock position fluctuation, x'_1, and wall static pressure fluctuation, p'_j. The trendlines in figure 5.14 are simply linear fits of the data. They represent the overall progression of the time delay as a function of x^*.

To fully understand figure 5.14, first consider the sign of the time delay. In essence, $\tau(x'_i, p'_j)$ quantifies the time between a fluctuation in the measured pressure and the corresponding fluctuation in shock position. A positive time delay means the pressure transducer "sees" the fluctuation before the shock is displaced. Conversely, a negative time delay means the shock fluctuates before the pressure transducer "sees" the fluctuation. A time delay of zero means that the shock fluctuates simultaneously with the pressure. The trendline also provides pertinent information because the direction in which a perturbation travels is identified by comparing the time delays of multiple pressure transducers. If an upstream transducer exhibits the fluctuation after a downstream transducer, that is the slope of the point distribution is positive, then the perturbation is clearly traveling upstream. Conversely, a negative slope signifies a downstream propagating perturbation. In figure 5.14, a perturbation is traveling upstream for $x^* < 50$ mm and a different perturbation is traveling downstream for $x^* > 50$ mm. The magnitude of the slope is equivalent to the propagation speed of the perturbation. A shallow slope indicates a quickly propagating perturbation while a steep slope is associated with slower propagation speeds.

5.4.3 How Perturbations $S^{\pm}$ Influence the Shock System

With the information from the previous subsection in mind, the impact of perturbations $S^{\pm}$ on the motion of shocks in the train is examined. Recall from section 5.3 that perturbations $S^{\pm}$ are

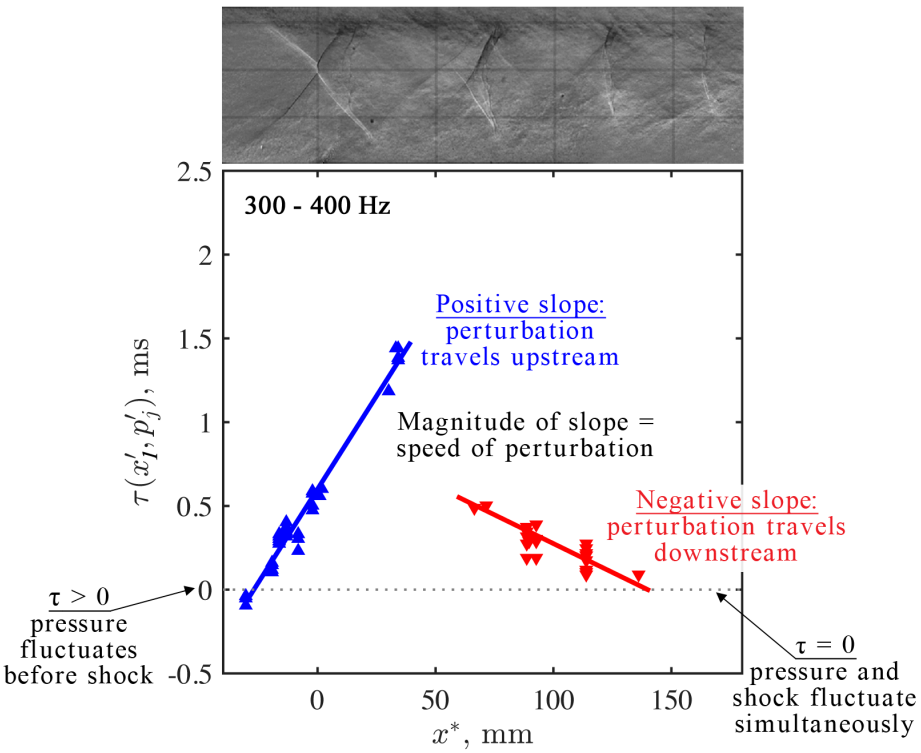

Figure 5.14: Time delay between pressure and leading shock position fluctuations ($300 < f < 400$ Hz).

associated with a broad range of frequencies (up to approximately 3 kHz). To decouple the impact of perturbations $S^{\pm}$ from that of perturbation D^{-}, only frequencies above 300 Hz are considered in this subsection (since perturbation D^{-} is only associated with low frequencies). Figure 5.15 shows the narrowband time delays, $\tau(x_i', p_j')$, with sufficiently high coherence for all frequencies between 300 and 3000 Hz. The different markers plotted as upwards triangles, downwards triangles, circles, and squares represent the time delays computed using the first, second, third, and fourth shock position time traces, respectively. Note that the results of different frequencies are not distinguished from one another because they follow the same trend. For reference, the shaded region corresponds to the location in the isolator where perturbations $S^{\pm}$ are generated (i.e., a region within the bottom-wall separation bubble) based on the $p_i - p_j$ cross-spectral analysis.

First, consider the narrowband time delays calculated using the leading shock position fluctuations, x_1' (upwards triangle markers in figure 5.15). The slope of the trendline is positive, thus the measured fluctuations are a result of upstream propagating perturbation S^{-}. Perturbation S^{-} is generated upstream of the second shock (i.e., within the shaded region of the figure) and it travels upstream at approximately 50–100 m/s, inducing pressure fluctuations as it passes each transducer. When the perturbation reaches the leading shock foot (i.e., at approximately $x^* = -30$ mm), the

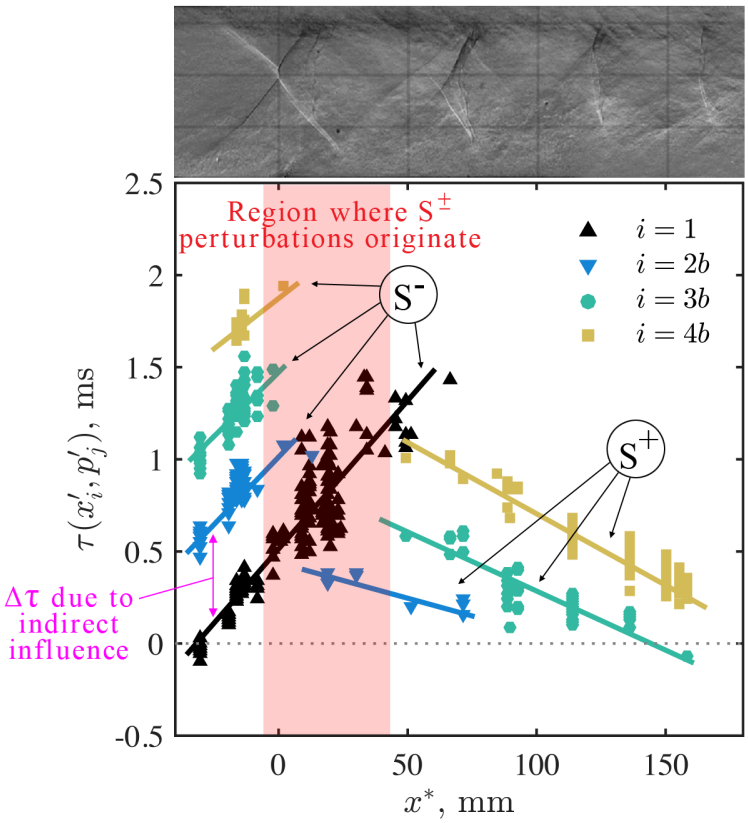

Figure 5.15: Time delay between pressure and shock position fluctuations ($300 < f < 3000$ Hz).

measured pressure fluctuates simultaneously with the leading shock (i.e., $\tau = 0$). This is a clear indication that the upstream propagating perturbation induces a movement in the leading shock as it passes the shock foot. It is hypothesized that the perturbation causes a locally significant change in boundary layer properties (e.g., a change in boundary layer height) which in ultimately responsible for instigating the shock movement.

Figure 5.15 also demonstrates that perturbation S^- impacts the motion of the downstream shocks. This is surprising because the perturbation is generated upstream of these shocks and travels away from them. Consider the time lags calculated using the downstream shock position fluctuations and the pressure fluctuations induced by perturbation S^-. These are the downwards triangle, circle, and square markers with a positive slope that are labeled "S^-" in the figure. These points are evidence that the downstream shock motion is correlated with the pressure fluctuations measured upstream of the shock itself. Note that the time delay increases for each consecutive shock, i.e., $\tau(x'_{i+1}, p'_j) = \tau(x'_i, p'_j) + \Delta\tau$. This means that the time between the pressure fluctuation and shock fluctuation increases for each downstream shock by an amount $\Delta\tau$ (see label in figure as an example). Thus, after the leading shock is displaced the downstream shocks are displaced sequentially after some time delay. The idea of sequential shock displacement was first

introduced in section 5.2 using the $x_i - x_j$ cross-spectral analysis. The time between the responses of consecutive shocks found from the $x_i - p_j$ cross-spectral analysis (i.e., $\tau(x'_i, p'_j) - \tau(x'_{i+1}, p'_j)$) closely resembles the time delay found previously with the $x_i - x_j$ cross-spectral analysis (i.e., $\tau(x'_i, x'_{i+1})$ from figure 5.9).

To explain this observed sequence of events, consider the following scenario. Assume that the leading shock moves downstream but the second shock has not moved. The change in distance between the two shocks implies that there are changes to the expansion and compression regions that make up the flow structure. As a result, the Mach number in front of the second shock is reduced and the pressure rise across the second shock would be less. However, the pressure rise across the shock must match the downstream condition that is imposed by the control valve. As such, the new conditions at the second shock are not possible. Therefore, the second shock must move downstream in order to have a higher inflow Mach number and larger pressure rise across the shock. The process is then repeated across consecutive shock pairs in the train and gives rise to the observed sequential displacements of shocks. In other words, the displacement of an upstream shock changes the inflow conditions to the downstream shock, causing the downstream shock to move such that the required pressure rise is met. The time delay between the consecutive shock movements is related to how fast the expansion/compression regions of the flow structure change from one condition to the next. This flow response time is relatively large (up to 0.7 ms). In comparison, a fluid element in the freestream flow travels the same distance in 0.02 ms (i.e., 35 times faster than the flow response time). The difference in time scales emphasizes that the movement of consecutive shocks is controlled by the rate of relaxation of the flow field, and not by an acoustic wave or other type of perturbation that is convected with the flow.

Based on these initial observations and arguments, it is concluded that perturbation S^- influences the shock system in a direct and an indirect way as follows:

1. **Direct influence on the leading shock**: As the perturbation propagates upstream and passes the leading shock foot, it causes a locally significant change in the boundary layer properties that induces a displacement in the shock position.

2. **Indirect influence on the downstream shocks**: The displacement of an upstream shock alters the flow structure of the expansion and compression regions between shocks. Thus, the flow conditions entering the downstream shock have changed. In order to satisfy the new inflow conditions and required pressure rise, the downstream shock is displaced accordingly.

Next, consider the narrowband time delays associated with downstream propagating perturbation S^+ (i.e., the trendlines with negative slope in figure 5.15). After perturbation S^+ is generated (within the shaded region) it travels downstream at approximately 100–300 m/s, inducing pressure fluctuations as it passes each transducer. When the pressure transducer is located near the shock

used to compute the cross-spectrum, the fluctuations in the measurements are almost simultaneous. Therefore, the perturbation directly influences the shock position as it travels past the shock foot. It is speculated that the perturbation also indirectly influences the downstream shocks in the same manner discussed previously. Both direct and indirect influences exist but the best correlated of the two will appear as the result of the cross-spectral analysis that is plotted in figure 5.15. This may explain some of the scatter in the data points.

Finally, recall perturbations $T^{\pm}$ that are generated by the side-wall separation bubble. These perturbations are analogous to perturbations $S^{\pm}$. The cause-and-effect relationship between the shock motion and perturbations traveling along the side-wall cannot be directly studied because of test model limitations, but the source, direction, and speed of $T^{\pm}$ are similar to that of $S^{\pm}$. Thus, it is assumed that $T^{\pm}$ are the same type of perturbations as $S^{\pm}$ and impact the shock train in the same way.

5.4.4 How Perturbation D^{-} Influences the Shock System

In this subsection, the narrowband time delay results of the $x_i - p_j$ cross-spectra are analyzed for frequencies less than 300 Hz. Perturbations $S^{\pm}$ and D^{-} all induce fluctuations at these low frequencies. Thus, the time delays are influenced by multiple perturbations and need to be carefully analyzed to distinguish the effects of each perturbation individually. It is assumed that perturbations $S^{\pm}$ act in the same way for all frequencies and thus the results here are no different than those discussed previously. This assumption allows for the development of a better understanding of perturbation D^{-}.

Figure 5.16 shows the low frequency narrowband time delays, $\tau(x_i', p_j')$, with sufficiently high coherence as a function of x^*. Once again, the markers plotted as upwards triangles, downwards triangles, circles, and squares represent the time delays computed using the first, second, third, and fourth shock position time traces, respectively. Unlike previous plots, the coordinate axis of this figure is extended to view a large portion of the region downstream of the shock train. For $x^* > 50$ mm, all four trendlines have a positive slope meaning that the perturbation is traveling upstream, inducing fluctuations in the pressure measurements as it passes the pressure transducers. The speed of the perturbation is approximately 50–100 m/s. In section 5.3, the results of the $p_i - p_j$ cross-spectral analysis showed evidence of both downstream (S^{+}) and upstream (D^{-}) propagating perturbations in this region of the flow. The $x_i - p_j$ time delays shown here provide clear additional evidence of upstream propagating perturbation D^{-} and emphasize that the shock motion is better correlated with pressure fluctuations caused by perturbation D^{-} compared to those created by S^{+} for low frequencies. In addition, the results illustrated in figure 5.16 clarify where perturbation D^{-} originates. Specifically, note the results of the pressures measured far downstream in the mixing region but just upstream of the diffuser (at approximately $x^* = 330$ mm). These pressure fluctua-

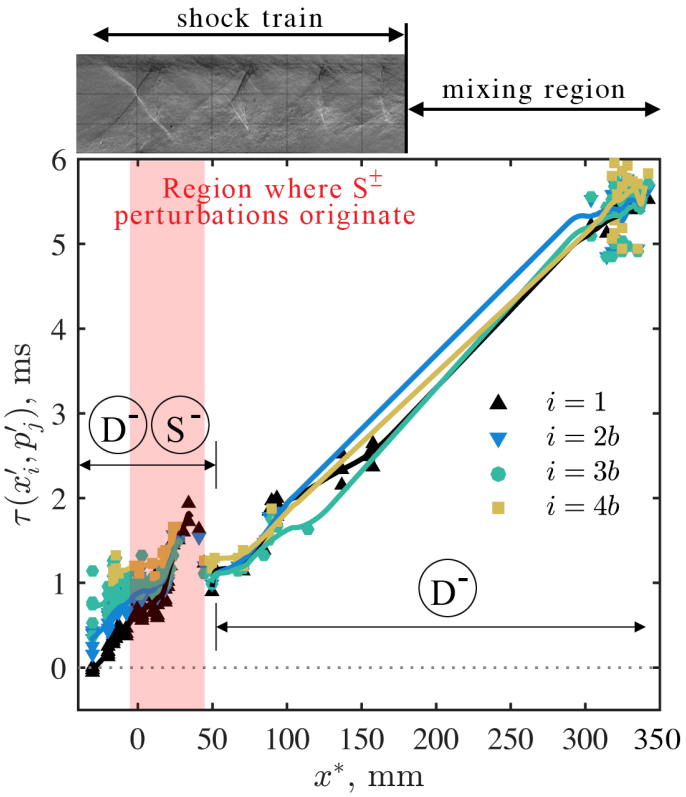

Figure 5.16: Time delay between pressure and shock position fluctuations ($f < 300$ Hz).

tions are correlated with the motion of all four shocks and the narrowband time delay is positive, meaning that the pressure fluctuation occurs before the corresponding shock displacement. Thus, it is concluded that perturbation D^- originates far downstream of the shock train, in the diffuser section of the wind tunnel.

Next, note that the magnitude of the time delay is large for pressures measured near shocks 2, 3, and 4. This means that a long period of time elapses between the pressure fluctuations and the position fluctuations of the downstream shocks. In other words, the perturbation travels upstream, without directly influencing the position of shocks 2, 3, and 4 as it passes them. In contrast, the leading shock fluctuates simultaneously with the pressures measured near the leading shock foot (i.e., $\tau = 0$). This means that perturbation D^- directly influences the position of the leading shock as it passes the shock foot. The magnitude of the time delays and the slope of the trendlines suggest that the displacement of the leading shock ultimately causes the sequential displacement of the downstream shocks. Thus, perturbation D^- does not have a direct influence on shocks 2, 3, and 4 but it does have an indirect influence on them. In this scenario, the measured time delay is equal to

the amount of time it takes the perturbation to travel at 50–100 m/s from the pressure transducer to the leading shock foot plus the amount of time required for the flow structure between consecutive shocks to readjust due to the indirect influence of the perturbation. Therefore, it is expected that $\tau(x'_{i+1}, p'_j) = \tau(x'_i, p'_j) + \Delta\tau$ where $\Delta\tau$ is the relaxation time of the flow between consecutive shocks. Figure 5.16 shows that the magnitude of $\Delta\tau$ is small but the accuracy in determining this value is limited due to the lack pressure data for $150 < x^* < 300$ mm and the scatter in the results. However, the $x_i - x_j$ cross-spectral analysis confirms the small value of $\Delta\tau$. Specifically, recall figure 5.9, which demonstrates that the time delay between consecutive shock motions goes to zero as the frequency approaches 50 Hz. Given the negligible magnitude of $\Delta\tau$ for this frequency range, the $x_i - p_j$ narrowband time delay in figure 5.16 is approximately equal to the time it takes the perturbation to propagate from the transducer to the leading shock foot, thus verifying that perturbation D^- directly influences the leading shock and indirectly influences shocks 2, 3, and 4.

At approximately $x^* = 50$ mm the magnitude and slope of the time delay suddenly change. This location is within the bottom-wall separation bubble and corresponds to where perturbation S^- is generated for low-frequencies. Thus, for $x^* < 50$ the time delays derived from cross-spectral analysis are influenced by multiple upstream propagating perturbations (S^- and D^-) which are responsible for the observed discontinuity in time delay. The spatial and temporal overlap means the two perturbations cannot be distinguished from one another. Therefore, no further analysis is conducted in the region $x^* < 50$ for low-frequencies.

5.5 Insight on the Perturbations from PIV Measurements

In this section, the velocity fields obtained from PIV measurements are explored to determine the physical nature of each perturbation.

5.5.1 Perturbation D^-: An Upstream Propagating Acoustic Wave

The results of the cross-spectral analysis clearly illustrate the presence of perturbation D^- on the bottom-wall of isolator. This perturbation is generated in the diffuser section and propagates upstream at approximately 50–100 m/s. These speeds are equivalent to 0.1 – 0.3 times the freestream flow velocity, u_∞. Given the low-speed nature of the perturbation, and the fact that it propagates against the (mostly) supersonic flow, it is hypothesized that it is an acoustic wave traveling upstream through the subsonic portion of the boundary layer. Such a wave must travel at a speed of $u - a$ (equal to 50–100 m/s), where u and a are the local flow speed and the speed of sound, respectively, at a given distance from the wall in the subsonic portion of the boundary layer.

Using the streamwise velocity found from PIV measurements and the measured stagnation temperature (i.e., the room temperature), the approximate temperature of the flow field is calculated

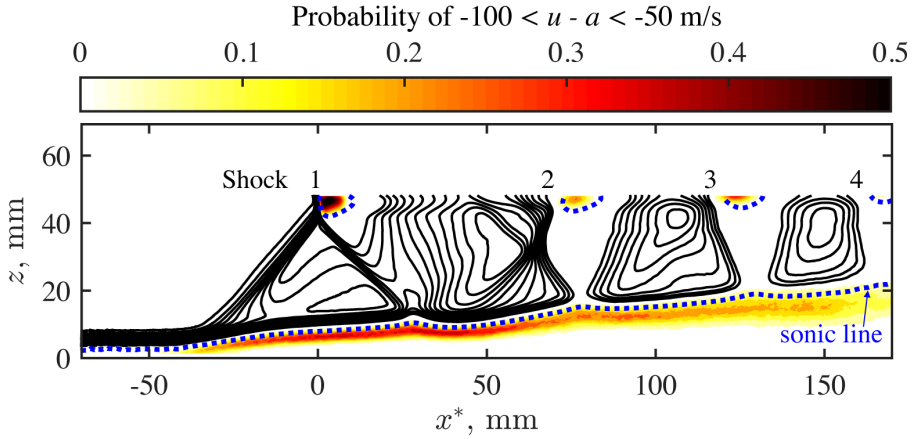

Figure 5.17: Probability map of $-100 < u - a < -50$ m/s to demonstrate where perturbation D^- propagates in the boundary layer. time-averaged velocity contours from 350 to 500 m/s (in increments of 10 m/s) are plotted as solid lines to illustrate the shock positions. The dotted line follows the sonic line.

assuming adiabatic flow. With temperature and flow speed known, the speed of sound, a, and the propagation speed of the acoustic wave as it travels upstream against the bulk flow, $u - a$, are calculated. Figure 5.17 shows the probability of $u - a$ being within the range of -100 to -50 m/s for every point of PIV measurement plane CL1 (see figure 2.6 for measurement plane location). For clarity, the time-averaged velocity contours from 350 to 500 m/s are overlaid in the figure to illustrate the shock locations. Essentially, the figure illustrates the region in the flow where a perturbation is likely to travel at the speed specified by the cross-spectral analysis. The results show that the most probable path of the acoustic wave is within the upper portion of the boundary layer, just below the sonic line.

Surprisingly, the $x_i - p_j$ cross-spectral analysis does not indicate that the upstream propagating acoustic wave influences the motion of the downstream shocks as it propagates past them. From schlieren images (see figure 2.2) and PIV measurements (see figure 5.17) it is known that the boundary layer rapidly grows after the leading shock foot. This leads to the hypothesis that the thick, turbulent downstream boundary layer is less sensitive to acoustic perturbations compared to the thin boundary layer at the leading shock foot. That is, the local changes to the boundary layer properties due to the acoustic wave are insignificant in the thick downstream boundary layer. When the acoustic wave reaches the leading shock foot it imparts a locally significant change to the local boundary layer properties (e.g., by changing the boundary layer height) enough to induce a displacement of the leading shock. This would explain why the $x_i - p_j$ cross-spectral analysis shows the acoustic wave interacting at the leading shock foot.

While the cross-spectral analysis and PIV results clearly show the path of the acoustic wave

through the boundary layer in the isolator section, the lack of downstream measurement capabilities and optical access prevent the study of the perturbation and its source in the diffuser section. To explain the experimental observations of this study, consider theories presented in the literature that propose a physical fluid phenomenon that generates upstream propagating acoustic waves. As discussed in section 1.4, Yamane *et al.* [1984*a*,*b*] measured a similar perturbation propagation speed of 100 m/s, leading them to hypothesize that upstream propagating acoustic waves induce the shock system unsteadiness. They conjectured that the acoustics are created by the oscillation of the air column in the diffuser section. If this were the case, the power spectra would show a narrowband low-frequency mode associated with the natural frequency of the pipe resonance (expected to be less than 100 Hz for the conditions of these experiments). The results of the current experiment (see figures 5.6 and 5.10) are relatively broadband in the low-frequency regime, meaning that the flow is not pulsating at a distinctive frequency as would be expected if the acoustic wave were generated by pipe resonance.

More fitting explanations for the generation of upstream propagating acoustic waves are obtained through previous studies of single normal shock fluctuations in a diffuser. For instance, Chen *et al.* [1979] used space-time correlations of pressure measurements to determine that flow separation along the walls of the diverging duct generates upstream propagating waves with significant spectral content below 70 Hz. These waves are related to the movement of the separation point and are ultimately responsible for the normal shock unsteadiness. Handa *et al.* [2003] also investigated single normal shocks in diffusers and their results suggest that high turbulence levels on the curved wall is responsible for the generation of the pressure perturbations. Both phenomenon described above may occur in the diffuser section of the current experiment and generate acoustic waves that propagate back upstream into the constant area isolator. However, further research is needed to verify the source of these upstream propagating acoustic waves that interact with the leading shock of the train.

5.5.2 Perturbations $S^{\pm}$, $T^{\pm}$: Acoustic Waves and Vortices Generated by Separation Bubbles

In this subsection, the perturbations generated by two separation bubbles are considered: perturbations $S^{\pm}$ generated by the separation bubble on the bottom-wall (called "separation bubble 1" in figure 5.12) and perturbations $T^{\pm}$ generated by the side-wall separation bubble located under the bottom lambda foot (called "separation bubble 2" in figure 5.12). The existence of boundary layer separation along the shock train is generally an accepted or assumed feature of shock trains. However, its properties, such as the point of separation, its length and thickness, are not well defined from works in the literature. Recall that for the current experimental configuration, "bubble 2" was investigated in chapter 4.4 using SPIV on cross-sectional planes. The SPIV measurements demonstrated that this rapidly enlarging separation bubble pushes the flow towards the center of the

duct, creating a highly three-dimensional shock structure. In this chapter, both bottom- and side-wall separation bubbles are examined using two-component PIV on streamwise vertical planes. Specifically, "bubble 1" and "bubble 2" are captured in PIV measurement planes CL1 and SW1, respectively. Recall that the locations and extent of these PIV measurement planes are illustrated in figure 2.6.

First, the locations of the separation bubbles are identified using PIV. Figures 5.18(a) and 5.18(b) illustrate the probability of reverse flow along the shock train for measurement planes CL1 and SW1, respectively. Time-averaged velocity contours from 300 to 500 m/s are overlaid in each figure to illustrate the shock locations. Figure 5.18(a) demonstrates that bottom-wall separation is most likely under the second shock in the train, i.e., at approximately $x^* = 75$ mm. The dashed line in the figure demonstrates where the probability of separation is 10%. Using this line as a reference, it is evident that separation is probable in the region $25 < x^* < 125$ mm. The PIV results also show that the bottom-wall separation bubble is intermittently separated because reverse flow is only evident in approximately 80% of the instantaneous velocity fields. In addition, the x-location of the separation bubble translates in time and thus the probability of seeing separation at a particular point in the flow is less than 80%. It is also possible that the y-location of the bubble varies in time. In this case, the separation bubble can exist on the bottom-wall but may not be evident in the measurement plane.

The side-wall separation bubble exhibited in figure 5.18(b) is much larger in comparison to the bottom-wall separation bubble discussed previously. On measurement plane SW, the probability of reverse flow is greater than 10% within a region $-40 < x^* < 50$ mm and the most probable region for flow separation is at approximately $x^* = -10$ mm. The time-averaged velocity contours illustrate that this most probable separation region is under the leading shock lambda foot. In addition, the time-averaged velocity contours show that there is a significant upstream influence on the shock structure near the wall. That is, the leading shock structure is curved such that the portion of the shock that is close to the wall is positioned further upstream. This is consistent with the previous SPIV measurements on cross-sectional planes (see chapter 4.4) that revealed the highly three-dimensional and curved nature of the leading shock. As a result of the upstream influence, the side-wall separation evident on measurement plane SW1 begins well upstream of the time-averaged Mach stem location seen on measurement plane CL1. Also note that the probability of reverse flow and the overall separation bubble size (i.e., the area enclosed by the dashed line) in figure 5.18(b) are underestimated because measurement plane SW1 is 9 mm away from the side-wall. Effectively, only the tallest portions of the separation bubble are measured; analogous to viewing the tip of an iceberg. As a result, no reverse flow present in many of the instantaneous velocity fields because the separation bubble is less than 9 mm tall. However, from the previous SPIV measurements on cross-sectional planes presented in chapter 4.4, it is known that the side-

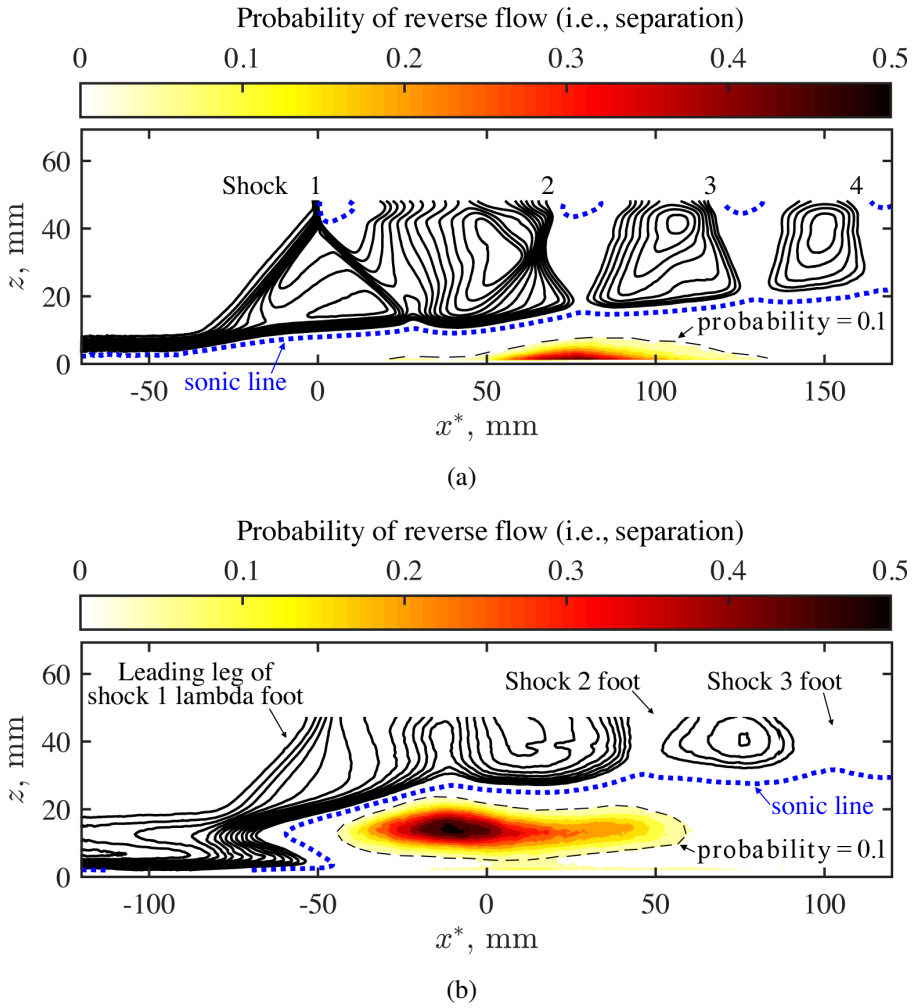

Figure 5.18: Probability of separated flow on: (a) measurement plane CL1; (b) measurement plane SW1. The thin dashed line around each separation bubble represents the extent of 10% separation probability. time-averaged velocity contours from 350 to 500 m/s (in increments of 10 m/s) are plotted as solid lines to illustrate the shock positions. The thick dotted line follows the sonic line.

wall separation bubble is present in 100% of the instantaneous velocity fields but is sometimes less than 9 mm tall. Finally, for both measurement planes, the position and extent of the flow separation agree with the observations from the oil flow visualization presented earlier.

Often in the literature the point of separation is assumed to be at the leading shock foot. However, the above results for the bottom-wall separation bubble show that the separation starts further downstream, past the leading shock, and in some instances the flow does not even separate. Benek [2016] studied the effects of duct width and boundary layer thickness on a single oblique shock reflection and hypothesized that thick boundary layers in the duct corners produce weak compression waves that influence the separation region. They speculate that if the compression waves from opposite corners interact upstream of the shock impingement then the adverse pressure gradient is

spread over a larger distance and it is easier for the flow to stay attached. The compression waves generated in the corners will intersect upstream of the shock impingement if 1) the duct aspect ratio is small or 2) the corner blockage is large and generates compression waves at a large angles away from the side-wall. In the current experimental setup, the thick side-wall separation bubble in conjunction with the low aspect ratio duct suggest that the theory of Benek [2016] holds for the resulting shock train. This would explain why the bottom-wall boundary layer only has a small, intermittent separation bubble.

Now the perturbations created by these separation bubbles are discussed. Separation bubbles in turbulent flows are known to exhibit two unsteady phenomena: 1) the roll-up of vortices in the shear layer above the recirculating region and their shedding downstream of the bubble, and 2) separation bubble breathing, i.e., contraction/expansion [Kiya & Sasaki, 1983; Driver, 1987; Weiss *et al.*, 2015]. These separation bubble instabilities are intrinsic to the bubble itself or externally induced (e.g., driven by the incoming turbulent boundary layers) as observed in some single shock boundary layer interaction (SBLI) configurations [Clemens, 2014].

Given the speed and direction in which perturbations S^- and T^- travel, it is proposed that these perturbations are acoustic waves generated by the separation bubble breathing mode. The acoustic waves are created as the surrounding boundary layer flow adjusts to the new separation bubble size or position. Similar to acoustic wave D^-, the acoustic waves generated by the separation bubble instabilities propagate upstream at 50–100 m/s and follow the same path through the upper portion of the boundary layer (see figure 5.17). The acoustic waves change the local flow properties and thus induce a displacement of the leading shock as they pass the shock foot. It is also hypothesized that downstream propagating acoustic waves are generated by the separation bubble breathing mode. However, these acoustic waves have a negligible impact on the downstream shock positions for the same reason that acoustic wave D^- does not impact shocks 2, 3, and 4 as it travels upstream. That is, the thick turbulent boundary layer under the downstream shocks is less sensitive to the local changes imparted on the flow from the acoustic wave.

Next, it is proposed that downstream propagating perturbations S^+ and T^+ are associated with streamwise vortical structures generated by the shear layer formed between the separation bubble and the unseparated flow. These vortices periodically shed from the shear layer and propagate downstream affecting the position and structure of the shocks. The existence of vortical structures is investigated by applying the vortex detection method proposed by Graftieaux *et al.* [2001] to the instantaneous PIV velocity fields. This method has also been utilized in several single SBLI studies [Dupont *et al.*, 2008; Souverein *et al.*, 2010; Oudheusden *et al.*, 2011]. The detection method defines a dimensionless scalar, Γ, at every fixed point in the measurement domain, P, as follows:

$$\Gamma(P) = \frac{1}{S}\int_S \sin(\theta_M)\mathrm{d}S \tag{5.1}$$

where S is a two dimensional area surrounding the point P and θ_M is the angle between the local velocity at point M (also a point in area S) and the vector connecting points P and M. The PIV velocity fields are sampled at discrete spatial locations and thus the above integral is approximated as:

$$\Gamma(P) = \frac{1}{N} \sum_{S} \sin(\theta_M) \tag{5.2}$$

where N is the number of points inside S. The dimensionless scalar result, Γ, has values between -1 and 1, with its sign related to the direction of the vortex rotation. Graftieaux *et al.* [2001] showed that the flow is locally dominated by rotation when $|\Gamma| > 2/\pi$. Typically, $|\Gamma|$ has values greater than 0.9 at the vortex center. Based on this definition, the vortex identifier is applied to the instantaneous velocity fields. In these calculations, the interrogation window size was chosen to be 4.5 $\times$ 4.5 mm. Note that the interrogation window size acts as a spatial filter and only weakly affects the location of the vortex center. This was verified by parametrically changing S. Thus, the size of S does not impact the conclusions drawn here.

Figure 5.19 shows examples of the vortex identifier magnitude, $|\Gamma|$, for instantaneous velocity fields with reverse flow. Parts (a) and (b) of the figure are results from PIV measurement planes CL1 and SW1, respectively. Velocity contours from 350 to 500 m/s are plotted as solid lines to illustrate the shock locations and the dashed contour line outlines the region of reverse flow. For both measurement planes, the existence of vortices in the separation bubble shear layer is made clear by the large magnitude of the vortex identifier (i.e., $0.92 < \Gamma < 0.98$). The center of each identified vortex, with $|\Gamma| > 2/\pi$, is circled in the figure. In comparison, the magnitude of Γ is generally less than 0.2 in regions far away from the separation bubble. Also note that the vortices are more difficult to detect downstream of the separation bubble. This is attributed to the difficulty in defining geometrical properties of a large-scale vortex superimposed on a small-scale turbulent velocity field, which is a common problem in vortex identification schemes.

Even though one instantaneous case for each PIV measurement plane is shown in figure 5.19, the results are representative examples of flow fields with separation. To demonstrate this, figure 5.20 shows the number of identified vortex centers versus the size of the separated area. The lack of any identified vortex centers in an instantaneous velocity field without reverse flow signifies that Γ is a marker of separation. Generally, the number of identified vortices increases linearly with the size of the separated area.

Finally, consider the speed of perturbations S^+ and T^+. These perturbations propagate downstream at approximately 100-300 m/s which is far too slow to be the speed of an acoustic wave convected with the flow. However, single SBLI experiments have shown that vortices shed away from the separation bubble at a convective speed of 0.3 to 0.7 u_∞ [Dupont *et al.*, 2008; Humble *et al.*, 2009; Souverein *et al.*, 2009; Oudheusden *et al.*, 2011]. This corresponds to approximately

150 to 350 m/s for the current experiment. Thus, the expected convective velocity of vortical structures is similar to the measured propagation speed of the perturbations. Furthermore, Varadarajan & Roe [2011] demonstrated that vortices convected across a shock wave are capable of traveling considerable distances and thus would be able to impact the downstream shocks.

5.5.3 Perturbations M^+ and N^+

The $p_i - p_j$ cross-spectral analysis in section 5.3 demonstrates two perturbations propagating downstream along the side-wall of the isolator: M^+ and N^+ associated with a narrowband of frequencies

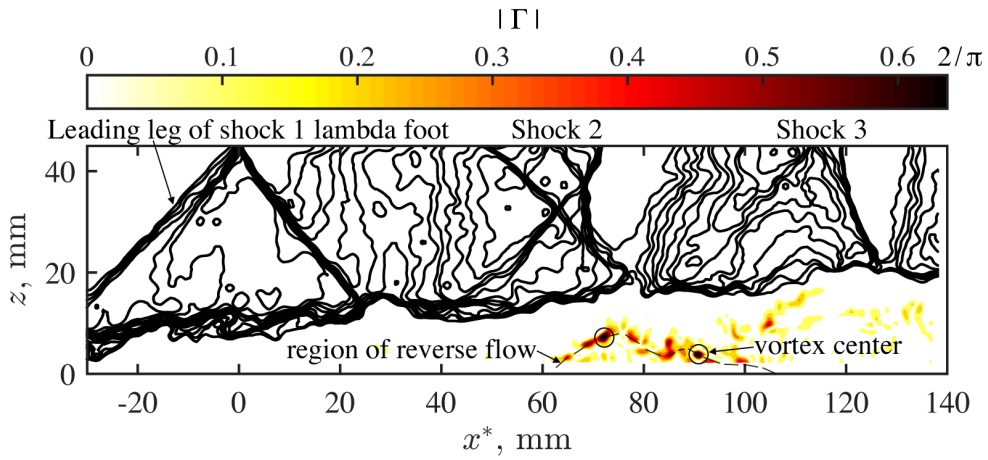

(a)

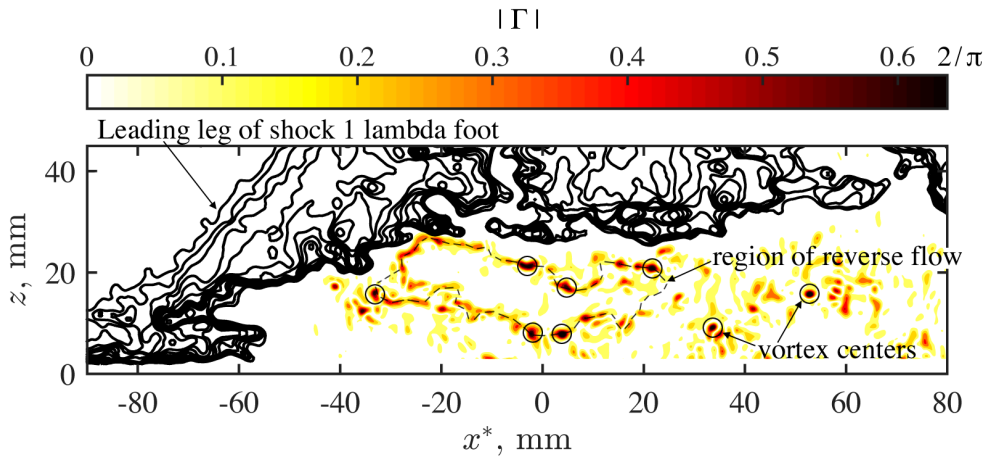

(b)

Figure 5.19: Magnitude of the vortex identifier, $|\Gamma|$, for instantaneous velocity fields with separation: (a) measurement plane CL1; (b) measurement plane SW1. Vortex centers are circled. The thin dashed line represents the extent of reverse flow. Velocity contours from 350 to 500 m/s (in increments of 10 m/s) are plotted as solid lines to illustrate the shock positions.

centered at 1.8 kHz and 3.1 kHz, respectively. Given the spacing between pressure transducers and the narrowband time delay from the cross-spectral analysis, it is evident that these perturbations propagate at 50 – 100 m/s; far too slow to be an acoustic wave convected downstream at a speed $u + a$. In addition, the vortex identification algorithm described earlier does not show any vortices in the PIV velocity fields where the perturbations exist. Generally, the details about perturbations M^+ and N^+ are difficult to obtain because 1) simultaneous side-wall pressure and schlieren measurements are not possible, hence the $x_i - p_j$ cross-spectral analysis cannot be conducted, and 2) no distinctive flow feature is evident in the PIV and oil flow visualizations that would suggest what fluid phenomenon creates the perturbations. Thus, the origin of the perturbations or how they interact with the shock system is unknown. However, based on the limited understanding gained so far, two possible explanations are provided.

One explanation for these observations in the pressure measurements is that perturbations M^+ and N^+ are simply signatures of the consecutive shock displacements. That is, as the shocks move they change the surrounding flow field and thus change the pressure measured by the transducers on the side-wall. This is supported by the fact that the time between consecutive shock displacements matches with the time it takes the perturbation to travel the same distance. However, there are two flaws in this argument. The first is that the perturbations are associated with a narrow band of frequencies while the shock motion is relatively broadband. Secondly, the bottom-wall does not

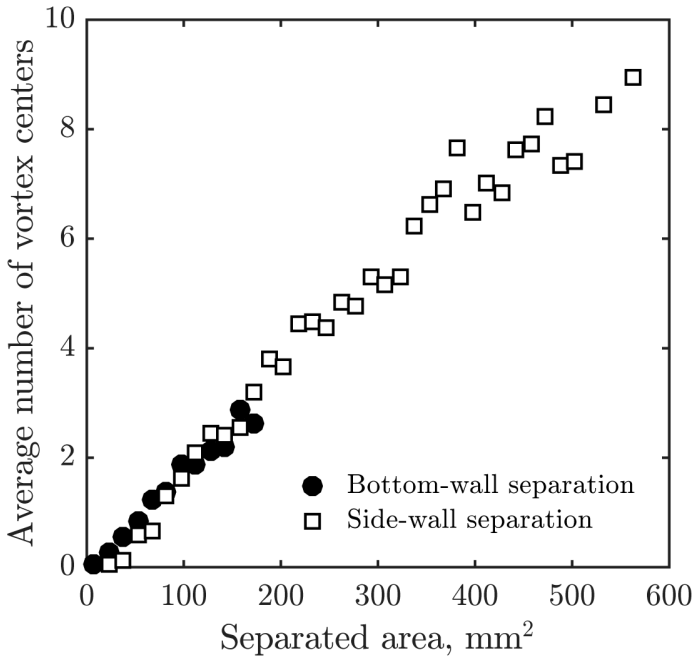

Figure 5.20: Average number of vortex centers (with $|\Gamma| > 2/\pi$) versus the size of the separated area in the instantaneous PIV velocity field.

show this same behavior and the responses of the side- and bottom-wall are expected to be similar.

A second explanation is that two side-wall separation bubbles change size and effectively create a nozzle effect that ultimately produces perturbation M^+. For example, if the bubble size grows then the available area for core flow to pass through is reduced. Thus, perturbation M^+ is the hydrodynamic change to the flow structure due to this nozzle effect. As evidence, the oil flow visualizations show that perturbation M^+ originates between the two separation bubbles. Similarly, perturbation N^+ originates near the third shock in a region where the flow is confined by thick boundary layer bulges. Thus, the strong high frequency modes evident in the shock motion and pressure fluctuations are possibly due to the successive expansions and contractions of the core flow area. Note that this explanation is similar to the theory of Sugiyama *et al.* [1988] as discussed in section 1.4. However, further analysis is needed to clearly identify the cause of these perturbations.

5.6 Discussion on the Scaling of Unsteadiness Properties

Finally, consider how the shock train unsteadiness properties scale with the various flow parameters. The development of a scaling argument in this flow is difficult for three reasons. The first reason is that the shock train unsteadiness is caused by multiple processes, each associated with a range of frequencies that are dependent on the scaling parameters specific to those processes. Thus, one single set of scaling parameters will not adequately describe the entire system. The second reason is that the perturbations may be coupled to each other causing the unsteadiness properties to scale with parameters that are seemingly irrelevant to the individual phenomena. For instance, an upstream propagating acoustic wave from the diffuser may interact with the bottom-wall separation bubble. Perturbing the separation bubble generates a second upstream propagating acoustic wave. In this scenario, the acoustic wave generated by the separation bubble depends on a fluid phenomenon in the diffuser section. It is also possible that these coupling effects result in non-linear responses. Finally, the third problem stems from the lack of research that adequately describes the entire set of flow parameters and the shock train unsteadiness properties, both of which are needed to construct and compare scaled quantities from different facilities. It is for these reasons that the shock train unsteadiness properties have been presented in dimensional form thus far.

In an attempt to overcome the third problem discussed above, consider the similar large scale, low frequency unsteadiness observed in many single SBLI, such as those induced by compression ramps, reflected shocks, and blunt-fin interactions [Dussauge *et al.*, 2006; Clemens, 2014]. These phenomena remain the subject of many research studies today and provide an ample set of data to use for comparison. However, there are obvious differences including: 1) single SBLI experiments only deal with a single incident shock and the associated reflected shock while the shock train is

composed of numerous shocks; 2) the geometry of the duct is different because single SBLI experiments have a physical structure in the flow creating and stabilizing the incident shock, while shock train experiments do not have this structure. With these differences in mind, the key similarity between the single SBLI case and the shock train is the existence of an unstable separation bubble that potentially influences the shock position.

Typically, in single SBLI experiments the characteristic frequencies of the shock motion and measured wall-pressures are scaled in terms of the dimensionless Strouhal number defined as follows:

$$St = fL/u_\infty \tag{5.3}$$

where L is a characteristic length scale. In many cases, L is defined as the length of the separation bubble. However, numerous other definitions of L have been used in the past. For example, in reflected shock interactions, L is often approximated as the distance between extrapolated intersection points of the incident and reflected shocks with the wall. In all of these cases, L is representative of the effects on the boundary layer caused by the shock impingement. Thus, for these types of scaling arguments L should depend on a characteristic length of the boundary layer. By analogy, the length scale of the shock train is defined as:

$$L = \theta/\sqrt{C_\theta} \tag{5.4}$$

where θ is the momentum thickness of the boundary layer just upstream of the shock train and C_θ is the confinement ratio, defined as the ratio of momentum thickness to the isolator hydraulic diameter, D_H (i.e., $C_\theta = 2\theta/D_H$). For this work $L = 5.00$ mm. Similar to single SBLI cases, the phenomena that generate perturbations in the shock train system are associated with the boundary layer and should scale with the boundary layer properties. Therefore, θ just upstream of the leading shock is expected to be an adequate length scale to represent the shock train dynamics to a first approximation. Note that this definition of L is essentially an approximation because it does not take into consideration that there are multiple separated regions that exist and locally drive the observed dynamics. Each region may have a different dependence on the properties of the incoming undisturbed boundary layer. However, for simplicity it is assumed that a simple θ dependence is sufficiently representative of boundary layer evolution through the shock train, and it is thus proposed here to be the relevant scaling quantity. It should also be noted that this θ scaling argument is different than what has been found to describe other global metrics of the shock train, such as the shock train length, overall pressure rise and pressure gradient. Previous studies have shown that these quantities depend on the cross-sectional size of the isolator which in turn is described by the hydraulic diameter [Waltrup & Billig, 1973; Carroll, 1988; Lin *et al.*, 1991]. Thus, the confinement ratio term is utilized in equation 5.4 in order to account for the cross-sectional size of the

duct relative to θ. An alternative and compact form of the definition proposed above is simply:

$$L = \sqrt{D_H \theta / 2} \tag{5.5}$$

In this form, L resembles the characteristic length scale used by Waltrup & Billig [1973]. In their work, the length of the shock train is normalized by $\sqrt{D_H \theta}$ in a simple quadratic relationship that scales the pressure profiles of shock trains at different conditions. The study by Waltrup & Billig [1973] is particularly impactful because it shows that the shock train is self similar in some sense, and although the flowfield is complex and not fully understood, its properties scale with the flow conditions upstream of the shock train.

Figures 5.21(a) and 5.21(b) show the evolution of the power spectra through the shock train system for pressure fluctuations measured on the bottom- and side-walls, respectively. The solid and dotted lines represent the results for pressures measured away from the corner and near the corner, respectively. The results are presented in the typical single SBLI fashion, where the power spectra, $PSD(p')$, are non-dimensionalized by frequency, f, and the standard deviation of pressure, $\sigma(p')$, and then plotted as a function of Strouhal number, St.

First, consider the results of the bottom-wall pressures shown in figure 5.21(a). Ahead of the shock train, the power spectrum is dominated by high Strouhal numbers associated with the incoming turbulence. Near the shock foot, the power at low Strouhal numbers rises due to the low-frequency motion of the leading shock. Then, a peak in the power spectrum emerges as the bottom-wall separation bubble is approached. For pressures near the corner, this peak is very broad and centered at a Strouhal number of 0.03. For pressures measured on the bottom-wall $y = W/2$ centerline, the peak is narrower and centered at a Strouhal number of approximately 0.014. These Strouhal numbers are strikingly similar to those found in single SBLI experiments, whose values lie within the range of $0.02 < St < 0.05$ [Dussauge *et al.*, 2006; Clemens, 2014]. For pressure measured along the $y = W/2$ centerline, the peak in the power spectrum becomes broader and shifts towards a higher Strouhal number of 0.03 within the separation bubble. This same trend has been observed in some single SBLI experiments as well [Dussauge *et al.*, 2006; Dupont *et al.*, 2006; Grilli *et al.*, 2012]. At the end of the separation bubble, more high frequency modes are present. These modes are attributed to other perturbations in the shock train system including those created by the side-wall separation bubbles. Note that the Strouhal numbers associated with the side-wall separation bubbles are different from the bottom-wall separation bubble due to differences in the bubble size and general characteristics. Funderburk & Narayanaswamy [2016] discussed this phenomenon for the large primary separation and small corner separation generated by a single SBLI. From the cross-spectral analysis it is known that communication through the boundary layer is prevalent in the downstream portion of the flow. This would explain why the

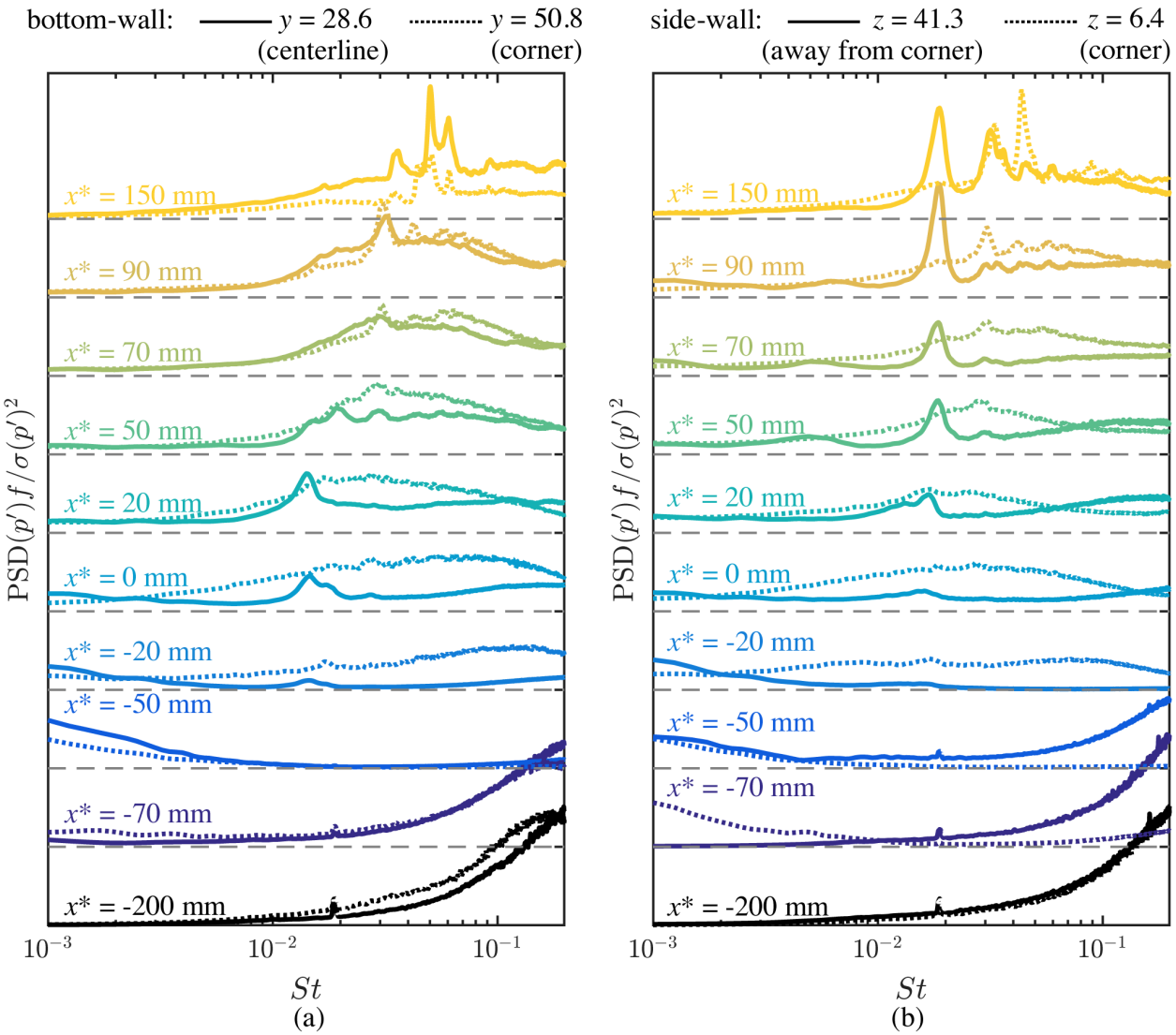

Figure 5.21: Evolution of the normalized power spectral density of pressure fluctuations as a function of Strouhal number. Pressure measured on the: (a) bottom-wall; (b) side-wall.

modes created by the side-wall separation bubbles are transmitted to the bottom-wall and evident in the power spectra.

A similar evolution in the power spectrum is evident for pressures measured near the corner on the side-wall (see figure 5.21(b)). That is, the power at low Strouhal numbers rises near the shock foot and then a peak centered at a Strouhal number of 0.03 develops through the separation bubble. Thus, both the bottom- and side-wall separations influence the normalized pressure power spectra in a similar manner. The pressures measured away from the corner on the side-wall do not directly pass through a separation bubble. Instead, the peaks in the power spectrum are due to perturbations M^+ and N^+ as well as perturbations generated elsewhere in the flow that influence the side-wall

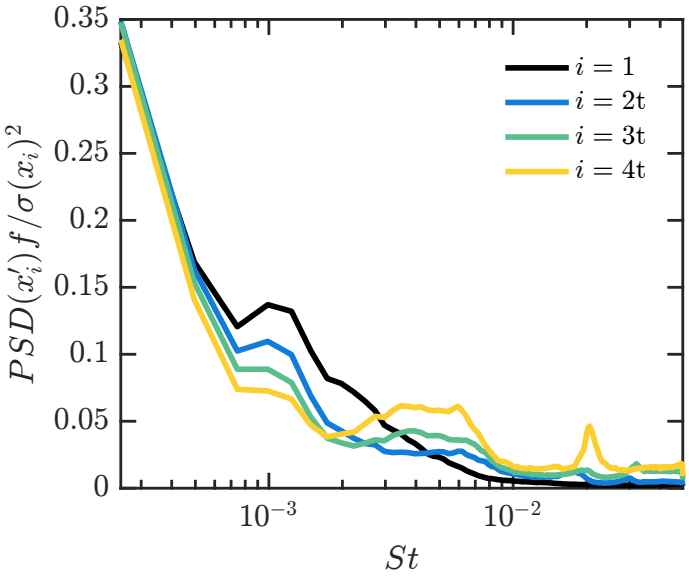

Figure 5.22: Normalized power spectral density of shock position fluctuations as a function of Strouhal number.

due to communication through the boundary layer.

The characteristic frequencies associated with the shock position fluctuations are scaled in the same way. Figure 5.22 shows the dimensionless shock position fluctuation power spectra as a function of Strouhal number. For clarity, only the results for x_1', x_{2t}', x_{3t}', and x_{4t}' are shown but similar results are obtained for the other shock position fluctuations. While there is some similarity in pressure power spectra, the shock train unsteadiness is drastically different from the unsteadiness observed in single SBLI experiments. Specifically, in a single SBLI, the shock fluctuates predominantly at a single frequency that corresponds to a Strouhal number of approximately 0.02 – 0.07 [Dussauge *et al.*, 2006; Oudheusden *et al.*, 2011]. In the case of the shock train, several modes are evident in the power spectra and the bulk of the shock motion is at very low frequencies (i.e., $St < 10^{-3}$). The additional modes are attributed to the fact that shock trains are influenced by multiple separation bubbles in addition to other types of perturbations (e.g., the acoustic waves originating from the diffuser section). The overall fluctuation amplitude of the shock train also differs from that of a traditional single SBLI. Dussauge *et al.* [2006] found that the shock oscillation amplitude is approximately 0.1 – 0.6 times the characteristic length scale L for a range of different single SBLI experiments. In comparison, the shock train observed here fluctuates up to $0.26H$ (or 18 mm) away from its time-averaged position. This corresponds to $2.4L$, a value significantly higher than the single SBLI cases. The difference in fluctuation amplitude is explained by the fundamental difference in the mechanism that generates the shocks. In single SBLI experiments, there is a physical structure in the flow that creates the shock wave and provides some stability to

the system. No such stabilizing structure exists for a shock train in a constant area duct. Instead, the shock train position is dictated by the back pressure condition. Thus, the shock train is located at a point in the isolator where the flow conditions and boundary layer properties allow for the downstream condition to be met.

5.7 Conclusions

Even when the bulk inflow and outflow conditions are constant, a shock train in a constant area duct exhibits inherent unsteadiness where it fluctuates about its time-averaged position. Shock train inherent unsteadiness has been observed in previous studies but the underlying mechanisms responsible for the unsteadiness have not been fully explored. This work specifically investigates the fluid phenomena that cause the inherent unsteadiness and links them to a complex, frequency-dependent dynamical system of perturbations that are present in the flow field and interact with the shock train.

To begin this work, the unsteadiness of the shock system is characterized. The results show that the amplitude and frequency content of position fluctuations are independent of pressure ratio. That is, these quantities do not depend on where the shock train is located for the range of conditions considered in this study. Thus, the underlying causes of the inherent unsteadiness are also expected to be independent of pressure ratio. It is also clear that consecutive shocks in the train have the same position fluctuation statistics (i.e., same average, maximum, and standard deviation). However, downstream shocks tend to fluctuate faster and exhibit high-frequency modes that indicate that the unsteady dynamics change through the shock train system.

Perturbations and their effects on the shock train are identified using cross-spectral analysis of shock positions and wall static pressure fluctuations. By investigating individual perturbations characterized by specific frequency ranges, important information describing the perturbation is identified, including where the perturbation originates, the propagation speed and direction of the perturbation as it travels through the isolator, and how the perturbation influences the shock system. Oil flow visualization and PIV measurements are used to identify the fluid feature associated with the perturbation and the fluid phenomenon that generates the perturbation. The following three perturbations are identified and studied in detail:

1. **Acoustic waves generated by separation bubble instabilities**: These acoustic waves are created by the dynamics of the various separation bubbles that exist within the shock train. For example, as the flow surrounding the separation bubble adjusts to a change in bubble size or position. For the flow conditions and isolator geometry of the current experiment, the acoustic waves form between shocks 1 and 2, then propagate upstream through the subsonic portion of the boundary layer at approximately 0.1–0.2 u_∞. The passage of the acoustic waves is

associated with wall static pressure fluctuations in the 0–3 kHz frequency range. Finally, the acoustic waves induce a displacement in the leading shock position as they pass the shock foot. Downstream propagating acoustic waves may also be generated by the separation bubble instabilities but they have negligible impact on the shock system.

2. **Vortices generated by the shear layer of the separation bubble**: These vortices shed from the separation bubbles and are convected downstream at approximately 0.27–0.55 u_∞. They are associated with wall static pressure fluctuations in the 0–3 kHz frequency range. The vortices persist for a significant distance, and thus are able to influence the positions of downstream shocks as they convect past each shock foot.

3. **Acoustic waves generated in the diffuser section**: These acoustic waves propagate upstream through the subsonic portion of the boundary layer at approximately 0.1–0.2 u_∞ and are associated with low frequency ($f < 300$ Hz) wall static pressure fluctuations. The acoustic waves do not influence the motion of the downstream shocks but do impact the leading shock position as they pass the shock foot.

Each of the three perturbations described above are found to have a direct and indirect influence on the unsteady motion of the shock train. A *direct influence* occurs when the perturbation causes a locally significant change in flow properties and as a result, the perturbation induces a shock displacement as it passes the shock foot. For example, the vortices generated by the separation bubble shear layer travel downstream and have a direct influence on the motion of all the downstream shocks that they pass. The acoustic waves (either generated in the diffuser or by the separation bubbles) only have a direct influence on the leading shock. The local effects of the acoustic waves are negligible in the downstream flow and thus do not impact the motion of the downstream shocks. This is attributed to the thick, distorted boundary layer that grows along the length of the shock train. In comparison, the thin, undisturbed boundary layer at the leading shock foot is more receptive to the disturbances created by the acoustic waves.

The shock motion due to the direct influence of the perturbation instigates a sequential displacement of the downstream shocks, referred to as the *indirect influence* of the perturbation. This process begins when the displacement of an upstream shock changes the flow structure of the expansion-compression region between shocks. In response, the downstream shock must move to satisfy the new inflow conditions and the required downstream pressure rise. The time delay between sequential shock motions corresponds to the response time of the flow structure. Ultimately, this flow response time should scale with the local wave speed and the size of the expansion-compression region. It is important to remember that the indirect influence is a consequence of the direct influence of the perturbation. Thus, without a direct influence there will be no indirect

influence. However, individual names are given for the two influences because they act on the shock system in different ways.

Overall, the shock train inherent unsteadiness is the result of the superposition of the direct and indirect influences of each perturbation. This superposition might not necessarily be linear since coupling between different perturbations may occur and lead to complex shock train dynamics. The system of perturbations described in this work were specifically identified for a shock train in a nominally Mach 2.0 flow through a constant area duct with an aspect ratio of approximately 1. Similar perturbation sources and mechanisms are expected in other experimental conditions but the exact details of the measured fluctuations may be different owing to the flow conditions and isolator geometry. For instance, the number, location, and size of the separation bubbles may change the nature of the generated acoustic waves and vortices. In addition, a different diffuser geometry may alter the frequency of the upstream propagating acoustic waves. To relate the induced fluctuations measured in this study to shock trains in other experimental conditions, a scaling argument for the shock train unsteadiness characteristics is attempted. In particular, the spectral characteristics of the shock position and wall static pressure are normalized using a Strouhal number based on a proposed length scale, $L = \theta/\sqrt{C_\theta}$. This scaling argument is inspired by the single SBLI experiments that share a similar unsteady separation bubble phenomenon. The shock train length scale is chosen because the fluid phenomena that cause inherent unsteadiness are associated with the boundary layer and are thus expected to scale with boundary layer properties such as the momentum thickness, θ. The confinement ratio, C_θ, is essentially a correction factor that takes the duct cross-sectional size into account. However, due to a lack of well documented measurements on shock trains generated under different conditions, the validity of this scaling on the spectral properties of the inherent unsteadiness cannot be proven unequivocally and additional work is required.

To conclude, we take a moment to compare this new shock train unsteadiness theory to the three previous theories in the literature (see chapter 1.4). Recall the first theory where Ikui *et al.* [1974*b*] hypothesized that the incoming turbulence induces the consecutive motions of shocks. In the current study, cross spectral analysis showed that the upstream pressure fluctuations are uncorrelated with the pressure fluctuations measured under the shock system. Thus, the source of the perturbation was disproved. However, their observation that the shocks respond in sequential order agrees with the observations of the current study.

In the second theory, proposed by Yamane *et al.* [1984*a*,*b*], it was hypothesized that the oscillation of the air column in the diffuser section induces upstream propagating acoustic waves that influence the shock system. Due to the broadband nature of the downstream pressure fluctuations and the narrowband nature expected from a pipe resonance, this source of unsteadiness is discredited. However, the speed of the perturbation is similar in both the previous work by Yamane *et al.*

[1984*a*,*b*] and the current work, leading to the hypothesis that the physical structure of the perturbation is an acoustic wave (note that this is called perturbation D^- in the current work). Yamane *et al.* [1984*a*,*b*] also found evidence of a downstream propagating perturbation but did not identify any information about this perturbation other than its direction and speed of 230 m/s. Given the relatively low-speed of this perturbation, it is possible that these are vortices shed from a separation bubble, similar to perturbation S^+ that has been observed in the current work.

Finally, recall the theory of Sugiyama *et al.* [1988]. They hypothesized that the shock train unsteadiness is induced by the oscillation of the separated boundary layer. That is, a throat is formed between the first shock and second shock owing to the boundary layer displacement thickness change in the flow direction. This is similar to the hydrodynamic effect used to explain perturbations M^+ and N^+ in the current work, which were not discussed or analyzed in detail due to diagnostic limitations on the side-wall and lack of evidence from the measurements that could be collected. However, this hydrodynamic argument is strong and has not been disproved by our current results. In addition, we propose that Sugiyama *et al.* [1988] found a weak correlation between the boundary layer height and the shock motion for two reasons: 1) it is difficult to consistently identify the height of a turbulent boundary layer with schlieren imaging and 2) the Sugiyama *et al.* [1988] measurements were limited to low frequencies (less than 500 Hz) whereas the current work indicates that the hydrodynamic effect is associated with higher frequencies (in the 1 – 3 kHz range). Nonetheless, more research is needed to clarify the details of this perturbation source.

From the above discussion it is clear that many aspects of the current work support arguments previously discussed in the literature. What is unique about this work is that the cross spectral analysis lets us decompose the measured fluctuations to identify multiple different types of perturbations, thus pulling together the existing theories. In addition, strong evidence is given to identify the underlying flow phenomena that cause the perturbations. We have also uncovered how perturbations travel through the system and interact with shocks by clarifying the direct and indirect influences.

Chapter 6

Forced Dynamics of Shock Trains

The boundary conditions of the isolator are not necessarily constant during the typical operation of a high-speed air-breathing engine. For example, transient combustion processes can occur in the initial ignition stage or as the fueling scheme changes during the desired flight trajectory. The goal of this chapter is to evaluate the shock system response to oscillatory downstream forcing. Unlike the rest of the work in this thesis, the data acquired in this chapter are collected as the downstream pressure changes due to a change in the control valve angle. The effects of two forcing parameters are specifically considered: the magnitude of the downstream disturbance (i.e., how much the valve angle changes) and the rise time of the disturbance (i.e., the time it takes for the valve to change angles). In all of these cases the maximum downstream pressure is kept below a certain value such that the flow remains started.

First, the forcing scheme is described in section 6.1. This includes a detailed examination of the imposed disturbance time history, which is important to characterize in order to understand the shock train response in relation to the change in downstream condition. In section 6.2, the shock train response is compared over a range of disturbance magnitudes and rise times. Many interesting phenomena are discussed in this section including the hysteresis effect and the diminished shock train response observed for short disturbance rise times.

6.1 Description of the Forcing Scheme

6.1.1 Definition of Disturbance Magnitude and Rise Time

Downstream forcing is introduced by periodically changing the angle of the control valve. An example time trace of the valve angle is shown in figure 6.1. Two features of the shock train are examined during the forcing process: 1) the leading shock position, x_1, and 2) the back pressure measured at the end of the isolator, p_b.

For every run, a shock train is first stabilized in the isolator by partially closing the control valve to an initial angle Θ_d. This valve angle establishes a desired back pressure, $p_{b,d}$, and leading

shock position, $x_{1,d}$. Then, over a designated amount of time, T_Θ, the valve closes to a new angle, Θ_u, such that downstream area for airflow is reduced. The following occur as a result of the valve angle transition: 1) the pressure in the diffuser increases, 2) the shock train moves upstream to a new location in the isolator, $x_{1,u}$, and 3) the back pressure increases to a new value, $p_{b,u}$. Once the valve reaches its final state, a time Δt passes before the valve opens back to the original angle, Θ_d. This opening/closing process is repeated at a frequency Ω for several cycles such that $\Omega = 1/[2(T_\Theta + \Delta t)]$. In response to the applied forcing, the back pressure oscillates between two values: $p_{b,d}$ and $p_{b,u}$. In addition, the leading shock oscillates between two positions in the test section: $x_{1,d}$ and $x_{1,u}$. Figures 6.2(a) and 6.2(b) schematically illustrate the $x_{1,d}$ and $x_{1,u}$ positions of the leading shock in the isolator section during this forcing process, respectively.

Notice the choice of subscripts in the previous discussion are conveniently used to indicate the state of the system. These subscripts are chosen based on the location of the shock train: "d" stands for "downstream" and "u" stands for "upstream". For example, $x_{1,d}$ is the downstream shock position and $x_{1,u}$ is the upstream shock position. Throughout this chapter, the transition from the downstream state to the upstream state is denoted as $d \rightarrow u$. Conversely, the upstream to

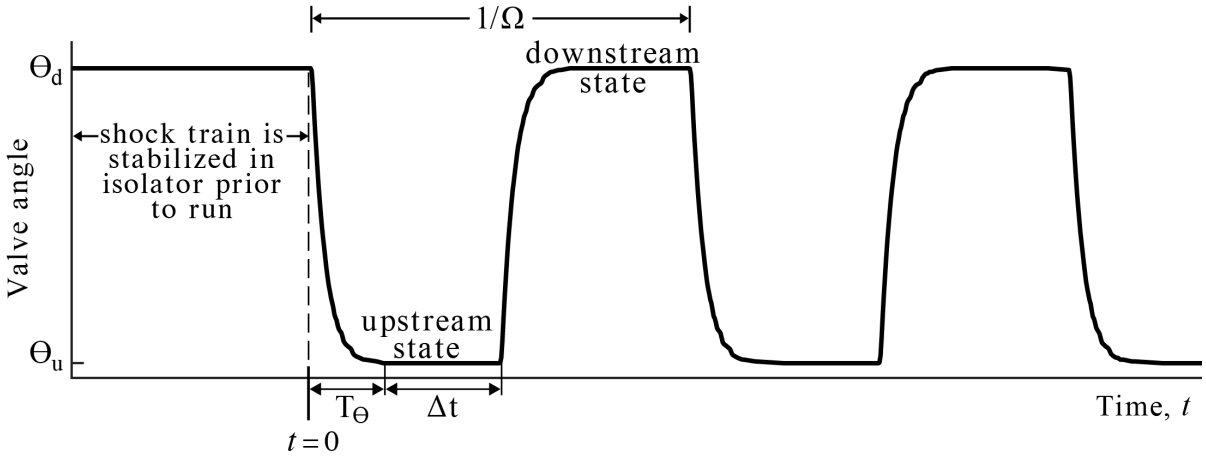

Figure 6.1: Example time trace of the valve angle.

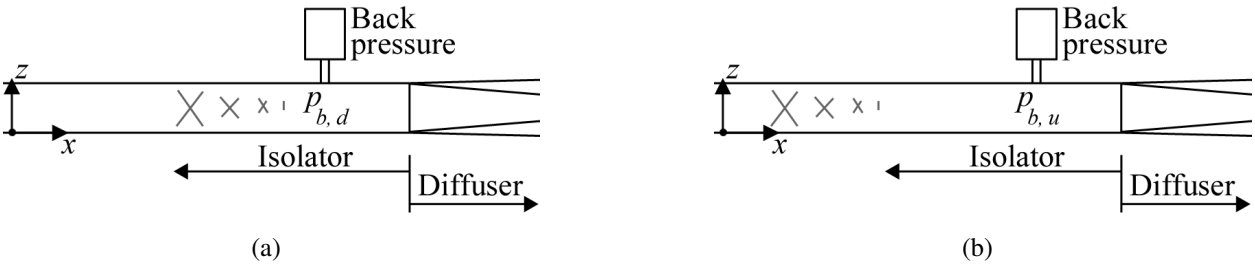

Figure 6.2: Schematic of the shock train location: (a) downstream state (i.e., when $\Theta = \Theta_d$); (b) upstream state (i.e., when $\Theta = \Theta_u$).

downstream transition is denoted as $u \rightarrow d$.

For this work, T_Θ is referred to as the *disturbance rise time*, i.e., how long it takes for the change in diffuser pressure to occur. This value is quantified using the time trace of the valve angle which is measured using an optical encoder. To compare the disturbance rise time to the natural dynamics of the shock system, we define a characteristic time of the inherent unsteadiness, T_c, as follows. From the quasi-steady state data analyzed in chapter 5, the root mean squared value of the shock position fluctuations, x_c', is found to equal 4.2 mm. The root mean squared speed of the shock as it fluctuates, u_c, is equal to 3.2 m/s. These values are defined as the characteristic fluctuation amplitude and speed, respectively. The ratio of these quantities, x_c'/u_c, describes the time scale of the inherent unsteadiness and is equal to approximately 1.3 ms. Thus, the quantity T_Θ/T_c describes how fast the forcing is relative to the natural dynamics of the system. The characteristic fluctuation amplitude, speed, and time of the inherent unsteadiness will be used in the analysis throughout this chapter.

The change in valve angle, $\Delta\Theta$, is referred to as the *magnitude of the disturbance*. Essentially, the valve angle describes the size of the throat that mechanically chokes the exit of the diffuser and drives the downstream pressure rise. Therefore, it is more physically meaningful to think of the valve angle in terms of the cross-sectional area blocked by the valve. For the circular valve plate used in the work, the projected cross-sectional area is: $A_B = \pi r^2 \cos\Theta$, where r is the radius of the valve plate. We present the cross-sectional area blocked by the valve, A_B, as a fraction of the total cross-sectional area of the diffuser, A_d: i.e., $B = A_B/A_d$. Thus, the magnitude of the disturbance, $\Delta\Theta$, can then be thought of in terms of a change in blockage area ratio: $\Delta A_B/A_d = \Delta B$.

6.1.2 Summary of Forcing Run Conditions

Shock trains are complex systems, so the forcing mechanism described above is designed to be simple in order to better identify the underlying physics. In this work, the shock train response is analyzed for ten different runs with different disturbance magnitudes and rise times. The conditions for each run are summarized in table 6.1.

The disturbance magnitude, $\Delta\Theta$, is varied between 0.37–1.84°. The corresponding change in the blockage area ratio, ΔB, is equal to 0.0058–0.0292. Note that these are very small changes which emphasize that the shock train system is highly sensitive to downstream disturbances. The disturbance rise time is varied between 50–157 ms. These values are approximately 38–121 times the characteristic time scale of the shock train inherent unsteadiness. Thus, the forcing is relatively slow compared to the natural dynamics of the system. Unfortunately, the valve is not capable of smaller rise times so our analysis is restricted. However, current capabilities of the control valve are sufficient to mimic the slow transient processes that might be present in a real high-speed air-breathing engine. Some runs described in table 6.1 have the same disturbance rise time but

Run	Ω, Hz	Δt, ms	$\Delta t/T_c$	T_Θ, ms	T_Θ/T_c	$\Delta\Theta$, deg	ΔB
1	9.99	1	0.8	49	38	0.79	0.0124
2	7.14	1	0.8	69	53	0.37	0.0058
3	7.14	1	0.8	69	53	1.00	0.0158
4	7.13	1	0.8	69	53	1.54	0.0245
5	5.02	2	1.5	98	75	0.43	0.0068
6	4.97	3	2.3	98	75	1.19	0.0186
7	5.00	2	1.5	98	75	1.84	0.0292
8	3.33	22	16.9	128	98	1.29	0.0213
9	2.00	93	71.5	157	121	0.49	0.0077
10	2.00	93	71.5	157	121	1.34	0.0221

Table 6.1: Summary of forcing run conditions.

different disturbance magnitudes. Thus, the rate at which the disturbance is applied to the system is different for these runs; the effects of which are studied later on in the chapter.

In addition to the disturbance magnitude and rise time, differences between forcing cases emerge due to limitations of the valve control mechanism. Specifically, the rise time of the disturbance is a function of the forcing frequency as seen in figure 6.3 and these two parameters cannot be decoupled. That is, both T_Θ and Ω cannot be independently controlled. For our run conditions, the forcing frequency, Ω, is varied between 2.00 – 9.99 Hz. As a result, Δt relatively short (less than 3 ms or $2.3T_c$) for runs with low disturbance rise times where $T_\Theta < 100$ ms. However, Δt increases to approximately 93 ms (or $71.5T_c$) for $T_\Theta = 157$ ms. Despite this, we are interested in the system dynamics during the transition between states and the differences in Δt do not impact the results discussed later on.

6.1.3 Time History of the Blockage Area Ratio

Before examining the shock train response to forcing, the time history of the the blockage area ratio is compared across all of the forcing cases. It is important to characterize the disturbance in order to understand the shock train response in relation to the change in downstream condition.

First, consider runs with the same rise time, T_Θ, but different disturbance magnitudes, ΔB. Here, we specifically look at runs 6 and 7 as examples. Note that the disturbance rise time is approximately $75T_c$ for both of these runs but the magnitude of the disturbance is 1.6 times greater in run 7. To adjust for different ΔB, the blockage area ratio is normalized from 0 to 1 as follows:

$$\widetilde{B} = \frac{B - \min(B)}{\max(B) - \min(B)} \tag{6.1}$$

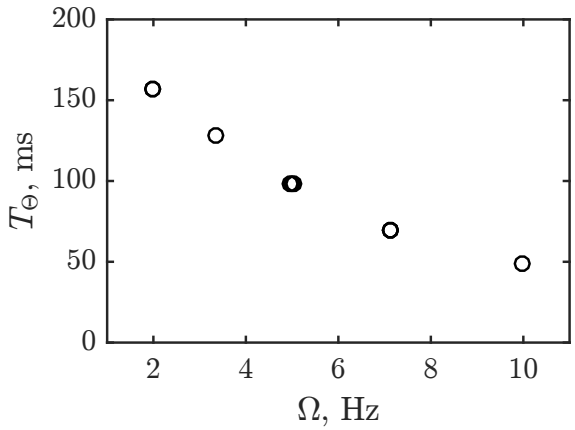

Figure 6.3: Disturbance rise time as a function of the valve forcing frequency.

Thus, $\widetilde{B} = 1$ when the area blockage is at a maximum and the shock system is at its upstream state. Conversely, $\widetilde{B} = 0$ when the area blockage is at a minimum and the shock system is at its downstream state. Figure 6.4 compares the time history of the normalized blockage area ratio, $\widetilde{B}$, as it increases and decreases for runs 6 and 7. The time shown on the x-axis is referenced from the onset of the valve angle change and is normalized by the disturbance rise time. Thus, $t/T_\Theta = 0$ at the beginning of the valve angle transition and $t/T_\Theta = 1$ at the end of the valve angle transition. Each plotted curve is a representative example of the $\widetilde{B}$ time history for a single transition but the results for the other transitions during the run are nearly identical (i.e., the maximum deviation

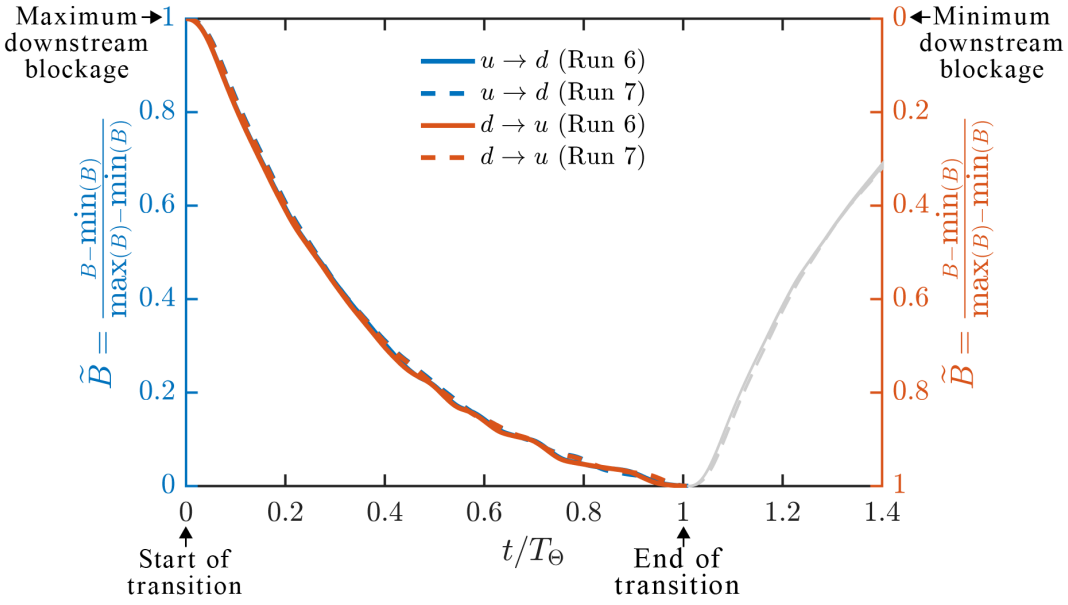

Figure 6.4: Comparison of the blockage area ratio time history for runs 6 and 7.

from the curve shown is less than 0.1%). The blue lines represent the $u \rightarrow d$ transition and the orange lines represent the opposite transition ($d \rightarrow u$). The gray lines represent the $\widetilde{B}$ time history during the next transition. Also note that the direction of the y-axis is reversed for the downstream to upstream transition in order to directly compare the time histories. With this in mind, figure 6.4 demonstrates that the time history of the blockage area ratio is the same regardless of which direction the valve is moving. The identical time histories of B allow a direct comparison of the shock train system response as it moves upstream and downstream because the forcing mechanism is the same.

Figure 6.4 also demonstrates that the time history of the normalized blockage area ratio for runs 6 and 7 are nearly identical. We find that this is generally true across all the cases. That is, the time history of $\widetilde{B}$ does not depend on the overall magnitude of the disturbance, ΔB. However as we will see later in this section, the time history of $\widetilde{B}$ does depend on T_Θ.

Clearly, the time rate of change of B (i.e., the speed at which the disturbance is imposed onto the system) differs for runs 6 and 7 because ΔB is different for these runs but T_Θ is the same. To formalize this idea, the time rate of change of the blockage area ratio, $|\mathrm{d}B/\mathrm{d}t|$, is calculated from the time-history measurements of B as the central difference between values. The results, normalized by the characteristic time scale of the inherent unsteadiness, T_c, are shown in figure 6.5. Note that only the $u \rightarrow d$ transition is shown but the same result is observed for the opposite transition. As expected, the blockage area ratio has a higher rate of change for run 7 compared to run 6. For comparison, the maximum value of $|\mathrm{d}B/\mathrm{d}t|$ is $6.1 \times 10^{-4}/T_c$ and $9.4 \times 10^{-4}/T_c$ for runs 6 and 7, respectively. While these rates differ for runs 6 and 7, the identical time histories of

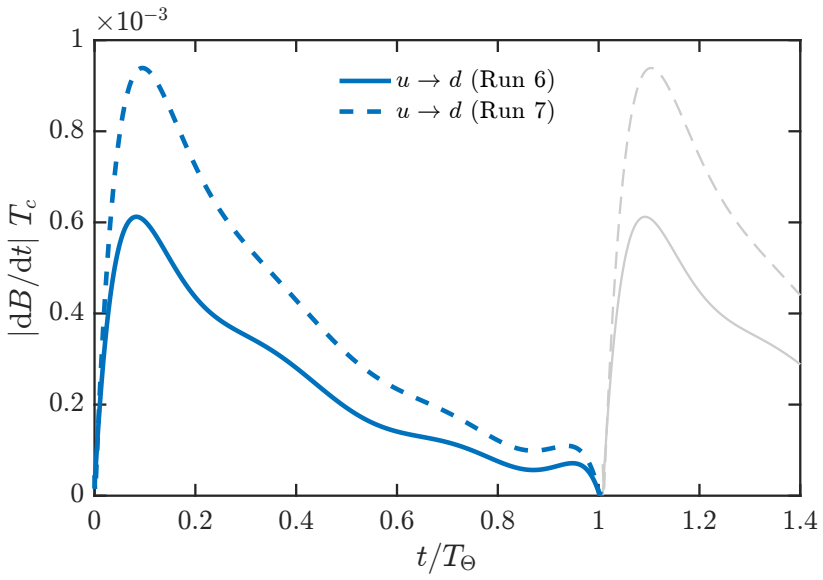

Figure 6.5: Example time histories of the blockage area ratio rate of change.

the normalized blockage area ratio allow a direct comparison of the shock train system response for runs with different ΔB but the same T_Θ.

Generally, the maximum rate of the blockage area ratio is proportional to the disturbance magnitude and rise time as follows:

$$|\mathrm{d}B/\mathrm{d}t| = c\frac{\Delta B}{T_\Theta} \tag{6.2}$$

where c is a proportionality constant. We find that c is a function of the disturbance rise time, T_Θ, as demonstrated by figure 6.6. Thus, for runs with the same disturbance rise time but different disturbance magnitude (e.g., runs 6 and 7 which have been thoroughly discussed in this section) have the same proportionality constant, c. Note that this relationship is specific to the control valve used in these experiments.

To understand why c varies across the different forcing conditions, consider the time history of the blockage area ratio for all 10 runs, shown in figure 6.7. Clearly, the disturbance rise time has a large impact on $\widetilde{B}$. For example, runs with a large disturbance rise time exhibit a higher $|\mathrm{d}B/\mathrm{d}t|$ at the beginning of the transition and a lower $|\mathrm{d}B/\mathrm{d}t|$ at the end of the transition compared to cases with low disturbance rise times. Thus, these differences must be accounted for when comparing cases with different disturbance rise times.

6.2 Shock Train Response to Forcing

The change in blockage area ratio sends disturbances upstream through the diffuser that ultimately effect the shock train. Multiple responses in the isolator are measured: 1) the back pressure measured at the end of the isolator, p_b, and 2) the location of the leading shock, x_1. For example, figure

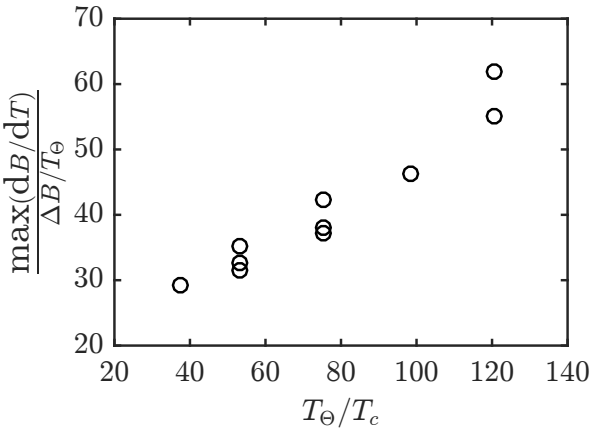

Figure 6.6: The maximum instantaneous rate of change in blockage area ratio versus the disturbance rise time.

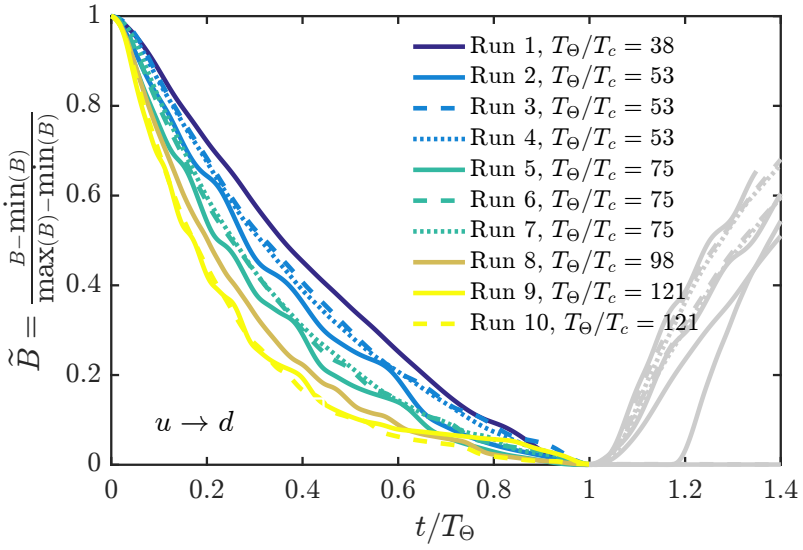

Figure 6.7: Comparison of the blockage area ratio time history for all ten runs.

6.8 shows a portion of the back pressure and shock position time traces for run 7. As back pressure increases, the shock train moves upstream (i.e., x_1 becomes smaller). Conversely, the shock train moves downstream as back pressure is decreased. For this run, the shock train does not stay in a particular state for a long period of time. That is, once the leading shock reaches its most upstream position it immediately changes direction and moves back downstream. Longer periods of quasi-steady state behavior (when the blockage area ratio is approximately constant) are observed for cases with higher disturbance rise times where $\Delta t/T_c \gg 1$.

6.2.1 Inherent Unsteadiness Superimposed Onto the Bulk Motion of the Shock Train

As demonstrated by figure 6.8, both the shock position and back pressure time traces exhibit low-magnitude fluctuations due to the inherent unsteadiness of the shock train system. These fluctuations are also higher frequency than the imposed oscillatory forcing (because $T_c \ll T_\Theta$). Averaging multiple cycles during a run essentially filters out the fluctuation component of the signal associated with the inherent unsteadiness. Thus, the resulting cycle-averaged curves describe the time history of the low-frequency, high-magnitude bulk shock train response due to the imposed forcing only. Figure 6.9 demonstrates this idea by comparing the time-resolved shock position time trace and the cycle-averaged time trace for run 7.

Before examining the bulk motion of the shock train, the inherent unsteadiness during forcing is compared to the inherent unsteadiness exhibited during quasi-steady state (i.e., when the control valve angle is kept constant and thus the pressure in the diffuser is approximately constant as well). To do so, the cycle-averaged time trace is subtracted from the time-resolved shock position

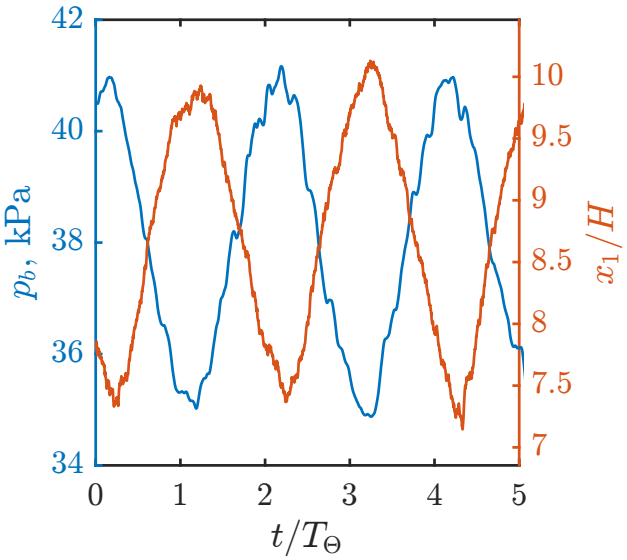

Figure 6.8: Example time traces of the back pressure and shock position response to forcing (run 7).

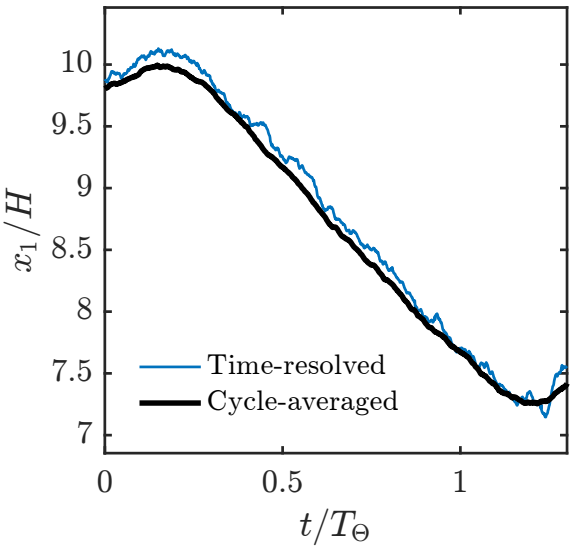

Figure 6.9: Comparison of a single transition to the cycle-averaged transition (run 7).

time trace. For comparison, the fluctuation component of the quasi-steady state cases is found by subtracting the constant, time-averaged value of the shock position. Thus, the low magnitude leading shock fluctuations of the quasi-steady state cases and the forcing cases can be directly compared.

Figure 6.10 consists of two histograms which demonstrate the similarities between the inher-

ent unsteadiness component of the signal for run 7 of the forcing cases and a single quasi-steady state case under similar back pressure conditions. Part (a) of the figure compares the shock position fluctuation magnitudes. Part (b) of the figure compares the speed of the leading shock as it fluctuates. Both quantities are normalized by the characteristic scales of the inherent unsteadiness (which are equal to the root mean squared values of the quasi-steady state cases). Many features of each histogram are nearly identical for the forcing and quasi-steady state cases. That is, both types of run conditions exhibit similar inherent unsteadiness statistics. For example, the maximum shock position fluctuation is roughly $3.8x_c'$ away from the cycle averaged curve for forcing run 7. This quantity is approximately the same as the maximum displacement of the shock from its time-averaged location during quasi-steady state.

In the above examples, forcing run 7 is used but the results are similar for other runs. Across all of the forcing conditions, the standard deviation and maximum values of shock position fluctuation amplitude deviate from the corresponding quasi-steady state values by less than $0.2x_c'$ and $0.7x_c'$, respectively. These differences are insignificant compared to the measurement accuracy of the schlieren feature detection algorithm (which is equal to $0.5x_c'$). Similarly, the standard deviation and maximum values of shock speed deviate from the corresponding quasi-steady state values by less than $0.2u_c$ and $1.7u_c$, respectively.

Figure 6.11 shows that the power spectral densities of the fluctuations caused by inherent unsteadiness are the same for forcing and quasi-steady state cases. Once again, forcing run 7 is used in this example but the results are approximately the same across all of the forcing cases.

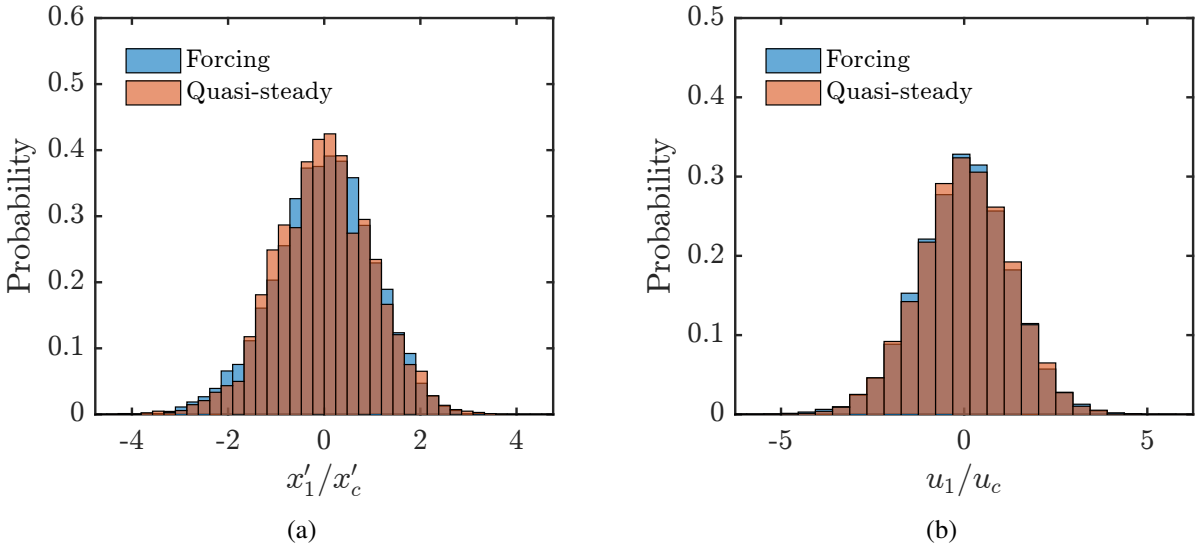

Figure 6.10: Probability density functions of: (a) shock position fluctuations due to inherent unsteadiness; (b) speed of the leading shock as it fluctuates.

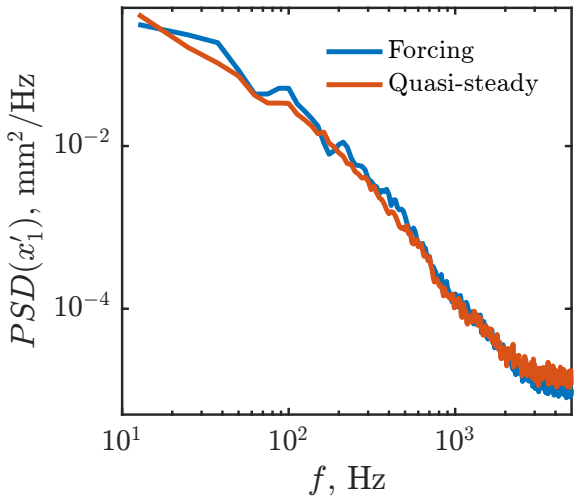

Figure 6.11: Power spectral density of the shock fluctuations.

There are two important results from the above observations. First, the power spectrum and many of the statistics describing the inherent unsteadiness are approximately the same for the forcing and quasi-steady state cases. Second, these measured metrics do not noticeably change across our range of forcing conditions. Thus, we argue that the component of the shock motion due to inherent unsteadiness is independent of the forcing parameters. This implies that the properties of the perturbations that cause inherent unsteadiness (e.g., the vortices and acoustic waves generated by the separation bubbles, etc.) do not appreciably change when the shock train changes position. This is also consistent with the results of chapter 5 (see figures 5.3(a) and 5.3(b), for example) that show many of the statistics of the unsteady behavior are, for the most part, insensitive to back pressure. As a result, the fluctuation component due to inherent unsteadiness is simply superimposed onto the bulk motion of the shock train when forcing is applied.

6.2.2 Example of the Shock Train Bulk Response to Forcing: Runs 6 and 7

We now consider the bulk shock train response to forcing by examining the cycle-averaged time history of back pressure and leading shock position. The results of runs 6 and 7 are used as examples in this section for the purpose of illustrating the key features of the shock train response. Then, the discussion and analysis is opened up to the other forcing cases in the following sections.

Recall that runs 6 and 7 have the same disturbance rise time ($T_\Theta = 75T_c$) but different disturbance magnitudes, ΔB. In run 6 the blockage area ratio changes by 0.0186 and in response the cycle-averaged back pressure changes by 3.96 kPa (a 10.7% increase from the original value of the back pressure at the downstream state, $p_{b,d}$) and the cycle-averaged shock position changes by

$32x_c'$. In run 7 the blockage area ratio changes by 0.0292 and in response the cycle-averaged back pressure and shock position change by 6.00 kPa (a 17.1% increase of $p_{b,d}$) and $45x_c'$, respectively. Note that the shock displacement induced by the forcing is significantly larger than the shock fluctuations caused by the inherent unsteadiness of the system. Clearly, the shock train system is sensitive to the blockage area ratio for these runs because the relative change in area is substantially smaller than the resulting change in back pressure and shock position. For the conditions of runs 6 and 7, $(\Delta p_b/p_{b,d})/\Delta B$ = 5.76 – 5.86 and $(\Delta x_1/x_c')/\Delta B$ = 1539 – 1717. These quantities are compared over a wider range of $\Delta\Theta$ and T_Θ in section 6.2.4.

To directly compare the results of different runs, the cycle-averaged time histories of x_1 and p_b are normalized between 0 and 1 as follows:

$$\widetilde{\eta} = \frac{\eta - \min(\eta)}{\max(\eta) - \min(\eta)} \tag{6.3}$$

where η is the parameter of interest. Thus, the minimum and maximum points of the cycle-averaged curves correspond to normalized values of 0 and 1, respectively. Figures 6.12 and 6.13 show the time history of the normalized cycle-averaged back pressure and shock train position, respectively, for runs 6 and 7. Just like figure 6.4, the time shown on the x-axis is referenced from the onset of the valve angle change and is normalized by the disturbance rise time. The blue lines represent the transition from $\Theta_u \rightarrow \Theta_d$ and the orange lines represent the $\Theta_d \rightarrow \Theta_u$ transition. The gray lines represent the time history during the next transition. In addition, the direction of the y-axis is reversed for the downstream to upstream transition in order to easily compare the $u \rightarrow d$ transition to the $d \rightarrow u$ transition.

Consider the cycle-average back pressure response shown in figure 6.12. All four curves have approximately the same time history. This implies that the normalized back pressure response is the same for: 1) runs with the same T_Θ but different ΔB, and 2) the $u \rightarrow d$ and $d \rightarrow u$ transitions of the same run. Thus, $\widetilde{p_b}$ transitions from one state to the next in a predictable manner based on $\widetilde{B}$ and it does not depend on the magnitude of the disturbance, ΔB. Runs 6 and 7 have the same normalized back pressure response because they also share the same $\widetilde{B}$ time history.

Figure 6.12 also demonstrates that the start of the back pressure response is delayed from the onset of the valve motion by an amount τ_{pb}, which for these runs is approximately 16 ms ($12.3T_c$). For the $u \rightarrow d$ transition, τ_{pb} is defined as the first point in time after the onset of the valve motion where $\widetilde{p_b} < 0.995$ and $\widetilde{p_b}$ is decreasing. Conversely, τ_{pb} is defined for the $d \rightarrow u$ transition as the first point in time after the onset of the valve motion where $\widetilde{p_b} > 0.005$ and $\widetilde{p_b}$ is increasing. In a similar manner, the end of the back pressure transition is defined as the first point after the onset of the valve transition where $\widetilde{p_b} < 0.005$ and $\widetilde{p_b} > 0.995$ for the $u \rightarrow d$ and $d \rightarrow u$ transitions, respectively. The time it takes for the back pressure to transition from its initial state to its final

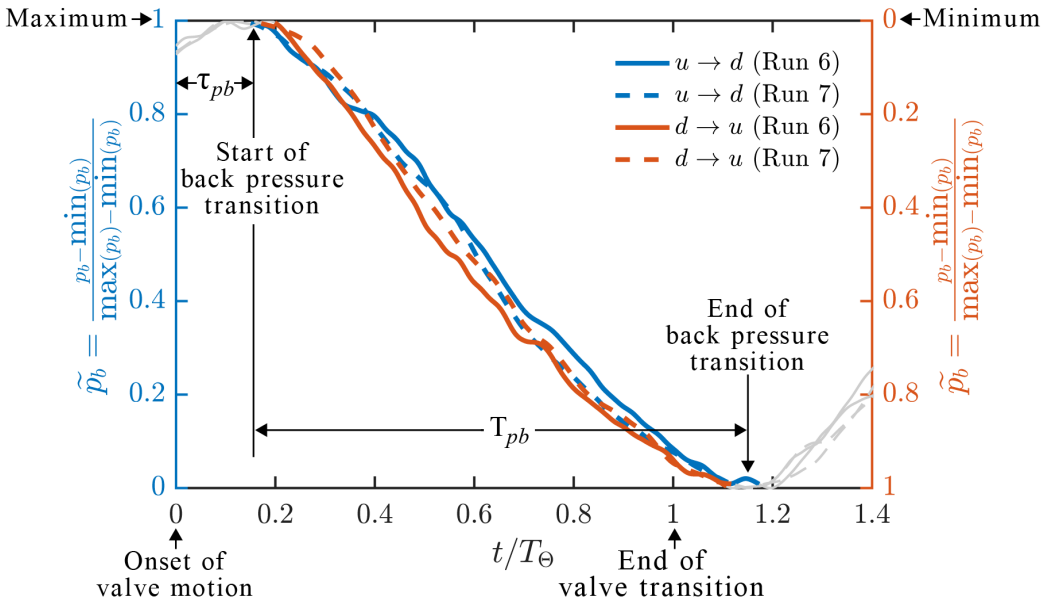

Figure 6.12: Back pressure response to forcing.

state, T_{pb}, is thus determined using the times at which transition begins and ends as defined above. For runs 6 and 7 we find that the back pressure rise time is approximately equal to the disturbance rise time (90 – 100 ms or equivalently $69T_c$ – $77T_c$).

Now consider the cycle-averaged shock position response shown in figure 6.13. Just like the back pressure, the shock position response is delayed from the onset of the valve motion. Using similar definitions to the ones described above, we define the delay time of the shock position response, τ_{x1}, and the rise time of the shock position response, T_{x1}. For runs 6 and 7, T_{x1} is approximately equal to T_Θ (i.e., $75T_c$). In addition, τ_{x1} is 26 ms (i.e., $20T_c$) and 23 ms ($18T_c$) for the $u \rightarrow d$ and $d \rightarrow u$ transitions, respectively. Interestingly, the shock train follows slightly different trajectories during the $u \rightarrow d$ and $d \rightarrow u$ transitions as demonstrated by the difference between the blue and orange lines. That is, the shock train position oscillates by the same amount in both transitions but there is a hysteresis effect such that the path traveled by the shock train differs. Thus, the location of the shock train is a function of the blockage area ratio time history and the direction in which the shock train is moving.

As a final comment on figure 6.13, note that there is no evidence of overshoot as the shock train reaches its final state. Hoeger *et al.* [2011] observed overshoot in their computational model with a disturbance rise time of 10 ms. Their results suggest that the overshoot is a function of the rate at which the control surface changes. Thus, the lack of overshoot in the current experiments could be due to the relatively slow disturbance. The properties of the shock train response defined in this section are quantified for the other forcing cases and discussed more thoroughly in the

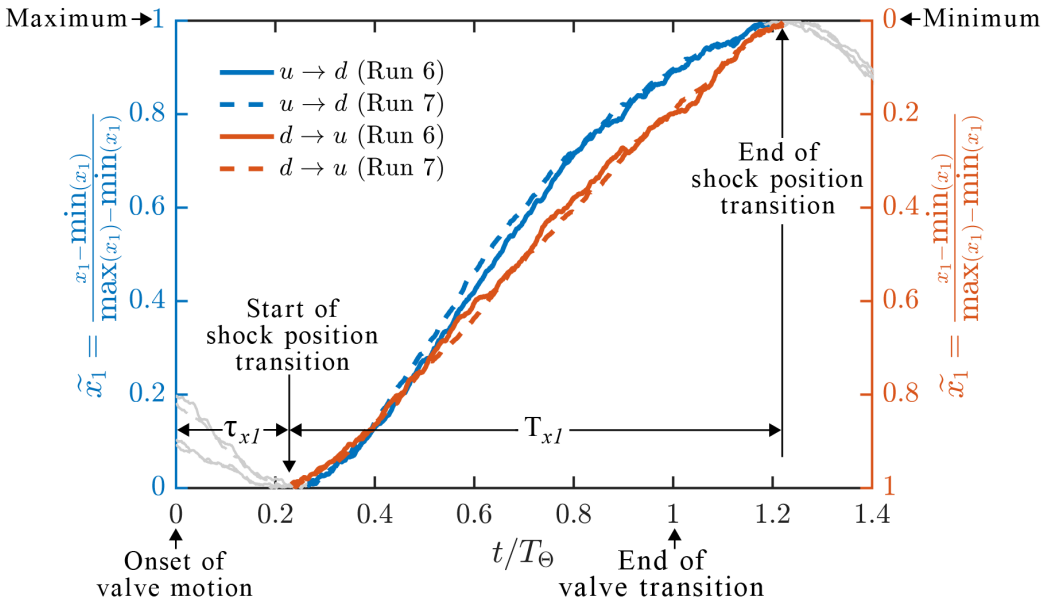

Figure 6.13: Shock train position response to forcing.

following sections. Specifically, the dependence of the response rise times on the disturbance rise time is explored in section 6.2.3. The magnitude of the shock train response in relation to the forcing parameters is examined in section 6.2.4. Next, the delay times are analyzed in section 6.2.5. Finally, the hysteresis effect is examined further in section 6.2.6 and a clearer relationship between the shock trajectory and the forcing parameters (ΔB and T_Θ) is established.

6.2.3 Rise Times of the Shock Train Response

In the previous section we found that the shock position rise time equals the back pressure rise time and the disturbance rise time for runs 6 and 7: $T_{x1} = T_{pb} = T_\Theta$. We now analyze these rise times for other forcing cases. Consider figure 6.14(a) which shows how the normalized shock position rise time, T_{x1}/T_c, varies with the normalized disturbance rise time, T_Θ/T_c. The dashed line indicates where $T_{x1} = T_\Theta$. Across our range of forcing conditions, the first order response of the shock train takes approximately the same amount of time to transition between states as the imposed disturbance. For the highest value of T_Θ, there is more scatter in the results and it appears that T_{x1} is slightly less than T_Θ. This is possibly due to the fact that less cycles are available to construct the cycle-averaged curve and thus the contribution from inherent unsteadiness may be slightly impacting the results. In addition, recalling figure 6.7, the forcing cases with a higher disturbance rise time have a long 'tail' at the end of the disturbance time history. That is, B varies vary slowly at the end of the cycle. As a result, the speed of the shock is also slow during this time period, making the clear end of the cycle harder to detect. For these reasons, additional

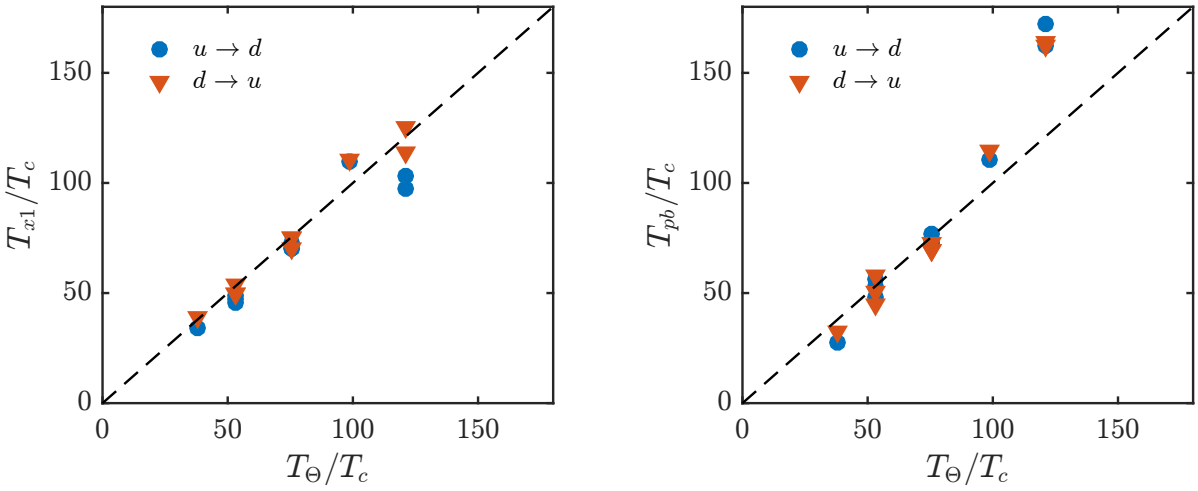

(a) (b)

Figure 6.14: Shock train response rise times versus the disturbance rise time: (a) shock position rise time; (b) back pressure rise time.

experiments are needed to clarify how the rise time of the shock train response varies for cases with long disturbance rise times.

Figure 6.14(b) shows how the normalized back pressure rise time, T_{pb}/T_c, varies with the normalized disturbance rise time, T_Θ/T_c. Once again, the dashed line indicates where these quantities are equal. Generally, for lower disturbance rise times we find that $T_\Theta = T_{pb}$. However, for higher disturbance rise times $T_\Theta < T_{pb}$. For the same reasons discussed in the previous paragraph, it is unclear if the data points at higher disturbance rise times are accurate.

Now consider the case of a very low disturbance rise time. In the limit, a disturbance may be instantaneously applied and thus $T_\Theta = 0$. In this case, it is physically unreasonable to think that the rise times of the responses are also zero because it takes time for the shock train to propagate upstream. This is either a convective or diffusive process, for example, related to the acoustic speed. In addition, viscous effects of the boundary layer can lengthen the time it takes the shock train to propagate to a new position. Thus, we hypothesize that T_{x1} and T_{pb} are greater than T_Θ as T_Θ is reduced to zero.

6.2.4 Sensitivity of the Shock Train Response

As seen previously, the magnitude of the shock train position and back pressure responses can be highly sensitive to the change in blockage area ratio. That is, small changes in the area blocked by the control valve tend to produce large shock train motions and back pressure changes. However, when comparing all of the forcing cases it is evident that the magnitude of the response also

depends on the disturbance rise time, T_Θ, and is not solely a function of ΔB.

The sensitivity of the system is defined as the ratio of the response magnitude to the disturbance magnitude. That is, the shock position sensitivity is equal to $(\Delta x_1/x_c')/\Delta B$. Similarly, the back pressure sensitivity is equal to $(\Delta p_b/p_{b,d})/\Delta B$. Figure 6.15 demonstrates that these sensitivities vary with disturbance rise time. As the disturbance rise time is decreased the system becomes less sensitive. Assuming a linear relationship, the sensitivity of the shock train location drops to a minimum value of 650 (i.e., $\Delta x_1/x_c' = 650\Delta B$) when the disturbance is instantaneously applied. The motion due to forcing will be indistinguishable from the inherent unsteadiness when $\Delta x_1 < x_1'$. This corresponds to a change in blockage area ratio less than 0.0015. For comparison, ΔB is varied between 0.0058 and 0.0292 in this study.

The sensitivity analysis yields two important conclusions that connect the dynamics of the forcing cases shown in this chapter to the dynamics of the shock train inherent unsteadiness. First, it emphasizes that the shock train can be impacted by small downstream disturbances even when the disturbance is instantaneously applied. Thus, it is plausible that downstream disturbances, for example turbulence in the diffuser, are capable of contributing to the shock system inherent unsteadiness. As seen previously in the inherent unsteadiness studies, acoustic waves travel upstream from the diffuser and interact with the shock system. The results of the forcing studies reinforce this idea. The second important result from the sensitivity analysis is that high frequency disturbances (i.e., disturbances with a short rise time) are damped out. This explains why the acoustic waves in the inherent unsteadiness studies are only associated with low frequency fluctuations.

In the above analysis, the minimum sensitivity of the system is determined by extrapolating the measured results. Unfortunately, mechanical restrictions of the control valve limit the smallest achievable rise time and thus the true minimum sensitivity of this system cannot be experimentally tested. More work is required to verify this property.

6.2.5 Delay Time of the Shock Train Response

In section 6.2.2, it was found that τ_{x1} is greater than τ_{pb} for forcing runs 6 and 7. Here, we examine how the delay times vary with the forcing parameters ΔB and T_Θ and discuss why the shock responds to forcing after the back pressure.

First, consider figures 6.16(a) and 6.16(b) that show how the shock position and back pressure delay times vary with the disturbance rise time, respectively. Note that the values on both the x- and y-axes are normalized by the characteristic time of the inherent unsteadiness, T_c. With this in mind, it is clear that both the shock position and back pressure delays are relatively long compared to the time scale of the inherent unsteadiness (i.e., $\tau_{x1} \gg T_c$ and $\tau_{pb} \gg T_c$). It is also apparent that τ_{pb} and τ_{x1} slightly decrease as the disturbance rise time increases. Next, consider figures 6.17(a) and 6.17(b) which show how the shock position and back pressure delay times vary with the change in

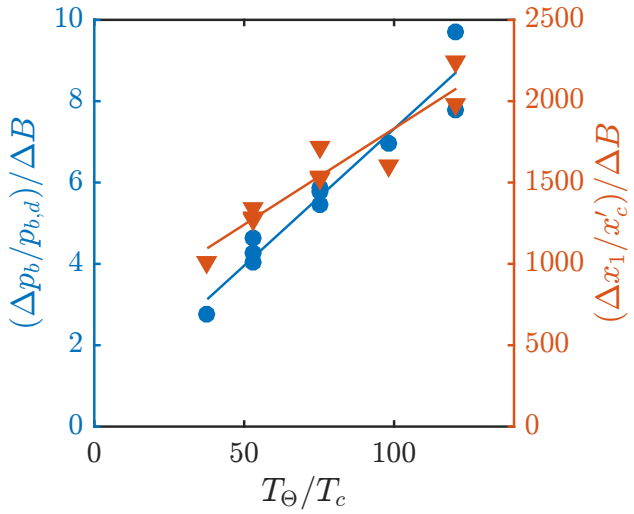

Figure 6.15: Sensitivity of the shock train response versus disturbance rise time.

blockage area ratio, respectively. Both measured time delays are approximately constant as ΔB is varied but there are groupings in the data that would suggest another variable impacts this response. We find next that this variable is the position of the shock train in the isolator, x_1.

Most importantly, figures 6.16 and 6.17 demonstrate that the shock position responds to forcing after the back pressure, i.e. $\tau_{x1} > \tau_{pb}$. In addition, the shock position delay time for the $u \rightarrow d$ transition is slightly larger than the delay time for the $d \rightarrow u$ transition. These observations are

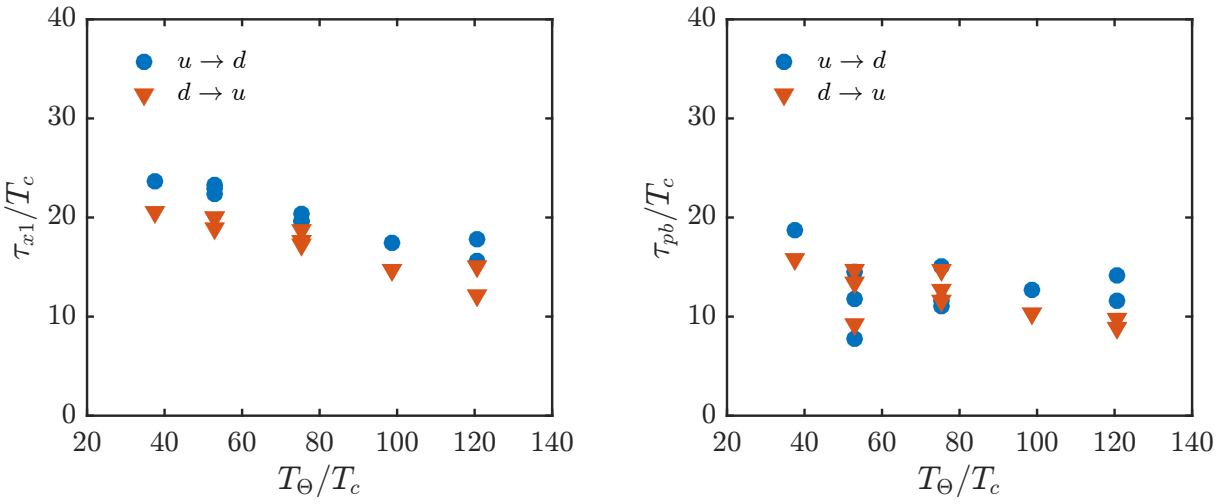

Figure 6.16: Delay times of the shock train versus the disturbance rise time: (a) shock position delay; (b) back pressure delay.

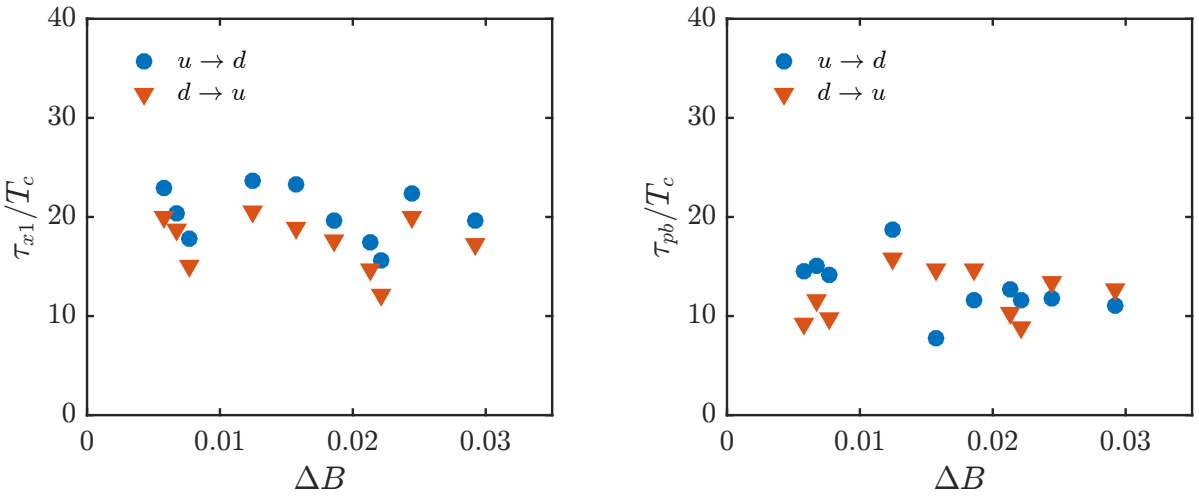

Figure 6.17: Delay times of the shock train versus the change in blockage area ratio: (a) shock position delay; (b) back pressure delay.

explained by recalling the impact of perturbation D^-, which was investigated thoroughly for the inherent unsteadiness cases in chapter 5. Perturbation D^- was found to be an acoustic wave generated in the diffuser section of the wind tunnel. The acoustic wave travels upstream through the subsonic portion of the boundary layer. From the cross-spectral analysis we found that the perturbation alters the back pressure as it passes the pressure transducer. It then travels upstream without influencing the motion of the downstream shocks because the magnitude of the perturbation is insignificant in the thick, distorted boundary layer that develops along the length of the shock train. When the acoustic wave passes the leading shock it induces a displacement and thus contributes to the inherent unsteadiness of the shock system. A similar series of events is present in the forcing cases. That is, the back pressure responds to the forcing prior to the shock position.

It is hypothesized that the change in valve angle generates upstream propagating acoustic waves analogous to perturbation D^-. In the quasi-steady state cases, the downstream disturbances are small and cause small fluctuations in the shock train position. For the forcing cases, the disturbance has a much larger magnitude causing the shock train to be displaced by a larger distance. However, the speed of the perturbation is found to agree in both situations as demonstrated by figure 6.18. In chapter 5.5 the perturbation speed was found to equal 50-100 m/s ($15.6u_c$ – $31.3u_c$) for the quasi-steady cases. The grey, shaded region in each part of the figure indicates this range of speeds. In the forcing experiments, the speed of the perturbation is determined using the difference between the back pressure and shock position delay times (i.e., $\tau_{pb} - \tau_{x1}$) and the distance between the shock position, x_1, and the back pressure measurement location. Given this information, the speed of the

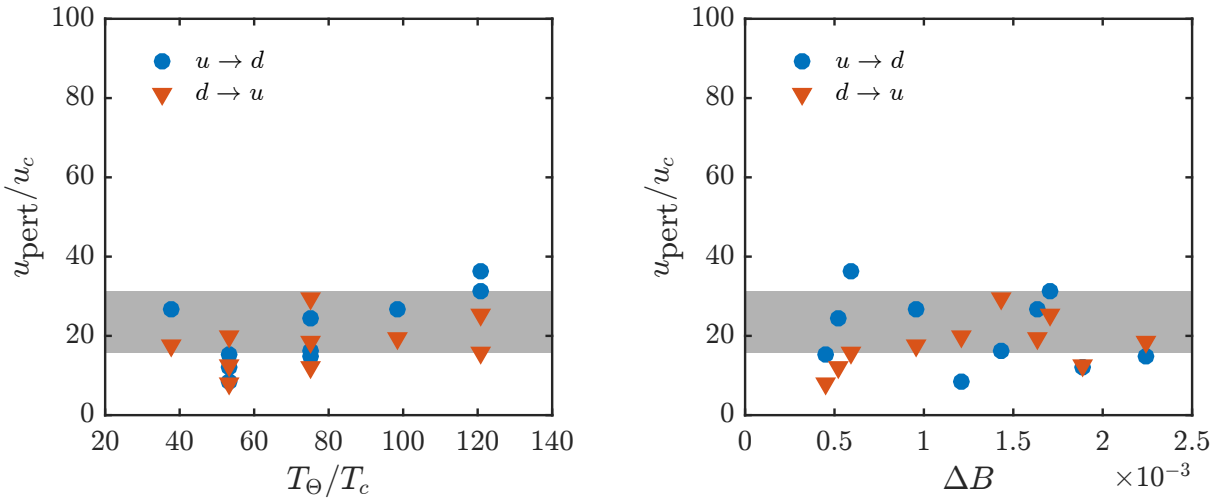

Figure 6.18: Speed of the leading shock versus the forcing parameters: rate at which the disturbance is applied to the system: (a) disturbance rise time; (b) blockage area ratio.

perturbation for the forcing cases is approximately 25–95 m/s ($7.8u_c$ – $29.6u_c$). The scatter in the results is likely due to the limited number of cycles used to average the shock train trajectories and the fact that an unsteadiness component is superimposed to the shock displacement imposed by the downstream forcing. Thus, the inherent unsteadiness of the system can slightly influence the results. Despite this scattering, the perturbation speed is approximately constant across all of the forcing cases and thus it is independent of the forcing parameters, at least within the range of conditions considered in this study.

The similarity of the quasi-steady and forcing perturbation speeds indicates that the same acoustic wave phenomenon is responsible for the shock motion. Thus, the acoustic wave generated by the valve travels upstream and first influences the back pressure. Then, the acoustic wave continues upstream and influences the position of the shock train. The shock position time delay τ_{x1} is larger for the $u \rightarrow d$ transition compared to the $d \rightarrow u$ transition because the shock train is farther upstream and it takes longer for the perturbation to reach the shock foot.

6.2.6 Hysteresis of the Shock Train Response

As shown previously, the magnitude of the shock train response depends on the forcing parameters but it is independent of whether the blockage area ratio is increasing or decreasing. In this subsection we find that the trajectory of the shock train depends on the direction in which is it traveling.

Recalling figure 6.13, there is a hysteresis effect during the shock position transition such that

the path traveled during the $u \rightarrow d$ transition is different than the path traveled during the $d \rightarrow u$ transition. Figure 6.19(a) shows the same cycle-averaged curves for run 7 but in this case the values are not normalized from 0 to 1. Instead, the shock trajectory during the $d \rightarrow u$ transition is corrected as follows:

$$\text{corrected } x_{1,d\rightarrow u} = -x_{1,d\rightarrow u} + \max(x_1) + \min(x_1) \tag{6.4}$$

Essentially, this correction reflects the cycle-averaged curve across the x-axis and shifts the result such that the minimum matches with the shock position trajectory during the $u \rightarrow d$ transition. Thus, the two transitions can be directly compared in time. From figure 6.19(a), it appears that shock train achieves a slightly higher velocity during the upstream to downstream transition. We hypothesize that the shock train speed is limited during the downstream to upstream transition because the shock train is moving against the bulk flow.

The shock position hysteresis, E_{x1}, is defined as the difference between $x_{1,u\rightarrow d}$ and the corrected $x_{1,d\rightarrow u}$. For example, figure 6.19(b) shows the hysteresis for the same cycle-averaged transitions shown in part (a) of the same figure. At the beginning of the cycle E_{x1} is negative because the downstream to upstream transition begins prior to the upstream to downstream transition. However, E_{x1} is positive for the majority of the transition. In addition, the amount of shock position hysteresis is normalized by the characteristic length scale of the inherent unsteadiness, x_c'. For run 7 shown in figure 6.19(b), the maximum hysteresis is almost 6 times greater than the root mean square of the shock position fluctuations caused by the inherent unsteadiness.

Figure 6.20(a) compares the maximum shock position hysteresis exhibited in the cycle-average transitions across all of the runs. Notice that the hysteresis is a nonlinear function of the change in shock position, Δx_1. Increasing Δx_1 increases the amount of hysteresis. Since Δx_1 is a function of both T_Θ and ΔB (see figure 6.15), it follows that the shock train trajectory is also dependent on these forcing parameters.

In a similar manner, the amount of back pressure hysteresis is quantified as follows:

$$E_{pb} = p_{b,u\rightarrow d} - [p_{b,d\rightarrow u} + \max(p_b) + \min(p_b)] \tag{6.5}$$

Figure 6.20(b) shows the amount of back pressure hysteresis versus the overall back pressure change. While there is some scatter evident, the results show very little hysteresis meaning that the $u \rightarrow d$ transition has the same back pressure time history as the $d \rightarrow u$ transition. In addition, the hysteresis does not appear to be a function of Δp_b or the forcing parameters (T_Θ and ΔB).

6.3 Conclusions

Oscillatory downstream forcing is applied to the shock train system in order to mimic disturbances produced by transient combustion processes. In this experiment, the disturbances are created by periodically changing the angle of the control valve, located downstream of the isolator section. This effectively reduces the size of the throat that mechanically chokes the exit of the diffuser and drives the downstream pressure rise. As a result of the downstream pressure oscillations, the shock train oscillates between two positions in the isolator and the back pressure oscillates between two values. The back pressure and shock position responses are compared across different cases to examine the effects of two forcing parameters: the disturbance rise time (i.e., the time it takes for the valve to change from its initial angle to its final angle) and the magnitude of the disturbance (i.e., how much the valve angle changes). For these experiments, the control mechanism of the valve limits the fastest rise time that can be obtained. Thus, the imposed forcing mimics a gradual downstream disturbance (i.e., it is slow compared to the natural dynamics of the system).

It is found that the shock position and back pressure responses have approximately the same rise time as the disturbance (i.e., they oscillate at the same frequency). In addition, the magnitude of the two responses scales with the disturbance magnitude. The disturbance rise time also impacts the magnitude of the response. Specifically, the shock train response becomes less sensitive to disturbances when the rise time is small. That is, large downstream disturbances create smaller shock train responses. For instantaneously applied disturbances, a minimum sensitivity of the

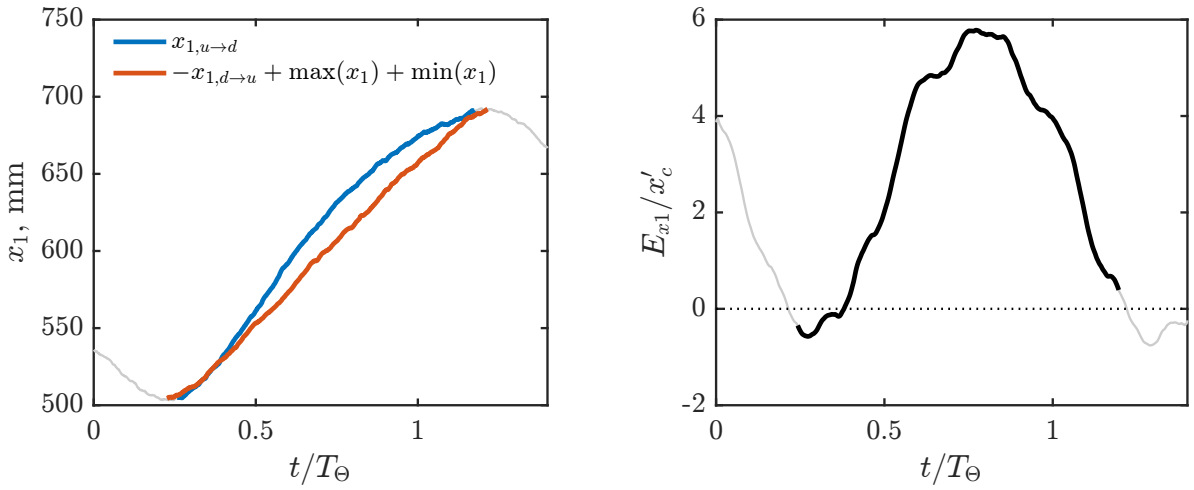

Figure 6.19: (a) Shock train position during the upstream to downstream transition compared to the corrected shock train position during the downstream to upstream transition; (b) example of the cycle-averaged shock position hysteresis, E_{x1}.

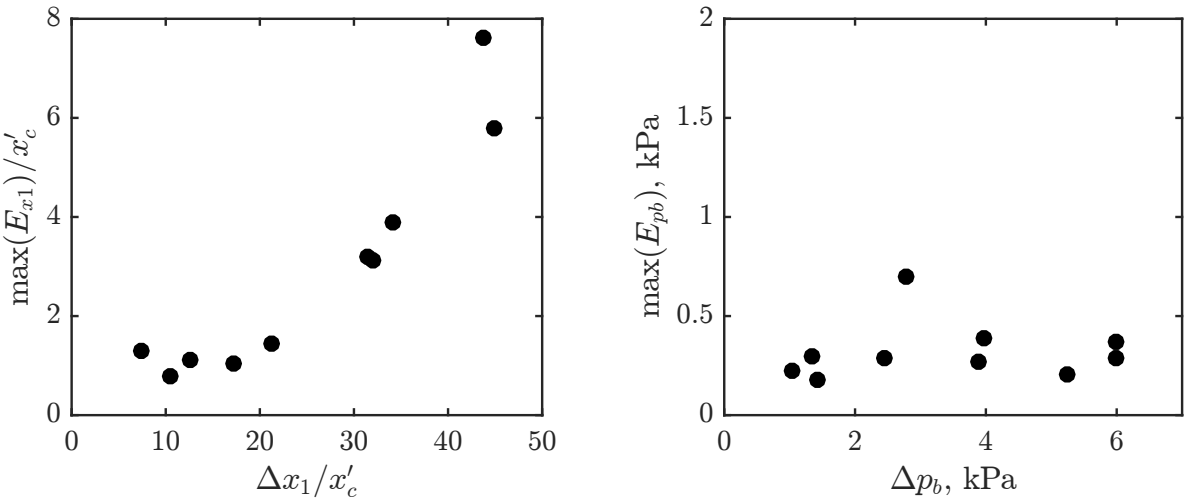

(a) (b)

Figure 6.20: (a) Maximum shock position hysteresis; (b) maximum back pressure hysteresis.

system is determined by extrapolating the measured results. Given this minimum sensitivity, we verify the plausibility of small downstream disturbances contributing to the inherent unsteadiness of the shock system.

Many similarities exist between the forcing dynamics and the dynamics of the quasi-steady state shock train. For instance, the fluctuation component caused by inherent unsteadiness is superimposed onto the bulk motion of the shock train as it oscillates due to forcing. The statistics and power spectrum of these low magnitude fluctuations are similar for both types of run conditions indicating that the perturbations that cause inherent unsteadiness are unaffected by the downstream forcing.

As discussed in chapter 5, the inherent unsteadiness of the quasi-steady shock train is partially due to perturbation D^-; an acoustic wave originating downstream of the isolator that propagates upstream through the boundary layer. In a sense, the downstream disturbance in the forcing cases is an amplified version of perturbation D^-. First, the forcing disturbance is generated downstream of the isolator just like perturbation D^-. The forcing disturbance also travels upstream at approximately the same speed. The finite speed of the disturbance explains why the shock position and back pressure responses are delayed from the onset of the valve angle change. The overall change in shock train position is greater for the forcing cases because the magnitude of the forcing disturbance is larger but the same acoustic wave phenomenon is ultimately responsible for the shock motion. The results of the forcing experiments also translate to the quasi-steady state dynamics. For instance, recall that perturbation D^- is associated with low frequency fluctuations. It is possible that the source of perturbation D^- also creates higher frequency perturbations but the shock

train response is less sensitive to these fluctuations with low rise times.

Finally, some features of the shock train response to forcing are different than the predicted response from computational studies presented in the literature. For example, no overshoot is evident in the shock position response. This could be due to the slow disturbance rise times that are imposed in this experiment. In addition, a hysteresis effect is evident that was not predicted by computational models. Specifically, the time history of the shock position trajectory depends on the direction in which the shock train is moving, despite having the same overall displacement in both directions. The shock train briefly reaches higher speeds as it travels downstream, possibly because it is assisted by the bulk fluid flow. As the shock train travels upstream, the shock speed is lower because it is travelling against the bulk fluid flow. The amount of the hysteresis depends on the magnitude of the overall shock displacement with small shock displacements exhibiting no hysteresis at all. In contrast, the back pressure response does not exhibit hysteresis. Thus, the back pressure time history is simply a function of the valve angle time history and does not depends on whether the valve is opening or closing.

Chapter 7

Summary and Conclusions

The structure and dynamics of a shock train in a constant area duct have been experimentally investigated using a combination of high-speed schlieren, pressure measurements, and PIV. The purpose of this study is to quantify and better understand the properties and processes of this complex flow, as well as its relationship with the isolator conditions. This is broadly motivated by efforts to develop more accurate modeling tools for high-speed air-breathing engine design.

Three topics related to shock trains are examined in this work. The first topic, shock train structure and three-dimensionality, is a necessary first step to characterize the system. We specifically study how the shock structure changes as the shock train moves upstream to a location where the approach conditions are different. We also observe and discuss how properties of the system that are important for isolator design, including the length and pressure rise, scale with the approach conditions. The pressure measurements used in the scaling analysis indicate a three-dimensional flow structure which is not apparent in schlieren imaging. PIV is used to identify separation regions and we determine that the conical structure of the leading shock is a consequence of these separation bubbles and the thick turbulent boundary layer that grows along the length of the system.

Despite significant structural changes, it is found that the shock train exhibits an inherently unsteady motion that is seemingly independent of the shock train location within the isolator. This motivates the second topic, which is directed towards identifying the fluid phenomena that cause the inherent unsteadiness. The work presented on this topic is particularly impactful because strong experimental evidence is given to explain the dynamics of the system which have either not been well supported in the literature or have not been discussed at all. Our results also indicate how small downstream disturbances can impact the shock train motion. This is important for understanding the mechanism linking the combustor and isolator dynamics. With this motivation in mind, the third topic discussed in this work is on the forced dynamics of shock trains. An oscillatory downstream forcing is applied and the resulting shock train dynamics are studied for various cases where the disturbance rise time and disturbance magnitude are varied. The major findings of each topic discussed in this thesis are summarized as follows.

7.1 Major Conclusions of This Work

7.1.1 Shock Train Structure

1. It is found that the Mach stem height increases and the leading shock of the lambda foot becomes stronger as pressure ratio increases. These results describe and qunatify the oblique-to-normal transition of the leading shock structure as the shock train moves upstream to a location in the isolator where the approach Mach number is higher and the confinement is smaller. The limited work that has previously considered the shock train structural transition emphasizes the importance of Mach number over the other properties of the isolator. Instead, the current work emphasizes the role of confinement by showing that this parameter can alter the Mach number bounds of the transition regime. For large flow confinement, the shock train remains oblique even as Mach number is decreased. Conversely, a small confinement allows for a normal shock train even at high Mach numbers.

2. Traditionally, the mixing region is qualitatively defined from schilieren or shadowgraph images as the portion of the pseudoshock where no shocks are observed. In this work, a formal method based on pressure measurements is proposed to identify the boundary between the shock train and mixing region. This method relies on the streamwise derivative of the pressure variance, which is large in the shock train region due to the inherent unsteady motion of shocks but small in the mixing region because the turbulent contribution to pressure fluctuations varies slowly in space. Using this method, the effects of pressure ratio on important isolator design properties, including the length and pressure rise of the system, are evaluated separately for the shock train and mixing region. Unlike most of the literature, these two pseudoshock components are separated because they are dominated by different physics. That is, the shock train is primarily an inviscid process that is dominated by shocks and the mixing region is dominated by turbulent, viscous forces. It is found that the mixing region becomes longer and has a higher pressure rise as the the pseudoshock moves upstream. Simultaneously, the shock train becomes more compact and compresses the flow more. However, the measured shock train length and pressure rise are independent of pressure ratio when properly normalized by the approach conditions. Specifically, the pressure rise across the shock train is a constant fraction of the pressure rise across a normal shock at the approach Mach number. The length of the shock train remains constant when corrected for changes in approach conditions using the Waltrup and Billig scaling factor defined as $Q = (M^2 - 1)Re_\theta^{1/4} C_\theta^{-1/2}$. As a consequence, the normalized properties of the mixing region must adjust to provide the additional length and amount of compression required by the downstream boundary conditions. This result emphasizes that the shock train and mixing region properties are affected differently when there is a change in the approach

conditions. Thus, it is important for pseudoshock models to account for these differences in order to accuratley predict the overall pseudoshock length and pressure rise.

3. For this experimental setup there is significant side-wall separation but no bottom-wall separation under the leading shock lambda foot. The lack of bottom-wall separation is believed to be caused by the relatively low aspect ratio isolator cross-section and the presence of thick boundary layers in the corners of the isolator. This shows that flow separation is not synonymous with the foot of the shock train and instead it is highly dependent on the confinement ratio in the isolator. Downstream of the shock train foot, the boundary layers on all four walls of the isolator rapidly thicken and restrict the available area for the core flow to travel through. As a result, the flow to converges towards the center of the duct and the leading shock develops a conical shape. The degree of axisymmetry associated with this structure is not apparent in schlieren images.

7.1.2 Shock Train Inherent Unsteadiness

1. The shock train is inherently unsteady, i.e., it fluctuates about its time-averaged position even though the bulk boundary conditions of the isolator are constant. The amplitude of these fluctuations is believed to depend on the approach flow conditions. Several studies have noted that large shock position fluctuations are associated with higher Mach numbers. However, only one study prior to this work has considered how the boundary layer properties impact the shock train inherent unsteadiness. Specifically, Xiong *et al.* [2017*b*] showed that moving the shock train upstream to a thinner boundary layer will lead to smaller shock fluctuations. However, the change in boundary layer properties and approach Mach number were not quantified or reported. Contrary to the previous work of Xiong *et al.* [2017*b*], in this study it is found that the amplitude and frequency content of shock position fluctuations do not change as the shock train moves upstream to a location where the boundary layer is different. That is, the unsteadiness quantities are independent of pressure ratio for the range of conditions considered in this study. Thus, the underlying causes of the inherent unsteadiness are also expected to be independent of pressure ratio. It is possible that the change in approach conditions experienced in this study is too small to significantly alter the unsteadiness properties. Thus, more work needs to be done to clarify this aspect.

2. In this work, consecutive shocks in the train have the same position fluctuation statistics (i.e., same average, maximum, and standard deviation). However, downstream shocks tend to fluctuate faster and exhibit high-frequency modes that indicate that the unsteady dynamics change through the shock train system.

3. A major contribution of this thesis is the identification of a complex, frequency-dependent dynamical system of perturbations that is responsible for the inherent unsteadiness of the shock system. The details of each perturbation are determined using a combination of cross-spectral analysis, oil flow visualization, and PIV. This work is distinct from the three theories currently in the literature for several reasons. First, multiple types of perturbations are identified, some of which had not been proposed before. Thus, cross-spectral analysis has proved to be an especially powerful tool for investigating individual perturbations characterized by specific frequency ranges. Second, the cross-spectral analysis details how perturbations interact with shock waves, which has never been discussed. Finally, the PIV measurements are the first of their kind and supply strong evidence of the underlying fluid phenomena that generate the perturbations. The points below outline the results for this topic:

   (a) Two sources of perturbations are uncovered: instabilities of separation bubbles within the shock train region and a downstream fluid phenomenon in the diffuser section, most likely turbulence or separation.

   (b) The fluid phenomenon in the diffuser generates acoustic waves that travel upstream through the upper, subsonic portion of the boundary layer. These acoustic waves induce low-frequency wall static pressure fluctuations as they propagate upstream but they do not influence the motion of downstream shocks. Once the leading shock foot is reached, the acoustic waves influence the leading shock motion, thus contributing the the inherent unsteadiness of the system. It is hypothesized that the acoustic waves are too weak to induce a motion in the downstream shocks due to the thick, distorted boundary layer that grows along the length of the shock train. In comparison, the thin, undisturbed boundary layer at the leading shock foot is more receptive to the disturbances created by the acoustic waves. Thus, only the motion of the leading shock is influenced by the perturbation as it travels upstream.

   (c) Acoustic waves are created as the flow surrounding a separation bubble within the shock train adjusts to a change in bubble size or position. Just like the acoustic waves generated in the diffuser, these acoustic waves propagate upstream through the upper, subsonic portion of the boundary layer. When the acoustic waves reach the leading shock foot they instigate a shock displacement. Unlike the acoustic waves generated in the diffuser, the separation bubble acoustic waves are associated with fluctuations across a broad range of frequencies. The measurements do not indicate downstream propagating acoustic waves induced by the separation bubble. It is hypothesized that these waves exist but are too weak to influence the motion of the downstream shocks (for the same reasoning described in item b of this list). Thus, the upstream propagating acoustics are clearly seen in the

cross-spectral analysis while the downstream propagating acoustics are not.

(d) Vortices are generated by the shear layer of a separation bubble and convect downstream. The vortices persist for a significant distance, and thus are able to influence the positions of downstream shocks as they convect past each shock foot. Just like the acoustic waves generated by the separation bubble, these vortices are associated with pressure and shock fluctuations across a broad range of frequencies.

(e) The perturbations generated by two separation bubbles are studied. The side-wall separation is large and consistently separated. The bottom-wall separation is small and intermittently separated. Both separation bubbles generate the same types of perturbations (i.e., acoustic wave and vortices) but the frequency content of the induced fluctuations are different due to the the differences in the boundary layer and separation bubble properties.

(f) We also identify downstream propagating perturbations on the side-wall of the isolator that are associated with narrowband high frequency modes. It is hypothesized that these perturbations are created by a local throat effect caused by streamwise changes in the boundary layer height. The work of Sugiyama *et al.* [1988] supports this hypothesis. Unfortunately, these perturbations are not thoroughly investigated in the current work due to limited diagnostic capabilities in this region.

(g) There is significant communication through the corners of the duct in the downstream portion of the shock train, where there are thick boundary layers. That is, perturbations may propagate from the side-wall to the bottom-wall and vice versa.

(h) We identify and define two ways that perturbations can impact the shock system: the *direct* and *indirect* influences. A direct influence occurs when the perturbation causes a locally significant change in flow properties and as a result, the perturbation induces a shock displacement as it passes the shock foot. We found that the separation bubble vortices directly influence the downstream shocks, whereas the acoustic waves directly influence the leading shock. The local effects of the acoustic waves are negligible in the downstream flow and thus do not impact the motion of the downstream shocks.

(i) The shock motion due to the direct influence of the perturbation instigates a sequential displacement of the downstream shocks, referred to as the *indirect influence* of the perturbation. Specifically, the motion of an upstream shock changes the flow structure between shocks and in response, the downstream shock must move to satisfy the new inflow conditions and required downstream pressure rise.

(j) Overall, the shock train inherent unsteadiness is the result of the superposition of the direct and indirect influences of each perturbation.

4. A scaling argument, inspired by the results of single SBLI experiments, is proposed in an effort to translate the unsteadiness results of this experiment to experiments in other facilities. Specifically, the spectral characteristics of the shock position and wall static pressure are normalized using a Strouhal number based on a proposed length scale, $L = \theta/\sqrt{C_\theta}$. This length scale is chosen because the fluid phenomena that cause inherent unsteadiness are associated with the boundary layer and are thus expected to scale with boundary layer properties such as the momentum thickness, θ. In the literature, the confinement ratio, C_θ, has been shown to influence many parameters of the shock train including its length and pressure rise. It also can impact the size of separation bubbles, one of the two fluid phenomena that generate perturbations. Thus, the confinement ratio is included in the scaling argument to essentially correct the momentum thickness based on the cross-sectional size of the duct. Due to a lack of well documented measurements on shock trains generated under different conditions, the validity of this scaling argument cannot be proven unequivocally and additional work is required.

7.1.3 Forced Dynamics of Shock Trains

1. Oscillatory forcing is applied downstream of the isolator and two responses are measured: the leading shock position and the back pressure, measured at the end of the isolator. Both responses oscillate at the same frequency as the disturbance (i.e., they have the same rise time).

2. The shock train dynamics that result from downstream forcing show many similarities to the inherent unsteadiness dynamics. In addition, the results of the forcing study can be extrapolated to explain certain observations in the inherent unsteadiness study. The points below outline these results:

   (a) For both the forcing and inherent unsteadiness studies, the same acoustic wave perturbation is responsible for the communication of downstream pressure changes in the diffuser to the shock train in the isolator section. This acoustic wave travels upstream through the subsonic portion of the boundary layer. A pressure fluctuation is measured as the acoustic wave passes the pressure transducer just upstream of the diffuser. Then, the leading shock fluctuates after an additional time delay. Thus, the two measured shock train responses are delayed from the onset of the disturbance and the delay times are related to the speed of an acoustic wave. The speed of the perturbation and the order of responses are the same in both the forcing and inherent unsteadiness cases, verifying that the acoustic wave mechanism is responsible for the shock motion.

   (b) The magnitude of the shock train response increases with the magnitude of the disturbance. Notably, the shock train is displaced by a greater amount in the forcing cases

because the disturbance that generates the upstream propagating acoustic wave is larger compared to the disturbance in the inherent unsteadiness cases. The magnitude of the shock train response also depends on the rise time of the disturbance. Specifically, decreasing the disturbance rise time reduces the sensitivity of the shock train response. That is, a disturbance with a given magnitude will create a smaller shock train response when the disturbance rise time is small. The minimum sensitivity occurs for an instantaneously applied disturbance. We determine the minimum sensitivity for this experiment by extrapolating the measured results and find that small downstream disturbances are capable of impacting the shock motion. Thus, it is plausible that acoustic waves are generated by turbulence in the diffuser and propagate upstream, contributing to the inherent unsteadiness of the system. This may also explain why the acoustic waves that contribute to the inherent unsteadiness are associated with low-frequency fluctuations. That is, the high-frequencies perturbations (with a short rise time) are essentially damped out.

(c) The fluctuation component caused by inherent unsteadiness is superimposed onto the bulk motion of the shock train as it oscillates due to forcing. The properties of these low-magnitude, high-frequency fluctuations are the same for the forcing and inherent unsteadiness cases, indicating that the perturbations that cause inherent unsteadiness are unaffected by the downstream forcing. These sources include the separation bubbles within the shock train and downstream turbulence in the diffuser section. The only difference between the two studies is the addition of a large magnitude downstream disturbance that generates additional upstream propagating acoustic waves in the forcing cases.

3. Several aspects of the shock train response to forcing differ from the predictions of computational models. For example, no overshoot is evident in the shock position response for our range of experimental conditions. This could be due to the relatively slow disturbance rise times that are imposed in this work. We also find that the shock position response exhibits a hysteresis effect that is not predicted by computational models. That is, the time history of the shock position trajectory depends on the direction in which the shock train is moving, despite having the same overall displacement in both directions. The amount of the hysteresis depends on the magnitude of the overall shock displacement with small shock displacements exhibiting no hysteresis at all. The back pressure response does not exhibit hysteresis. Thus, the back pressure time history is simply a function of the valve angle time history and does not depends on whether the valve is opening or closing.

7.2 Future Work

This thesis answers many questions about the shock train structure and dynamics. However, our understanding of these subjects could be improved with the following work:

1. Optical access from the top and bottom-walls of the isolator model would allow for simultaneous schlieren and pressure measurements from a different perspective than what we currently have. The goal of this endeavour would be to study perturbations M^+ and N^+, which were identified as part of the inherent unsteadiness theory but could not be thoroughly studied due to diagnostic limitations. In this work, we proposed a source of these perturbations which could be verified by imroving the diagnostic capabilities.

2. Optical access or the addition of pressure ports on the diffuser of the wind tunnel would allow for this component of the flow field to be studied. For example, the source perturbation D^- (i.e., the acoustic wave originating from the diffuser) could be examined. Ultimately, this would enable future work on the mechanism connecting the shock train dynamics to the dynamics of the combustor.

3. Additional detailed experiments are needed to quantify the inherent unsteadiness of the shock train in other isolator geometries and flow conditions. This information could be used to test the scaling relationship proposed in chapter 5.

4. The shock train response to forcing has only been examined for a narrow set of disturbance magnitudes and rise times. Replacing the control valve with a more flexible control mechanism would allow this topic to be expanded upon. For instance, the minimum sensitivity of the shock train response could be experimentally evaluated if we had the ability to impose a shorter disturbance rise time.

Appendix A

Example PIV Results of the Shock Train

In this appendix, two-component PIV velocity vector fields are used to derive the flow properties through the shock train. This information is the first of its kind and is useful for developing a basic understanding of the shock train. It would also be beneficial to validate the results of computational with the experimentally obtained values presented here.

Figures A.1 and A.2 are examples of the measured instantaneous u- and w-velocity fields, respectively. Figures A.3 and A.4 show the instantaneous temperature and Mach number of the flow field computed using the measured velocities and by assuming the flow is steady and adiabatic. The instantaneous kinetic energy of the flow field, shown in figure A.5, is computed by assuming that the v-velocity component is zero. The turbulent kinetic energy (TKE), TKE dissipation rate (ϵ), and Reynolds stresses (R_{ij}) are time-averaged quantities and are computed using 300 instantaneous velocity fields. The results for these quantities are shown in figures A.6–A.10. Note that the contribution due to the v-velocity component is assumed to be zero for the calculations of TKE and ϵ.

For each figure in this appendix, part (a) illustrates the measurements collected on the $y = W/2$ centerplane (i.e., a composite result measured on the streamwise vertical planes CL1 and CL2). Part (b) of each figure illustrates the measurements collected 9 mm from the wall (i.e., a composite result measured on the streamwise vertical planes SW1 and SW2). Since each figure is a composite of the results from two different measurement planes, the top half of the figure is from a different run than the bottom-half. The solid, horizontal line in each figure indicates where the plotted information switches from the bottom PIV field of view to the top PIV field of view.

In all of the figures, the x-axis is arbitrarily set so that x^* is zero at the leading shock Mach stem for easy comparison. In the instantaneous cases, the measured velocity fields were chosen such that the leading shock location is approximately the same for both runs used for the composite image. For time-averaged figures, the results are slightly shifted such that the time-averaged leading shock Mach stem location is the same for both runs. The shift in the x-direction is less than 5 mm. Finally, the results in all figures are slightly smoothed using a median filter in a 1×1 mm neighborhood.

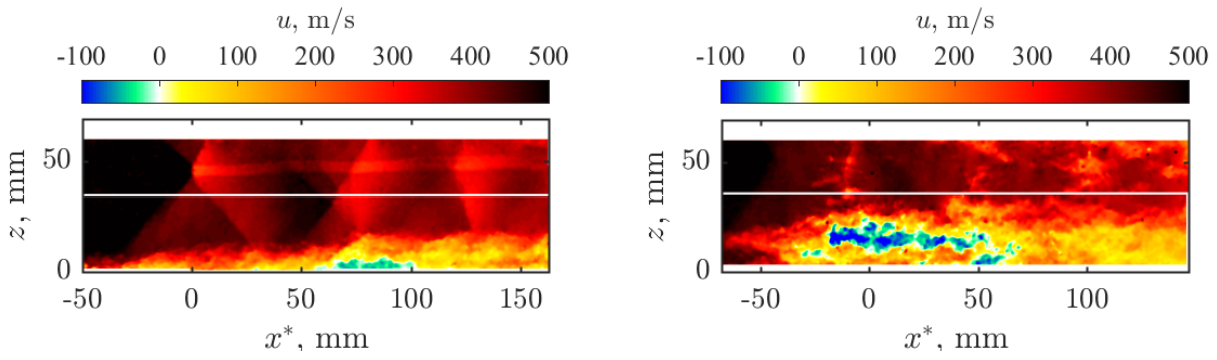

Figure A.1: Instantaneous u-velocity: (a) $y = W/2$ centerplane; (b) streamwise vertical plane 9 mm from the wall.

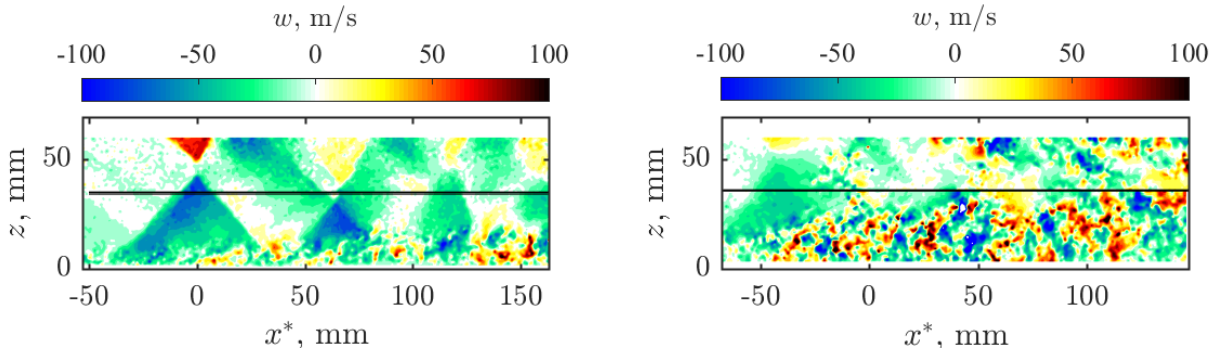

Figure A.2: Instantaneous w-velocity: (a) $y = W/2$ centerplane; (b) streamwise vertical plane 9 mm from the wall.

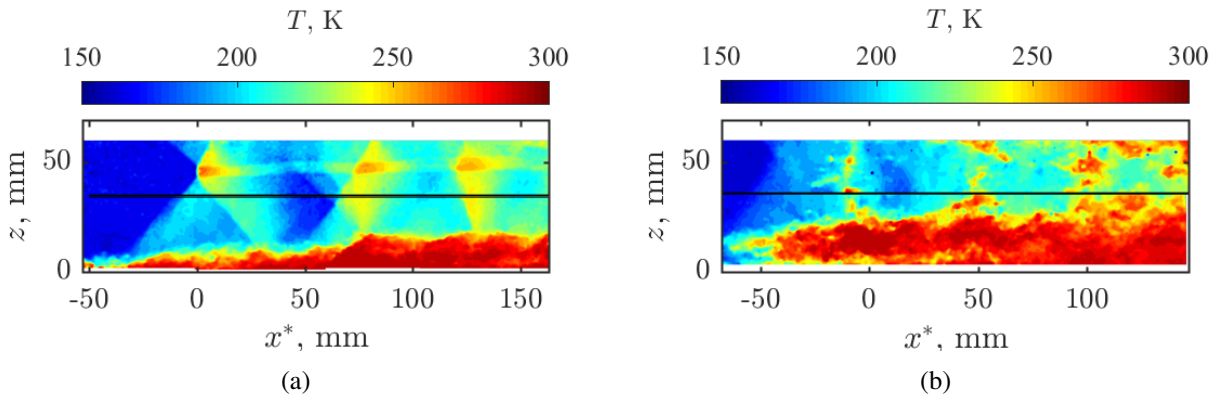

Figure A.3: Instantaneous temperature calculated assuming steady, adiabatic flow: (a) $y = W/2$ centerplane; (b) streamwise vertical plane 9 mm from the wall.

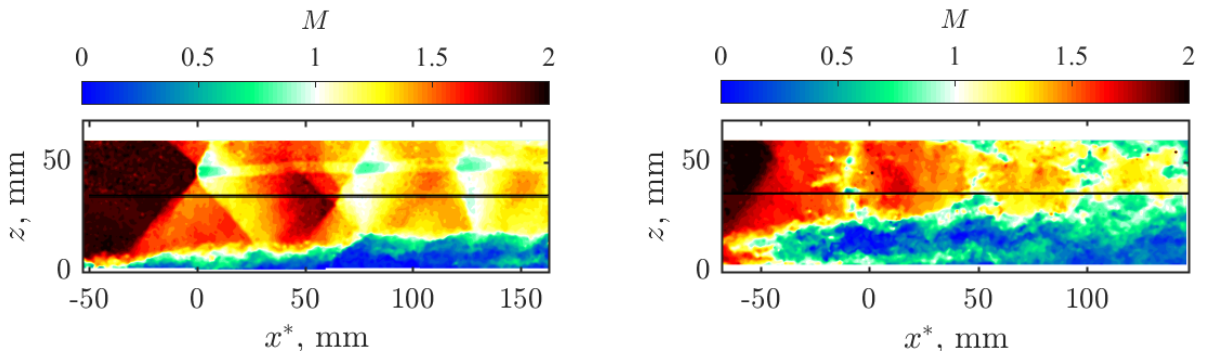

(a) (b)

Figure A.4: Instantaneous Mach number: (a) $y = W/2$ centerplane; (b) streamwise vertical plane 9 mm from the wall.

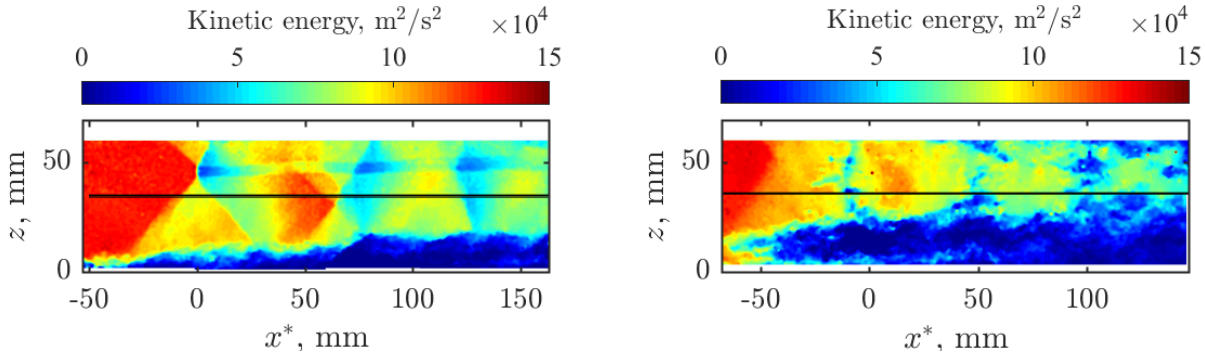

(a) (b)

Figure A.5: Instantaneous kinetic energy calculated assuming $v = 0$: (a) $y = W/2$ centerplane; (b) streamwise vertical plane 9 mm from the wall.

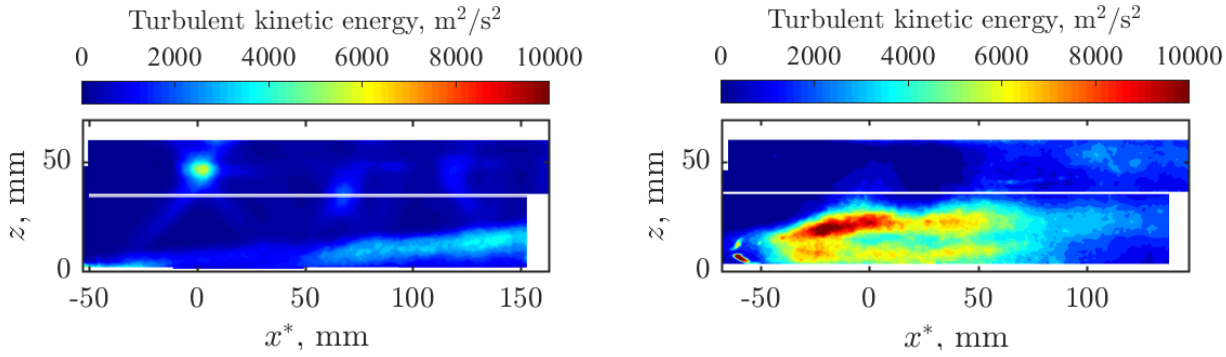

(a) (b)

Figure A.6: Turbulent kinetic energy calculated assuming $\langle (v')^2 \rangle = 0$: (a) $y = W/2$ centerplane; (b) streamwise vertical plane 9 mm from the wall.

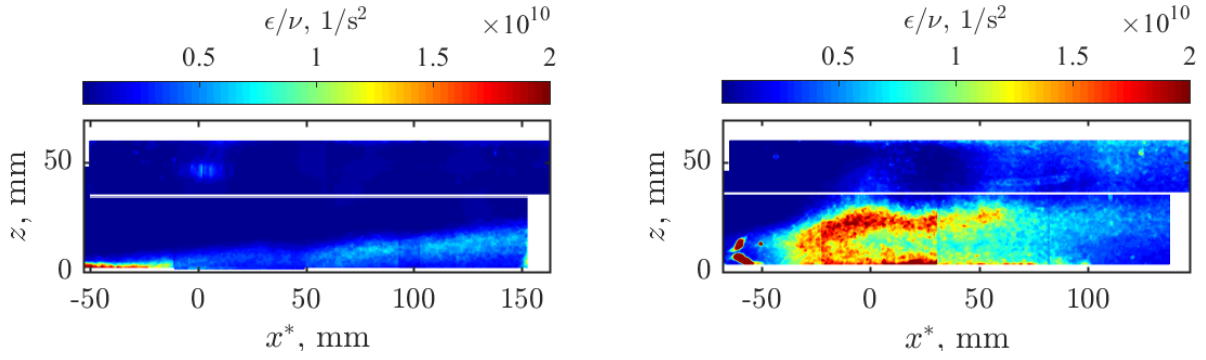

Figure A.7: Ratio of turbulent kinetic energy dissipation rate to kinematic viscosity, ϵ/ν: (a) $y = W/2$ centerplane; (b) streamwise vertical plane 9 mm from the wall. Calculations are made by assuming 1) all v' gradients are zero and 2) u' and w' gradients in the y-direction are zero.

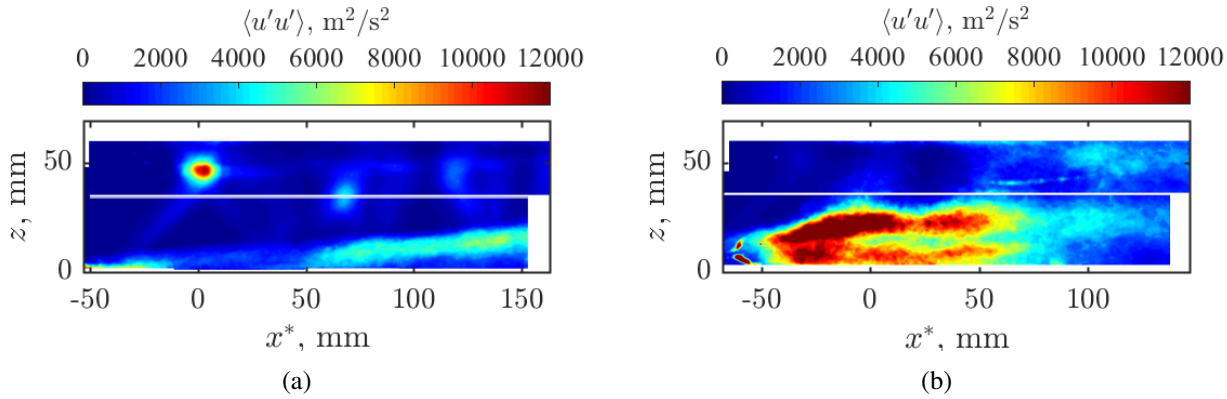

Figure A.8: Reynolds stress, $\langle u'u' \rangle$: (a) $y = W/2$ centerplane; (b) streamwise vertical plane 9 mm from the wall.

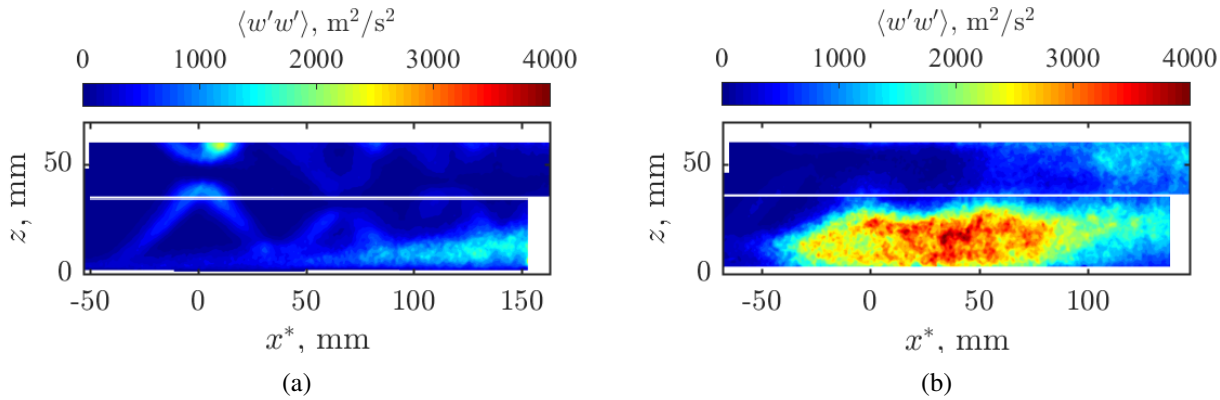

Figure A.9: Reynolds stress, $\langle w'w' \rangle$: (a) $y = W/2$ centerplane; (b) streamwise vertical plane 9 mm from the wall.

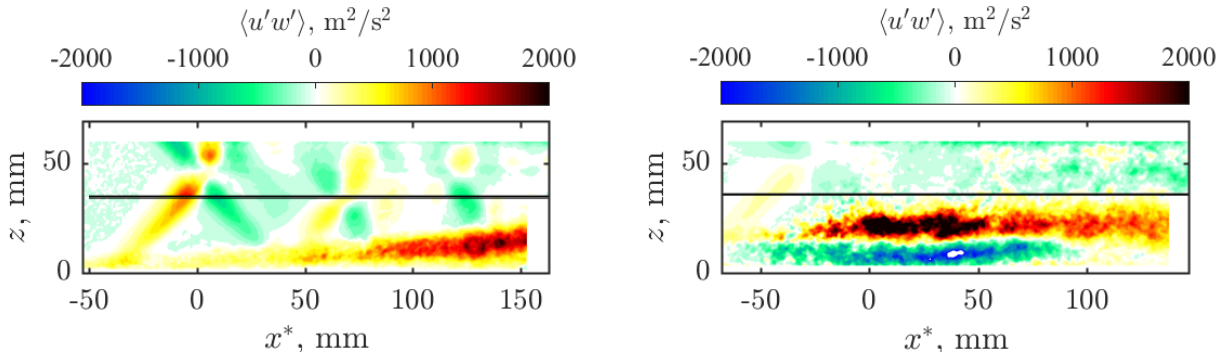

Figure A.10: Reynolds stress, $\langle u'w' \rangle$: (a) $y = W/2$ centerplane; (b) streamwise vertical plane 9 mm from the wall.

Appendix B

Shock Feature Tracking Algorithm

As demonstrated in the main text, schlieren imaging provides valuable information on the time-evolution of several shock morphological features. The tracking algorithm described next provides a quick and reliable way of automatically detecting these features in each instantaneous schlieren image.

First, the original schlieren image is manipulated in order to emphasize the shock of interest. Figure B.1 shows the manipulation process for a small section of an instantaneous schlieren image depicting the leading leg of the first shock lambda foot. On the left of the figure is the original image, I. The shock becomes more pronounced by taking the gradient of I in the x-direction. Normalizing the gradient image such that each pixel has a value between 0 and 1 produces the image $J1$. Image $J2$ is produced by inverting the values of I and then normalizing between 0 and 1. The final image, J, is the product of $J1$ and $J2$. The multiplication process effectively weights the pixel value of the final image based on the gradient and intensity of the original image. Thus,

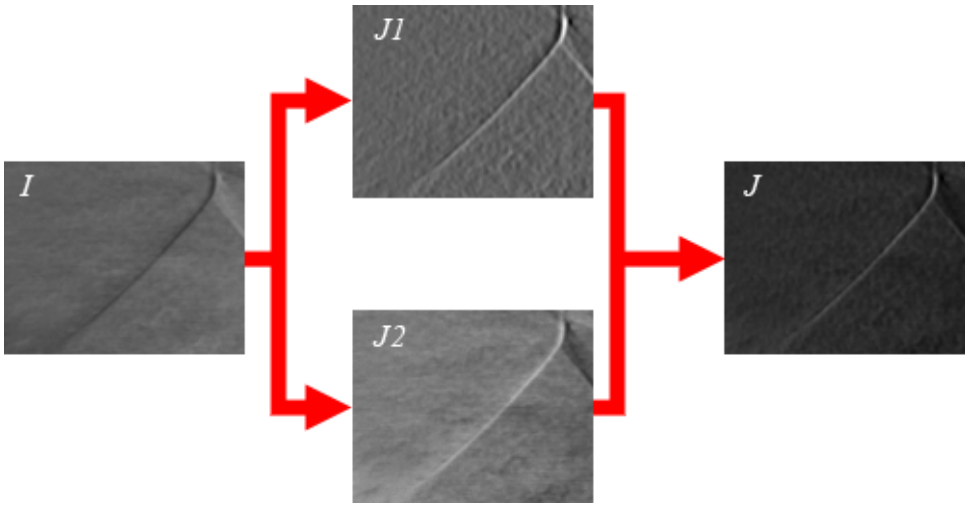

Figure B.1: Example of the image manipulation steps used in the tracking algorithm for a left-running shock. I is the original image, $J1$ is the normalized gradient of I, $J2$ is the normalized inversion of I, and J is the product of $J1$ and $J2$.

the shock is emphasized while the effects of turbulence and other similar phenomena that create gradual density gradients are minimized. The above example is for a left-running wave. A similar process is used for right-running waves except image $J2$ is not inverted because the intensity values of the shock are already high compared to the surrounding flow.

The shock morphological features are directly quantified using image J. For example, to quantify the shock angle, a linear fit is applied to the highest intensity points in each row of image J where the shock of interest is present. An outlier detection step is then used to refine the fitted line. The angle of the shock is thus equal to the inverse tangent of the slope of the fitted line. A smaller number of high intensity points in image J are selected near the boundary layer to fit a second line. The location of the shock foot is found by interpolating the selectively fit line at a specified location near the edge of the boundary layer. These line fitting processes produce measurements for most of the shock features discussed in the text including α_L, α_R, x_{1l}, x_{1r}, x_{2b}, x_{2t}, x_{3b}, x_{3t}, x_{4b}, and x_{4t}.

A different approach is used to quantify the leading shock Mach stem features. Specifically, a Harris corner detector [Harris & Stephens, 1988] is applied to image J in order to quantify the x- and $z-$locations of the top and bottom triple points. The Mach stem height, s, is thus equal to the difference in z-locations. If no Mach stem exists (i.e., the leading shock is oblique) then only one corner is detected. The Mach stem is slightly angled in some of the instantaneous images. In other words the x-locations of the two triple points are different. The streamwise location of the Mach stem, x_1, is defined using the highest intensity pixel in image J at the mid-point of the Mach stem (i.e., at the z-location equal to the average of the upper and lower triple point z-locations).

After applying the tracking algorithm to a set of instantaneous schlieren images, the results are checked manually. The tracking algorithm correctly quantifies the shock features in over 98% of

(a) (b)

Figure B.2: Example instantaneous schlieren images where: (a) x_{2c} is clearly defined; (b) x_{2c} is difficult to distinguish.

the images. The incorrectly quantified features are fixed manually. The only feature that cannot be reliably tracked using the algorithm described above is the corner point of the second shock, x_{2c}. This is because the left- and right-running waves that comprise the second shock are often difficult to detect away from the boundary layer. For example, figure B.2 shows two example schlieren images of the second shock where: (a) the intersection point is clearly defined and (b) the intersection point is difficult to distinguish. Clearly, in figure B.2(b) select portions of the shock are not visible by eye in the original image I and thus the intensities in image J are low and are not easily distinguished from the surrounding flow. To over come this, x_{2c} is selected by hand for each instantaneous image of a single run. When the intersection point of the left- and right-running waves is not visible by eye then the portion of the shock near the boundary layer is extrapolated to find x_{2c}.

Since the results of the tracking algorithm are visually confirmed using the original schlieren image, the uncertainty of the shock locations (i.e., x_i) is simply dependent on the thickness of the shock itself. The thickest shock is approximately 7 mm and thus the uncertainty in the tracking algorithm is conservatively estimated to be ± 2 mm. The thickness of the shock also impacts the measured shock angles, α_L and α_R. In a worst-case scenario the shock angle uncertainty is $\pm 2^\circ$.

Finally, note that the tracking algorithm has been refined over time. Original methods used only intensity or intensity gradients (not a combination of the two quantities) to detect shock features. As a result, older algorithms are more prone to incorrectly quantifying the shock features. However, by correcting the results by hand, the outcome is approximately the same as the results of the newer tracking algorithm to within measurement uncertainty.

Appendix C

Mathematical Definition of Cross-Spectral Quantities

Consider the fluctuation components of two discrete time signals, $x_i'[t]$ and $x_j'[t]$. Typically, the cross-correlation of the two signals, $C(x_i', x_j')$, is used to quantify the (discrete) time delay, T, between the fluctuations as follows:

$$C(x_i', x_j')[T] = \sum_{t=-\infty}^{\infty} x_i'[t+T]x_j'[t] \tag{C.1}$$

The time delay at which the two signals are maximally correlated is defined to be the *broadband time delay*. The broadband time delay is a convenient measure that indicates which time trace exhibits a fluctuation first. However, it is not a comprehensive description of the dynamic shock train system since it does not take into account the frequency dependence of the time delay. In order to describe the dynamics of the system as a function of frequency consider the cross-spectrum. The cross-spectrum of two signals, $\psi(x_i', x_j')$, is defined as the discrete time Fourier transform of the (discrete time) cross-correlation function [Oppenheim *et al.*, 1989] as follows:

$$\psi(x_i', x_j')[f] = \mathscr{F}\{C(x_i', x_j')[T]\} \tag{C.2}$$

where f is the frequency. In this work, the cross-spectrum is computed using the Welch averaging method with a Hamming window and 50% overlap such that the resulting spectral resolution of the cross-spectrum is 25 Hz.

In general, the cross-spectrum is a complex function, with real and imaginary components. The magnitude of the complex cross-spectrum normalized by the product of the power spectra of the individual signals (i.e., of x_i' and x_j') is referred to as *coherence spectrum*, $Co(x_i', x_j')$, and enables one to identify significant frequency-domain correlation between the two time series:

$$Co(x_i', x_j')[f] = \frac{\mid \psi(x_i', x_j')[f] \mid^2}{\psi(x_i', x_i')[f] \quad \psi(x_j', x_j')[f]} \tag{C.3}$$

The phase delay, defined as the argument of the complex cross-spectrum, is converted to a frequency-

dependent *narrowband time delay*, $\tau(x_i', x_j')$, between the signals as follows:

$$\tau(x_i', x_j')[f] = -\frac{\arg\{\psi(x_i', x_j')[f]\}}{2\pi f} \tag{C.4}$$

Appendix D

$p_i - p_j$ Narrowband Time Delays

In section 5.3 of the main text, a detailed analysis is presented on the cross-spectral time delay calculated using two pressure fluctuation time traces measured 10.9 mm apart on the bottom-wall $y = W/2$ centerline. Here, the time delays are presented for $p_i - p_j$ cross-spectra calculated using two pressure time traces measured at other various points in the isolator. Parts (a)–(e) of figure D.1 show the cross-spectral time delay for the following pressure measurement locations:

(a) both pressures measured on the side-wall at $z = 41.3$ mm (i.e., away from the corner) with 21.8 mm spacing between transducers in the x-direction;

(b) both pressures measured on the side-wall at $z = 6.4$ mm (i.e., near the corner) with 21.8 mm spacing between transducers in the x-direction;

(c) one pressure measured on the bottom-wall near the corner (at $y = 50.8$ mm) and the second pressure measured at the same axial location on the bottom-wall $y = W/2$ centerline (i.e., at $y = 28.6$ mm);

(d) one pressure measured on the side-wall near the corner (at $z = 6.4$ mm) and the second pressure measured at the same axial location on the side-wall away from the corner (at $z = 41.3$ mm);

(e) one pressure measured on the side-wall near the corner (at $z = 6.4$ mm) and the second pressure measured at the same axial location on the bottom-wall near the corner (at $y = 50.8$ mm).

The masked regions in the figure indicate where the coherence is small and thus the pressure signals are considered to be uncorrelated. Also note that the transducer spacing varies across the different cases so the time delays presented in figure D.1 are scaled such that they reflect the amount of time it takes a perturbation to travel 10.9 mm. As discussed in the main text, the sign of the time delay identifies what direction the perturbation is traveling. Use table D.1 to determine the direction in which the perturbation propagates given the sign of the time delay in figure D.1.

Figure D.1	$\tau(p_i', p_j') > 0$	$\tau(p_i', p_j') < 0$
(a)	upstream	downstream
(b)	upstream	downstream
(c)	towards the corner	away from the corner
(d)	towards the corner	away from the corner
(e)	towards the side-wall	towards the bottom-wall

Table D.1: Direction in which a perturbation travels based on the sign of the time delay.

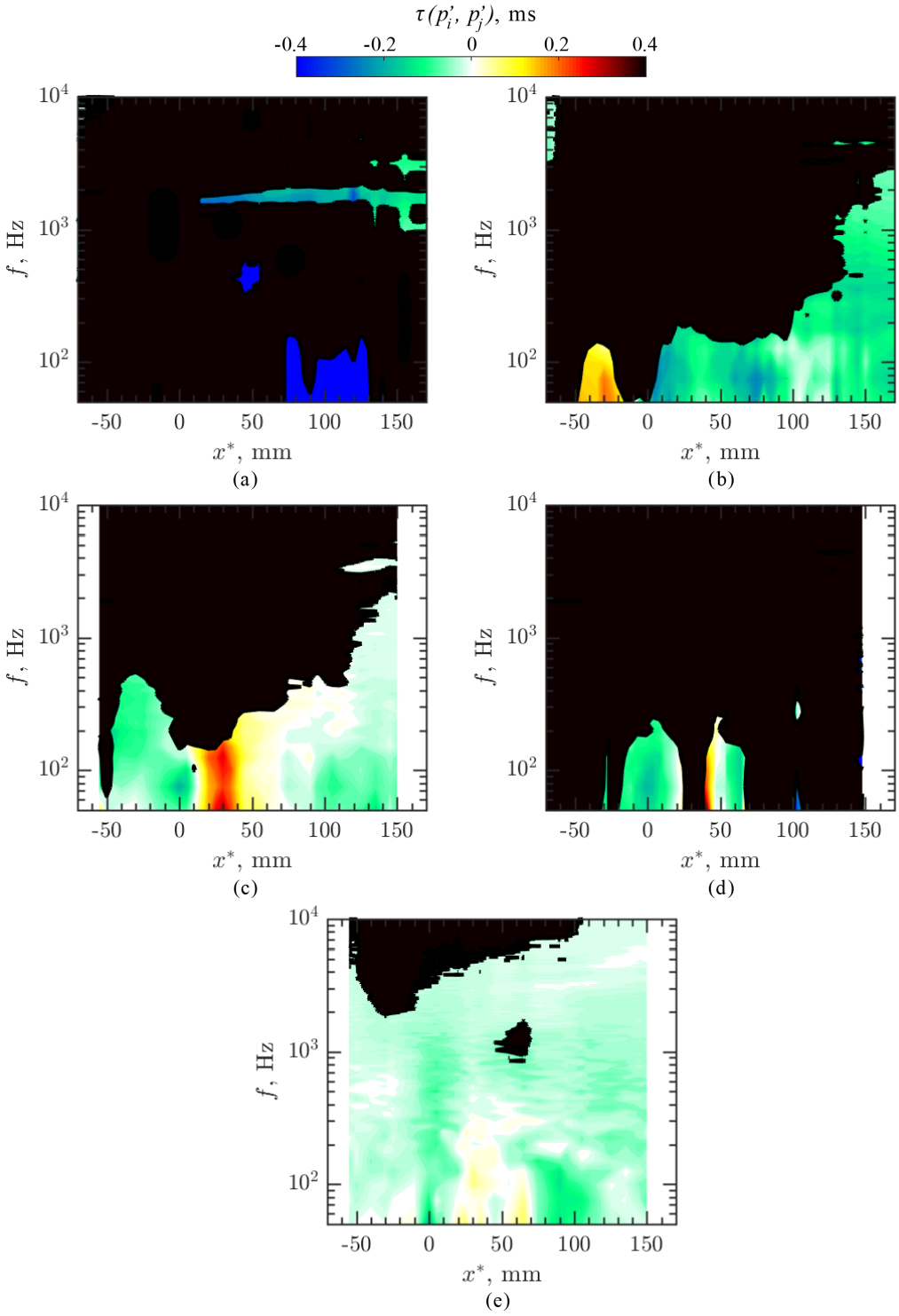

Figure D.1: $p_i - p_j$ time delay contour plots calculated using two pressure time traces measured at locations $L_1 = (x_1, y_1, z_1)$ and $L_2 = (x_2, y_2, z_2)$: (a) $L_1 = (x_1, 57.2, 41.3)$ and $L_2 = (x_1 + 21.8, 57.2, 41.3)$ mm; (b) $L_1 = (x_1, 57.2, 6.4)$ and $L_2 = (x_1 + 21.8, 57.2, 6.4)$ mm; (c) $L_1 = (x_1, 50.8, 0)$ and $L_2 = (x_1, 28.6, 0)$ mm; (d) $L_1 = (x_1, 57.2, 6.4)$ and $L_2 = (x_1, 57.2, 41.3)$ mm; (e) $L_1 = (x_1, 57.2, 6.4)$ and $L_2 = (x_1, 50.8, 0)$ mm.

Bibliography

BENEK, J. A., SUCHYTA-C. J. BABINSKY H. 2016 Simulations of incident shock boundary layer interactions. In *54th AIAA Aerospace Sciences Meeting (2016-0352)*.

CARROLL, B. F., DUTTON-J. C. 1988 Characteristics of multiple shock wave/turbulent boundary layer interactions in rectangular ducts. In *1st National Fluid Dynamics Conference*.

CARROLL, B. F., LOPEZ-FERNANDEZ P. A. DUTTON J. C. 1993 Computations and experiments for a multiple normal shock/boundary-layer interaction. *Journal of Propulsion and Power* **9** (3), 405–411.

CHEN, C. P., SAJBEN, M. & KROUTIL, J. C. 1979 Shock-wave oscillations in a transonic diffuser flow. *AIAA Journal* **17** (10), 1076–1083.

CLEMENS, N. T., NARAYANASWAMY-V. 2014 Low-frequency unsteadiness of shock wave/turbulent boundary layer interactions. *Annual Review of Fluid Mechanics* **46** (1), 469–492.

COX-STOUFFER, S. K. & HAGENMAIER, M. A. 2001 The effect of aspect ratio on isolator performance. In *39th AIAA Aerospace Sciences Meeting and Exhibit (2001-0519)*.

CROCCO, L. 1958 One-dimensional treatment of steady gas dynamics. In *Fundamentals of Gas Dynamics* (ed. H. W. Emmons), , vol. 3, pp. 110–130. Princeton, NJ: Princeton University Press.

DO, H., IM S.-K. MUNGAL M. G. CAPPELLI M. A. 2011 The influence of boundary layers on supersonic inlet flow unstart induced by mass injection. *Experiments in Fluids* **51** (3), 679–691.

DRIVER, D. M., SEEGMILLER-H. L. MARVIN J. G. 1987 Time-dependent behaviour of a reattaching shear layer. *AIAA Journal* **25** (7), 914–919.

DUPONT, P., HADDAD, C. & DEBIÈVE, J. F. 2006 Space and time organization in a shock-induced separated boundary layer. *Journal of Fluid Mechanics* **559**, 255–277.

DUPONT, P., PIPONNIAU, S., SIDORENKO, A. & DEBIÈVE, J. F. 2008 Investigation by particle image velocimetry measurements of oblique shock reflection with separation. *AIAA Journal* **46** (6), 1365–1370.

DUSSAUGE, J.-P., DUPONT, P. & DEBIEVE, J.-F. 2006 Unsteadiness in shock wave boundary layer interactions with separation. *Aerospace Science and Technology* **10** (2), 85–91.

ELSINGA, G. E., VAN OUDHEUSDEN, B. W. & SCARANO, F. 2005 Evaluation of aero-optical distortion effects in PIV. *Experiments in Fluids* **39** (2), 246–256.

FIÉVET, R., KOO, H., RAMAN, V. & AUSLENDER, A. H. 2017 Numerical investigation of shock-train response to inflow boundary-layer variations. *AIAA Journal* **55** (9), 2888–2901.

FISCHER, C. & OLIVIER, H. 2014 Experimental investigation of wall and total temperature influence on a shock train. *AIAA Journal* **52** (4), 757–766.

FOTIA, M. L. & DRISCOLL, J. F. 2012 Isolator-combustor interactions in a direct-connect ramjet-scramjet experiment. *Journal of Propulsion and Power* **28** (1), 83–95.

FUNDERBURK, M. & NARAYANASWAMY, V. 2016 Experimental investigation of primary and corner shock boundary layer interactions at mild back pressure ratios. *Physics of Fluids* **28** (086102).

GARCIA, D. 2010 Robust smoothing of gridded data in one and higher dimensions with missing values. *Computational Statistics & Data Analysis* **54** (4), 1167–1178.

GEERTS, J. S. & YU, K. H. 2015 Application of focusing schlieren deflectometry to an isolator shock train. In *53rd AIAA Aerospace Sciences Meeting (2015-1486)*.

GEERTS, J. S. & YU, K. H. 2016 Three-dimensional nature of shock trains in rectangular scramjet isolators. In *54th AIAA Aerospace Sciences Meeting (2016-1164)*.

GNANI, F., ZARE-BEHTASH, H. & KONTIS, K. 2015 Pseudo-shock waves and their interactions in high-speed intakes. *Progress in Aerospace Sciences* **82**, 36–56.

GRAFTIEAUX, L., MICHARD, M. & GROSJEAN, N. 2001 Combining PIV, POD and vortex identification algorithms for the study of unsteady turbulent swirling flows. *Measurement Science and Technology* **12**, 1422–1429.

GRILLI, M., SCHMID, P. J., HICKEL, S. & ADAMS, N. A. 2012 Analysis of unsteady behaviour in shockwave turbulent boundary layer interaction. *Journal of Fluid Mechanics* **700**, 16–28.

HANDA, T., MASUDA, M. & MATSUO, K. 2003 Mechanism of shock wave oscillation in transonic diffusers. *AIAA Journal* **41** (1), 64–70.

HANDA, TARO, MASUDA, MITSUHARU & MATSUO, KAZUYASU 2005 Three-dimensional normal shock-wave/boundary-layer interaction in a rectangular duct. *AIAA Journal* **43** (10), 2182–2187.

HARRIS, C. & STEPHENS, M. 1988 A combined corner and edge detector. In *Procedings of the Alvey Vision Conference 1988*, pp. 147–151.

HOEGER, T. C., KING, P. I., DONBAR, J. M. & COX-STOUFFER, S. 2011 2-D transient CFD model of an isolator shock train. In *17th AIAA International Space Planes and Hypersonic Systems and Technologies Conference (2011-2221)*.

HUANG, H., TAN, H., WANG, J., SUN, S. & NING, L. 2014 A fluidic control method of shock train in hypersonic inlet/isolator. In *50th AIAA/ASME/SAE/ASEE Joint Propulsion Conference (2014-3846)*.

HUMBLE, R. A., SCARANO, F. & OUDHEUSDEN, B. W. 2009 Unsteady flow organization of a shock wave/turbulent boundary layer interaction. In *IUTAM Symposium on Unsteady Separated Flows and their Control*, , vol. 14.

HUNT, R. L., EDELMAN, L. M. & GAMBA, M. 2018 Scaling of pseudoshock length and pressure rise. In *56th AIAA Aerospace Sciences Meeting (2018-1617)*.

HUTZEL, J. R., DECKER, D. D., COBB, R. G., KING, P. I., VETH, M. J. & DONBAR, J. M. 2011 Scramjet isolator shock train location techniques. In *49th AIAA Aerospace Sciences Meeting (2011-402)*.

IKUI, T., MATSUO, K. & NAGAI, M. 1974*a* The mechanism of pseudo-shock waves. *Bulletin of JSME* **17** (108), 731–739.

IKUI, T., MATSUO, K., NAGAI, M. & HONJO, M. 1974*b* Oscillation phenomena of pseudo-shock waves. *Bulletin of JSME* **17** (112), 1278–1285.

IKUI, T., MATSUO, K. & SASAGUCHI, K. 1981 Modified diffusion model of pseudo-shock waves considering upstream boundary layers. *JSME Bulletin* **24** (197).

KIRKUP, L. & FRENKEL, R. B. 2006 *An introduction to uncertainty in measurement*. Cambridge University Press.

KIYA, M. & SASAKI, K. 1983 Structure of a turbulent separation bubble. *Journal of Fluid Mechanics* **137**, 83–113.

KOO, H. & RAMAN, V. 2012 Large-eddy simulation of a supersonic inlet-isolator. *AIAA Journal* **50** (7), 1596–1613.

LAURENCE, S. J., KARL, S., MARTINEZ SCHRAMM, J. & HANNEMANN, K. 2013 Transient fluid-combustion phenomena in a model scramjet. *Journal of Fluid Mechanics* **722**, 85–120.

LE, D. B., GOYNE, C. P. & KRAUSS, R. H. 2008 Shock train leading-edge detection in a dual-mode scramjet. *Journal of Propulsion and Power* **24** (5), 1035–1041.

LIN, K.-C., TAM, C.-J., JACKSON, K. R., EKLUND, D. R. & JACKSON, T. A. 2006 Characterization of shock train structures inside constant-area isolators of model scramjet combustors. In *44th AIAA Aerospace Sciences Meeting (2006-0816)*.

LIN, P., RAO, G. V. R. & O'CONNOR, G. M. 1991 Numerical analysis of normal shock train in a constant area isolator. In *27th Joint Propulsion Conference (91-2162)*.

LINDSTROM, C. D., DAVIS, D., WILLIAMS, S. & TAM, C. 2009 Shock-train structure resolved with absorption spectroscopy part II: analysis and CFD comparison. *AIAA Journal* **47** (10), 2379–2390.

MATSUO, K., MIYAZATO, Y. & KIM, H.-D. 1999 Shock train and pseudo-shock phenomena in internal gas flows. *Progress in Aerospace Sciences* **35** (1), 33–100.

MERKLI, P. E. 1976 Pressure recovery in rectangular constant area supersonic diffusers. *AIAA Journal* **14** (2), 168–172.

MIYAZATO, Y., MATSUO, K. & KASADA, R. 2009 Experimental and theoretical investigations of normal shock wave/turbulent boundary-layer interactions at low Mach numbers in a square straight duct. In *47th AIAA Aerospace Sciences Meeting (2009-925)*.

MORAJKAR, R. 2017 Role of secondary flows on flow separation induced by shock / boundary layer interaction in supersonic inlets. PhD thesis, University of Michigan.

MORGAN, B., DURAISAMY, K. & LELE, S. K. 2012 Large-eddy and RANS simulations of a normal shock train in a constant-area isolator. In *50th AIAA Aerospace Sciences Meeting (2012-1094)*.

MORGAN, B., DURAISAMY, K. & LELE, S. K. 2014 Large-eddy simulations of a normal shock train in a constant-area isolator. *AIAA Journal* **52** (3), 539–558.

NILL, L. & MATTICK, A. 1996 An experimental study of shock structure in a normal shock train. In *34th Aerospace Sciences Meeting and Exhibit (96-0799)*.

OKA, T., ONO, D. & MIYAZATO, Y. 2014 Study of shock trains and pseudo-shock waves in constant area ducts. *52nd AIAA Aerospace Sciences Meeting (2014-0949)* pp. 1–14.

OM, D. & CHILDS, M. E. 1985 Multiple transonic shock-wave/turbulent boundary-layer interaction in a circular duct. *AIAA Journal* **23** (10), 1506–1511.

OPPENHEIM, A. V., SCHAFER, R. W. & BUCK, J. R. 1989 *Discrete-time signal processing*, 2nd edn. Prentice Hall.

ORTWERTH, P. J. 2001 Scramjet vehicle integration. In *Scramjet Propulsion, Progress in Astronautics and Aeronautics*. Reston, VA: AIAA.

OUDHEUSDEN, B. W., JÖBSIS, A. J. P., SCARANO, F. & SOUVEREIN, L. J. 2011 Investigation of the unsteadiness of a shock-reflection interaction with time-resolved particle image velocimetry. *Shock Waves* **21**, 397–409.

PING, K. X., ZHI, C. & LI, Z. K., HUAI-Q. 2017 Investigations on the shock train structures and unsteadiness. *21st AIAA International Space Planes and Hypersonics Technologies Conference (2017-2388)* .

RODI, P. E., EMAMI, S. & TREXLER, C. A. 1996 Unsteady pressure behavior in a ramjet/scramjet inlet. *Journal of Propulsion and Power* **12** (3), 486–493.

SAJBEN, M., DONOVAN, J. F. & MORRIS, M. J. 1992 Experimental investigation of terminal shock sensors for mixed-compression inlets. *Journal of Propulsion and Power* **8** (1), 168–174.

SAMIMY, M. & LELE, S. K. 1991 Motion of particles with inertia in a compressible free shear layer. *Physics of Fluids A: Fluid Dynamics* **3** (8), 1915–1923.

SCIACCHITANO, A., NEAL, D. R., SMITH, B. L., WARNER, S. O., VLACHOS, P. P., WIENEKE, B. & SCARANO, F. 2015 Collaborative framework for PIV uncertainty quantification: comparative assessment of methods. *Measurement Science and Technology* **26** (7), 074004.

SHAPIRO, A. H. 1953 *Dynamics and thermodynamics of compressible fluid flow*. The Ronald Press Company.

SMART, M. K. 2015 Flow modeling of pseudoshocks in backpressured ducts. *AIAA Journal* **53** (12), 3577–3588.

SOUVEREIN, L. J., DUPONT, P., DEBIÈVE, J.-F., DUSSAUGE, J.-P., VAN OUDHEUSDEN, B. W. & SCARANO, F. 2010 Effect of interaction strength on unsteadiness in shock-wave-induced separations. *AIAA Journal* **48** (7), 1480–1493.

SOUVEREIN, L. J., OUDHEUSDEN, B. W., SCARANO, F. & DUPONT, P. 2009 Application of a dual-plane particle image velocimetry (dual-PIV) technique for the unsteadiness characterization of a shock wave turbulent boundary layer interaction. *Measurement Science and Technology* **20** (074003).

SRIKANT, S., WAGNER, J. L., VALDIVIA, A., AKELLA, M. R. & CLEMENS, N. 2010 Unstart detection in a simplified-geometry hypersonic inlet-isolator flow. *Journal of Propulsion and Power* **26** (5), 1059–1071.

SU, W.-Y., JI, Y.-X. & CHEN, Y. 2016 Effects of dynamic backpressure on pseudoshock oscillations in scramjet inlet-isolator. *Journal of Propulsion and Power* **32** (2), 1–13.

SUGIYAMA, H., TAKEDA, H., ZHANG, J., OKUDA, K. & YAMAGISHI, H. 1988 Locations and oscillation phenomena of pseudo-shock waves in a straight rectangular duct. *JSME International Journal* **31** (1), 9–15.

SUGIYAMA, H., TSUJIGUCHI, Y. & HONMA, T. 2008 Structure and oscillation phenomena of pseudo-shock waves in a straight square duct at Mach 2 and 4. In *15th AIAA International Space Planes and Hypersonic Systems and Technologies Conference (2008-2646)*.

SULLINS, G. A. & MCLAFFERTY, G. H. 1992 Experimental results of shock trains in rectangular ducts. In *AIAA 4th International Aerospace Planes Conference (92-5103)*.

SUN, L. Q., SUGIYAMA, H., MIZOBATA, K. & FUKUDA, K. 2003 Numerical and experimental investigations on the Mach 2 pseudo-shock wave in a square duct. *Journal of Visualization* **6** (4), 363–370.

TAN, H.-J. & GUO, R.-W. 2007 Experimental study of the unstable-unstarted condition of a hypersonic inlet at Mach 6. *Journal of Propulsion and Power* **23** (4), 783–788.

TAN, H.-J., LI, L.-G., WEN, Y.-F. & ZHANG, Q.-F. 2011 Experimental investigation of the unstart process of a generic hypersonic inlet. *AIAA Journal* **49** (2), 279–288.

VALDIVIA, A., YUCEIL, K. B., WAGNER, J. L., CLEMENS, N. T. & DOLLING, D. S. 2014 Control of supersonic inlet-isolator unstart using active and passive vortex generators. *AIAA Journal* **52** (6), 1207–1218.

VARADARAJAN, P. A. & ROE, P. L. 2011 Geometrical shock dynamics and engine unstart. In *41st AIAA Fluid Dynamics Conference and Exhibit (2011-3909)*.

WAGNER, J. L., YUCEIL, K. B. & CLEMENS, N. T. 2010 Velocimetry measurements of unstart of an inlet-isolator model in Mach 5 flow. *AIAA Journal* **48** (9), 1875–1888.

WAGNER, J. L., YUCEIL, K. B., VALDIVIA, A., CLEMENS, N. T. & DOLLING, D. S. 2009 Experimental investigation of unstart in an inlet/isolator model in Mach 5 flow. *AIAA Journal* **47** (6), 1528–1542.

WALTRUP, P. J. & BILLIG, F. S. 1973 Structure of shock waves in cylindrical ducts. *AIAA Journal* **11** (10), 1404–1408.

WANG, C., ZHANG, K. & CHENG, K. 2006 Pressure distribution measurements in scramjet isolators under asymmetric supersonic flow. In *44th AIAA Aerospace Sciences Meeting and Exhibit (2006-818)*.

WEISS, A. & OLIVIER, H. 2012 Influence of a normal slot boundary layer suction system onto a shock train. In *28th International Symposium on Shock Waves* (ed. K. Kontis), , vol. 2, pp. 141–146. Springer Berlin Heidelberg.

WEISS, J., MOHAMMED-TAIFOUR, A. & SCHWAAB, Q. 2015 Unsteady behavior of a pressure-induced turbulent separation bubble. *AIAA Journal* **53** (9).

WIENEKE, B. 2015 PIV uncertainty quantification from correlation statistics. *Measurement Science and Technology* **26** (7), 074002.

XIONG, B., FAN, X.-Q., WANG, Y., ZHOU, L. & TAO, Y. 2017*a* Back-pressure effects on unsteadiness of separation shock in a rectangular duct at Mach 3. *Acta Astronautica* **141**, 248–254.

XIONG, B., WANG, Z.-G., FAN, X.-Q. & WANG, Y. 2017*b* Experimental study on the flow separation and self-excited oscillation phenomenon in a rectangular duct. *Acta Astronautica* **133**, 158–165.

YAMANE, R., KONDO, E., TOMITA, Y. & SAKAE, N. 1984*a* Vibration of pseudo-shock in straight duct, 1st report, fluctuation of static pressure. *Bulletin of JSME* **27** (229), 1385–1392.

YAMANE, R., TAKAHASHI, M. & SAITO, H. 1984*b* Vibration of pseudo-shock in straight duct, 2nd report, correlation of static pressure fluctuation. *Bulletin of JSME* **27** (229), 1393–1398.